NASA CR - 66699
November 1968

PARAMETRIC STUDY OF B-58 ACCELERATION RESPONSE TO TURBULENCE AND COMPARISONS WITH FLIGHT DATA

By R. P. Peloubet, Jr. and R. L. Haller

Prepared under Contract No. NAS 1-7491

FORT WORTH DIVISION
GENERAL DYNAMICS CORPORATION
Fort Worth, Texas

for

Langley Research Center
NATIONAL AERONAUTICS AND SPACE ADMINISTRATION

PREFACE

This report was prepared by the Fort Worth Division of General Dynamics, Fort Worth, Texas under NASA Contract Number NAS 1-7491 and presents the work which was conducted under that contract during the time period from August 1967 through August 1968.

The project was monitored by Mr. A. G. Rainey of the NASA Langley Research Center.

TABLE OF CONTENTS

Table of Contents (Cont'd)

LIST OF TABLES

List of Tables (Con'd)

LIST OF FIGURES

List of Figures (Cont'd)

List of Figures (Cont'd)

List of Figures (Cont'd)

List of Figures (Cont'd)

List of Figures (Cont'd)

SUMMARY

The results of an investigation to compare gust response acceleration transfer functions computed by analysis to those measured during a B-58 flight test program are presented. The manner in which the B-58 data were measured and reduced to power spectral density and transfer function form is described. The degree of correlation between computed and measured B-58 natural frequencies and mode shapes is shown. Acceleration transfer functions computed for flight conditions which matched the flight conditions that existed during selected flight test gust runs are compared with the measured transfer functions. The results of analyses which were repeated for small variations in parameters employed in the calculation of the transfer functions are presented to show their separate effects. The effects of two-dimensional turbulence and spectral averaging are presented.

INTRODUCTION

The analysis of the response of an aircraft to flight through random turbulence can be divided into three parts. The first part consists of defining atmospheric turbulence properties such as gust velocity power spectral density (PSD) and the probability of encountering turbulence of any specified intensity.

The second part of the analysis consists of determining the airplane's response characteristics. When the airplane is treated as a linear system, its response characteristics are usually defined as the sinusoidal response of the airplane to flight through a continuous sinusoidal gust velocity profile fixed in space, with a one-foot-per-second maximum amplitude. The response characteristics are a function of the gust velocity wave length or frequency of excitation produced by penetrating the wave profile at a constant speed. This function is referred to as the gust response transfer function.

The third part of the analysis consists of combining the gust velocity PSD data and the airplanes gust response transfer function to determine the PSD of the response of the aircraft to atmospheric turbulence. The quantities $\bar{A}$ (rms response per unit rms gust velocity) and N_o (characteristic frequency) are computed from the response PSD. Included in the third part of the analysis is the interpretation of the $\bar{A}$ and N_o data to determine fatigue life, strenght requirements, and ride quality of the aircraft.

The investigation reported herein was aimed at the second part of the analysis, namely, the calculation of the transfer functions. The purpose of this investigation was to compute B-58 gust response transfer functions for flight conditions which match the flight conditions when gust response transfer functions were measured on the B-58. In addition, the relative importance of parameters and assumptions which affect the computed transfer functions were evaluated.

The scope of the investigation was limited to the response of the aircraft to the vertical gust velocity component. Only gust response transfer functions for accelerations along the fuselage centerline were considered with particular emphasis on the pilot station, center-of-gravity, and an aft fuselage station. Hence, this investigation will be of most value in evaluating means of computing transfer functions for ride quality assessment.

Transfer functions from three separate flight test gust response runs were selected for comparison purposes. The airplane configuration and flight condition during each flight test gust response run were matched as closely as possible. The airplane dry weight distribution and fuel distribution were matched for computing the normal modes of vibration employed in the analysis. Transfer functions were computed for the exact location of the accelerometers used to measure transfer functions. The Mach number, true airspeed, air density, c.g. location, and stability augmentation system gains used in the analysis matched the average conditions which existed during each gust run. For one of the flight conditions small variations were made to the matching parameters. Transfer functions were computed for variations in fuselage station, Mach number (and corresponding true airspeed), air density, c.g. location, and stability augmentation gains. The number of degrees of freedom employed in the analysis were varied. The effect of employing an aeroelastic mode as a degree of freedom was evaluated. The effect of replacing the unsteady aerodynamic forces in the equations of motion by quasi-steady aerodynamic terms was evaluated. The sensitivity of the transfer functions to two-dimensional turbulence effect was investigated. The effect of spectral averaging which is required in obtaining measured transfer functions from flight test data was evaluated by applying the equivalent averaging process in the calculation of the computed transfer functions. Finally, the effect of variations in structural damping and natural frequency were investigated. In addition to comparing measured and computed transfer functions directly, comparisons were made between the $\bar{A}$ and N_o data from computed and measured transfer functions.

B-58 GUST RESPONSE FLIGHT TEST PROGRAM

The purpose of the B-58 gust response flight-test program was to measure data for evaluating the fatigue life of the B-58 structure. A three view drawing of the B-58 is shown in figure 1. The tests were conducted during the time period from October 1961 through August 1962. The data which were selected for comparison were measured during August 1962. Emphasis was placed on measuring transfer functions rather than limiting attention to the gust response PSD. Since the PSD of the gust velocity during a single gust run is not necessarily representative of the gust velocity PSD obtained over a very long time period, the response PSD for a single run would not necessarily be representative. However, the transfer functions should be independent of the gust velocity PSD. Furthermore, the probability data needed to predict the probability of encountering turbulence of any specified level is directly related to a specified gust velocity PSD. These data were available for the Dryden gust velocity PSD. Therefore, each measured transfer function was combined with the Dryden gust velocity PSD (normalized to a one foot per second rms gust velocity) to obtain the response PSD for a standard gust PSD. This response PSD was then used to compute the $\bar{A}$ and N_o data. These data together with the gust velocity probability data, were then used to predict the expected number of response peaks exceeding any specified level for any specified number of flight hours. Finally, the expected number and magnitude of the stress peaks were used to predict the fatigue life of the structure.

Gust Probe

To measure the gust velocity a Douglas Aircraft 5-Probe Differential Pressure Head was attached to a boom mounted on the nose of the B-58. A sketch of the gust boom and probe is shown in figure 2. The basic head consists of two angle of attack probes, two angle of sideslip probes, and a total pressure probe mounted on a semi-spherical head. The angle of attack probes are mounted in the vertical plane at an angle of 45^{o} with the horizontal plane. These probes measure differential pressure. Two similar angle of sideslip probes are located in

Wing
Centerline Chord - 651.1 in
Semi-Span = 341.1655 in
Wing Area to Centerline = 1542.6 Ft^2
MAC = 434.05
L.E. MAC = 197.0
L.E. Sweep Angle = 60^o
T.E. Sweep Angle = -10^o

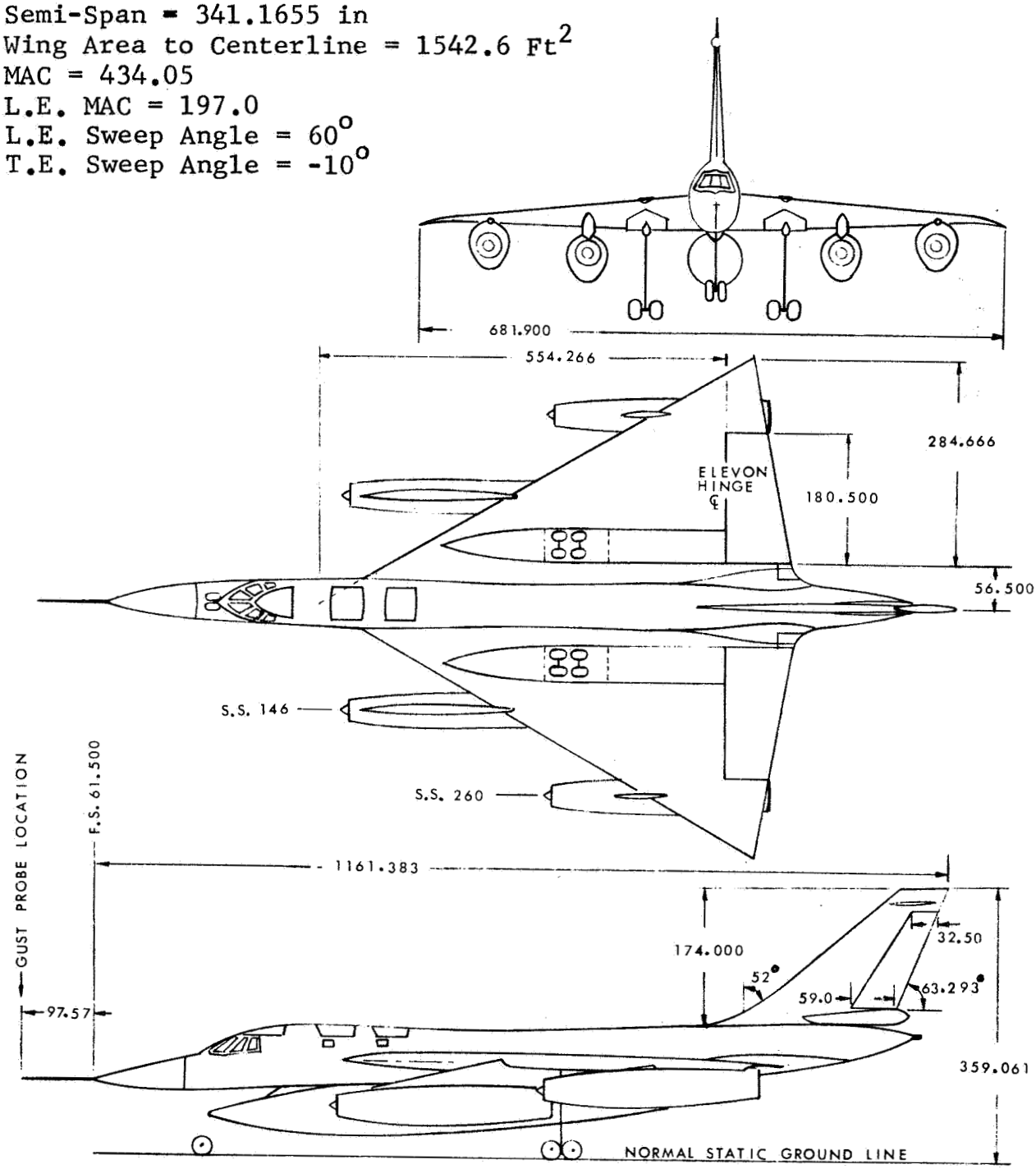

Figure 1 B-58 Three View

GUST BOOM

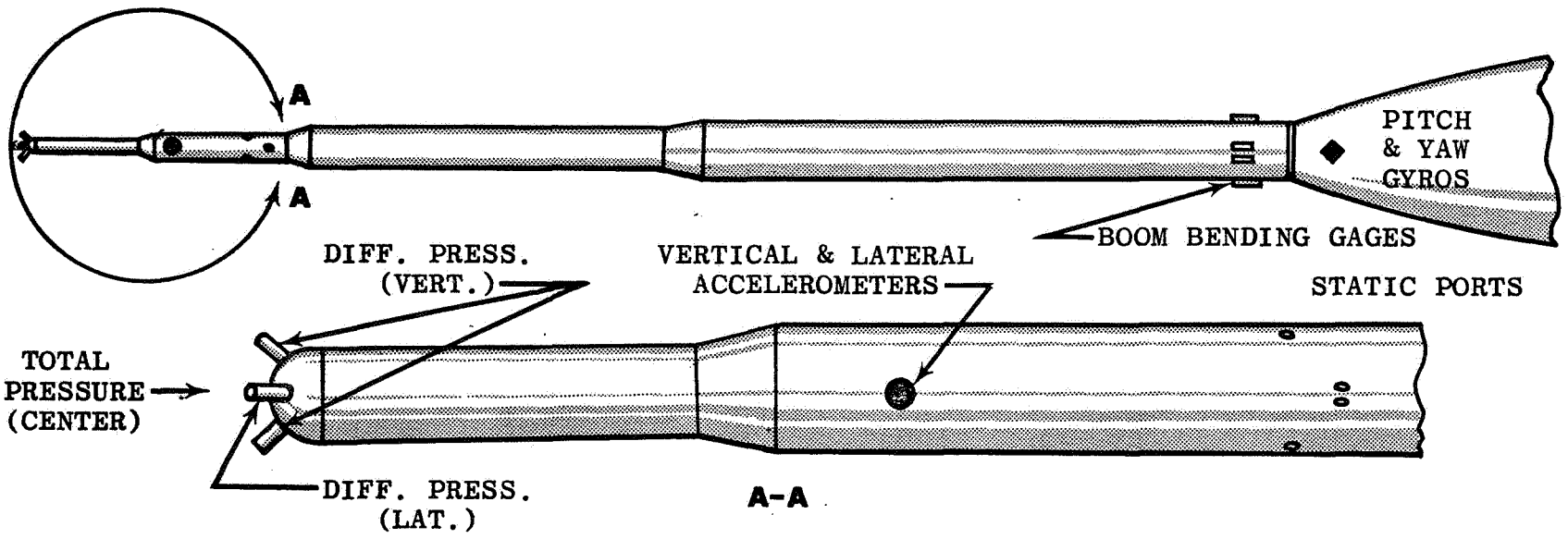

$$G_V = V_T \Delta\alpha - V_T \Delta\alpha' - V_T \int_0^t \Delta\dot{\theta}\, dt + \int_0^t \Delta a_Z\, dt$$

G_V	$V_T \Delta\alpha$	$V_T \Delta\alpha'$	$V_T \int_0^t \Delta\dot{\theta}\, dt$	$\int_0^t \Delta a_Z\, dt$
Vertical Gust Velocity	Total Change In Vert. Vel. At D.P. Head.	Position Correction of D.P. Head. Due To Boom Bending	Position Correction of D.P. Head. Due To Airplane Rotation	Vel. Correction For Airplane Vert. Vel. At D.P. Head.

Figure 2 Gust Probe

the horizontal plane and also measure differential pressure. Total pressure is measured at the center of the head. A static pressure sensing system is incorporated into the rear portion of the probe. Two separate static pressure systems are provided. Two vertically opposed pairs of orifices are used for computation of airspeed and altitude and for determination of vertical gust velocity. Two horizontally opposed pairs of orifices are used for the calculation of lateral gust velocity.

The vertical gust velocity is obtained from equation (1) which is also shown in figure 2. The first term on the right side of equation (1) is the total vertical velocity sensed at the pressure head.

$$w_g = v\Delta\alpha - v\Delta\alpha' - v\int_o^t \Delta\dot{\theta}\,dt + \int_o^t \Delta a_z dt \qquad (1)$$

The angle of attack at the pressure head is determined from the differential pressure measured by the angle of attack probes and the dynamic pressure is obtained from the total pressure and static pressure. The product of true airspeed and angle of attack gives the total vertical velocity at the head. The second term on the right corrects for changes in angle of attack sensed at the head due to boom bending. This correction is obtained from strain gauges at the base of the boom. The next term corrects for the airplane pitch angle. The pitch angle is obtained by integrating the pitch rate measured by a pitch rate gyro located in the nose of the airplane. The last term corrects for the angle of attack sensed at the head due to total airplane vertical motion. This term is obtained by integrating an accelerometer located very near the pressure head.

The lateral gust velocity is obtained in a completely analogous manner using the side slip differential pressure probes, strain gauges measuring boom side bending, a yaw rate gyro and a lateral accelerometer.

The gust probe is described in detail in reference 1 and 2.

Acceleration Instrumentation

The B-58 was instrumented with a large number of strain gauges for measuring stress response. More emphasis was placed on measuring stress response transfer functions than acceleration transfer functions because the ultimate goal was to

determine fatigue life. However, accelerometers were located at each of the points indicated in figure 3. Since the acceleration data were considered to have lower priority than the stress data, the acceleration data were not reduced to transfer function form for all accelerometers for each gust run. However, the data measured by the vertical accelerometers at the pilot station, A428, at the nominal center-of-gravity, A1, and at the tail cone, A11, were reduced to transfer function form for a large number of gust runs. These gust runs are listed in Table 1. Since transfer functions obtained from measurements by these three accelerometers are of most interest, from the ride quality point of view, they were chosen for comparison with computed transfer functions.

Airborne Recording System

A block diagram of the airborne recording system is shown in figure 4. The frequency range of interest for measuring data was between 0 and 10 cps. Bridge type instrumentation, such as, strain gauges, accelerometers, and pressure transducers were excited with a 100 cps voltage. Potentiometer type instrumentation such as rate gyros and position indicators were excited with a D. C. voltage. The applied intelligence, such as, strain or acceleration, amplitude modulated the excitation or carrier frequency.

The calibration rack contained a calibration unit. Calibration runs were made before and after each data run. During a data run the AM signal entering the calibration rack bypassed the calibration unit and was fed into an amplifier.

The output of the calibration rack was fed into a voltage controlled oscillator. The AM signal frequency modulated a standard RDB carrier frequency. Only RDB bands 11, 12 and 13 with carrier frequencies of 7.35 KC, 10.5 KC and 14.5 KC were used for the bridge type instrumentation. The frequency modulated output was then multiplexed with as many as seven other channels of intelligence which were treated in essentially the same manner. The multiplexed output signal was then amplified

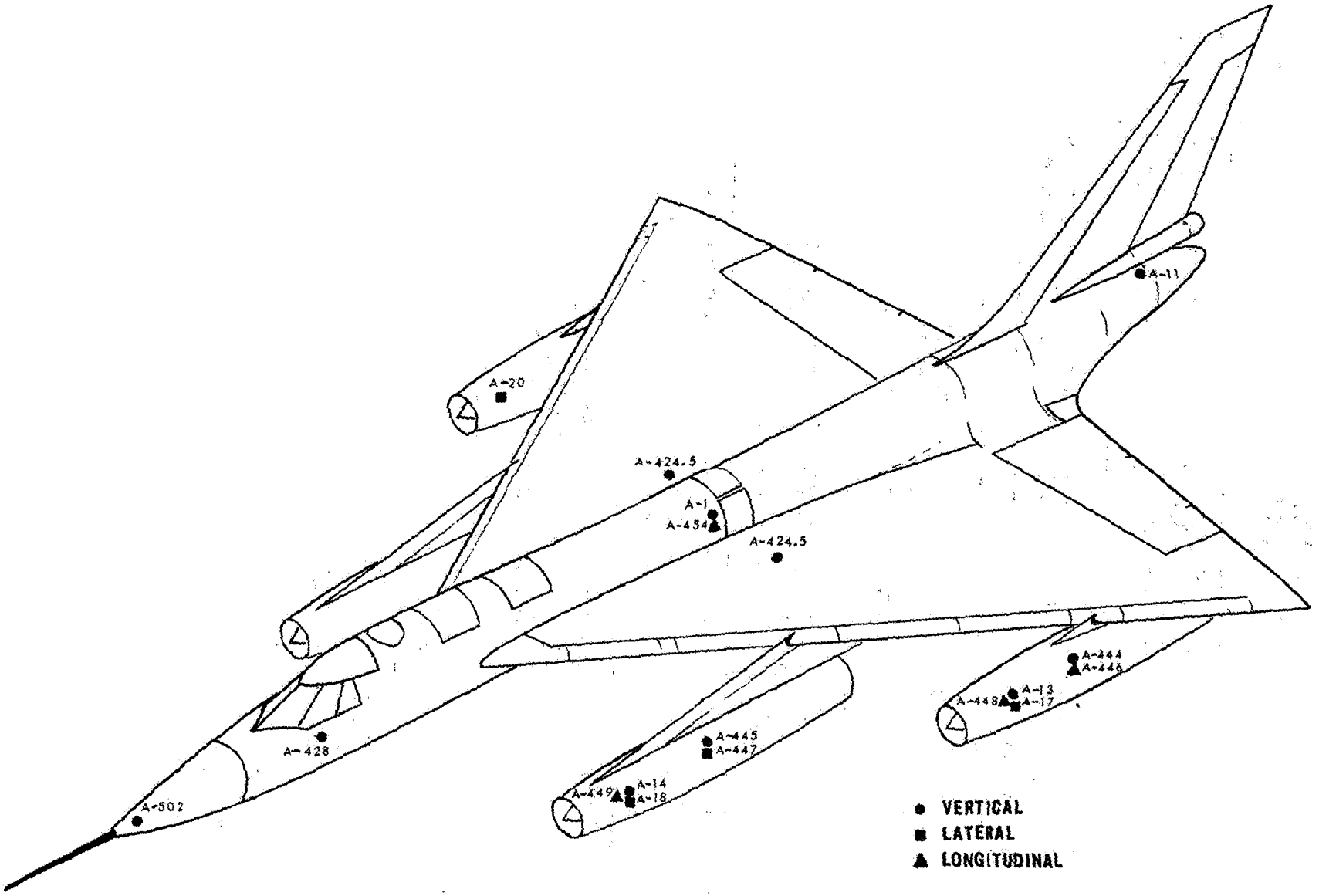

Figure 3 Accelerometer Installation

Table 1 B-58 Flight Test Gust Response Runs

Flight No.	Run No.	Gross Wt.	Mach No.	Airspeed (Ft/Sec)	A 428		A 1		A 11	
					$\bar{A}$	N_o	$\bar{A}$	N_o	$\bar{A}$	N_o
131	10	82575	.93	1069.0	.03188	2.473	.05440	1.957	.1159	2.436
134	9	92117	.92	1061.0	.03177	2.344	.04104	1.823	.09073	1.868
134	8	95894	.92	1060.4			.04342	1.760	.1024	2.105
131	6	97673	.92	1067.0	.00826	.912	.04821	1.988	.1037	2.441
133	3	97591	.92	1058.7					.01467	3.369
134	7	98350	.93	1062.0	.03178	2.411	.04334	1.711	.1041	2.070
114	3	117330	.93	1042.6	.02247	2.717	.05298	1.475	.1196	1.771
113	3	111080	.94	1065.0	.01692	2.484	.06267	1.489	.05794	2.293
113	4	108495	.94	1067.0	.02456	2.300	.05309	1.510	.1148	1.756
113	1	134446	.94	1064.0	.01875	2.416	.05052	1.380	.07906	1.638
113	2	131679	.94	1063.0	.01806	2.586	.05231	1.434	.08551	1.644
131	5	132198	.92	1061.0	.02776	2.506	.04009	1.617	.08559	2.154
130	1	131007	.93	1057.0						
131	7	94776	.80	926.0	.03138	2.357	.03628	1.901	.06906	2.584
114	2	133762	.81	899.9			.03210	1.353	.05904	1.824
131	4	134706	.80	920.0	.02782	2.355	.02966	1.616	.05710	2.514
131	3	137430	.80	921.0	.02814	2.391	.03019	1.638	.05888	2.454
132	5	143137	.80	915.8	.03204	2.152	.02999	1.394	.05192	2.148
134	1	161024	.79	916.0	.02459	2.135	.02115	1.507	.00593	.939
131	2	139584	.65	744.0	.02229	2.045	.02200	1.452	.0397	2.228
131	1	141131	.62	713.0	.02285	1.905	.02303	1.429	.04028	2.173
131	9	91660	.40	466.0	.01470	1.443	.01607	1.026	.02279	1.699
131	8	92515	.40	468.0	.01359	1.493	.01472	1.081	.02139	1.801
130	2	94872	.39	447.0	.01724	1.082	.01873	.8310	.02556	1.510
132	1	98534	.40	451.0	.01621	1.300	.01629	.9149	.02260	1.700

Alt. = 2000 Ft.

A 1 - C.G. Vertical
A 428 - Pilot Station Vertical
A 11 - Aft Fuselage Vertical

AIRBORNE RECORDING SYSTEM

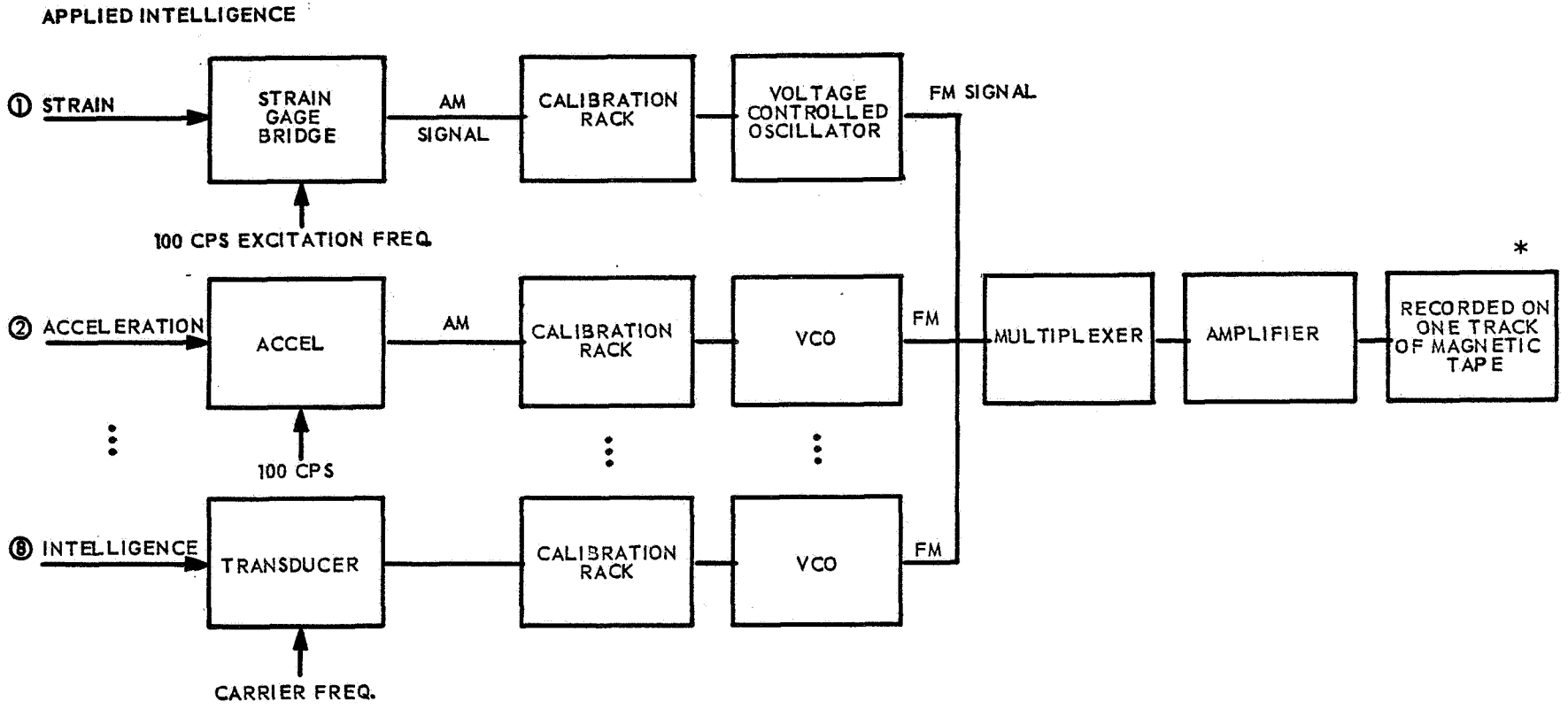

* CAN RECORD 24 TRACKS ON ONE TAPE.
EACH TRACK CAN HAVE 8 MULTIPLIED CHANNELS (RDB 6–13)

CALIBRATION MADE BEFORE AND AFTER EACH RUN.

Figure 4 Airborne Recording System

and recorded on the track of a magnetic tape. As many as 24 tracks of intelligence could be recorded simultaneously. Each track could contain as many as 8 multiplexed channels.

In addition to the 24 tracks of intelligence, two tracks were used to record a 16 KC signal for WOW and flutter corrections in the playback system and to make skewed tape corrections. Two tracks were used to record time reference signals (000 to 999 seconds). One track was used to record an audio signal containing pilot and engineer comments.

The airborne recording system was manufactured by Victor. The magnetic tape speed during the gust runs was 15 inches per second. The airborne recording system is described in more detail in reference 1.

Recording Playback System

A diagram of the Recording Playback System is shown in figure 5. The magnetic tape recorded in flight was fed into a tape playback unit. The 16 KC reference signals were fed into 16 KC discriminators. The output of the 16 KC discriminators were used to control the tape playback speed in order that any low frequency variations in the recording speed would be duplicated by the playback speed. High frequency tape speed variations were made by a electronic amplitude and phase adjustment on each RDB frequency discriminator from the output of the 16 KC discriminators. Differences between output of the two 16 KC discriminators were used to make skewed tape corrections.

The playback unit selected and read each track of the magnetic tape. The signal was fed into a preamplifier. The output of the preamplifier which was a signal containing the 8 multiplexed FM channels was fed into eight separate filters and discriminators. Each filter passed one of the RDB frequency bands and fed the output into a discriminator. The outputs of the 8 discriminators were 8 separate AM channels. Each AM channel was fed into a demodulator. The output was the original applied intelligence.

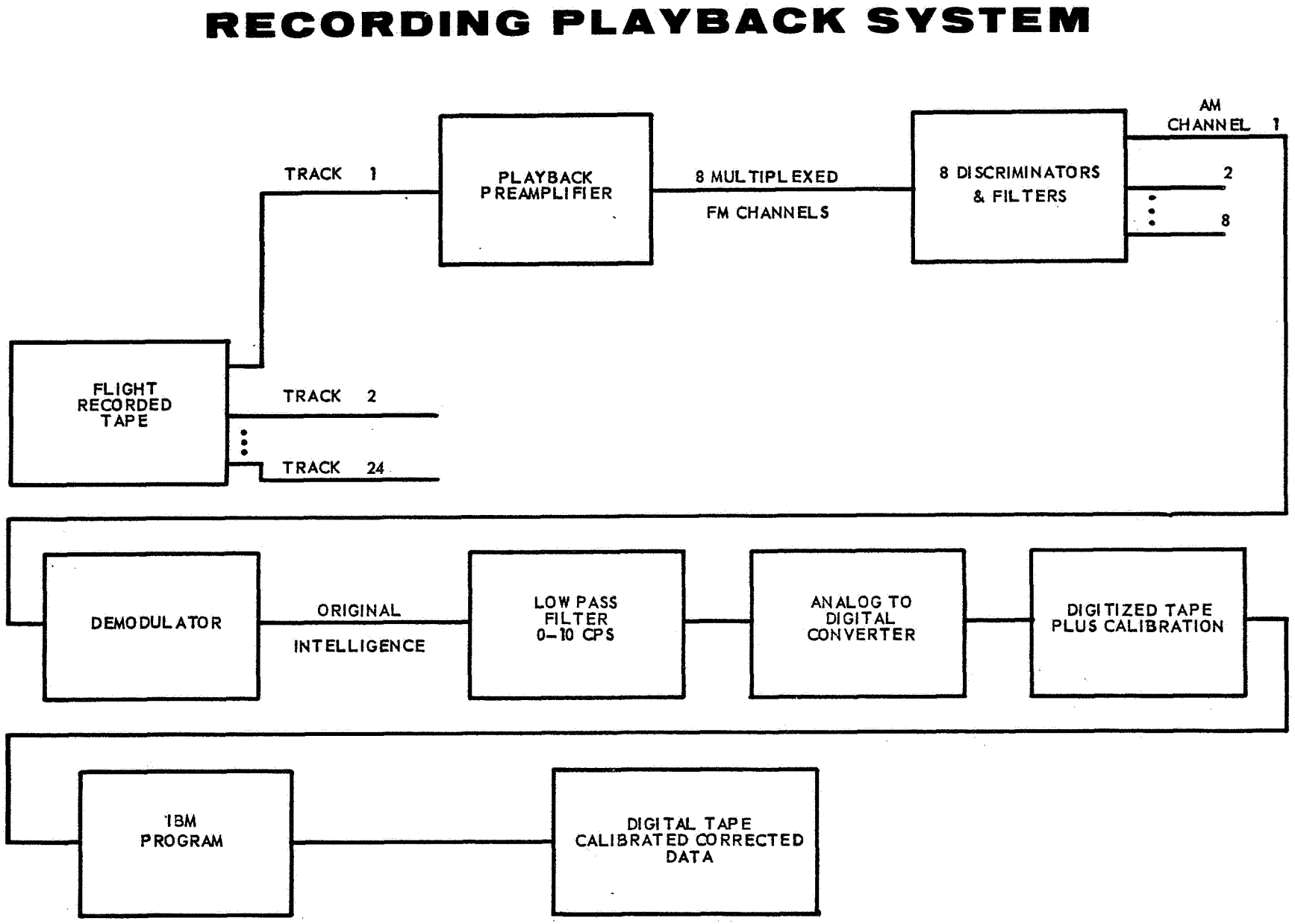

Figure 5 Recording Playback System

The output of the demodulator was fed into a low pass filter which is down 3 Db at 8 cps. This operation was performed to minimize the effect of fold-back in subsequenct PSD computations. The output of the filter was fed into a analog to digital converter which read the data at equal time intervals and recorded it on magnetic tape. For power spectral analyses the response data was sampled at 1/20th of a second intervals and the data used to compute the gust velocity was sampled at 1/40th of a second intervals. The reason for the difference in sampling rates is explained in the subsequent discussion of the reduction of the data to transfer function form. The Analog to Digital converter was a Model 210, High-Speed Digital Data Recording System, built by Beckman System Divisions. The output of the analog to digital converter was a digitized tape of the data runs and calibration runs.

This tape was fed into a IBM program which used the calibration data to calibrate and scale the measured data to engineering units of stress, acceleration, rate, etc. The output was digital tape of calibrated corrected data.

The tape playback unit was manufactured by Victor. The discriminators and demodulators, etc, were manufactured by Electro Mechanical Research Company. The recording playback system is described in more detail in reference 1.

Reduction of Data to Transfer Function Form

All measured data used to compute the gust velocity, as expressed by equation (1), were sampled at the rate of 40 samples per second by the analog to digital converter. The pitch rate and the vertical acceleration at the gust probe were integrated numerically. However, before integrating a mean value and a linear ramp were subtracted from the digitized pitch rate and acceleration data. This was accomplished by fitting the data with a least squares first order polynomial and then subtracting the polynomial from the data.

Since the integrated and non-integrated data of equation (1) are combined to obtain the gust velocity it is important that the numerical integration technique produce exactly a 90^{o} phase shift, in order that the combined data is not distorted by the numerical integration. The integration of the pitch rate and acceleration in equation (1) were performed by Tick's

integration method,

$$y_n = y_{n-1} + \Delta t \quad (.182x_n + .636x_{n-\frac{1}{2}} + .182x_{n-1}) \tag{2}$$

where y is the integral of x. The transfer function for the integration method has a 90° phase shift:

$$H(\omega) = -j\left[\frac{-.636\ \Delta t \sin\left(\frac{\omega\Delta t}{2}\right) - .182\ \Delta t \sin\ (\omega\Delta t)}{1 - \cos\ (\omega\Delta t)}\right] \tag{3}$$

Tick's method requires 40 samples per second data in order to yield 20 samples per second data after integration. This is the reason that the gust data were sampled 40 times per second where as the response data were sampled only 20 times per second.

After all terms in equation (1) were combined the resulting gust velocity data were fitted with a least squares third order polynomial and the polynomial was subtracted from the data. This operation was performed in an attempt to remove very low frequency spurious signals from the data. An illustration of gust velocity data before and after this operation is shown in reference 3.

From this point, the gust data and the response data were integrated by the same method. Since no subsequent operation required the addition of integrated and non-integrated data the 90° phase shift requirement for the integration technique was relaxed. All subsequent numerical integrations employed the rectangular integration method,

$$y_n = y_{n-1} + \Delta t\ x_n \tag{4}$$

which has the following transfer function

$$\begin{aligned} |H(\omega)| &= \left(\frac{\Delta t}{2}\right) \quad \frac{1}{\sin\left(\frac{\omega\Delta t}{2}\right)} \\ \phi(\omega) &= \tan^{-1}\left(\frac{-\cos\left(\frac{\omega\Delta t}{2}\right)}{\sin\left(\frac{\omega\Delta t}{2}\right)}\right) \end{aligned} \tag{5}$$

Transfer functions are obtained from quotients in which the numerator and denominator have been obtained through the same numerical integration processes. Hence, the errors introduced by equation (4) being less than a perfect integrator are the same for both numerator and denominator and cancel in the quotient. Therefore, the use of equation (4) should introduce no errors in either the magnitude or phase angle of the transfer functions.

The mean of both the gust velocity and the response data was computed by the following relation.

$$\bar{x} = \frac{1}{N} \sum_{n=1}^{N} x_n' \tag{6}$$

where N is the total number of data points for the gust velocity or each response item. Since all gust runs were approximately four minutes the value of N was approximately 4800. The mean was then subtracted from the data.

$$x_n = x_n' - \bar{x} \tag{7}$$

The data was then prewhitened by the following operation.

$$\hat{x}_n = x_n - x_{n-1} \tag{8}$$

The prewhitening operation has the following transfer function magnitude.

$$H(\omega) = 2 \sin \left(\frac{\omega \Delta t}{2}\right) \tag{9}$$

The prewhitening operation was applied to both the gust velocity data and the response data.

The autocorrelation function was computed for the prewhitened data as follows.

$$\hat{R}(m) = \frac{1}{N-m} \sum_{n=1}^{N-m} \hat{x}_n \hat{x}_{n+m} \tag{10}$$

The maximum number of lags, M , was 150. Since the increment was 1/20 of a second, the Nyquist frequency was 10 cps. The choice of 150 lags implies 150 estimates of the power spectrum at 1/15 cps frequency intervals.

The so called "raw" estimates of the PSD were obtained by the following relation.

$$\hat{L}_h = 4\Delta t \sum_{m=0}^{M} e_m \hat{R}(m) \cos\left(\frac{hm\pi}{M}\right) \qquad (11)$$

where $e_m = \frac{1}{2}$ $\quad m = 0, M$

$e_m = 1$ $\quad 0 < m < M$

The so called "smoothed" estimates of the PSD were obtained by the following relations.

$$\begin{aligned} \hat{\phi}_o &= \tfrac{1}{2}\hat{L}_o + \tfrac{1}{2}\hat{L}_1 \\ \hat{\phi}_h &= \tfrac{1}{4}\hat{L}_{h-1} + \tfrac{1}{2}\hat{L}_h + \tfrac{1}{4}\hat{L}_{h+1} \qquad 1 \leq h \leq M-1 \qquad (12) \\ \hat{\phi}_M &= \tfrac{1}{2}\hat{L}_{M-1} + \tfrac{1}{2}\hat{L}_M \end{aligned}$$

The cross correlation functions were computed for the pre-whitened data by the following relations

$$\hat{R}_{xy}(m) = \frac{1}{N-m} \sum_{n=1}^{N-m} \hat{x}_n \hat{y}_{n+m} \qquad (13)$$

$$\hat{R}_{yx}(m) = \frac{1}{N-m} \sum_{n=1}^{N-m} \hat{y}_n \hat{x}_{n+m} \qquad (14)$$

where x and y are used to indicate gust velocity and response data respectively in equations (13) through (22).

Raw estimates of the cospectrum $\hat{c}_{xy}(h)$ and the quad-spectrum $\hat{q}_{xy}(h)$ were then obtained by the following relations

$$\hat{c}_{xy}(h) = 4\,\Delta t \sum_{m=0}^{M} e_m \left[\frac{\hat{R}_{xy}(m) + \hat{R}_{yx}(m)}{2} \right] \cos \frac{hm\pi}{M} \qquad (15)$$

$$\hat{q}_{xy}(h) = 4\,\Delta t \sum_{m=0}^{M} e_m \left[\frac{\hat{R}_{xy}(m) - \hat{R}_{yx}(m)}{2} \right] \sin \frac{hm\pi}{M} \qquad (16)$$

Raw estimates of the cross spectrum are then expressed as

$$\hat{L}_{xy}(h) = \hat{c}_{xy}(h) - i\,\hat{q}_{xy}(h) \qquad (17)$$

The raw cross spectrum estimates were then smoothed using the relations expressed in equation (12).

All smoothed spectral and cross spectral estimates were then "post darkened" by dividing by the square of the magnitude of the prewhitening transfer function.

$$\phi_x(h) = \frac{\hat{\phi}_x(h)}{4 \sin^2 \left(\frac{\pi h}{2M} \right)}$$

$$\phi_{xy}(h) = \frac{\hat{\phi}_{xy}(h)}{4 \sin^2 \left(\frac{\pi h}{2M} \right)} \qquad (18)$$

$$\phi_y(h) = \frac{\hat{\phi}_y(h)}{4 \sin^2 \left(\frac{\pi h}{2M} \right)}$$

The transfer functions were computed by two methods. One method yields only information on the magnitude of the transfer function and was obtained from the ratio of the response PSD to the gust PSD as follows.

$$\left| H_s(h) \right| = \left[\frac{\phi_y(h)}{\phi_x(h)} \right]^{\frac{1}{2}} \qquad (19)$$

The other method yields information on both the magnitude and phase angle of the transfer function and is obtained from the ratio of the cross spectrum to the gust PSD.

$$H_c(h) = \frac{\phi_{xy}(h)}{\phi_x(h)} \tag{20}$$

or the magnitude can be expressed as

$$\left|H_c(h)\right| = \frac{\left[c_{xy}^2(h) + q_{xy}^2(h)\right]^{\frac{1}{2}}}{\phi_x(h)} \tag{21}$$

and the phase angle can be expressed as

$$\theta(h) = \tan^{-1}\left[\frac{-q_{xy}(h)}{c_{xy}(h)}\right] \tag{22}$$

The coherency function was computed from the transfer functions as obtained by both methods.

$$\gamma^2(h) = \frac{\left|H_c(h)\right|^2}{H_s^2(h)} \tag{23}$$

Using the relationships developed by Goodman (reference 4), confidence bands on the transfer functions were computed.

$$\left|H_U(h)\right|^2 = \left|\frac{H_c(h)}{1-E/100}\right|^2 \tag{24}$$

$$\left|H_L(h)\right|^2 = \left|\frac{H_c(h)}{1+E/100}\right|^2 \tag{25}$$

where H_U and H_L are the upper and lower confidence bands respectively and

$$E(\gamma^2) = \left\{ \frac{1-\gamma^2}{\gamma 2} \left[(1-c)^{-M/N-M} - 1 \right] \right\}^{\frac{1}{2}} \quad (26)$$

where c is the confidence limit (c = .90 means 90% confidence limit).

The transfer functions H_U, H_c and H_L, were then combined successively with the Dryden gust spectrum to obtain a response spectrum based on a standard gust spectrum.

$$\phi(\omega) = \left| H(\omega) \right|^2 \phi_D(\omega) \quad (27)$$

where

$$\phi_D(\omega) = \frac{2L}{V} \frac{\left[1 + 3\left(\frac{\omega L}{V}\right)^2\right]}{\left[1 + \left(\frac{\omega L}{V}\right)^2\right]^2} \quad (28)$$

These response spectra were then integrated to obtain the $\bar{A}$ and N_o as follows

$$\bar{A}^2 = \frac{\pi}{M \Delta t} \sum_{h=1}^{M} \phi_h \quad (29)$$

$$N_o^2 = \frac{1}{\bar{A}^2} \frac{\pi}{M \Delta t} \sum_{h=1}^{M} \left(\frac{h\pi}{M \Delta t}\right)^2 \phi_h \quad (30)$$

Hence, an $\bar{A}$ and N_o pair was obtained using the measured H_c transfer function and the upper and lower 90% confidence limits on H_c.

Selection of Flight Conditions

From table 1 gust runs 131-10, 134-7 and 131-3 were chosen for comparing measured and computed transfer functions. These gust runs were chosen primarily because the pilot station acceleration coherency functions for these three runs were the

best of the data available. Secondary considerations, such as, an objective to compare transfer functions at two Mach numbers and for both a heavy and light gross weight also led to the selection of these three runs. The transfer functions H_s and H_c together with the coherency function γ^2 for each of these three runs are shown in figures 6, 7 and 8.

If the relationship between the vertical component of the gust velocity measured at the gust probe (input) and the vertical acceleration measured at the pilot station (output) is linear and if no errors or noise have been introduced into the measurement of the input and the output then the coherency function would be unity. Therefore, the proximity of the coherency function to the unity level can be used as a means of judging the quality of the measured transfer function or the degree of confidence in its validity. Since the coherency function cannot exceed the unit level, low confidence is indicated by low values of the coherency function. In figures 6 through 8 it can be seen that the coherency function is high in the frequency range where the magnitude of the transfer function is high (high signal to noise ratio) and the coherency function is low where the transfer function magnitude is low (low signal to noise ratio). The transfer function obtained from the cross spectra, H_c, was used rather than H_s for comparison with the computed transfer functions because H_c is not affected by some error sources that do affect H_s, reference 5.

The $\bar{A}$ and N_o data obtained by combining the transfer functions H_U, H_c and H_L with the Dryden gust spectrum with a 500 feet scale of turbulence are listed in table 2. The data are listed for the pilot station accelerometer A428, nominal center-of-gravity accelerometer A1, and the tail cone accelerometer A11.

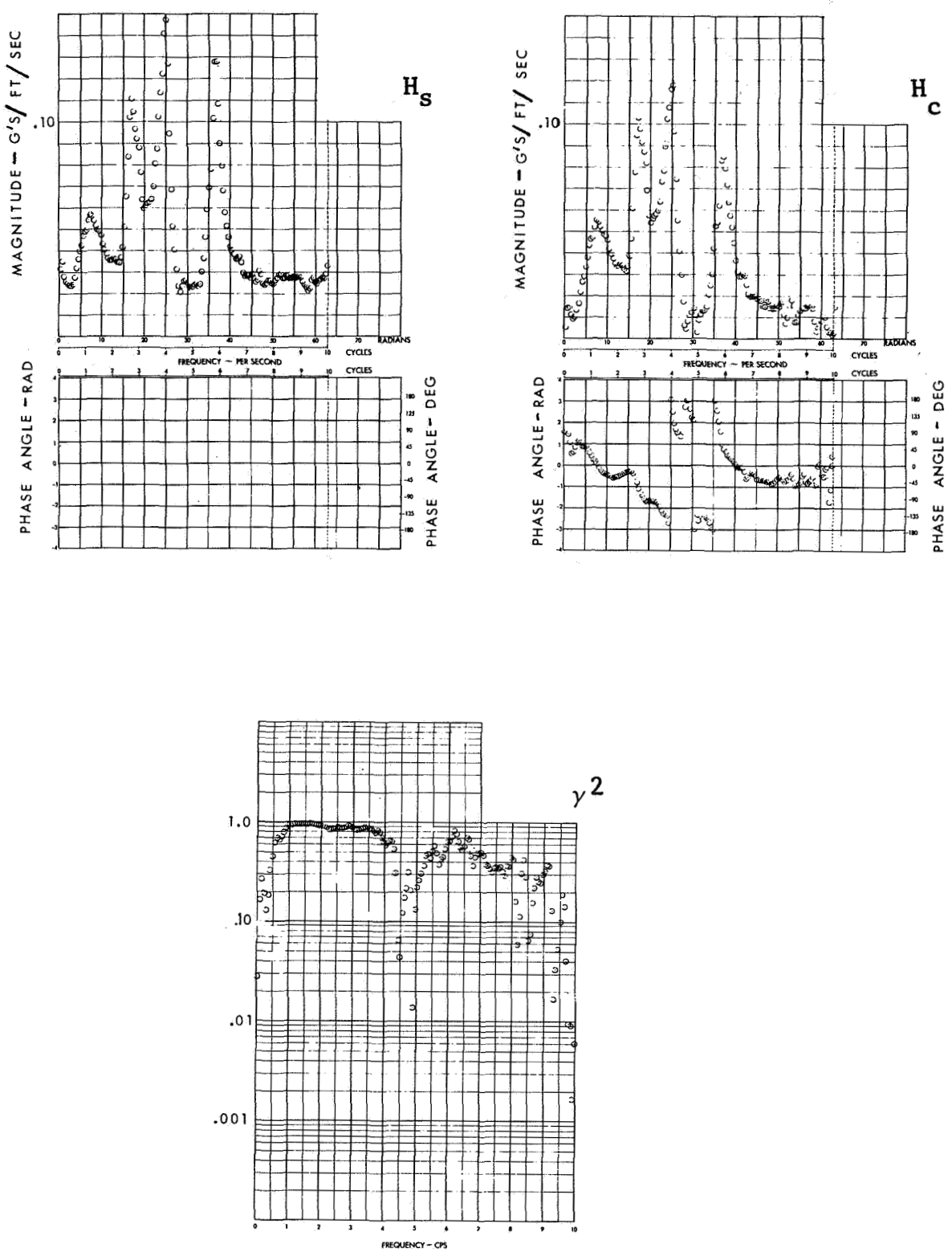

Figure 6 Pilot Station Acceleration Transfer Functions and Coherency Function for Gust Run 131-10

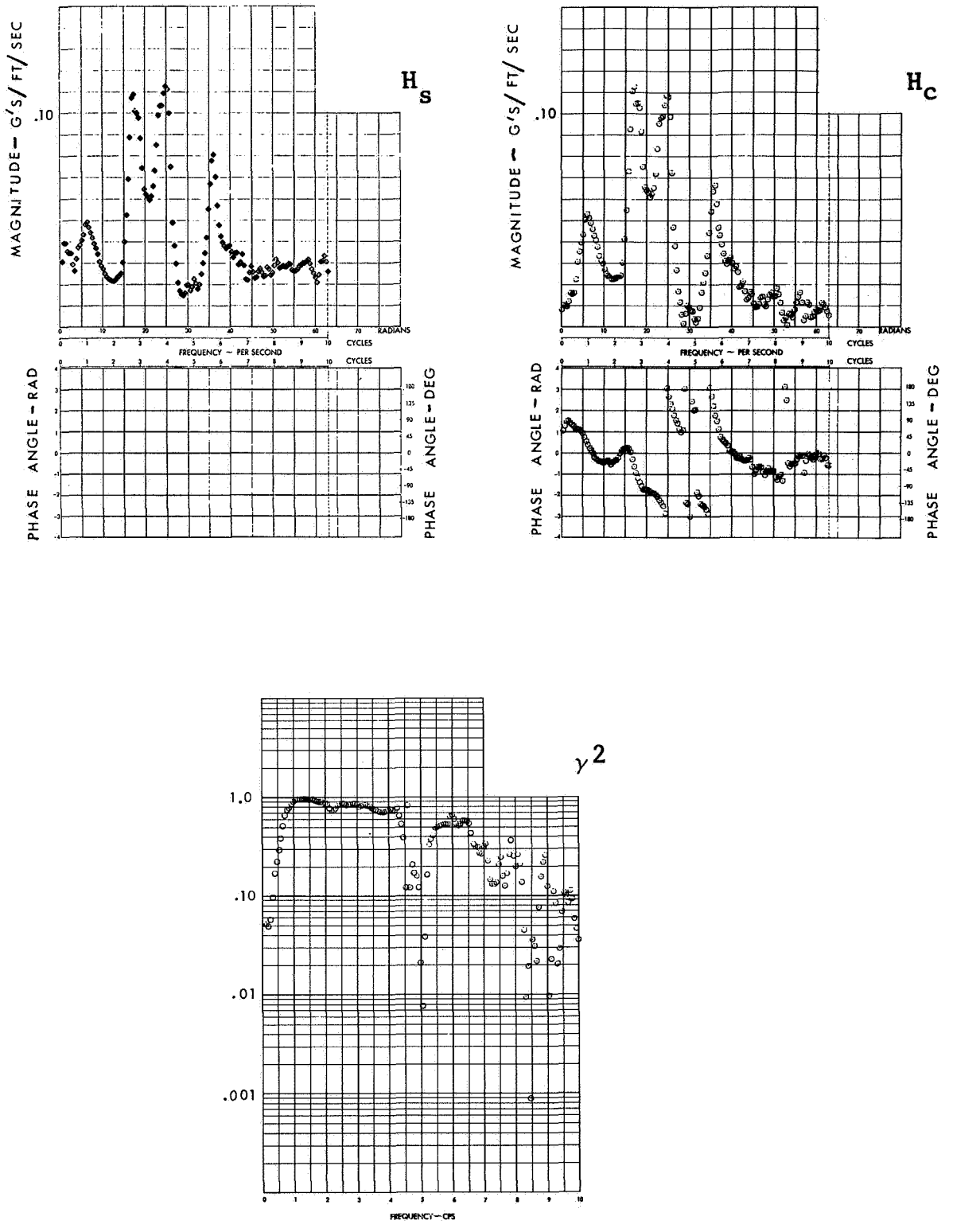

Figure 7 Pilot Station Acceleration Transfer Functions and Coherency Function for Gust Run 134-7

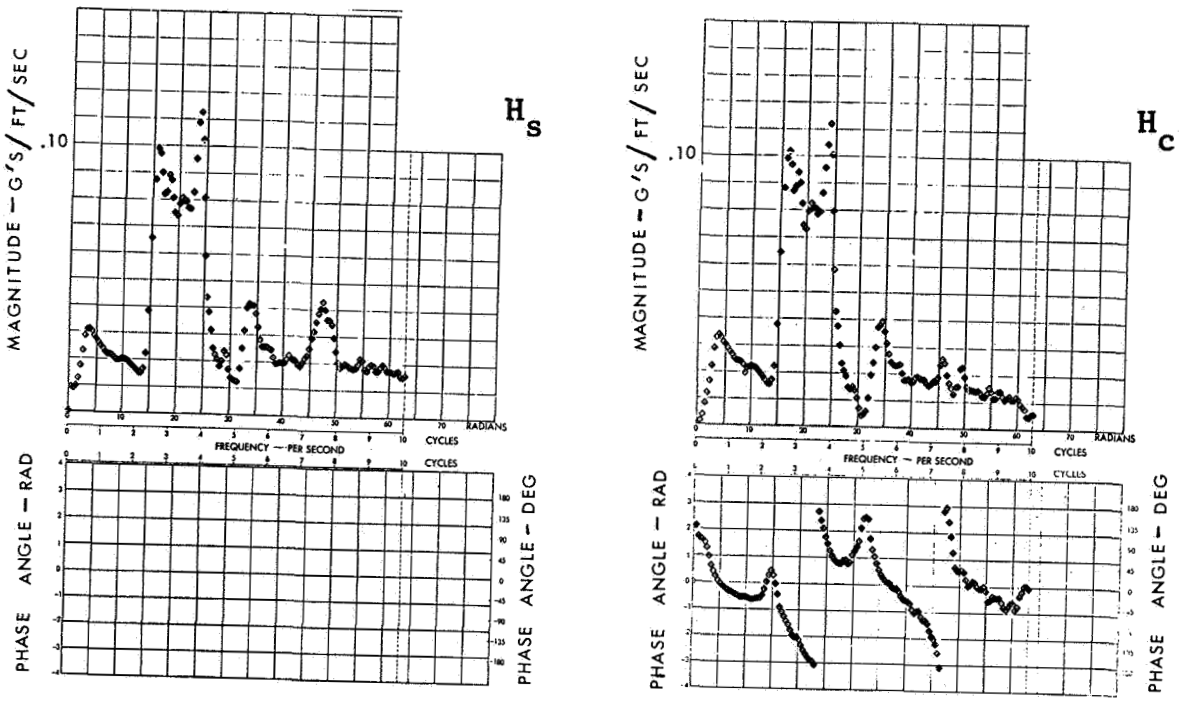

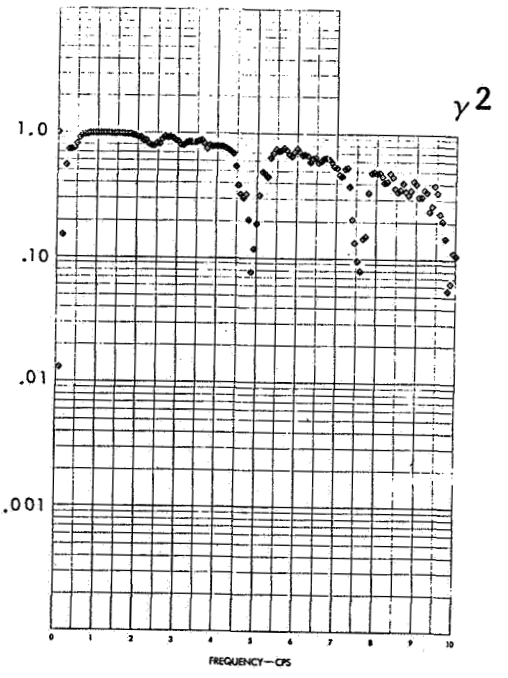

Figure 8 Pilot Station Acceleration Transfer Functions and Coherency Function for Gust Run 131-3 .

Table 2 Measured $\bar{A}$ and N_o Data

Run	H	A428		A1		A11	
		$\bar{A}$	N_o	$\bar{A}$	N_o	$\bar{A}$	N_o
131-10	H_U	.04016	2.638	.0926	6.428	.1345	2.521
	H_c	.03188	2.473	.0544	1.957	.1159	2.436
	H_L	.02811	2.421	.0495	1.897	.1051	2.350
134-7	H_U	.1080	8.159	.3379	9.180	.3216	8.635
	H_c	.03178	2.411	.04334	1.711	.1041	2.070
	H_L	.02766	2.399	.03901	1.696	.09341	2.025
131-3	H_U	.03262	2.862	.03465	2.708	.06740	2.589
	H_c	.02814	2.391	.03019	1.638	.05888	2.454
	H_L	.02550	2.327	.02756	1.553	.05336	2.371

METHOD OF ANALYSIS

The response of the aircraft was computed by solving sets of simultaneous equations obtained by applying Lagrange's equations of motion.

$$\frac{d}{dt}\frac{L}{\partial \dot{q}_r} - \frac{\partial L}{\partial q_r} = Q_r \qquad r=1, \ldots N \qquad (31)$$

where L = $T-U$
T = kinetic energy
U = potential energy
Q_r = generalized force on the rth generalized coordinate
q_r = rth generalized coordinate

The deflection at any point on the aircraft is assumed to be equal to a summation of the deflections at the point due to each of the generalized coordinates. For example, the vertical displacement at a point would be expressed as

$$h(x,y,z,t) = \sum_{r=1}^{N} h_r(x,y,z)\, q_r(t) \qquad (32)$$

where x,y,z = Cartesian coordinate system attached to the aircraft
$h(x,y,z,t)$ = total vertical deflection at point (x,y,z) at time t
$h_r(x,y,z)$ = vertical deflection at point (x,y,z) due to unit deflection of the rth generalized coordinate

When natural modes of vibration of the structure are used as generalized coordinates, the equations reduce to the following form

$$M_{rr}\ddot{q}_r + D_{rr}\dot{q}_r + \omega_r^2 M_{rr} + M_{r1}\, q_1 + \ldots + M_{rs}\, q_s + \ldots + M_{rN}\, q_N = Q_r \qquad (33)$$

where M_{rs} = generalized mass term
D_{rr} = generalized damping term
ω_r = natural frequency of the rth mode

The generalized force includes the generalized aerodynamic force produced by the gust and the generalized aerodynamic force produced by the airplane response. For sinusoidal motion, equation (33) reduces to the following expression, in matrix form, after dividing each equation by $-\omega^2$.

$$\begin{bmatrix} A_{11} & A_{12} & \cdots & A_{1N} \\ A_{21} & A_{22} & \cdots & A_{2N} \\ \vdots & \vdots & & \vdots \\ A_{N1} & A_{N2} & \cdots & A_{NN} \end{bmatrix} \begin{Bmatrix} q_1 \\ q_2 \\ \vdots \\ q_N \end{Bmatrix} = - \begin{Bmatrix} A_{1g} \\ A_{2g} \\ \vdots \\ A_{ng} \end{Bmatrix} \tag{34}$$

where $[\,]$ is a square matrix

$\{\,\}$ is a column matrix

$$A_{rs} = \left[1-\left(\frac{\omega_r}{\omega}\right)^2 \quad (1+jg_r) \right] M_{rr} + Q_{rr}/\omega^2 \qquad \text{for} \quad r = s$$

$$A_{rs} = M_{rs} + Q_{rs}/\omega^2 \qquad \text{for} \quad r \neq s$$

$$A_{rg} = Q_{rg}/\omega^2$$

ω = exciting frequency (gust velocity frequency)

g_r = structural damping coefficient for the rth mode.

The complex magnitude of the generalized coordinates are related to the generalized coordinates by the equation:

$$q_r = \bar{q}_r e^{i\omega t}$$

The natural frequencies and mode shapes are basic input data in the equations of motion.

Generalized Aerodynamic Terms

The generalized aerodynamic terms on the left side of equation (34) are of the form

$$Q_{rs} = \int_S h_r \, \Delta p_s \, dS \tag{35}$$

where Δp_s is the pressure between the upper and lower surface of the aircraft due to the sth generalized coordinate oscillating with unit amplitude and the integration is over the lifting surface planform.

The generalized aerodynamic terms on the right side of equation (34) are of the form

$$Q_{rg} = \int_S h_r \Delta p_g \, dS \tag{36}$$

where Δp_g is the pressure difference between the upper and lower surface of the vehicle due to the downwash produced by a unit sinusoidal gust wave traveling across the aircraft in the negative flight direction.

The oscillatory pressure distribution over the wing was obtained by the kernel function method which can be expressed as follows, reference 6.

$$w(x,y) = \int_S\int \Delta p(\xi \eta) \, K \, (x-\xi \, , \, y-\eta \, , \, k, \, M) \, d\xi \, d\eta \tag{37}$$

where ξ, η is a coordinate system identical to the x,y coordinate system that is employed in order to relate the pressure at points (ξ, η) due to the downwash at point (x,y).

K = kernel function

k = reduced frequency

M = Mach number

w(x,y) = downwash at point x,y.

A solution to equation (37) was obtained by expressing the unknown pressure as

$$\Delta p(x,y) = \sum_{\mu} \Delta p_{\mu} \, (x,y) \, a_{\mu} \tag{38}$$

where Δp_{μ} (x,y) is a known predetermined pressure distribution, and a_{μ} is an unknown coefficient.

Equation (38) was substituted into equation (37) and the integration performed by the numerical method shown in reference 7 to obtain one equation relating downwash at one point to the coefficients. The operation was repeated for μ different downwash locations to obtain a set of μ equations with μ unknowns.

$$\{ w \} = [B] \{ a \} \tag{39}$$

Solving for a - coefficients by equation (39) and substituting into equation (38) the pressure distribution is obtained. When computing Q_{rs} terms the downwash at a point is expressed by

$$w_s = V\alpha_s + i\omega h_s \tag{40}$$

where h_s and α_s are the deflection and streamwise slope at a point on the surface due to unit deflection of the sth generalized coordinates. When computing pressure due to the gust velocity, for the Q_{rg} terms, h and α are expressed as follows:

$$h_g = \frac{-b}{Vk} \sin \left(\frac{kx}{b}\right)$$

and

$$\alpha_g = \frac{1}{V} \cos \left(\frac{kx}{b} \right) \tag{41}$$

The origin of the x axis was located at the gust probe so that the phase angles of the computed transfer functions could be compared directly to the phase angles of the measured transfer functions. Twenty-five downwash points were employed on each side of the fuselage centerline. The location of these downwash points are shown on figure 9.

Aerodynamic terms for the portion of the fuselage forward of the wing-fuselage intersection were computed by slender body theory. Aerodynamic terms for the nacelles and pylons were computed by quasi-steady theory using wind tunnel data. The total aerodynamic matrices for all components were then summed.

$$[Q_{rs}] = [Q_{rs}]_{wing} + [Q_{rs}]_{fuselage} + [Q_{rs}]_{nacelles} \tag{42}$$

The total gust aerodynamic terms, Q_{rg}, were obtained in the same manner. Rigid body translation, rigid body pitch and the first eight symmetric modes of vibration were used as degrees of freedom. The elements of the total aerodynamic matrix which were computed for rigid body translation and rigid body pitch for the lowest value of frequency (1/15 cps) were used to determine the slope of the lift curve, C_{L_α}, and aerodynamic center (a.c.) resulting from this method of analysis. The computed C_{L_α} and a.c. for each of the three selected flight conditions are tabulated in table 3 for comparison with the corresponding data obtained from wind tunnel tests of rigid B-58 model.

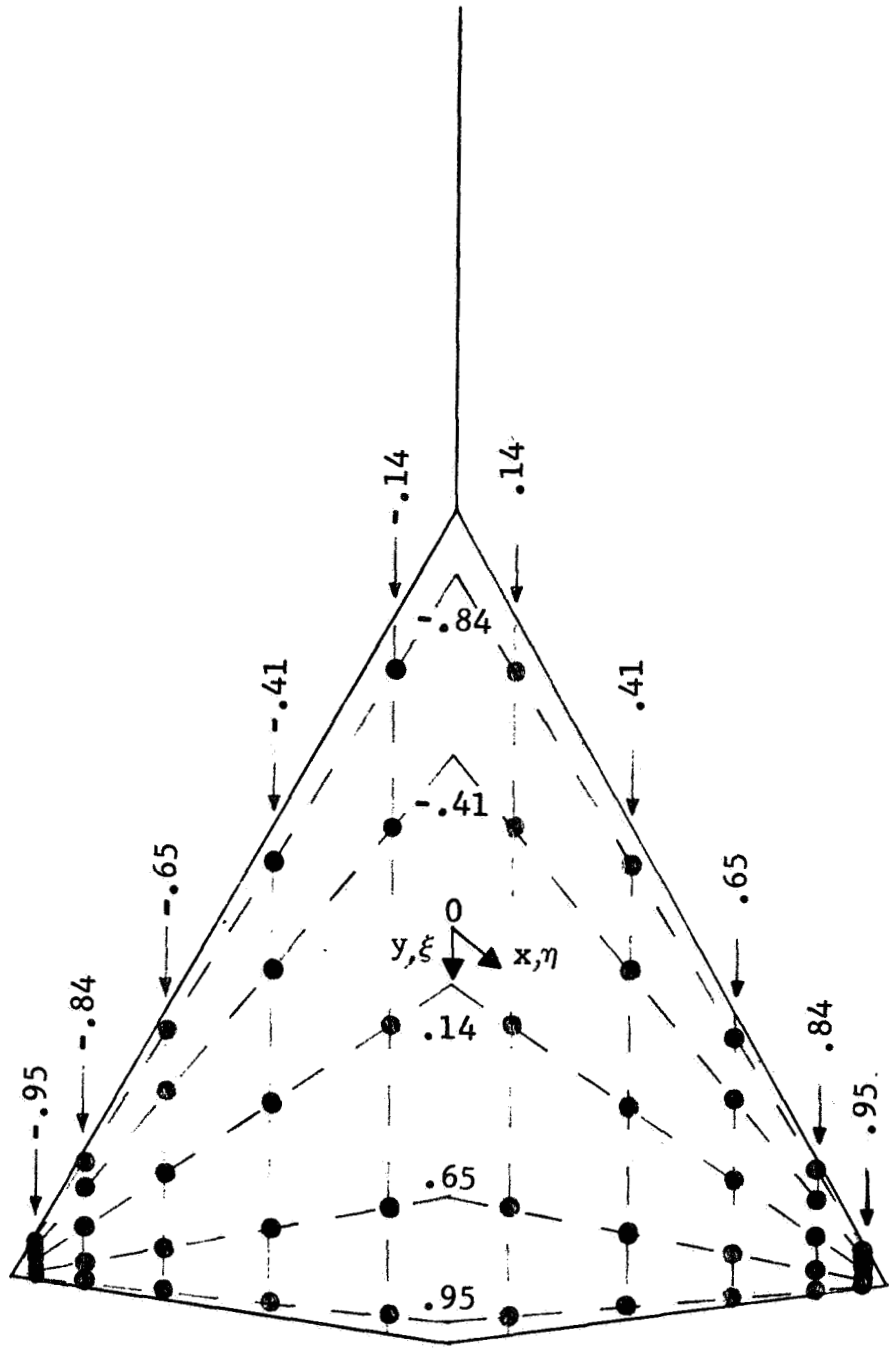

Figure 9 Location of Downwash Collocation Points

Table 3 Rigid Airplane Stability Derivatives

	Run 134-7 and 131-10	Run 131-3
Measured C_{L_α}	3.1742	2.8419
Measured a.c. % MAC	37.1	34.0
Computed Wing + Nacelle C_{L_α}	3.2171	2.9148
Computed Wing + **Nacelle** a.c. % MAC	38.23	35.62
Computed fuselage C_{L_α}	.03482	.03482
Computed fuselage a.c. % MAC	-82.53	-82.53
Computed Total C_{L_α}	3.252	2.949
Computed Total a.c. % MAC	36.95	34.23
Adjusting Constant C_1	.9774	.9616
Adjusting Constant C_2	.8572	1.1193

It can be seen that the comparison is quite good. However, to force perfect agreement in the low frequency range the magnitude of the pressure computed for rigid body motion were adjusted by first computing the constants C_1 and C_2 in the following equations:

$$C_1 \left(C_{L_\alpha}\right)_{\text{wing + nacelle}} + C_2 \left(C_{L_\alpha}\right)_{\text{fuselage}} = \left(C_{L_\alpha}\right)_{\text{measured}}$$

$$C_1 \left(C_{M_\alpha}\right)_{\text{wing + nacelle}} + C_2 \left(C_{M_\alpha}\right)_{\text{fuselage}} = \left(C_{M_\alpha}\right)_{\text{measured}} \tag{43}$$

These two constants were used to adjust the two columns in the total aerodynamic matrix which contain the pressure produced by rigid body translation and rigid body pitch in the following manner.

$$C_1 \left[Q_{rT} \; Q_{rP} \right]_{\text{wing + nacelle}} + C_2 \left[Q_{rT} \; Q_{rP} \right]_{\text{fuselage}} = \left[Q_{rT} \; Q_{rP} \right]_{\substack{\text{adjusted} \\ \text{total}}} \tag{44}$$

The required values of C_1 and C_2 are listed in table 3. The adjustment to the wing and nacelle terms are very small whereas the adjustment to the fuselage terms is relatively large. However, the fuselage terms are a small part of the total aerodynamic terms before and after adjusting. The same constants were applied to the column of gust aerodynamic terms Q_{rg} in the same manner. No attempt was made to adjust the aerodynamic terms which contain pressure produced by each of the flexible degrees of freedom.

Longitudinal Stability Augmentation System

The stability augmentation system (SAS) requires the calculation of additional aerodynamic terms. A block diagram of the B-58 SAS is shown in figure 10. It can be seen that the elevon deflection (deflecting symmetrically as an elevator) can be expressed as the product of an acceleration transfer function times the acceleration and a pitch rate transfer function times the pitch rate.

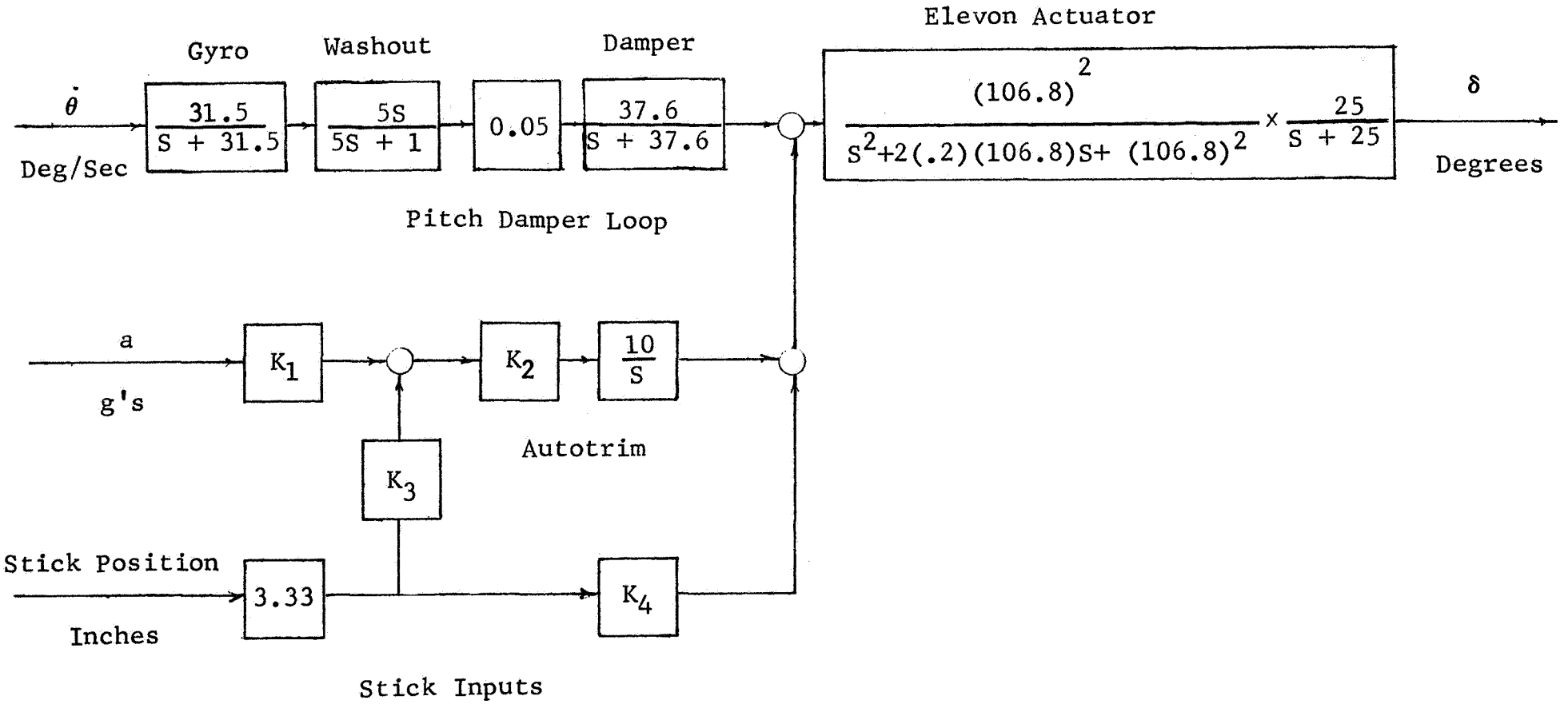

Figure 10 B-58 Longitudinal Stability Augmentation System

$$\delta(\omega) = H_a(a)\, a(\omega) + H_{\dot\theta}(\omega)\, \dot\theta(\omega) \tag{45}$$

The acceleration and pitch rate at the acceleration and pitch SAS sensor location can be expressed as

$$a(\omega) = -\omega^2 \left[h_1 \bar q_1 + h_2 \bar q_2 + \ldots + h_N \bar q_N \right] \tag{46}$$

$$\dot\theta(\omega) = i\omega \left[\theta_1 \bar q_1 + \theta_2 \bar q_2 + \ldots + \theta_N \bar q_N \right] \tag{47}$$

where h_r and θ_r are the vertical deflection and slope at the sensor location for unit deflection of the rth generalized coordinate.

Substituting equations (46) and (47) into (45) yields an expression for the elevon deflection with the following form

$$\delta(\omega) = \delta_1(\omega)\, \bar q_1 + \delta_2(\omega)\, \bar q_2 + \ldots + \delta_N(\omega)\, \bar q_N \tag{48}$$

The pressure produced by this elevon deflection can be expressed as

$$\Delta p_\delta(\omega) = \delta_1(\omega)\, \Delta p_{\delta_o}(\omega) \bar q_1 + \delta_2(\omega)\, \Delta p_{\delta_o}(\omega) \bar q_2 + \ldots + \delta_N(\omega)\, \Delta p_{\delta_o}(\omega) \bar q_N \tag{49}$$

where $\Delta p_{\delta_o}(\omega)$ = pressure produced by unit elevon deflection.

Consequently, the N x N generalized aerodynamic matrix produced by the addition of the SAS can be expressed as the product of a column and row matrix as follows,

$$\left[Q_{r\delta} \right] = \begin{Bmatrix} Q_{1\delta_o} \\ Q_{2\delta_o} \\ \vdots \\ Q_{N\delta_o} \end{Bmatrix} \left\lfloor \delta_1(\omega)\ \delta_2(\omega)\ \ldots\ \delta_N(\omega) \right\rfloor \tag{50}$$

where

$$Q_{r\delta_o} = \iint h_r \, \Delta p_{\delta_o} \, dS \qquad (51)$$

The aerodynamic terms defined by equation (51) were computed by strip theory. The elevon span was divided into six strips for these calculations. The $Q_{T\delta} = 1$ element for the lowest frequency (1/15 cps) was used to evaluate C_{L_δ} as predicted by strip theory. The values of C_{L_δ} obtained for each of the three flight conditions are tabulated in table 4 for comparison with measured wind tunnel data obtained from a rigid mode. All $[Q_{r\delta}]$ terms were multiplied by the ratio of measured to computed C_{L_δ}. No attempt was made to alter the location of the a.c. due to elevon deflection as predicted by strip theory. The computed and measured a.c. locations are also shown in table 4 for comparison.

Table 4 Rigid Control Surface Stability Derivatives

	Run 134-7 and 131-10	131-3
Measured C_{L_δ} - per radian	1.355	1.2291
Measured (a.c.) - % MAC	83.00	71.4
Computed C_{L_δ} - per radian	1.9918	1.989
Computed (a.c.) - % MAC	84.20	84.20

For analyses of the unaugmented airplane (SAS OFF) the aerodynamic elements described by equation (42) were employed. For analyses of the augmented airplane (SAS ON) the $[Q_{r\delta}]$ terms expressed by equation (50) were added to the $[Q_{rs}]$ matrix of equation (42). A matrix of control surface generalized mass terms $[M_{r\delta}]$ were computed in an analogous manner and added to the $[M_{rs}]$ matrix when SAS was engaged.

$$\left[M_{r\delta}\right] = \begin{Bmatrix} M_{1\delta_o} \\ M_{2\delta_o} \\ \vdots \\ M_{N\delta_o} \end{Bmatrix} \left\lfloor \delta_1(\omega) \quad \delta_2(\omega) \cdots \quad \delta_N(\omega) \right\rfloor \tag{52}$$

$$M_{r\delta_o} = \int_{\text{Elevon}} h_r \, h_{\delta_o} \, dm \tag{53}$$

Gust Response Calculations

The equations of motion were solved for the generalized coordinate complex magnitudes over a frequency range from 1/15 cps to 10 cps at 1/15 cps increments. To obtain acceleration transfer functions, the response of the generalized coordinates were combined in the following manner:

$$H_a(\omega) = \sum_{r=1}^{N} -\omega^2 \, h_r \, \bar{q}_r \tag{54}$$

where h_r is the deflection due to unit amount of the rth generalized coordinate at the point where the acceleration is to be computed.

The acceleration response PSD was computed by combining the square of the magnitude of the transfer function with the Dryden gust spectrum with unit rms gust velocity.

$$\phi_a(\omega) = \left|H_a(\omega)\right|^2 \phi_D(\omega) \tag{55}$$

The $\bar{A}$ and N_o data were computed by substituting the computed response PSD into equations (29) and (30). A 500 feet scale of turbulence was employed in the calculation of $\bar{A}$ and N_o throughout the investigation.

COMPUTED NATURAL MODES OF VIBRATION

During the test program of the B-58 airplane two ground vibration tests were conducted. The first test was conducted on airplane number 2 with the airplane supported on its landing gear. The second ground vibration test (GVT) was conducted on airplane number 42 with the airplane supported on a soft suspension system. The results of the second ground vibration test, and a description of the soft suspension system is reported in reference 8. The airplane number 42 ground vibration test is considered to be more representative of the free-free modes and frequencies of the airplane because of the soft suspension support system, therefore these test results have been chosen as the baseline for mode shape correlation. The gross weight of this configuration was 142,872 lb.

Mathematical Model of the Structure

The simulation of the B-58 wing structure is shown in figure 11. Stiffness matrices were computed for each beam segment between intersecting spars and bulkheads. The torsional stiffness of the individual regions inclosed by spars, bulkheads and upper and lower skin surfaces were represented by torque boxes. Similar representations of the nacelles, pylons and fuselage were employed. The fuselage forward of the wing was represented by a beam. The individual stiffness matrices were combined to obtain a stiffness matrix defining force deflection relations for 598 coordinates.

Lumped masses were located at 99 of the coordinates defined by the stiffness matrix. By combining the mass matrix with the flexibility matrix associated with the mass points, the eigenvalue problem was formulated for determining the natural frequencies and mode shapes.

Stiffness Matrix Modifications

The lumped mass distribution which matches the 142,872 lb. configuration of airplane 42 during the ground vibration tests was computed. These mass data were then used with the stiffness matrix mathematical model of the structure to compute normal modes of vibration. The comparison of frequencies between these two sets of data are listed in table 5.

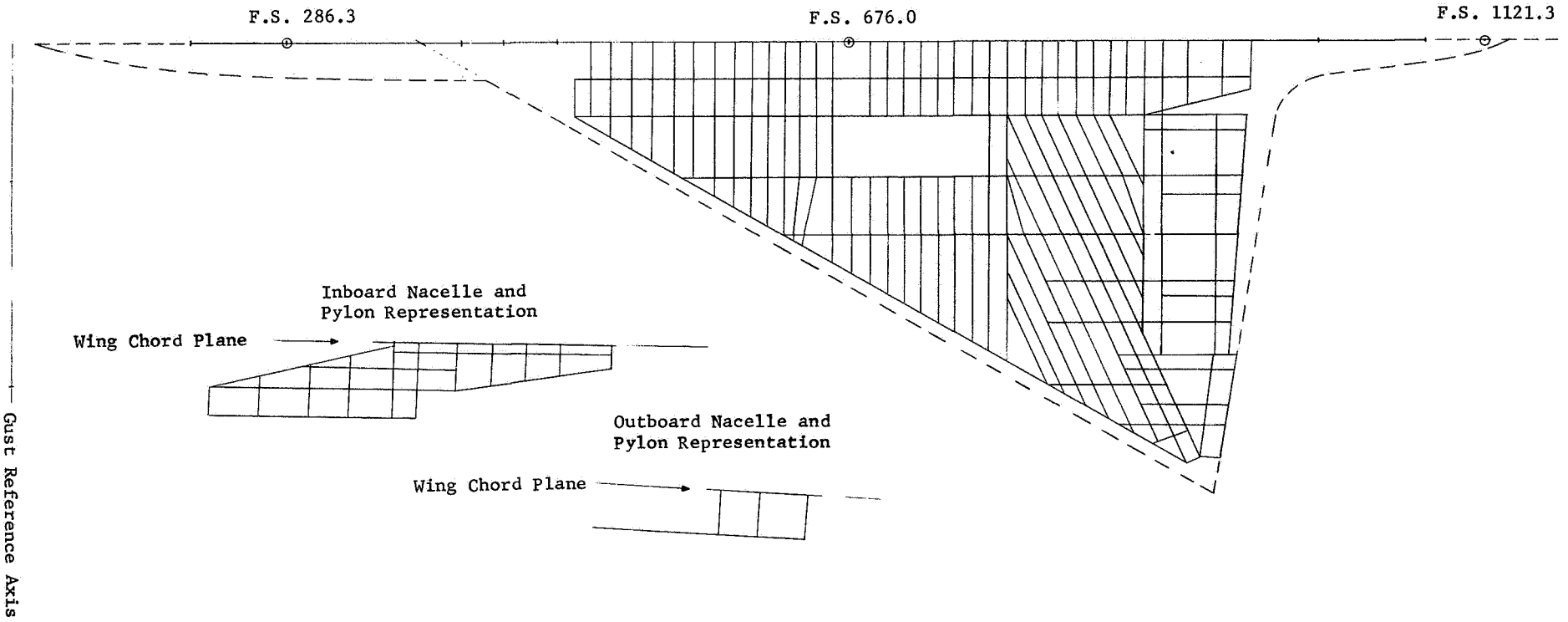

Figure 11 B-58 Structural Simulation

Table 5 Comparison of GVT and Computed Frequencies With Original Stiffness Matrix

Mode Number	GVT (cps)	Analysis (cps)	GVT/Analysis
1	2.7	2.24	1.205
2	3.2	2.68	1.194
3	3.5	3.29	1.064
4	4.1	3.88	1.057
5	5.0	4.94	1.013

The mode shapes compare very well between the ground vibration test and the analysis. Modes 1 and 2 consist primarily of wing and fuselage deformations whereas modes 3, 4 and 5 consist primarily of engine motion. Modifications of the stiffness matrix were then made with the aim of increasing the frequencies of mode 1 and 2 without significantly changing the frequencies of modes 3, 4 and 5; and without significantly changing the mode shapes of any of the modes. The major changes which were incorporated to accomplish the above goal are described below:

1. The fuselage vertical bending stiffness was increased an average of 40 percent. (This increase was not uniform over the entire fuselage length)

2. Since the lower cover of the main gear wheel well is not a load carrying member and hence the wheel well is a rather flexible torque box, neither the lower nor upper cover skins on the wheel well were included in the original stiffness matrix representation. The contribution of the upper skin in both spanwise and chordwise bending as well as torsion was included in the new idealization.

3. The fuselage weight and fuselage fuel were originally represented as lumped masses along the wing fuselage intersection (span station 32). These lumped masses were lumped along the fuselage centerline (span station zero).

4. The airplane was supported on a soft mount during the ground vibration tests. The soft mounting produced a rigid body pitch frequency of 0.15 cps and a rigid body vertical translation frequency of 0.91 cps. The previously computed modes corresponded to free-free modes with the airplane freely suspended in space. The soft mounting system was added to the revised stiffness matrix representation.

The above mentioned changes in the stiffness matrix representation improved the correlation between GVT modes and analysis, but the correlation was still far from satisfactory. To improve the frequency correlation, the mathematical model of the structure was stiffened in selected regions rather than uniformly. These increases in stiffness can be justified only on the basis of producing better agreement between measured and computed natural frequencies and mode shapes. These changes in the stiffness matrix representation of the structure are described below:

1. The fuselage and inboard rib (span station 56) were increased in modulus by 12.4%.

2. The wing spar modulus was everywhere increased by 40%.

3. Local beefup on the wing leading edge in the vicinity of the inboard pylon was also made in an attempt to increase the inboard nacelle pitch frequency.

4. The wing torsional stiffness between the inboard and outboard pylons was increased by 35% to cause the outboard nacelle pitch frequency to be increased.

The natural frequencies which were computed after these changes in the stiffness matrix were incorporated are shown in table 6 for comparison with the GVT data.

Table 6 Comparison of GVT and Computed Frequencies With Modified Stiffness Matrix

MODE	GVT FREQ.	COMPUTED FREQ.	GVT/COMPUTED
Rigid Body Pitch	.15	.246	.609
Rigid Body Translation	.91	.908	1.001
Flexible Mode 1	2.70	2.720	.996
Flexible Mode 2	3.20	3.150	1.014
Flexible Mode 3	3.50	3.460	1.012
Flexible Mode 4	4.10	3.790	1.082
Flexible Mode 5	5.00	4.840	1.032

These computed mode shapes are compared to the measured mode shapes in Appendix A.

Based on the above correlation of modes and frequencies, the simulation of the actual stiffness by the mathematical model was considered adequate. Free-free modes for the gross weight condition discussed above were computed. These modes show that the soft suspension system has very little effect upon the computed modes and frequencies.

Normal Modes for Selected Flight Conditions

Since there are no structural changes between the airplane number 42 structure and the airplane number 7 structure (which was the airplane used for measuring gust response data), the same stiffness data used in the mode correlation work could be used in the calculation of normal modes for the selected flight conditions. There were however, significant changes in the unfueled weight of the two airplanes.

The fuel weights by tanks for the three selected flight conditions were combined with the airplane number 7 dry weight and distributed to the simulation panel points. The first eight flexible free-free modes for the three selected flight conditions were then computed. These modes are shown in Appendix B. The natural mode frequencies are listed in table 7.

Table 7 Computed Natural Frequencies

Mode	Run 131-10 Freq.-cps	Run 134-7 Freq.-cps	Run 131-3 Freq.-cps
1	2.949	2.901	2.676
2	3.365	3.339	3.192
3	3.493	3.485	3.467
4	4.143	4.113	3.827
5	5.572	5.397	5.021
6	6.602	6.505	6.276
7	7.289	7.162	6.813
8	9.235	9.202	8.698

The amplitudes of the modes for the three selected flight conditions along the fuselage centerline are shown in figure 12. These curves show which modes have the largest relative amplitudes and will contribute most to the fuselage centerline response.

The gross mass properties which were matched for each gust run are list in table 8.

Table 8 Gross Mass Properties

Run No.	G.W. lb.	C.G. F.S.(in)	C.G. % MAC	I_{pitch} lb. in^2
131-10	82,575	659.37	25.2	1.6824×10^9
134-7	98,350	658.50	25.0	1.7774×10^9
131-3	137,430	666.31	26.8	2.4913×10^9

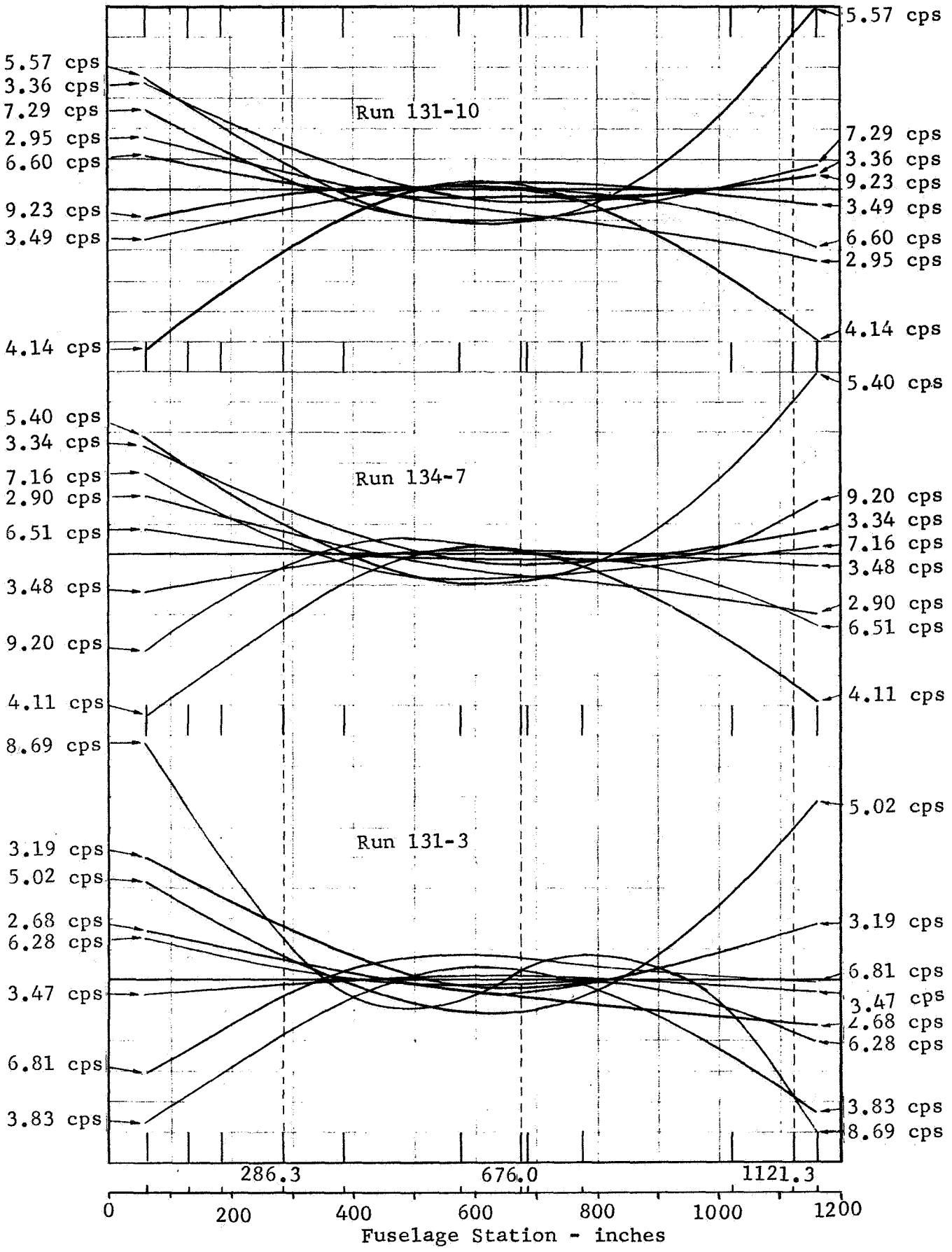

Figure 12 Fuselage Centerline Vertical Deflections for Each Computed Natural Mode

CORRELATION WITH MATCHED FLIGHT CONDITIONS

In addition to matching the gross weight and center of gravity, the Mach number (M), true airspeed (V), and air density (ρ), and SAS gains which existed during each of the three selected gust runs were matched exactly in the analyses and are listed in table 9.

Table 9 Matched Flight Conditions

RUN NO.	ρ slugs/ft^3	Mach	V ft/sec	SAS GAINS		
				K_1	K_2	Pitch Damper
131-10	.002068	.93	1069	.5	.149	.05
134-7	.002092	.93	1062	.5	.161	.05
131-3	.002073	.80	921	1.0	.062	.05

As mentioned earlier the aerodynamic terms associated with the rigid body degrees of freedom were adjusted to force the slope of the lift curve and aerodynamic center to agree exactly (at zero frequency) with measured data from wind tunnel tests of a rigid model. After the first eight symmetric modes of vibration were added to the rigid body degrees of freedom, the flexible slope of the lift curve and aerodynamic center as predicted by the analysis at 1/15 cps were computed. The measured and computed slope of the lift curve (C_{L_α}) and the aerodynamic center (a.c.) are listed for comparison in table 10.

Table 10 Comparison of Flexible Stability Derivatives

Run No.	Measured				Analysis Flexible	
	Rigid		Flexible			
	C_{L_α}	a.c. F.S.	C_{L_α}	a.c. F.S.	C_{L_α}	a.c. F.S.
131-10	3.1742	711.01	2.804	696.30	3.1589	710.52
134-7	3.1742	711.01	2.804	696.30	3.1605	710.58
131-3	2.8419	697.56	2.618	688.97	2.8434	697.68

The data in the above table, listed under measured flexible derivations were obtained by applying flexibility correction factors to the measured rigid data. Hence, a comparison of the flexible data is equivalent to comparing flexibility effects predicted by a static aeroelastic analysis with that predicted by the method used to predict transfer functions as the frequency approaches zero. The flexible degrees of freedom produce virtually no change in the rigid stability derivatives at 1/15 cps.

Correlation With Gust Run 131-10

Comparisons between computed and measured transfer functions for run 131-10 are shown in figure 13. The upper portions of the plots are the magnitudes of the transfer functions and the lower portion is the phase angle between the response and the gust velocity at the gust probe location. The transfer function as measured at the pilot station (A428), near the nominal center of gravity (A1), and at the fuselage tail cone (A11) are shown from left to right. All plots were made by the SC4020 automatic plotter.

The first peak near 1.25 cps corresponds to the frequency of the short period mode. The analysis predicts the short period frequency very well but slightly overpredicts the magnitude of the peak at the pilot station while under predicting the peak at the other two stations. In general, the analysis predicts peaks which are much higher than measured for each of the natural

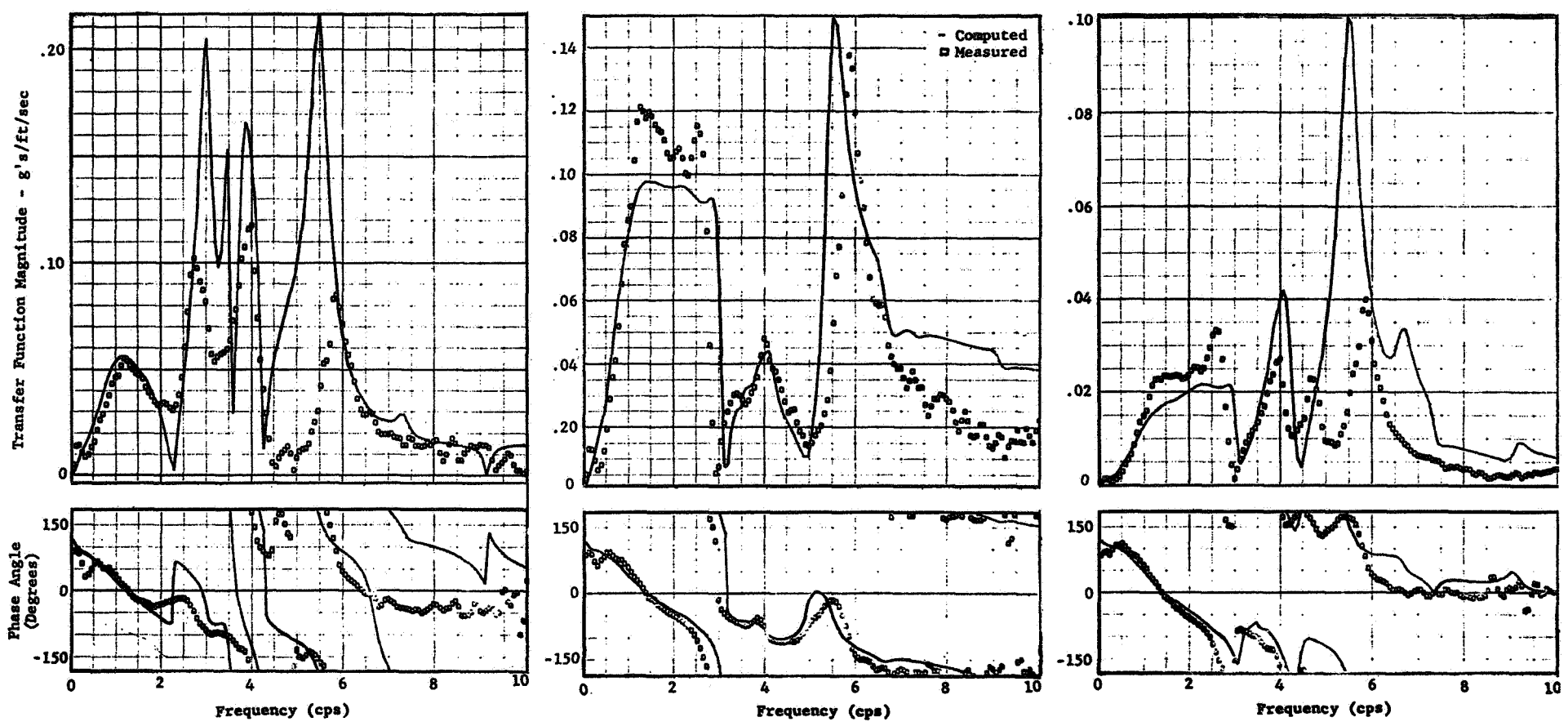

Analysis Parameters

ρ = .002068 slugs/ft^3, Mach = 0.93, V = 1069 ft/sec, SAS ON, N = 10, C.G. = 25.2% MAC

Figure 13 Comparison of Computed and Measured Transfer Functions, Run 131-10, For Matched Flight Conditions

frequencies. The best correlation between transfer function magnitudes occurs at the nominal center of gravity station. It is also noted that the peak frequency associated with the first natural mode is higher for the computed transfer functions than for the measured transfer functions. This indicates that the mathematical model of the structure would have produced better frequency correlation if it had not been stiffened to force better agreement with ground vibration test results. The phase angle plots from the analysis have similar shapes to the measured data. The best phase angle correlation is obtained for accelerometer A1 and A11.

The ratio of the computed to the measured transfer functions are plotted in figure 14. The upper portion of each plot shows the ratio of the magnitudes of the computed and measured transfer functions. Perfect agreement occurs where this ratio is unity. The lower portion of the curve shows the difference in phase angles between the computed and measured transfer functions. Perfect agreement occurs where this difference is zero. These plots indicate good magnitude and phase angle correlation in the frequency range between 0.5 and 2.0 cps. The phase angle correlation over the entire frequency range is best for the A1 accelerometer.

The computed and measured transfer functions are plotted together with the upper and lower 90 percent confidence limits in figure 15. The lower row of plots show the measured H_c transfer function compared with its upper and lower 90 percent confidence limits. The band between the upper and lower confidence limits broadens above 4 cps where the coherency function begins to decrease. In the upper row of plots the computed transfer function is compared with the upper and lower confidence limits on the measured H_c transfer function. The only computed transfer function that comes close to falling within the confidence limits is the one at the nominal c.g.

Correlation With Gust Run 134-7

Comparisons between computed and measured transfer functions for run 134-7 are shown in figure 16. The analysis predicts a short period mode frequency somewhat higher than measured and predicts the magnitude of the short period mode peak to be lower

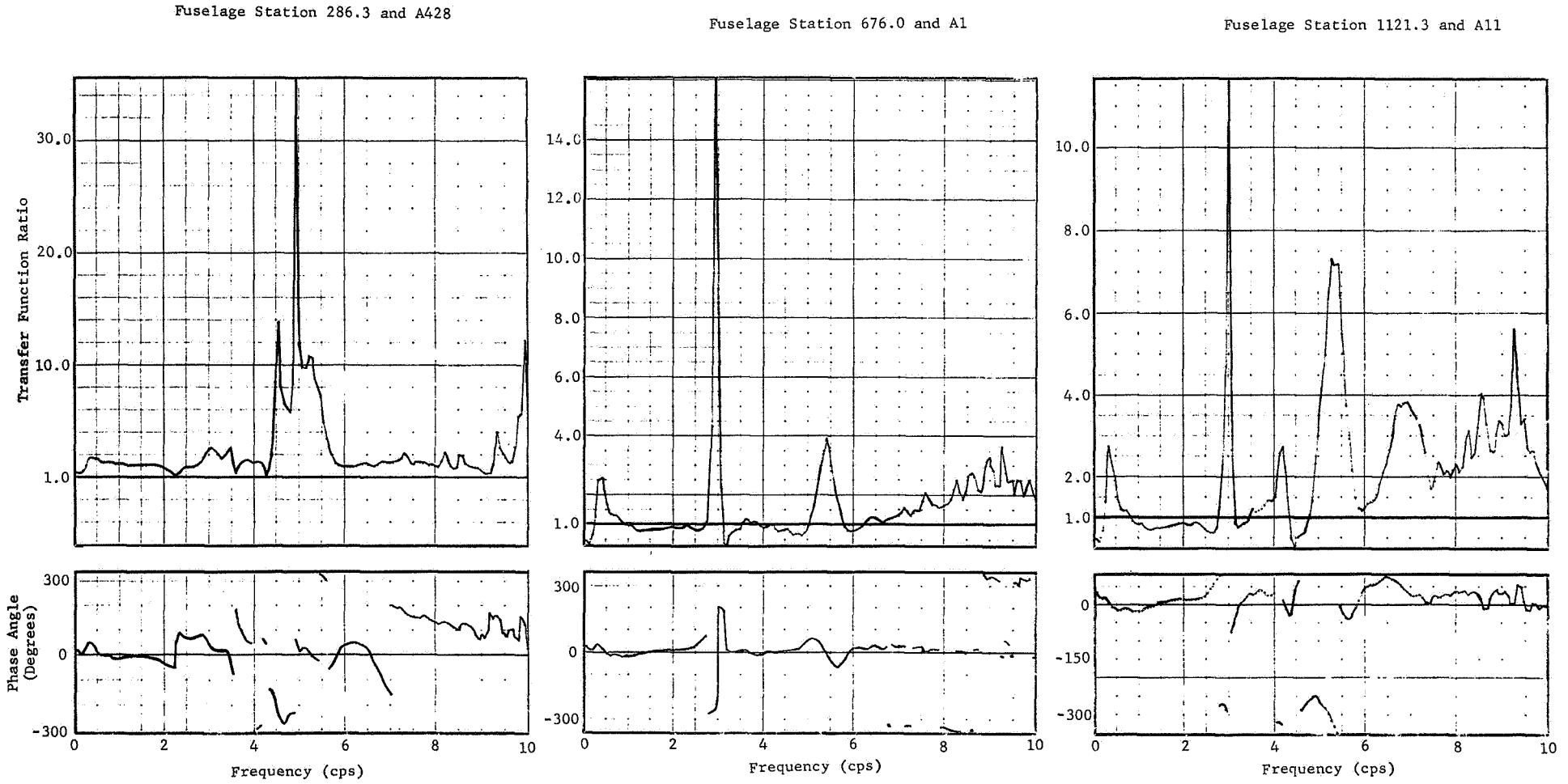

Analysis Parameters

ρ = .002068 slugs/ft^3, Mach = 0.93, V = 1069 ft/sec, SAS ON, N = 10, C.G. = 25.2% MAC

Figure 14 Ratio of Computed to Measured Transfer Functions, Run 131-10, For Matched Flight Conditions

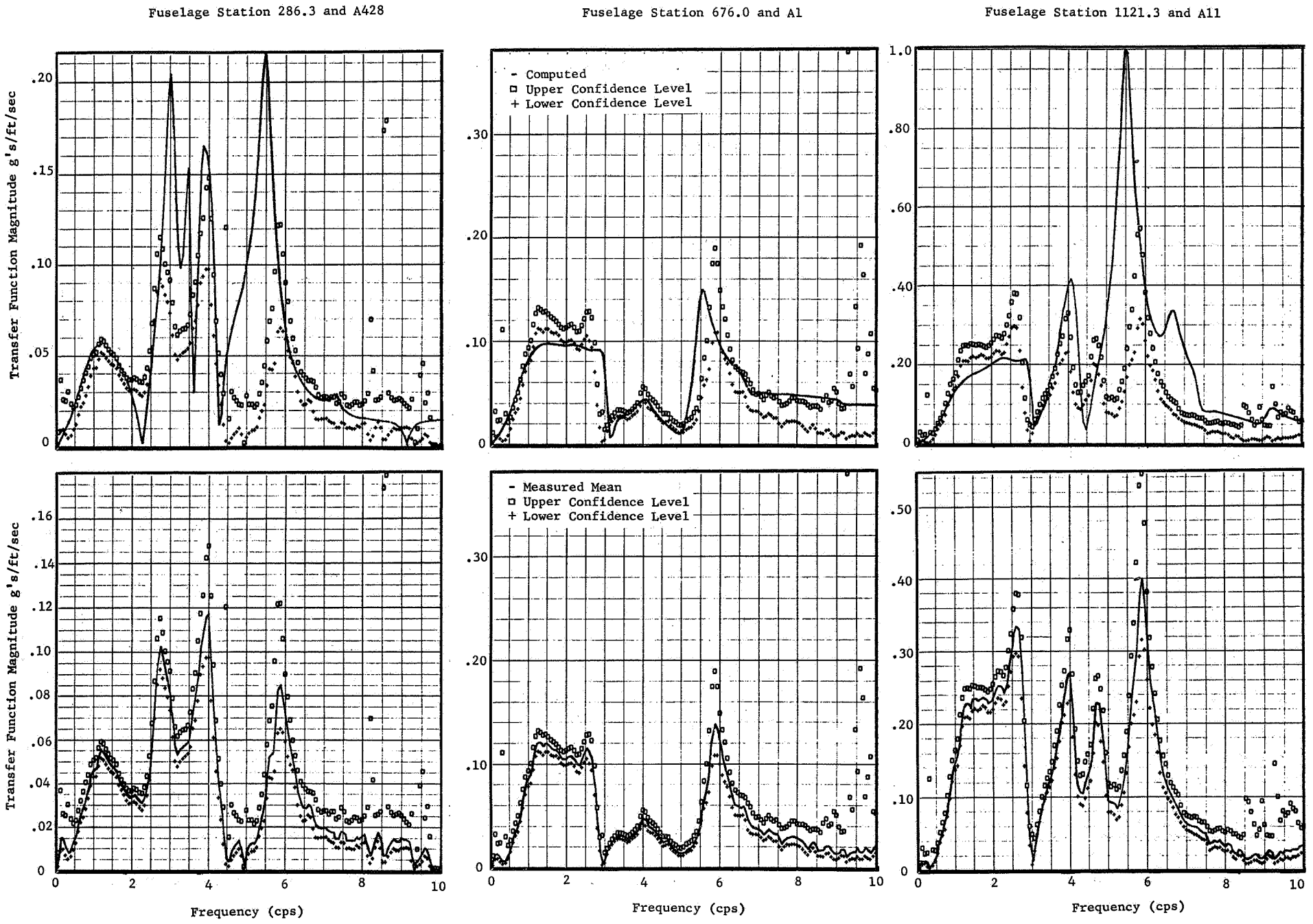

Figure 15 Comparison of Computed and Measured Transfer Functions with Upper and Lower 90% Confidence Limits, Run 131-10

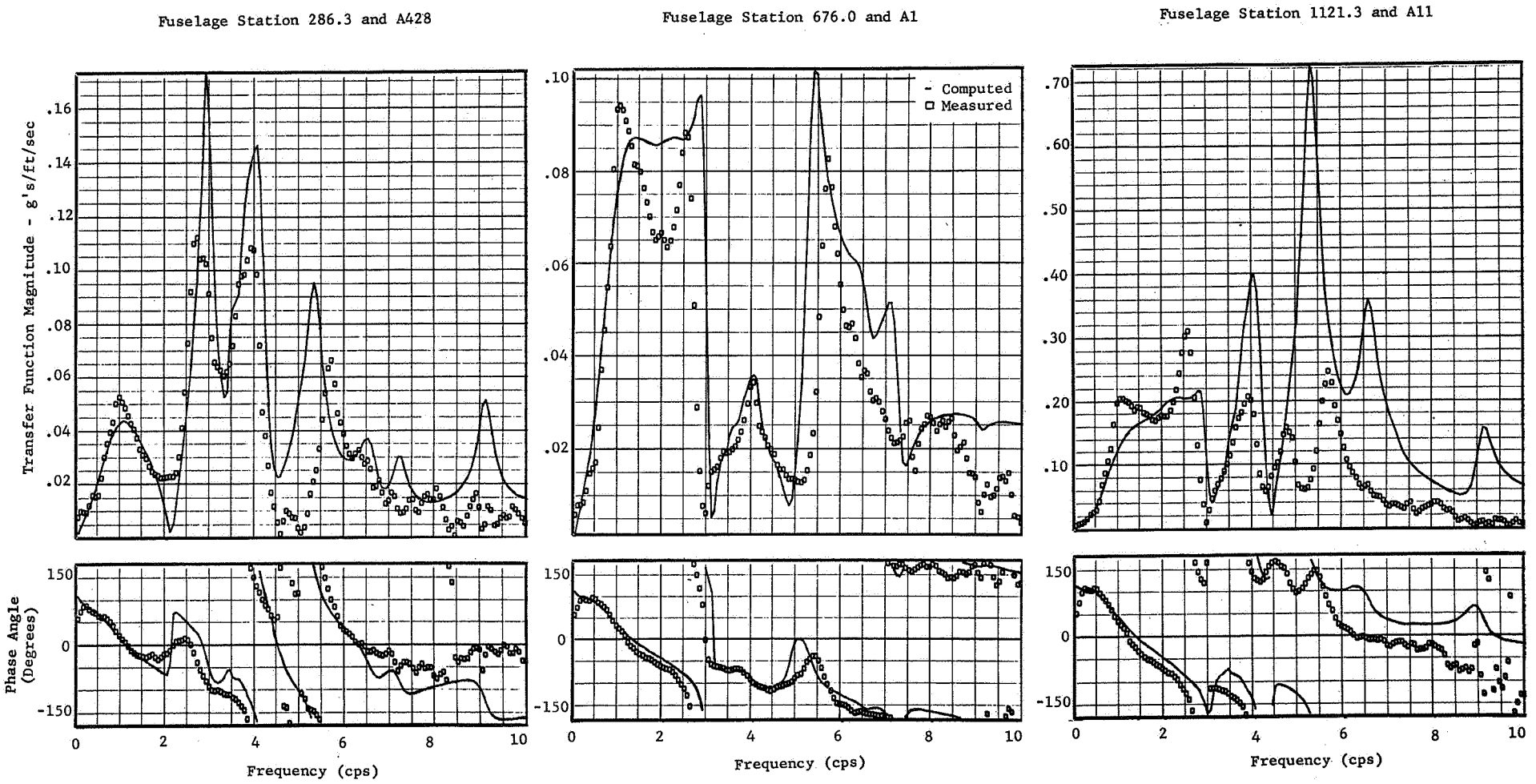

Analysis Parameters

ρ = .002092 slugs/ft^3, Mach = 0.93, V = 1062 ft/sec, SAS ON, N = 10, C.G. = 25.0% MAC

Figure 16 Comparison of Computed and Measured Transfer Functions, Run 134-7, For Matched Flight Conditions

than measured at all three stations. The computed peaks associated with each of the normal modes of vibration are all higher than the measured peaks as they were for run 131-10. However, the phase angle correlation is better for run 134-7 than 131-10. For both runs the correlations at the nominal c.g., A1, is the best of the three stations. The ratios of the computed to measured transfer functions for run 134-7 are shown in figure 17. In general, the large ratios of magnitudes occurs where peaks on the computed transfer functions are compared with non-peak magnitudes on the measured curves and vis versa.

The computed and measured transfer functions for run 134-7 are plotted in figure 18 for comparison with the upper and lower 90 percent confidence limits of the measured H_c transfer function. The computed transfer function at station 676 again comes the closest to falling within the confidence limits. At stations 286.3 and 1121.3 the computed transfer function peaks associated with the natural modes of vibration, exceed the peaks in the upper 90 percent confidence level curves.

Correlation With Gust Run 131-3

Comparisons between computed and measured transfer functions for run 131-3 are shown in figure 19. The magnitude and frequency associated with the short period mode are considerably less for this gust run than for the previous two gust runs. The analysis predicts the magnitude and phase angle of the transfer functions in the vicinity of the short period mode very well for accelerometers A428 and A1 but underestimates the magnitude for accelerometer A11. The computed peak near 2.6 cps is less than measured at all three stations and the computed peak near 3.7 cps is larger than measured at all three stations. Overall, the correlation between computed and measured transfer functions is best at the c.g. accelerometer, A1.

The ratios of the computed to measured transfer functions for run 131-3 are shown in figure 20.

The computed and measured transfer functions for run 131-3 are plotted in figure 21 for comparison with the upper and lower 90 percent confidence limits of the measured H_c transfer function. The computed transfer function at station 286.3 falls within the confidence limits from zero to approximately 2 cps even though the confidence bands are very narrow. However, the computed transfer function peak near 3.7 cps far exceeds the peak in the upper 90 percent confidence limit. The transfer function at

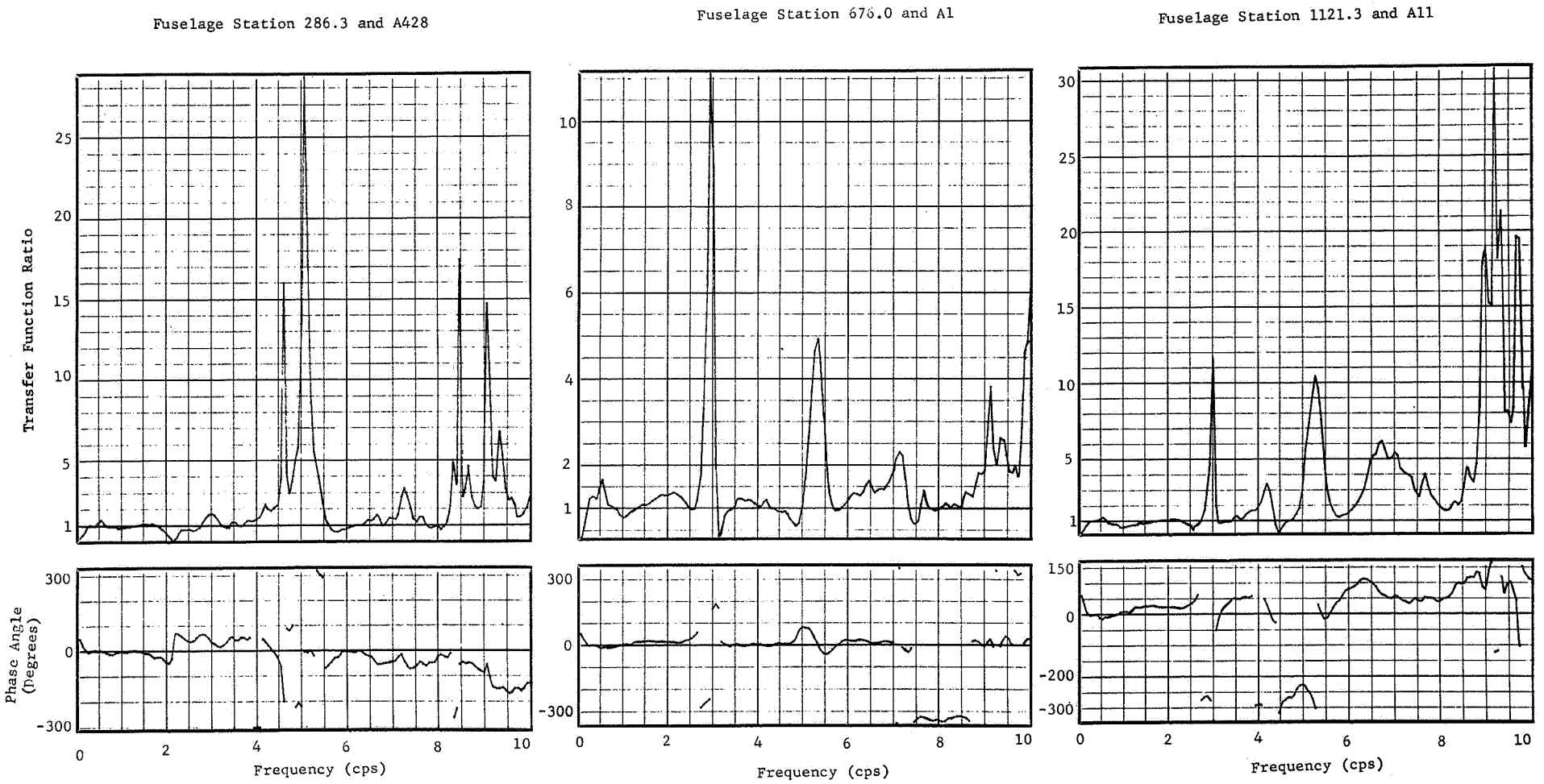

Analysis Parameters

ρ = .002092 slugs/ft^3, Mach = 0.93, V = 1062 ft/sec, SAS ON, N = 10, C.G. = 25.0% MAC

Figure 17 Ratio of Computed to Measured Transfer Functions, Run 134-7, For Matched Flight Conditions

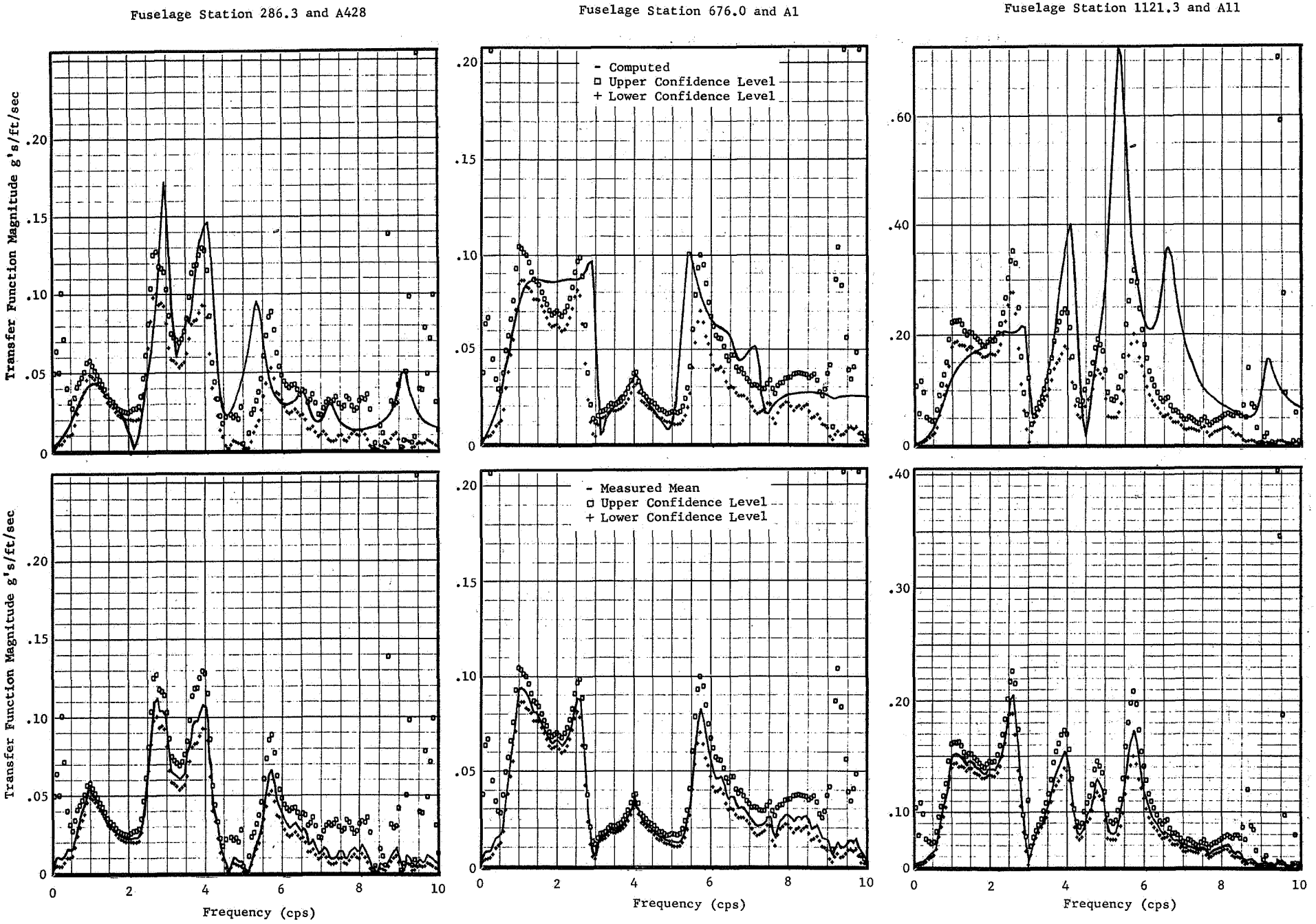

Analysis Parameters

ρ = .002092 slugs/ft^3, Mach = 0.93, V = 1062 ft/sec, SAS ON, N = 10, C.G. = 25.0% MAC

Figure 18 Comparison of Computed and Measured Transfer Functions with Upper and Lower 90% Confidence Limits, Run 134-7

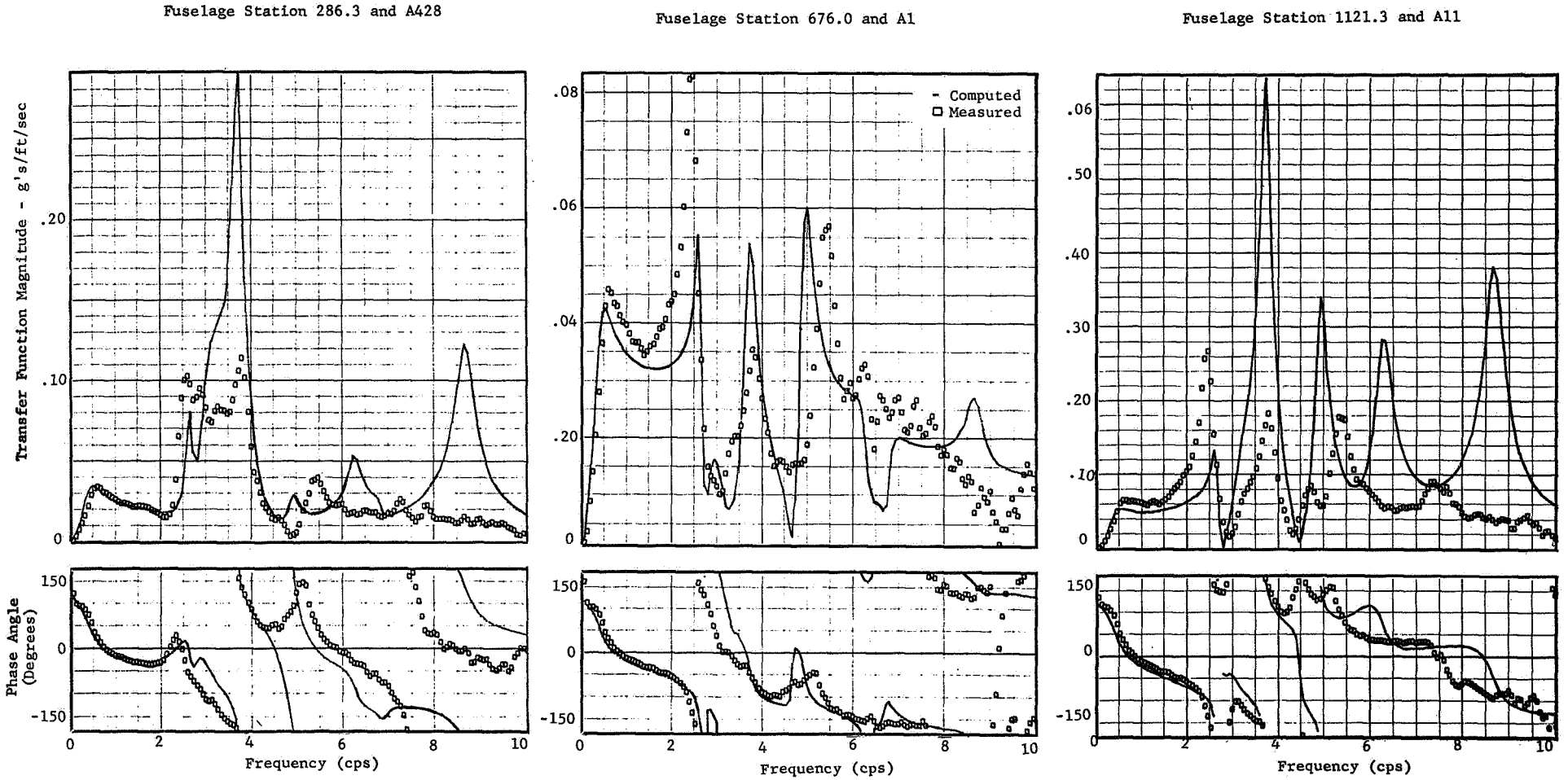

Analysis Parameters

ρ = .002073 slugs/ft^3, Mach = 0.80, V = 921 ft/sec, SAS ON, N = 10, C.G. = 26.8% MAC

Figure 19 Comparison of Computed and Measured Transfer Functions, Run 131-3, For Matched Flight Conditions

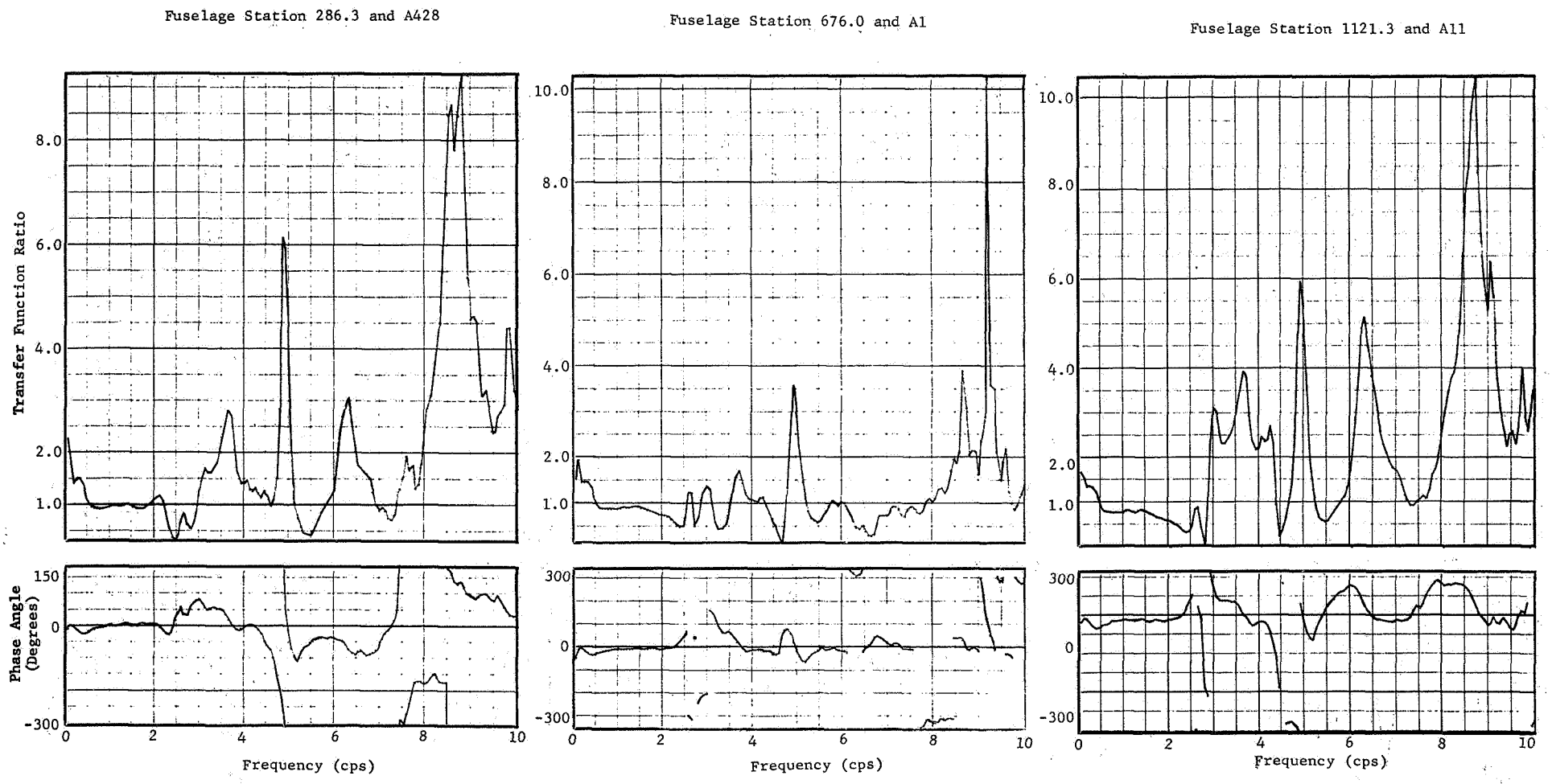

Analysis Parameters

ρ = .002073 slugs/ft^3, Mach = 0.80, V = 921 ft/sec, SAS ON, N = 10, C.G. = 26.8% MAC

Figure 20 Ratio of Computed to Measured Transfer Functions, Run 131-3, For Matched Flight Conditions

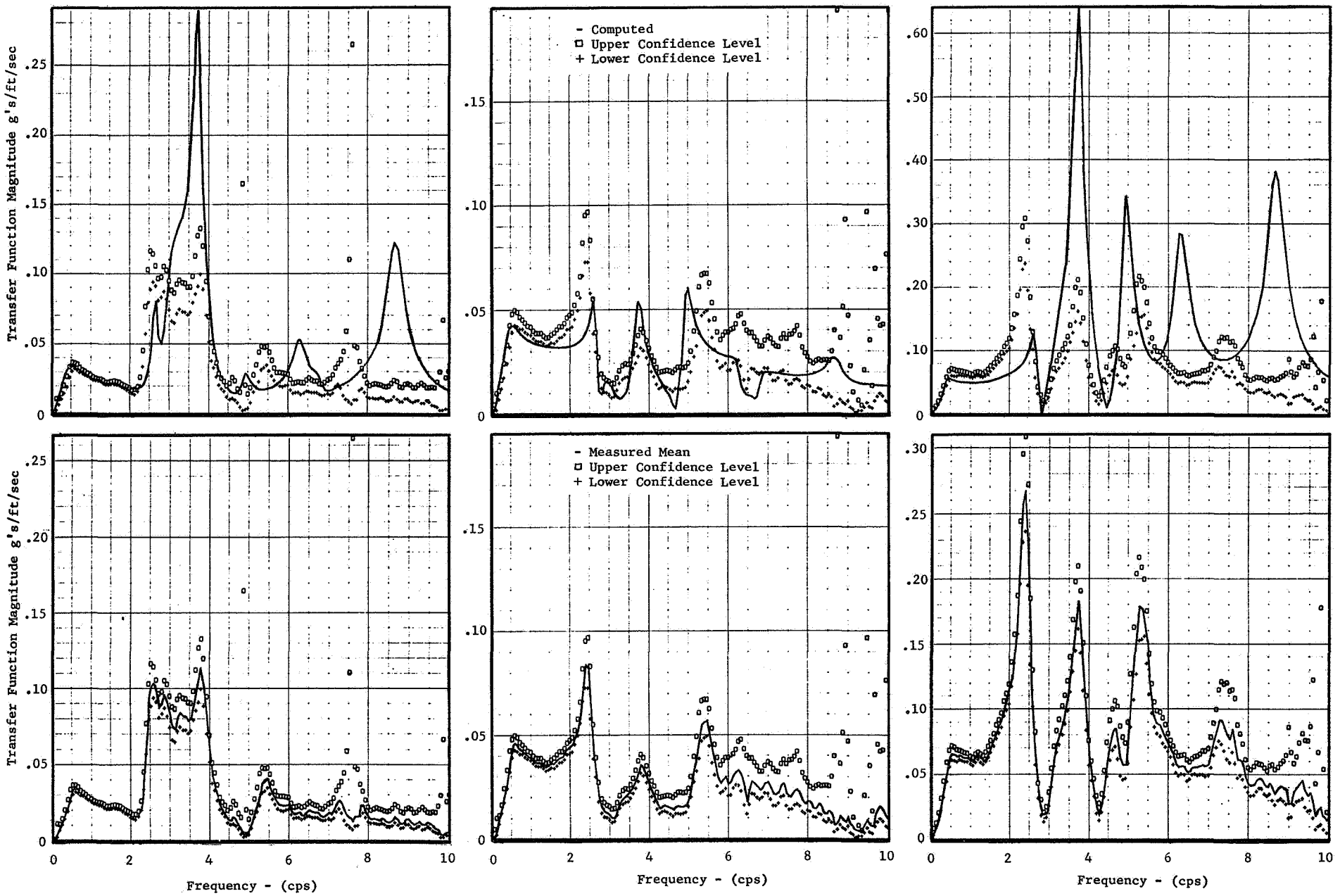

Analysis Parameters

ρ = .002241 slugs/ft^3, Mach = 0.80, V = 921 ft/sec, SAS ON, N = 10, C.G. = 26.8% MAC

Figure 21 Comparison of Computed and Measured Transfer Functions with Upper and Lower 90% Confidence Limits, Run 131-3

station 676 comes closer to falling inside the confidence limits throughout the frequency range than does the other two computed transfer functions. The computed transfer function at station 1121.3 fall far outside the confidence limits.

$\bar{A}$ and N_o Versus Cutoff Frequency

The $\bar{A}$ and N_o data were evaluated with the upper limit of integration treated as a variable and defined as a cutoff frequency. The cutoff frequency was varied from 1/15 cps to 10 cps in frequency increments of 1/15 cps. Plots of $\bar{A}$ and N_o versus cutoff frequency for run 131-10 are shown in figure 22. Both computed and measured data are plotted. The two sets of curves compare very well to at least 2 cps. Above 2 cps the computed data in general is higher than the measured data. The computed data compares best with the data measured at accelerometer A1. At the 10 cps cutoff frequency the computed $\bar{A}$ and N_o data at the pilot station, A1, tail cone, A11, are higher than measured.

Plots of computed and measured $\bar{A}$ and N_o versus cutoff frequency for run 134-7 are shown in figure 23. The comparison between computed and measured $\bar{A}$ is much better for this gust run than for gust run 131-10 across the entire frequency range. Comparisons between computed and measured N_o data are good for cutoff frequencies below 4 cps. Above 4 cps the computed data is consistently higher than measured.

Plots of computed and measured $\bar{A}$ and N_o data versus cutoff frequency for run 131-3 are shown in figure 24. The computed $\bar{A}$ data compares very well with the measured data at the c.g. accelerometer A1. However, the computed $\bar{A}$ data are much higher than measured at the pilot station accelerometer, A428, and the tail cone accelerometer, A11, for cutoff frequencies above 3.5 cps. The N_o computed data also agrees very well with the measured data at accelerometer A1. However, the computed N_o is much higher than measured at A428 and A11 for cutoff frequencies above 3.5 cps.

The $\bar{A}$ and N_o data computed with a 10 cps cutoff frequency are listed in table 11 for comparison with the measured data.

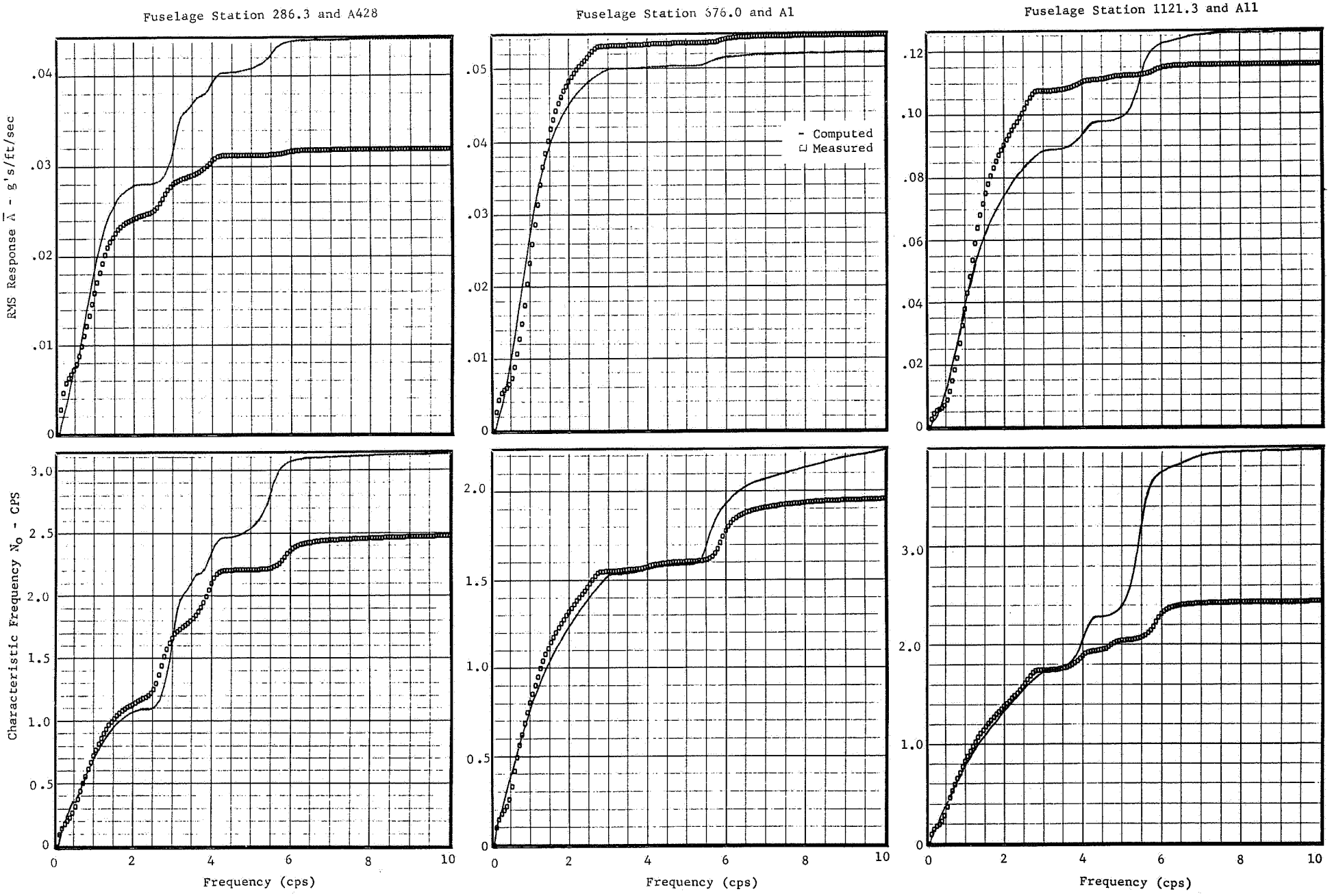

Analysis Parameters

ρ = .002068 slugs/ft^3, Mach = 0.93, V = 1069 ft/sec, SAS ON, N = 10, C.G. = 25.2% MAC

Figure 22 Comparison of Computed and Measured $\bar{A}$ and N_o vs Cutoff Frequency, Run 131-10

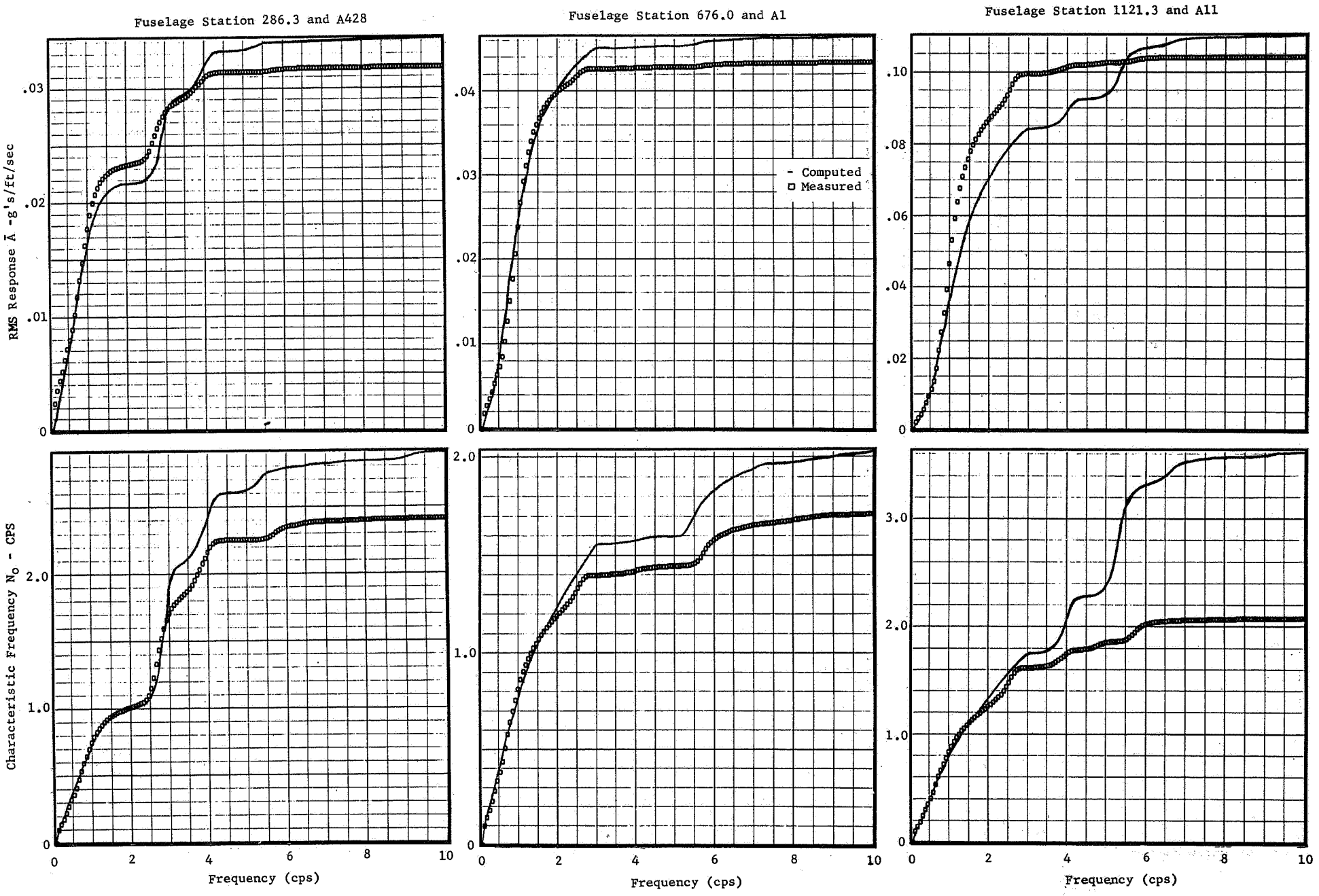

Analysis Parameters

ρ = .002092 slugs/ft^3, Mach = 0.93, V = 1062 ft/sec, SAS ON, N = 10, C.G. = 25.0% MAC

Figure 23 Comparison of Computed and Measured Ā and N_o vs Cutoff Frequency, Run 134-7

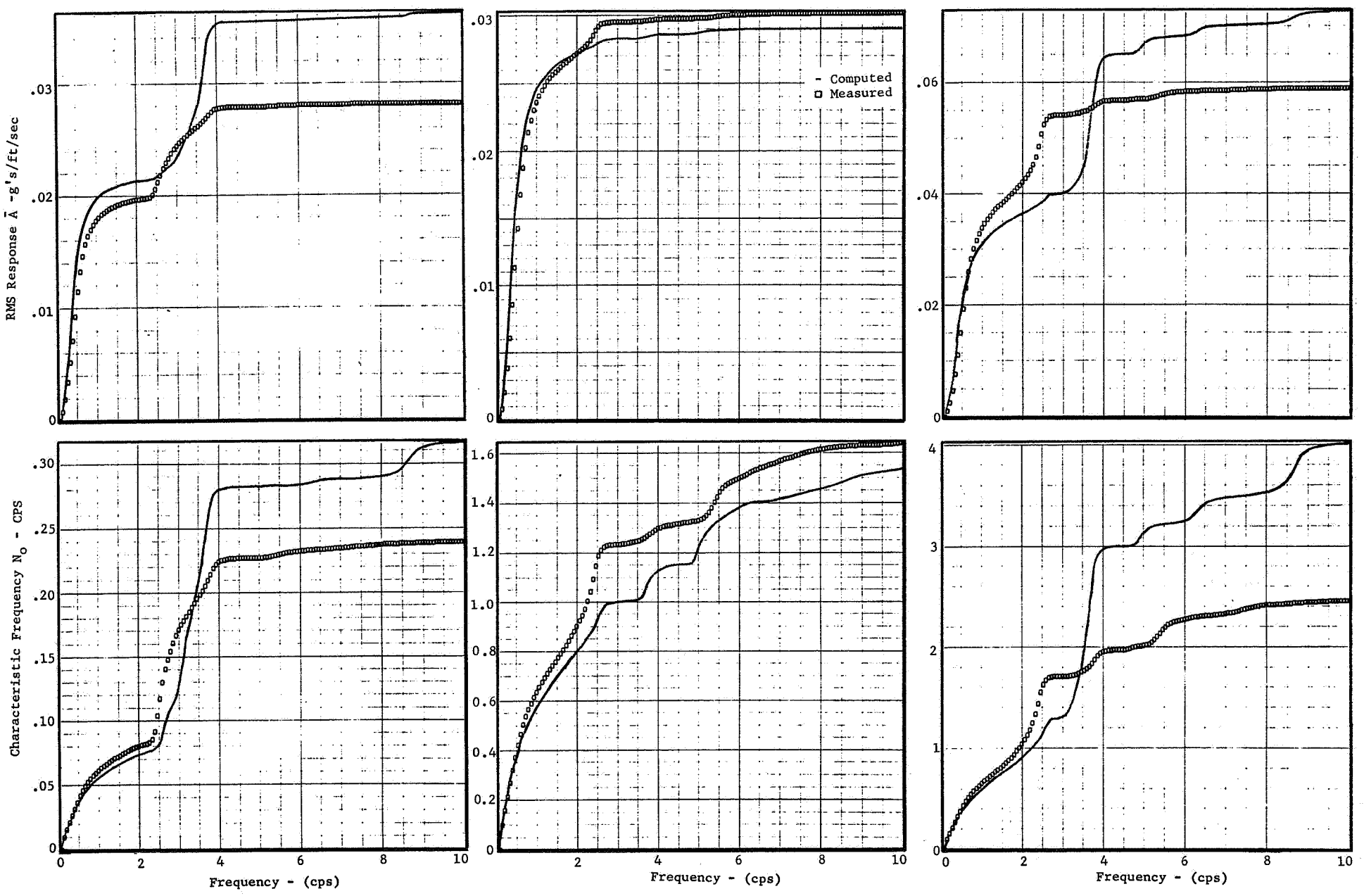

Analysis Parameters

ρ = .002241 slugs/ft^3, Mach = 0.80, V = 921 ft/sec, SAS ON, C.G. = 26.8% MAC

Figure 24 Comparison of Computed and Measured Ā and N_o vs Cutoff Frequency, Run 131-3

Table 11 $\bar{A}$ and N_o Data For Matched Flight Conditions

Run No.	Accel.	Computed		Measured	
		$\bar{A}$	N_o	$\bar{A}$	N_o
131-10	A428	.04406	3.1297	.03188	2.473
	A1	.05210	2.2366	.05440	1.957
	A11	.12593	3.9741	.11590	2.436
134-7	A428	.03427	2.9014	.03178	2.411
	A1	.04634	2.0303	.04334	1.711
	A11	.10991	3.6259	.1041	2.070
131-3	A428	.03617	3.1636	.02814	2.391
	A1	.02909	1.5378	.03019	1.638
	A11	.07264	4.020	.05888	2.454

AIR DENSITY VARIATIONS

The B-58 gust runs were made at an altitude of approximately 2000 feet above sea level. The altitude of the airplane above the terrain during the gust runs varied between 700 to 1200 feet, approximately. During the early part of the investigation it was assumed that the air density during each run was equal to the air density at 2000 feet altitude for a standard day. Computed transfer functions for run 131-3 at 2000 feet altitude were treated as a standard for comparison with other transfer functions to evaluate the effect of small parameter variations. To investigate the effect of altitude variations the transfer functions for gust run 131-3 were computed for a standard day density at 4000 feet and again at sea level. Subsequently, the average temperature and average pressure which existed during each gust run was used to compute an average density. The average density for gust run 131-3 was equivalent to the density at 4600 feet on a standard day. The actual average air density during gust run 131-3 and the values used in the analyses to evaluate the effect of density variations are listed in table 12.

Table 12 Air Density Variations For Run 131-3

Measured		Analysis		Density Ratio	
Density $Slug/Ft^3$	Std. Day Alt. (Ft.)	Density $Slug/Ft^3$	Std. Day Alt. (Ft.)	$\frac{\text{Analysis}}{\text{Measured}}$	$\frac{\text{Analysis}}{\text{2000 Ft.}}$
.0020730	4600	.002073	4600	1.0	0.93
		.0021110	4000	1.02	0.95
		.002241	2000	1.08	1.00
		.002377	0	1.15	1.07

Run 131-3 With Standard Day 2000 Feet Altitude Density

Comparisons between the computed transfer functions using a 2000 feet standard day density, with the measured transfer functions are shown in figure 25. The larger air density increases the frequency and magnitude of the short period mode. The frequency of the short period mode can be approximated very well by the following simple formula

$$f = \frac{1}{2\pi} \sqrt{\frac{(a.c. - c.g.)\, C_{L_\alpha}\, S\, \frac{\rho V^2}{2}}{I_{c.g.}}} \qquad (56)$$

where

a.c. is the fuselage station of the aerodynamic center

c.g. is the fuselage station of the center-of-gravity

$I_{c.g.}$ is the mass moment of inertia of the airplane about its c.g.

Since the density at 2000 feet is 8 percent greater than the density at 4600 feet the expected increase in frequency of the short period mode as estimated by equation (56) would be approximately 4 percent. Comparing the computed transfer functions for 4600 and 2000 feet (figures 19 and 25) it can be seen that the short period frequency increases approximately 4 percent. This increase improves the correlation between measured and computed transfer functions in the frequency range near the short period mode for the c.g. and aft fuselage locations while providing about the same degree of correlation at the pilot station. The ratio of the computed transfer functions at 2000 feet to the measured transfer functions for run 131-3 are shown in figure 26.

To see the effect of increasing the density more clearly, the ratio of the computed transfer function for a 4600 feet altitude density to the computed transfer function for a 2000 feet altitude density is shown in figure 27. The density ratio for these two altitudes is 0.93. The ratio of the transfer function magnitudes is not constant but the ratio is less than unity over most of the frequency range. Large variations occur near peaks and valleys in the transfer functions. Small shifts in peak and valley frequencies produce large variations in the ratios. Phase angle variations are very small across the entire frequency range.

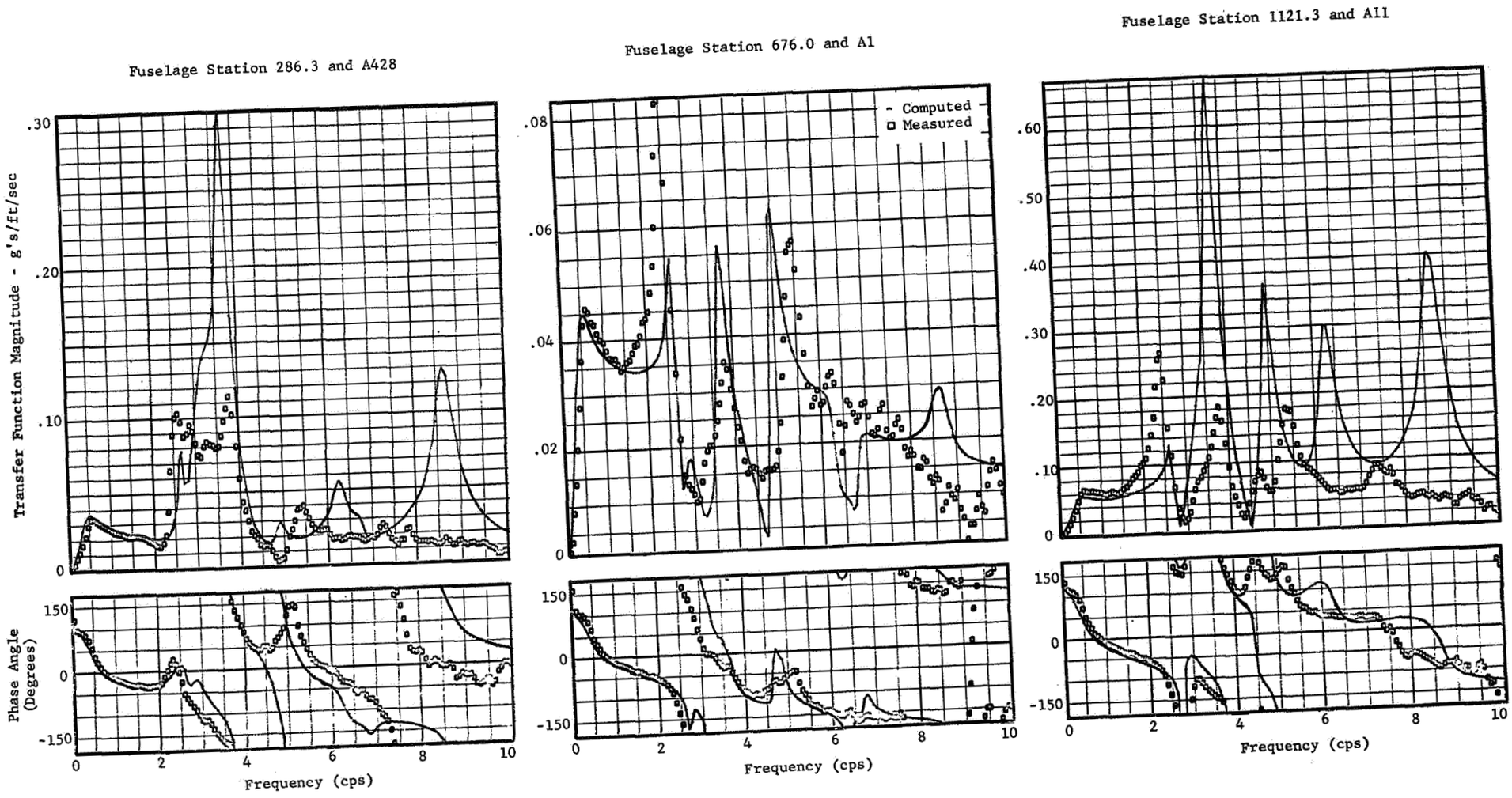

Analysis Parameters

ρ = .002241 slugs/ft^3, Mach = 0.80, V = 921 ft/sec, SAS ON, N = 10, C.G. = 26.8% MAC

Figure 25 Comparison of Computed and Measured Transfer Functions, Run 131-3, 2000 Feet Altitude

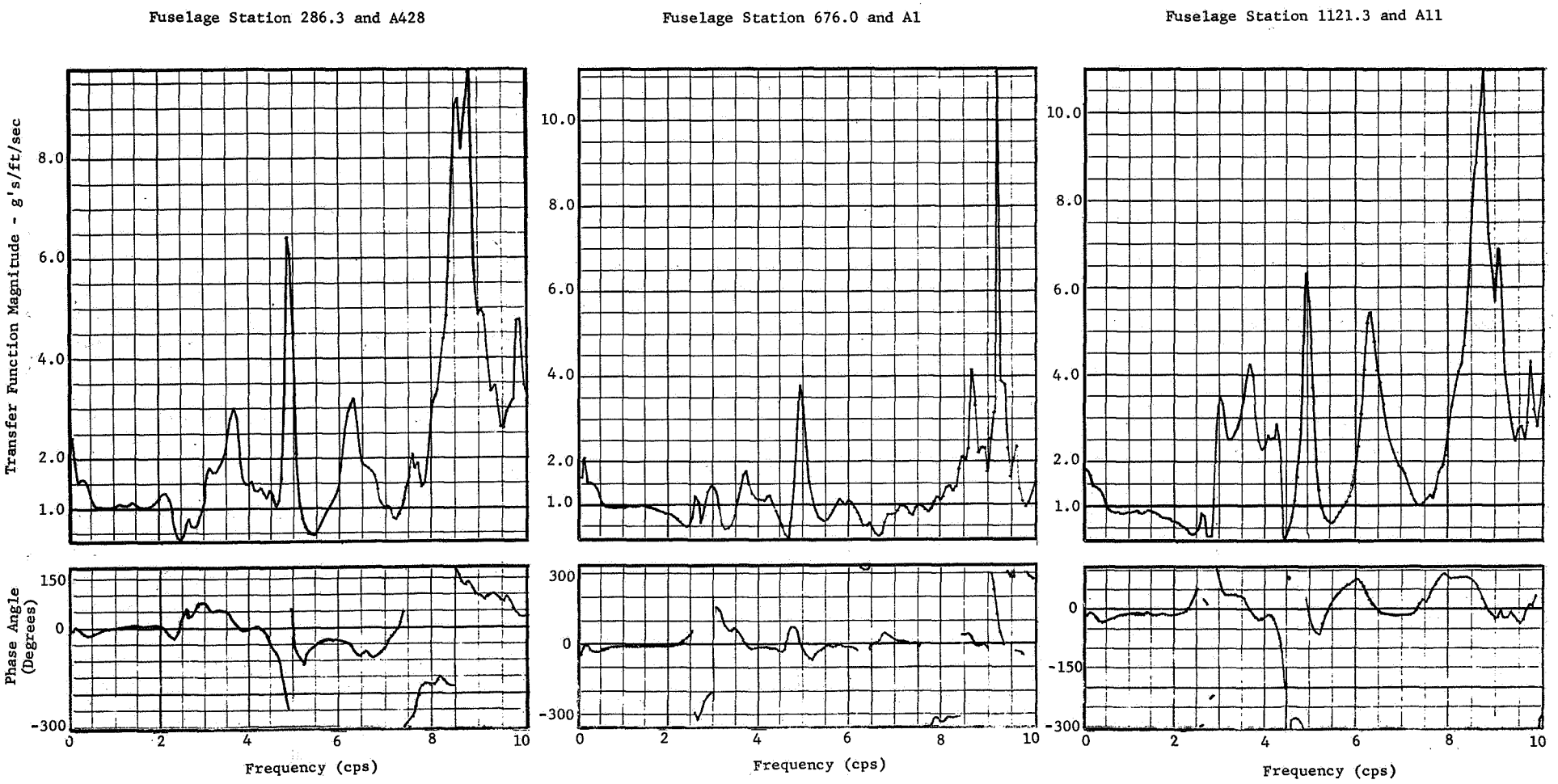

Analysis Parameters

ρ = .002241 slugs/ft^3, Mach = 0.80, V = 921 ft/sec, SAS ON, N = 10, C.G. = 26.8% MAC

Figure 26 Ratio of Computed to Measured Transfer Functions, Run 131-3, 2000 Feet Altitude

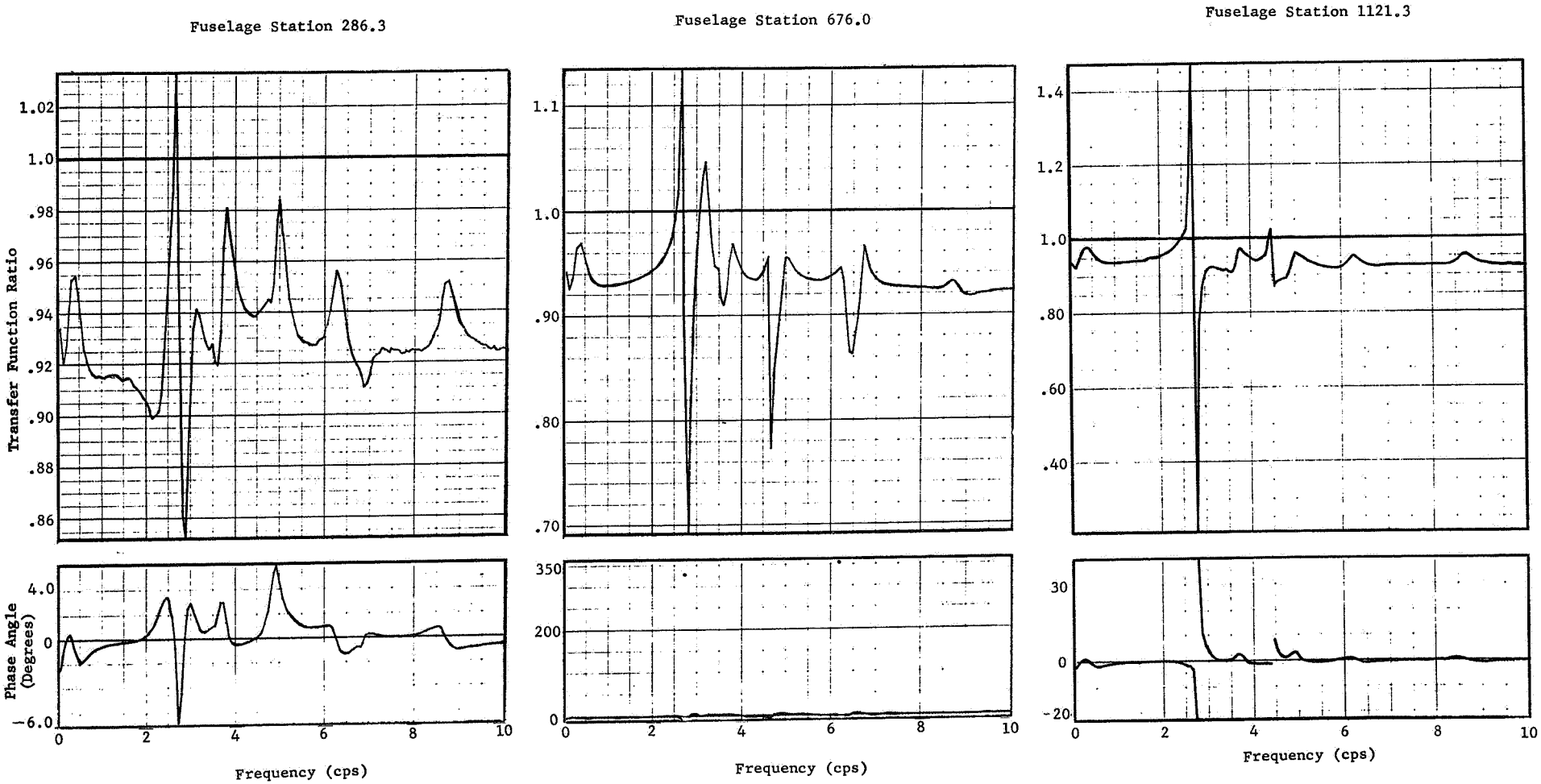

Analysis Parameters

Mach = 0.80, V = 921 ft/sec, SAS ON, N = 10, C.G. = 26.8% MAC

Figure 27 Ratio of Computed Transfer Functions at 4600 Feet Altitude to 2000 Feet Altitude, Run 131-3

Run 131-3 With Standard Day Sea Level Altitude Density

Comparisons between the computed transfer functions using sea level standard day density with the measured transfer functions are shown in figure 28. The increased density further increases the frequency and magnitude of the short period mode over that obtained for the 2000 feet altitude. The correlation with the measured transfer function in the frequency range near the short period mode is improved at the c.g. accelerometer A1 and aft fuselage accelerometer A11 but the correlation is degraded at the pilot stations accelerometer A428. The ratios of the computed transfer functions for sea level density to the measured transfer functions are shown in figure 29.

The ratio of the computed transfer functions for sea level altitude density to computed transfer functions for 2000 feet altitude density are shown in figure 30. The density ratio between these two altitudes is 1.07. The ratios of the magnitudes again varies with frequency but is greater than unity over most of the frequency range. Again the phase angle variations are very small.

$\bar{A}$ and N_o Variations With Air Density

The computed transfer functions for altitudes of 4600, 4000, 2000 and sea level were combined with the Dryden gust spectrum with a 500 feet scale of turbulence to obtain $\bar{A}$ and N_o data. These data for ten degrees of freedom, two degrees of freedom (rigid body translation and pitch) and one degree of freedom (rigid body translation) are listed in table 13. For small density variations, the $\bar{A}$ data vary approximately proportional to the density whereas the N_o data are almost invariant with density.

To obtain good correlation between computed and measured $\bar{A}$ values for accelerometers A428 and A11 by air density variations, would require densities for altitudes that are unreasonably higher than 4600 feet. An altitude increase would not significantly improve the comparison of the N_o values or the comparison between transfer functions.

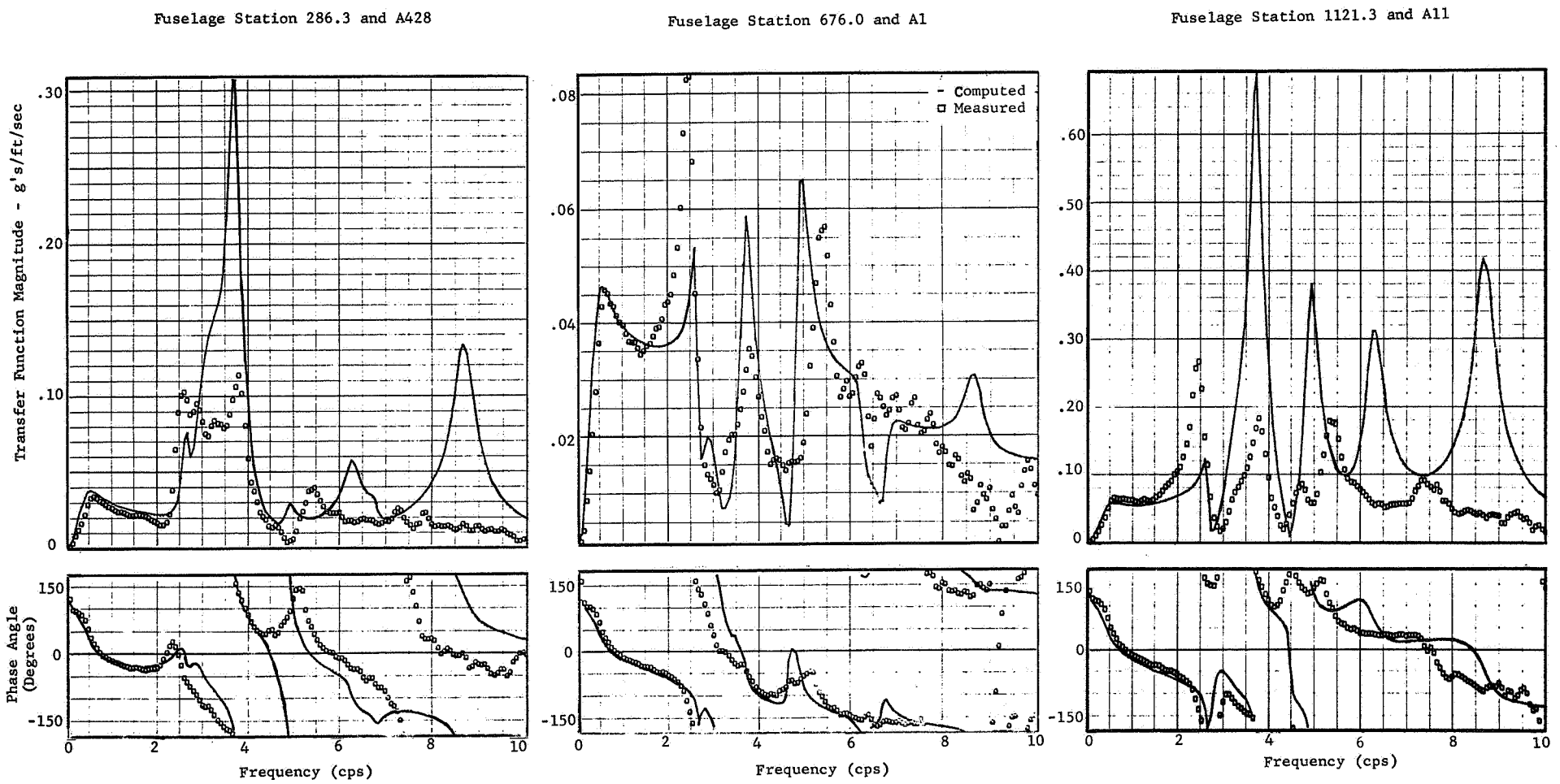

Analysis Parameters

ρ = .002377 slugs/ft^3, Mach = 0.80, V = 921 ft/sec, SAS ON, N = 10, C.G. = 26.8% MAC

Figure 28 Comparison of Computed and Measured Transfer Functions, Run 131-3, Sea Level

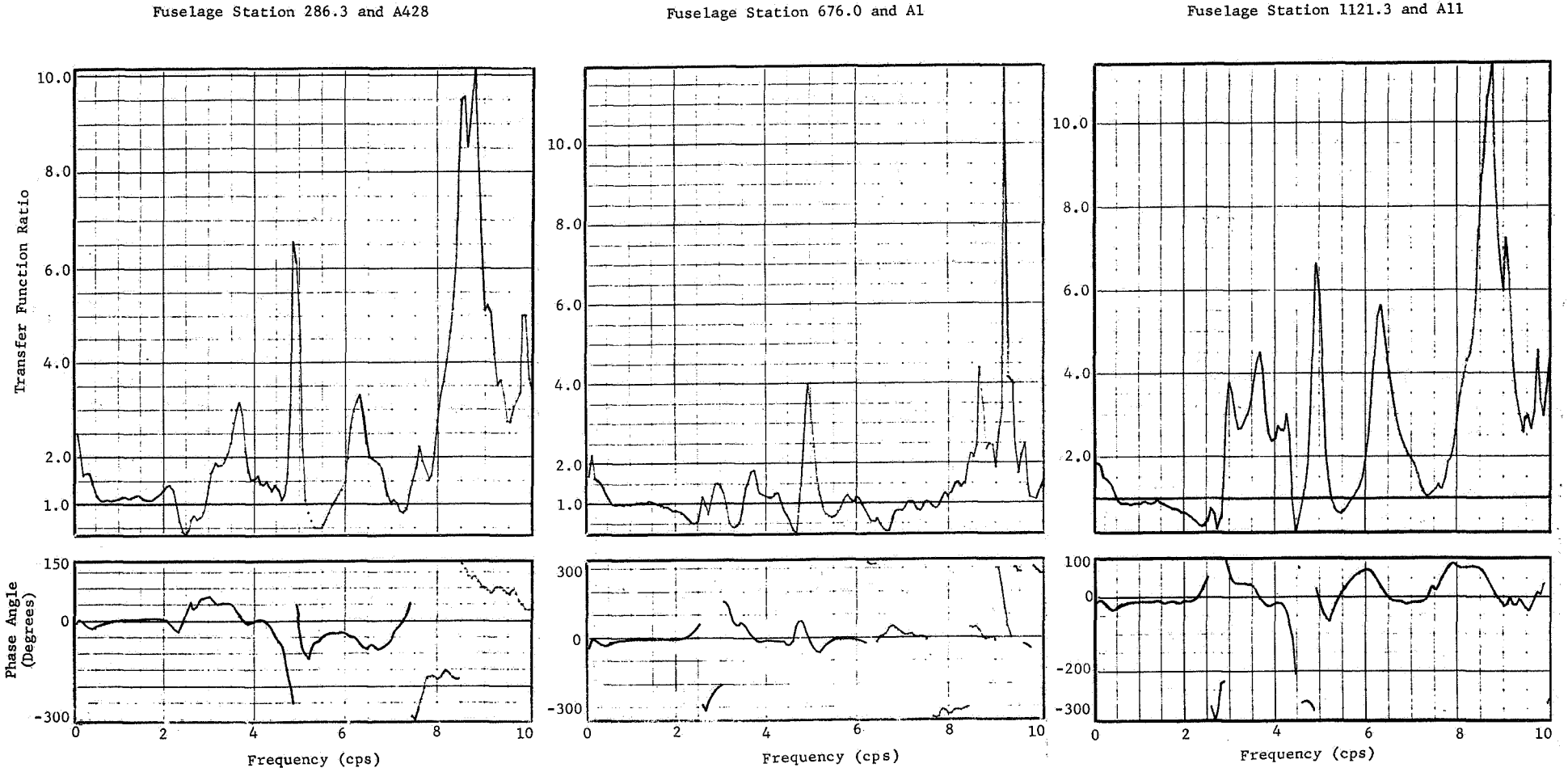

Analysis Parameters

ρ = .002377 slugs/ft^3, Mach = 0.80, V = 921 ft/sec, SAS ON, N = 10, C.G. = 26.8% MAC

Figure 29 Ratio of Computed to Measured Transfer Functions, Run 131-3, Sea Level

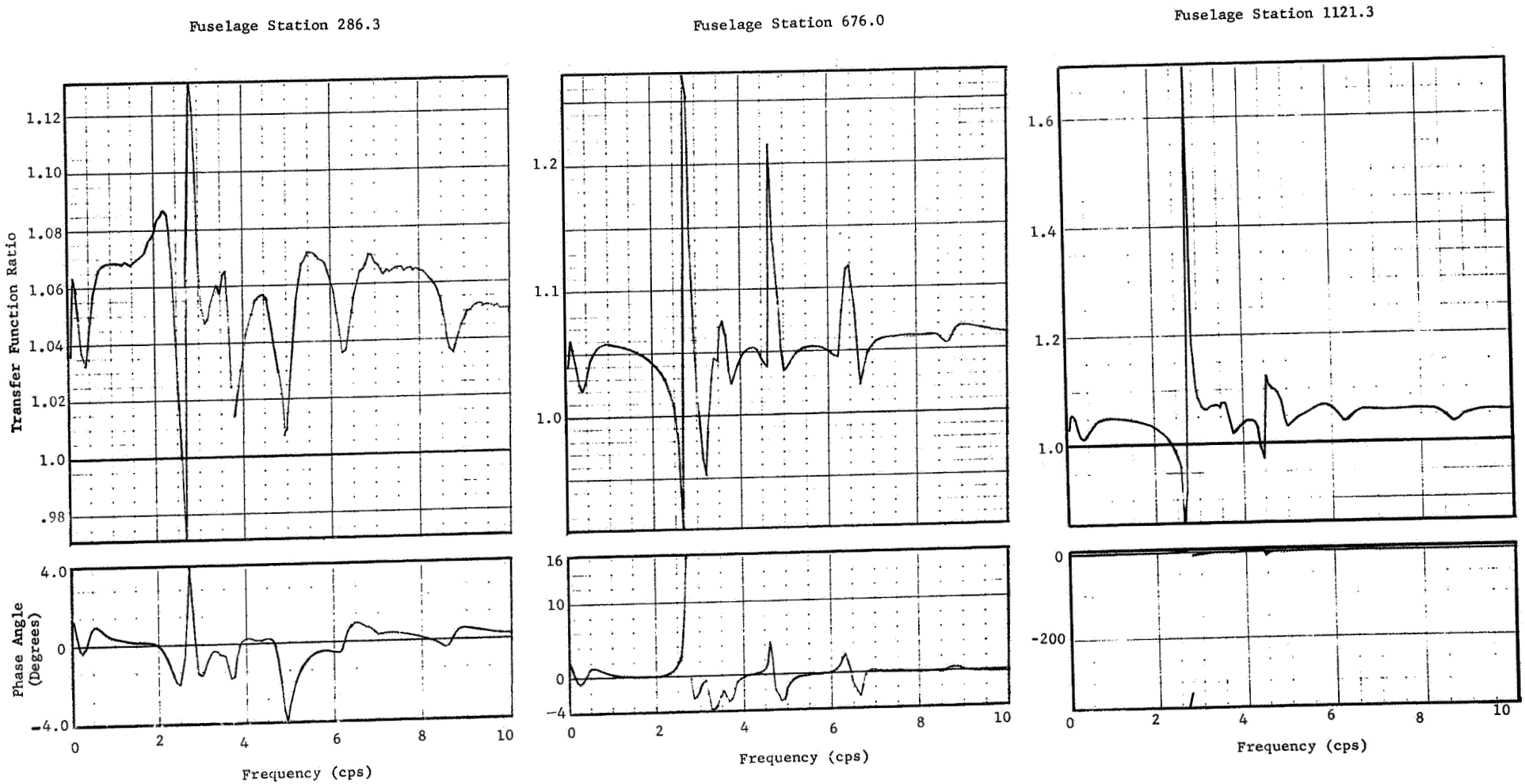

Analysis Parameters

Mach = 0.80, V = 921 ft/sec, SAS ON, N = 10, C.G. = 26.8% MAC

Figure 30 Ratio of Computed Transfer Functions at Sea Level Altitude to 2000 Feet Altitude, Run 131-3

Table 13 $\bar{A}$ and N_o Variations With Air Density, Run 131-3

F.S. (in)	Accel.	Computed								Measured	
		H = sea level ρ = .002378		H = 2000 Ft. ρ = .002241		H = 4000 ρ = .002111		H = 4600 ρ = .002073		H = 4600 ρ = .002073	
		$\bar{A}$	N_o	$\bar{A}$	N_o	$\bar{A}$	N_o	$\bar{A}$	N_o	$\bar{A}$	N_o
N = 10											
286.3	A428	.04045	3.1444	.03855	3.1525	.03668	3.1614	.03617	3.1636	.02814	2.391
676.0	A1	.03199	1.5513	.03071	1.5443	.02944	1.5393	.02909	1.5378	.03019	1.638
1121.3	A11	.08035	4.0586	.07690	4.0427	.07355	4.0251	.07262	4.0201	.05888	2.454
N = 2											
286.3	A428	.02324	1.4808	.02224	1.4566	.02119	1.4392	.02090	1.4344	.02814	2.391
676.0	A1	.03127	1.4679	.02998	1.4417	.02868	1.4183	.02832	1.4118	.03019	1.638
1121.3	A11	.04163	1.8744	.03991	1.8354	.03825	1.8039	.03779	1.7952	.05888	2.454
N = 1											
286.3	A428	.02819	1.4680	.02679	1.4577	.02543	1.4479	.02506	1.4452	.02814	2.391
676.0	A1	.02819	1.4680	.02679	1.4577	.02543	1.4479	.02506	1.4452	.03019	1.638
1121.3	A11	.02819	1.4680	.02679	1.4577	.02543	1.4479	.02506	1.4452	.05888	2.454

VARIATIONS IN NUMBER OF DEGREES OF FREEDOM

Ten DOF (degrees of freedom) were used as a standard number of DOF in all the investigations for comparisons with measured data. In addition, transfer functions were also computed for one and two DOF. The calculation of transfer functions require considerable data processing and digital computer calculations. It is easier to anticipate or estimate characteristics of the one and two DOF transfer functions with a few slide rule calculations than transfer functions for many DOF. Hence, the one and two DOF transfer functions sometimes provide a more easily recognizable signal that an error exists in the analysis than does the ten DOF transfer functions. In addition, the phase angle of the transfer functions are more easily understood for one and two DOF transfer functions.

Computed transfer functions for run 131-3 using 2000 feet altitude density are shown in figure 31 for ten, two and one DOF. Rigid body translation and pitch are used for the two DOF whereas only rigid body translation is used for the one DOF.

Consider the equation of motion for one DOF rigid body translation assuming quasi-steady aerodynamics and assuming the gust velocity is measured at the a.c.

$$m\ddot{h} + \frac{\rho V^2}{2} S C_{L_\alpha} \frac{\dot{h}}{V} = \frac{\rho V^2}{2} S C_{L_\alpha} \frac{w_g}{V} \qquad (57)$$

where h is the vertical translation,

m is the mass of the airplane, and

S is the wing area

Assuming sinusoidal motion, the transfer functions between gust velocity (positive up) and acceleration (positive up) can be expressed as

$$\frac{\ddot{h}}{w_g} = \frac{S C_{L_\alpha} \rho V/2}{m - i\left(\frac{S C_{L_\alpha} \rho V}{4\pi f}\right)} \qquad (58)$$

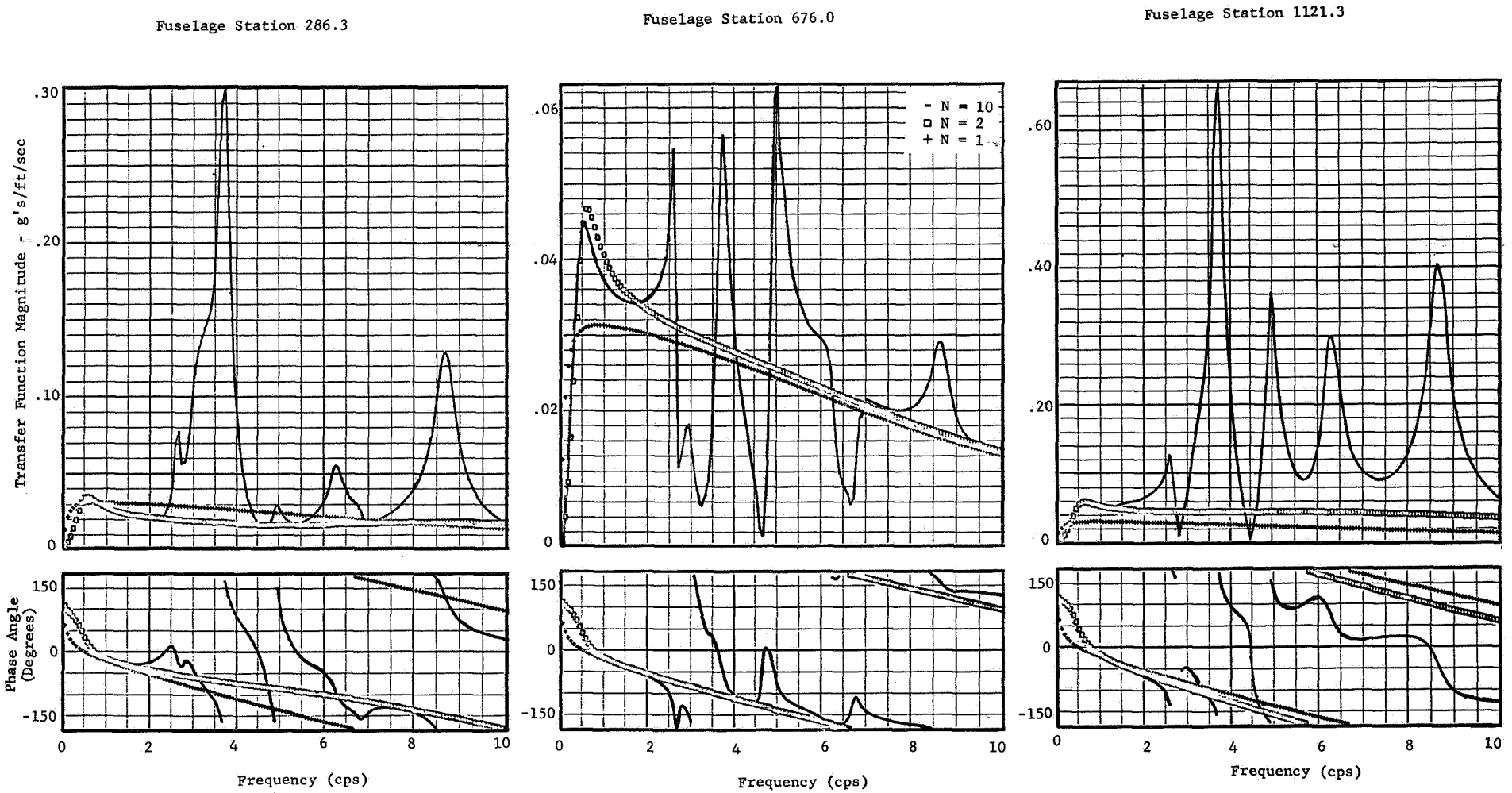

Analysis Parameters

ρ = .002241 slugs/ft^3, Mach = 0.80, V = 921 ft/sec, SAS ON, C.G. = 26.8% MAC

Figure 31 Computed Transfer Functions for Ten, Two and One Degrees of Freedom, Run 131-3

The magnitude and phase angle of the transfer function can be expressed as

$$\left| \frac{\ddot{h}}{w_g} \right| = \frac{S\, C_{L_\alpha} \frac{\rho V}{2}}{\sqrt{m^2 + \left(\frac{S\, C_{L_\alpha}\, \rho V}{4\pi f} \right)^2}} \tag{59}$$

$$\theta_o = \tan^{-1} \frac{S\, C_{L_\alpha}\, \rho V}{4\pi f m} \tag{60}$$

The limits of the magnitude as frequency approaches zero and infinity, respectively, are shown below.

$$\lim_{f \to o} \left| \frac{\ddot{h}}{w_g} \right| = 0 \tag{61}$$

$$\lim_{f \to \infty} \left| \frac{\ddot{h}}{w_g} \right| = \frac{S\, C_{L_\alpha}\, \rho V}{2m}$$

The numerical values of the constants in equation (57) through (61) are listed below for run 131-3.

$S = 1542.6 \text{ Ft}^2$

$C_{L_\alpha} = 2.84$

$\rho = .002241 \text{ slug/ft}^3$

$V = 921. \text{ ft/sec}$

$m = 4270. \text{ slugs}$

Equation (59) is evaluated at several frequencies and listed in table 14 in units of g's per foot per second of gust velocity for comparison with the magnitude of the transfer function computed for one DOF.

Table 14 Comparison of Equation (59) With One DOF Magnitude

(cps)	Eq. (59)	One DOF (SAS OFF)
0	0	------
1/15	.01210	.01208
6/15	.03031	.02979
1.0	.03244	.03142
21/15	.03266	.03109
10	.03289	.03196
∞	.03289	------

Equation (59) evaluated for run 131-3 approaches the level .03289 asympotically as frequency increases. Comparing, with the one DOF transfer function magnitude plotted on figure 31 shows good agreement from zero to 0.5 cps. Between 0.5 cps and 1.0 cps the one DOF transfer function plotted on figure 31 reaches a peak and decreases with frequency beyond that point. This reduction is primarily due to the reduction in the magnitude of the lift produced by the traveling gust velocity wave when unsteady aerodynamics are employed. Hence, the simple quasi-steady equation for the one DOF transfer function should approach the unsteady one-DOF-transfer function at the low frequency end. Throughout the frequency range the quasi-steady one DOF magnitude provides an upper limit that should never be exceeded by the unsteady one DOF transfer function.

Since the gust velocity is sensed a distance ℓ upstream of the a.c. there will be a time delay between the instant the peak of the traveling gust wave passes the gust sensor and the instant it passes the a.c. Assuming the lift produced by the gust velocity is a maximum at the instant the gust velocity peak arrives at the a.c. the additional phase angle lag produced entirely by the

distance between the gust sensor and the a.c., can be expressed as follows

$$\theta_{\ell} = \frac{\ell}{V} \quad f(360) \tag{62}$$

Subtracting equations (62) from (59), the total phase angle for the one DOF quasi-steady transfer function can be expressed as

$$\theta = \tan^{-1} \frac{S\, C_{L_\alpha}\, \rho V}{4\, \pi\, f m} - \frac{\ell}{V} \quad F(360) \tag{63}$$

The distance ℓ between gust sensor and a.c. for run 131-3 is 61.1 feet. Equation (63) is evaluated for several frequencies and listed in table 15 for comparison with the one DOF phase angle obtained from the analysis with SAS OFF.

Table 15 Comparison of Equation (63) With One DOF Phase Angle

(cps)	Eq. (63)	One DOF (SAS OFF)
0	90^{o}	----------
1/15	65^{o}	66.21^{o}
6/15	13.26^{o}	10.84^{o}
1	-14.28^{o}	-19.57^{o}
21/15	-16.54^{o}	-33.60^{o}
10	132.45^{o}	97.33^{o}

It can be seen that equation (63) predicts the one DOF phase angle of figure 31 very well. The difference in phase angles increases with frequency and can be attributed to the increasing phase angle predicted by unsteady aerodynamics as frequency increases. Equation (59) and (63) also predict the magnitude and phase angle of the one DOF transfer functions for run 131-10 and 134-7.

When rigid body pitch is added as a DOF the two DOF transfer functions predict the response in the short period frequency range

very well. Referring to figure 31, it can be seen that both the magnitude and phase angle of the two DOF transfer functions agree very well with the ten DOF transfer functions from zero to approximately 2 cps. Above 2 cps the elastic degrees of freedom have a pronounced effect on the transfer functions.

Variation in Transfer Functions at Station 286.3 with Number of Degree of Freedom

Transfer functions were computed at station 286.3 (pilot station accelerometer A428) for run 131-3 (using 2000 feet air density) for 3, 4, 5, 6, 7, 8 and 9 DOF by adding natural modes 1, 2, 3, 4, 5, 6, 7 successively to the two rigid body degrees of freedom. The transfer functions for 3 through 8 DOF are plotted in figure 32. It is of interest to note that the peak near 2.6 cps for the 3 DOF transfer function is approximately 13 percent higher than measured. This peak is reduced by the addition of the second natural mode for the 4 DOF transfer functions to a level that is approximately 5 percent below the measured value. The 5 DOF transfer function is very similar to the 4 DOF indicating that the third natural mode contributes very little to the acceleration at station 286.3. The addition of the fourth natural mode to obtain the 6 DOF transfer function reduces the peak near 2.6 cps to a level that is approximately 22 percent below the measured level. In addition, the peak near 3.7 cps produced by adding the fourth mode is so large it maskes the peak near 3.1 cps on the 4 and 5 DOF transfer functions. The magnitude of the peak near 3.7 cps is approximately 2.7 times the measured value. The effect of adding modes 5 and 6 successively to obtain the 7 and 8 DOF transfer functions is to add peaks at 4.9 cps and 6.2 cps without significantly altering the peaks associated with the 6 DOF transfer functions. The 9 DOF transfer function is not plotted but it can be described as very similar to the 8 DOF transfer function with a slight shoulder in the magnitude near 6.7 cps. The effect of adding both modes 7 and 8 can be seen by referring back to the 10 DOF transfer function plotted on figure 31. The eighth mode adds a large peak near 8.7 cps. The measured data show no indication of this peak. It should also be noted that the addition of each degree of freedom improves the phase angle comparison.

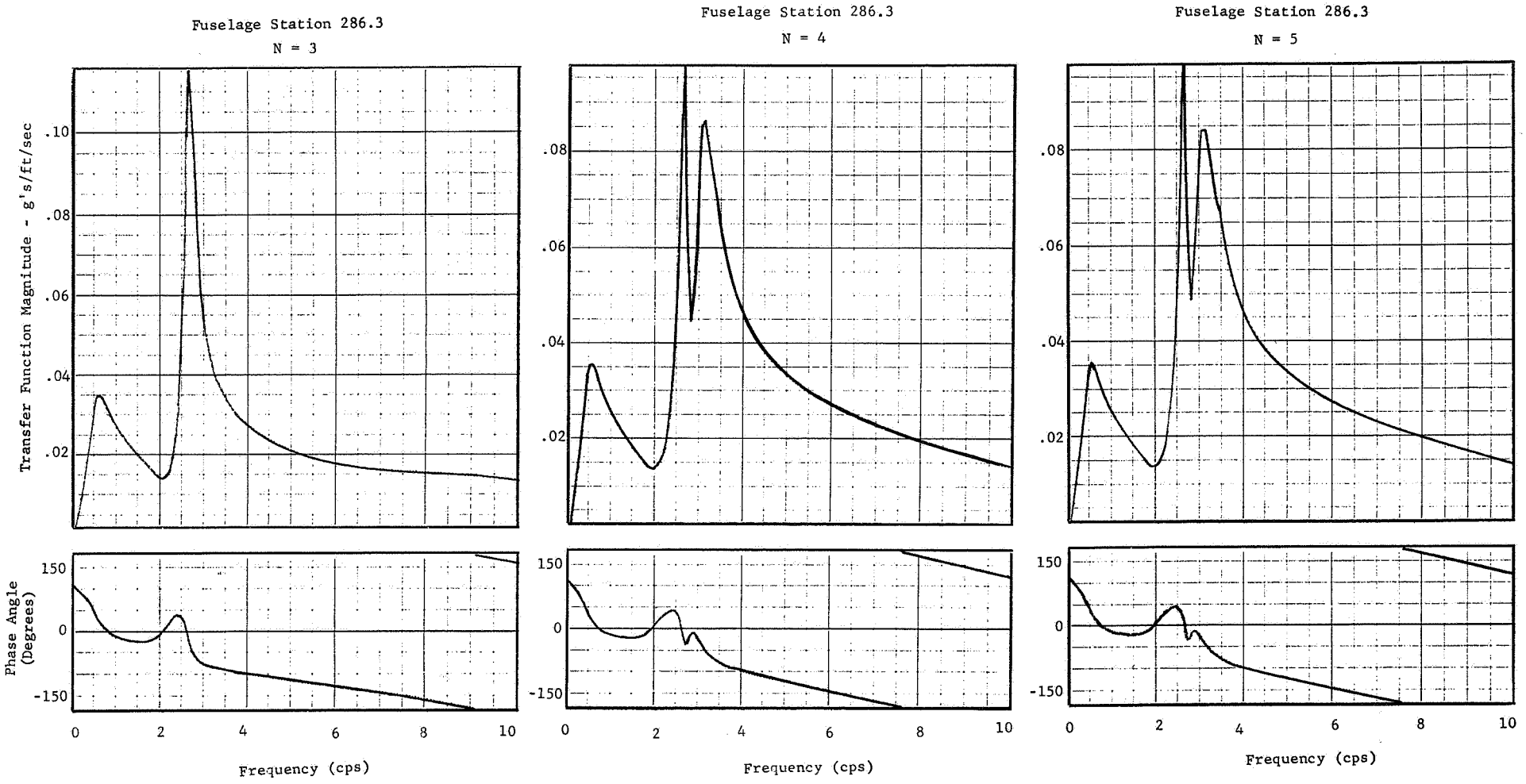

Analysis Parameters

ρ = .002241 slugs/ft^3, Mach = 0.80, V = 921 ft/sec, SAS ON, C.G. = 26.8% MAC

Figure 32 Variations in Computed Transfer Functions at Station 286.3 With Number of DOF, Run 131-3

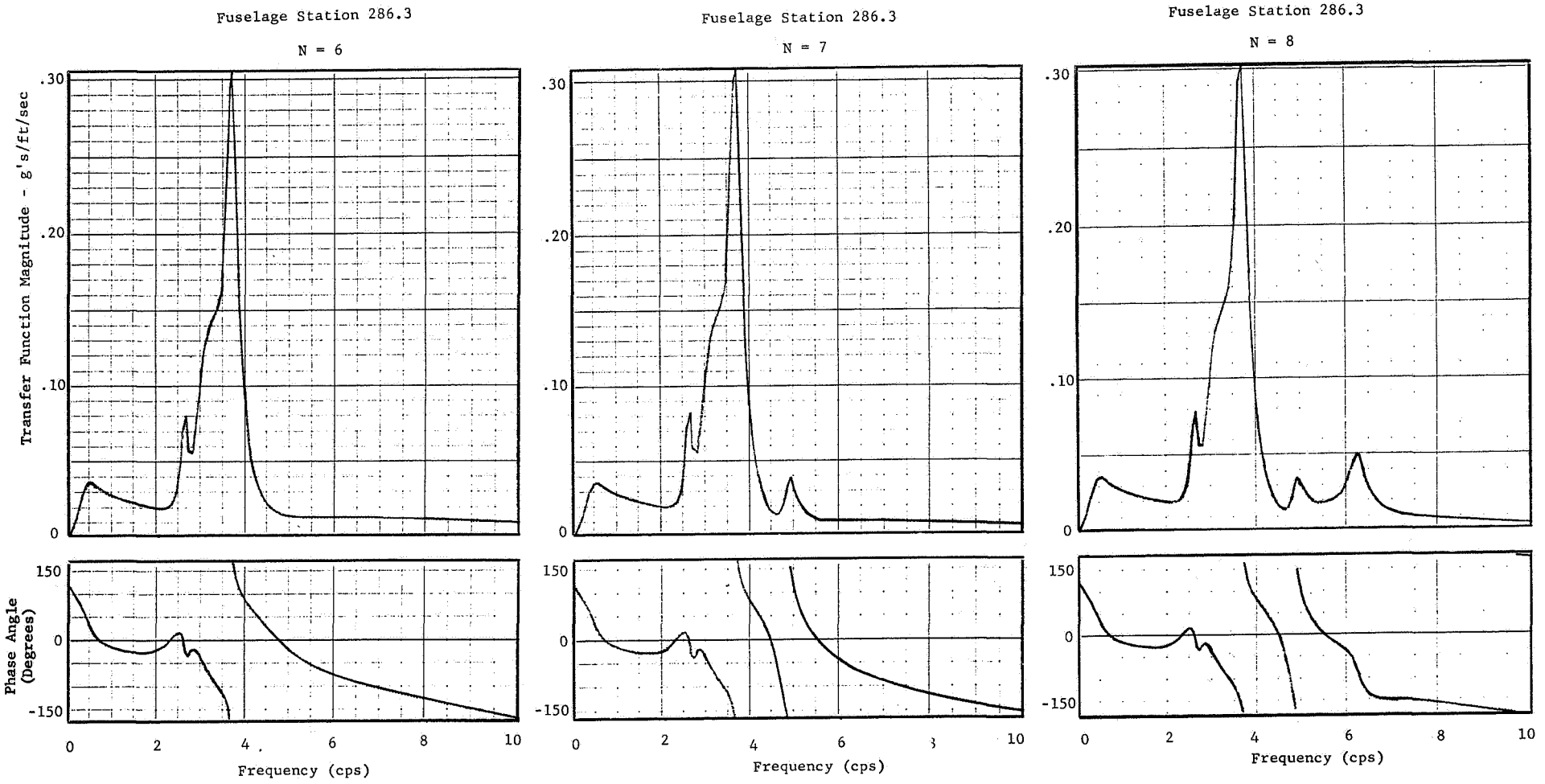

Analysis Parameters

ρ = .002241 slugs/ft^3, Mach = 0.80, V = 921 ft/sec, SAS ON, C.G. = 26.8% MAC

Figure 32 (Continued) Variation in Computed Transfer Function at Station 286.3 With Number of DOF, Run 131-3

Variation in Transfer Functions at Station 676.0 With Number of Degrees of Freedom

Transfer functions for 3, 4, 5, 6, 7 and 8 DOF for station 676.0, A1, are plotted in figure 33 for run 131-3 as computed for a 2000 feet altitude. It is of interest to note that the magnitude of the peak near 2.6 cps for the 3 DOF transfer function is also approximately 13 percent higher than measured as previously observed for comparisons with A428. The addition of the second mode for the 4 DOF transfer functions reduces this peak to a level that is approximately 7 percent below the measured peak which is also very similar to the effect produced at A428. A small peak near 3 cps is also added. The 5 DOF transfer function is again almost the same as the 4 DOF transfer function. The addition of the fourth natural mode to obtain the 6 DOF transfer functions reduces the peak near 2.6 cps to a level that is approximately 31 percent below the measured level (compared with 22 percent for the similar comparison at A428). The fourth mode adds a peak near 3.7 cps with a magnitude which is approximately 1.63 times the measured value. The addition of the fifth normal mode (7 DOF) produces a peak at 5.0 cps without significantly effecting the other peaks. The measured data has a peak at 5.4 cps with almost the same amplitude. The addition of mode 6 (8 DOF) adds a shoulder and a valley at approximately 6.2 cps without significantly changing the other peaks. The addition of the seventh natural mode produces very little change. The effect of adding both the seventh and eighth mode can be seen by referring back to the 10 DOF transfer function on figure 31. The eighth mode adds a peak near 8.7 cps but no corresponding peak appears on the measured data. In general, the phase angle correlation improves as additional degrees of freedom are added for A1 as was the case for A428.

Variation in Transfer Functions at Station 1121.3 with Number of Degrees of Freedom

Transfer functions for 3, 4, 5, 6, 7 and 8 DOF for station 1121.3, A11, are plotted in figure 34 for run 131-3 as computed for a 2000 feet altitude. The peak near 2.6 cps has a magnitude that is approximately 10 percent less than the corresponding peak in the measured data. Therefore, the 3 DOF transfer functions provide good correlation with the short period frequency

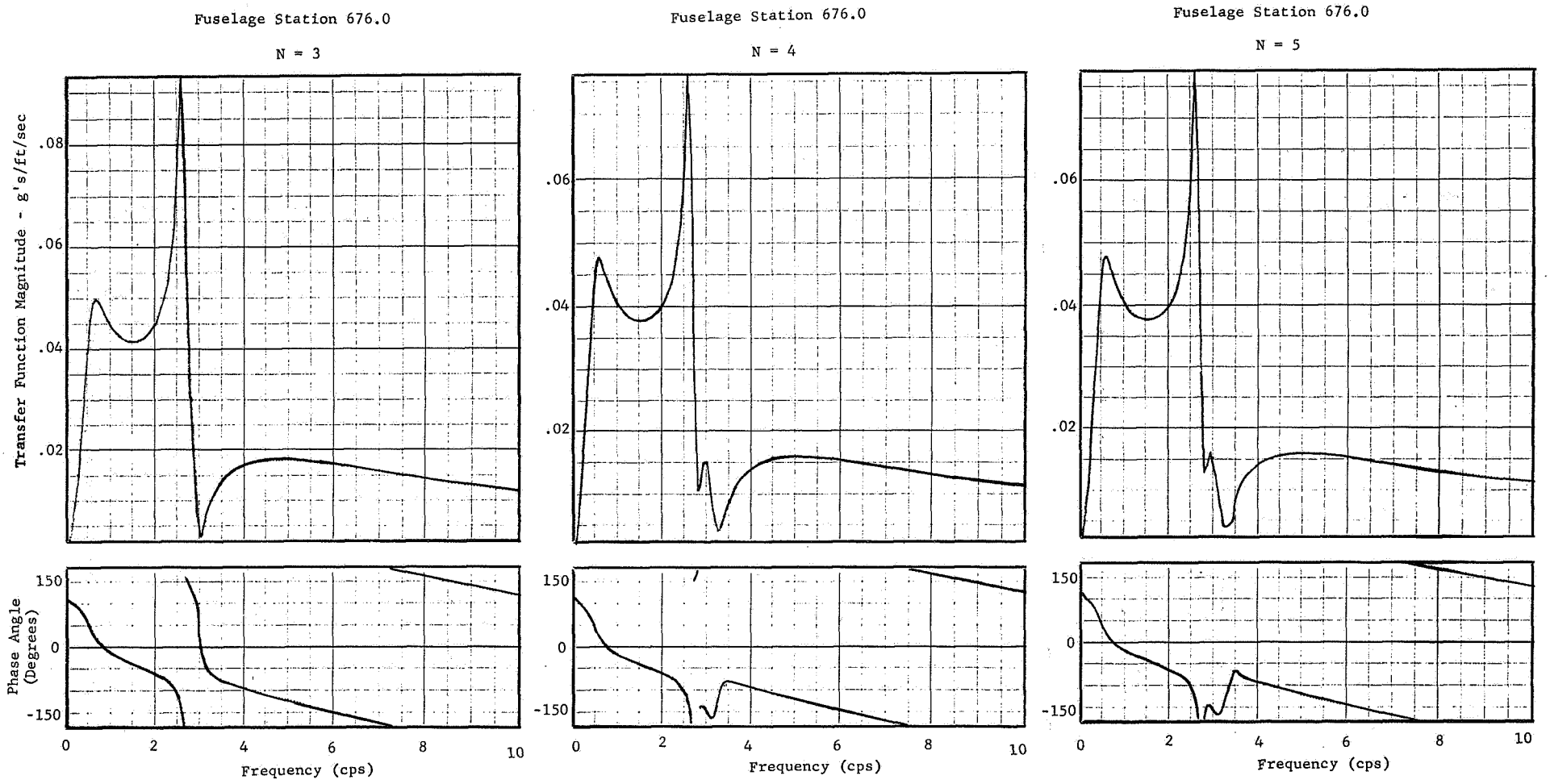

Analysis Parameters

ρ = .002241 slugs/ft^3, Mach = 0.80, V = 921 ft/sec, SAS ON, C.G. = 26.8% MAC

Figure 33 Variations in Computed Transfer Functions at Station 676.0 With Number of DOF, Run 131-3

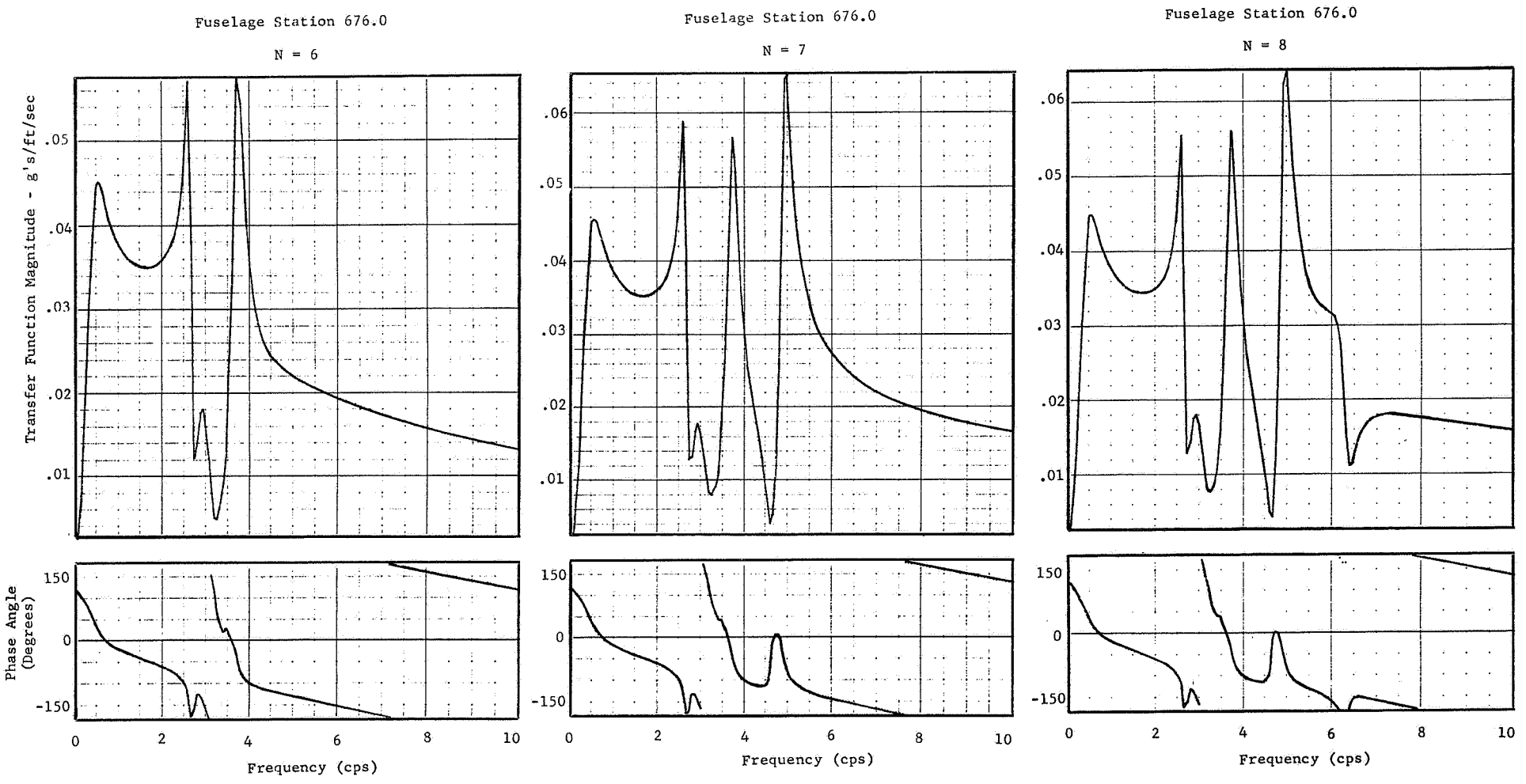

Analysis Parameters

ρ = .002241 slugs/ft^3, Mach = 0.80, V = 921 ft/sec, SAS ON, C.G. =26.8% MAC

Figure 33 (Continued) Variation in Computed Transfer Function at Station 676.0 With Number of DOF, Run 131-3

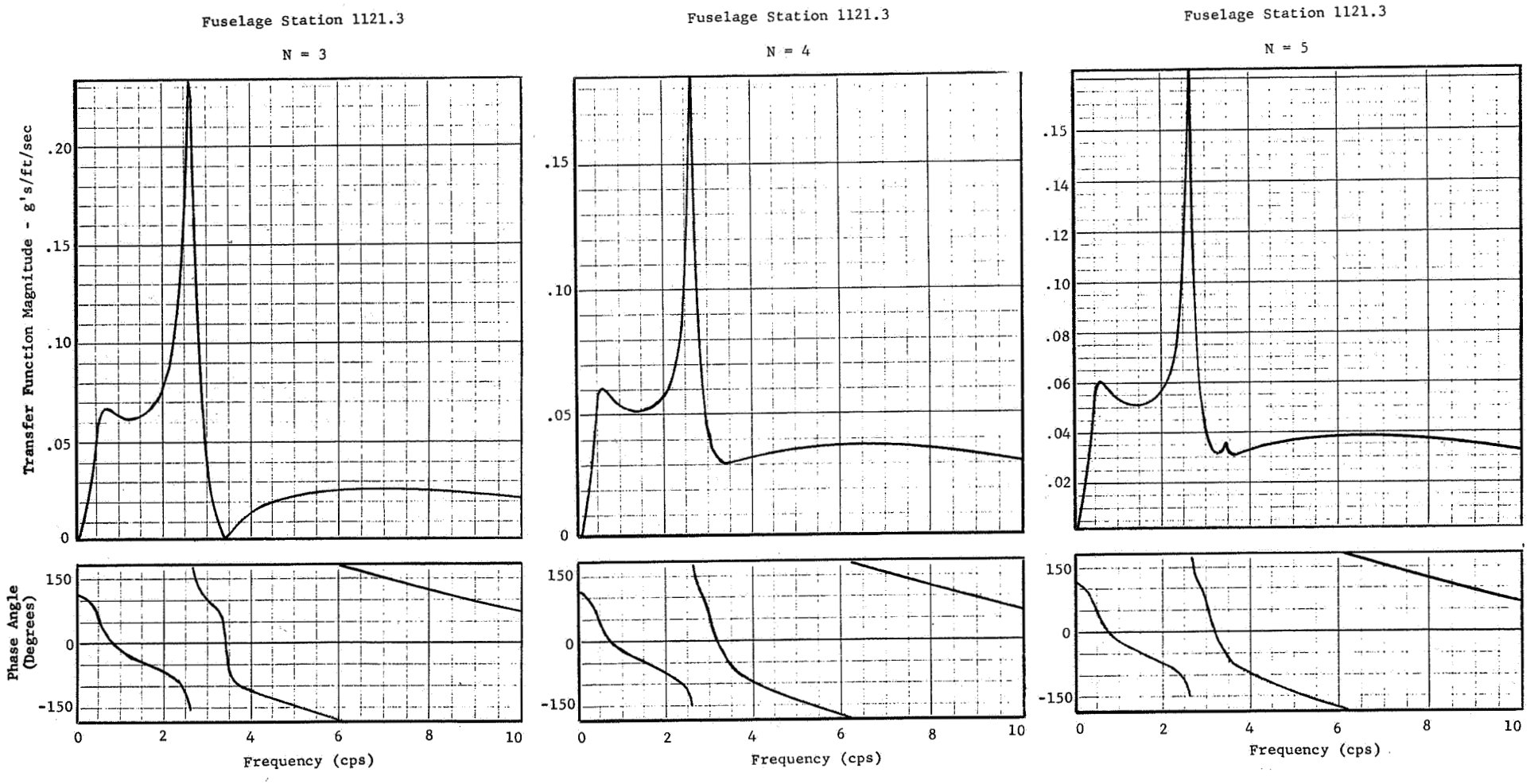

Analysis Parameters

ρ = .002241 slugs/ft^3, Mach = 0.80, V = 921 ft/sec, SAS ON, N = 10, C.G. = 26.8% MAC

Figure 34 Variations in Computed Transfer Functions at Station 1121.3 With Number of DOF, Run 131-3

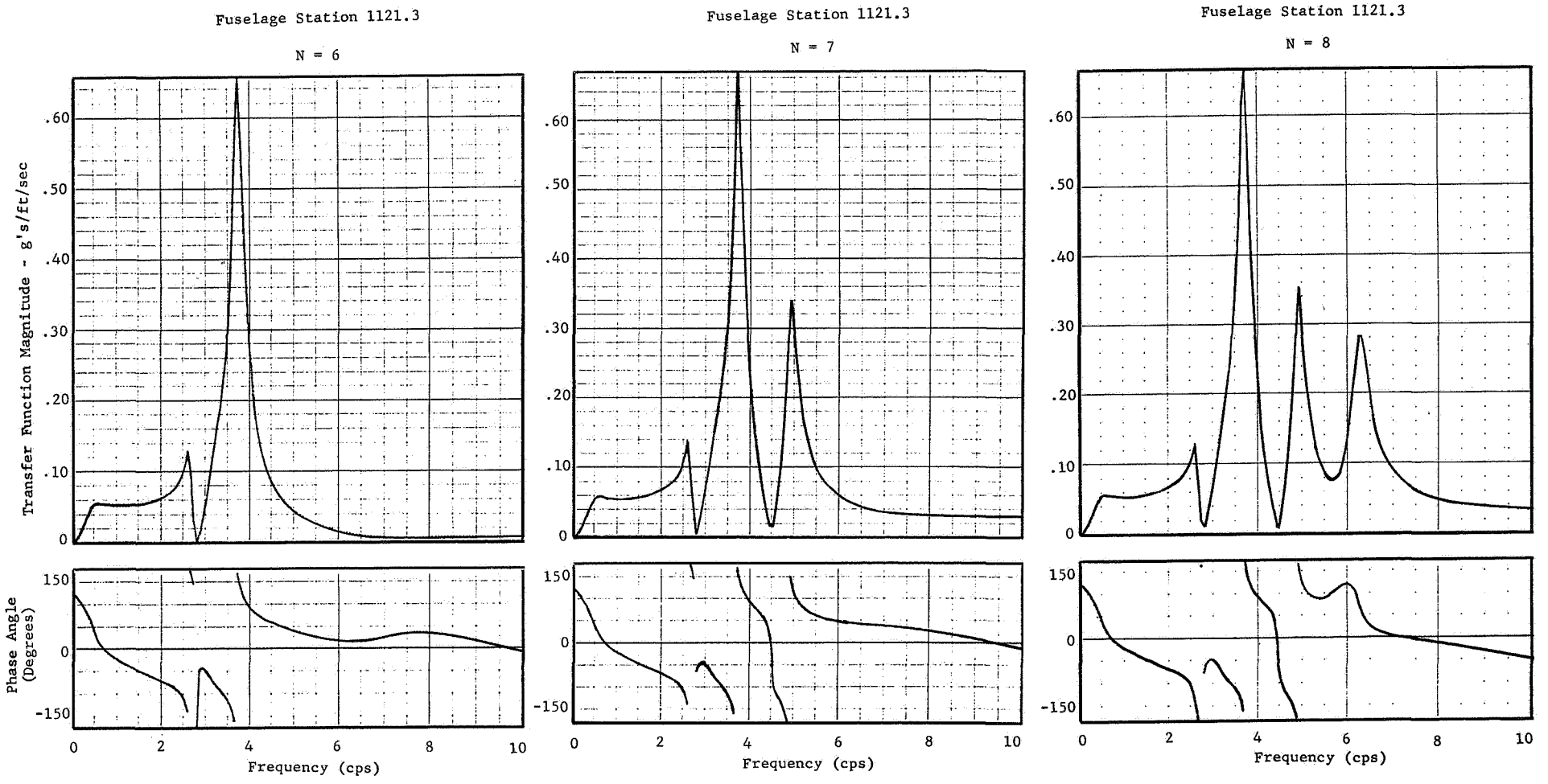

Analysis Parameters

ρ = .002241 slugs/ft^3, Mach = 0.80, V = 921 ft/sec, SAS ON, N = 10, C.G. = 26.8% MAC

Figure 34 (Continued) Variation in Computed Transfer Function at Station 1121.3 With Number of DOF, Run 131-3

and the first natural mode peak for all three accelerometer stations. The computed peak magnitude at A428 and A1 are approximately 13 percent greater than measured and the computed peak at A11 is approximately 10 percent less than measured. The addition of the second normal mode (4 DOF) reduces the 2.6 cps peak amplitude approximately 25 percent below the peak on the 3 DOF transfer function. The addition of the third mode produces no significant change to the 2.7 cps peak and adds a small peak near 3.5 cps. The addition of the fourth natural mode (6 DOF) reduces the peak at 2.6 cps to approximately 70 percent of its value on the 5 DOF transfer functions. The fourth mode also adds a large peak at 3.7 cps which maskes the small peak at 3.5 cps. The magnitude of the peak at 3.7 cps is approximately 3.6 times the measured value. The addition of the fifth mode (7 DOF) produces a peak near 4.9 cps without significantly effecting the other peaks. The magnitude of the peak near 4.9 cps is approximately twice the magnitude of the measured peak at 5.3 cps. The addition of the sixth mode (8 DOF) produces a peak near 6.3 cps without significantly changing the other peaks. The addition of the seventh mode produces very little change. The effect of adding both the seventh and eighth modes can be seen by referring to the 10 DOF transfer function plotted in figure 31. The phase angle comparison with accelerometer A11 appears to continually improve with the addition of degrees of freedom.

$\bar{A}$ and N_o Variations with Number of Degrees of Freedom

The variation of $\bar{A}$ and N_o with number of degrees of freedom for run 131-3 are shown in table 16. The computed value of $\bar{A}$ at station 676.0 (A1) for 2 DOF is very close to the measured value and changes very little with added DOF. However, the computed values of $\bar{A}$ at stations 286.3 (A428) and 1121.3 (A11) as predicted by 2 DOF are considerably less than the measured data. As would be expected from observing the transfer functions, the $\bar{A}$ for these two stations increases very sharply from the 5 DOF values to the 6 DOF values. As the number of degrees of freedom are increased beyond 6 DOF the $\bar{A}$ for both A428 and A11 continue to increase. The correlation between computed and measured values of $\bar{A}$ is better for 3 DOF than for 10 DOF.

Table 16 Variations of $\bar{A}$ and N_o With Number of Degrees of Freedom

$\bar{A}$

F.S. (in)	Accel.	Computed (2000 Ft. Alt.)										Measured $\bar{A}$
		N = 1	N = 2	N = 3	N = 4	N = 5	N = 6	N = 7	N = 8	N = 9	N = 10	
286.3	A428	.02679	.02224	.02468	.02635	.02639	.03791	.03798	.03796	.03804	.03855	.02814
676.0	A1	.02679	.02998	.03274	.03151	.03152	.03075	.03098	.03074	.03064	.03071	.03019
1121.3	A11	.02679	.03991	.05059	.04415	.04400	.06776	.07250	.07396	.07378	.07690	.05888

N_o

F.S. (in)	Accel.	Computed (2000 Ft. Alt.)										Measured N_o
		N = 1	N = 2	N = 3	N = 4	N = 5	N = 6	N = 7	N = 8	N = 9	N = 10	
286.3	A428	1.4577	1.4566	1.9232	2.2057	2.2093	2.8518	2.8671	2.8778	2.8724	3.1525	2.391
676.0	A1	1.4577	1.4417	1.4085	1.2724	1.2718	1.3835	1.5657	1.5292	1.5126	1.5443	1.638
1121.3	A11	1.4577	1.8354	1.7556	1.8034	1.8141	3.0621	3.2548	3.4882	3.4957	4.0427	2.454

The N_o values computed for 2 DOF are considerable less than the measured values. The N_o values also increase sharply from the 5 DOF values to the 6 DOF values. The N_o values at A428 and A11 for 6 DOF exceed the measured values and the difference increases with the addition of more DOF.

Although there are many differences between the computed and measured transfer functions, it is the large response of the fourth natural mode of vibration in the computed transfer functions that is primarily the reason for the poor correlation between $\bar{A}$ and N_o data at accelerometer A428 and A11.

VARIATIONS IN FUSELAGE STATION

Transfer functions were computed for run 131-3 with a 2000 feet density altitude for twelve fuselage stations ranging from the nose to the tail extremities of the fuselage centerline. Computed transfer functions (1) and station 186.3 (100 inches forward of accelerometer A428 location), (2) at the station 286.3 (coinciding with accelerometer A428 location), and (3) at a station 386.3 (100 inches aft of accelerometer A428 location) are shown in figure 35. Comparing the magnitude of the transfer function at station 186.3 and 286.3 it can be seen that the computed transfer function at station 186.3 compares more favorable with the measured data from zero to 3 cps. Above 3 cps, the comparison is not as good. The phase angle correlation is approximately the same. Comparing the computed transfer function at stations 286.3 and 386.3 it can be seen that the computed transfer function at station 386.3 compares less favorably with the measured data from zero to 3 cps but the comparison is better above 3 cps. The phase angle correlation is about the same below 3 cps but somewhat degraded above 3 cps.

Computed transfer functions (1) at station 576.0 (100 inches forward of accelerometer A1 location), (2) at station 676.0 (coinciding with the accelerometer A1 location), and (3) at station 776.0 (100 inches aft of the accelerometer A1 location) are shown in figure 36. A 100 inch forward shift degrades the correlation between the magnitude of the computed and measured data. The degree of phase angle correlation is about the same from zero to 8 cps. The computed transfer function magnitude

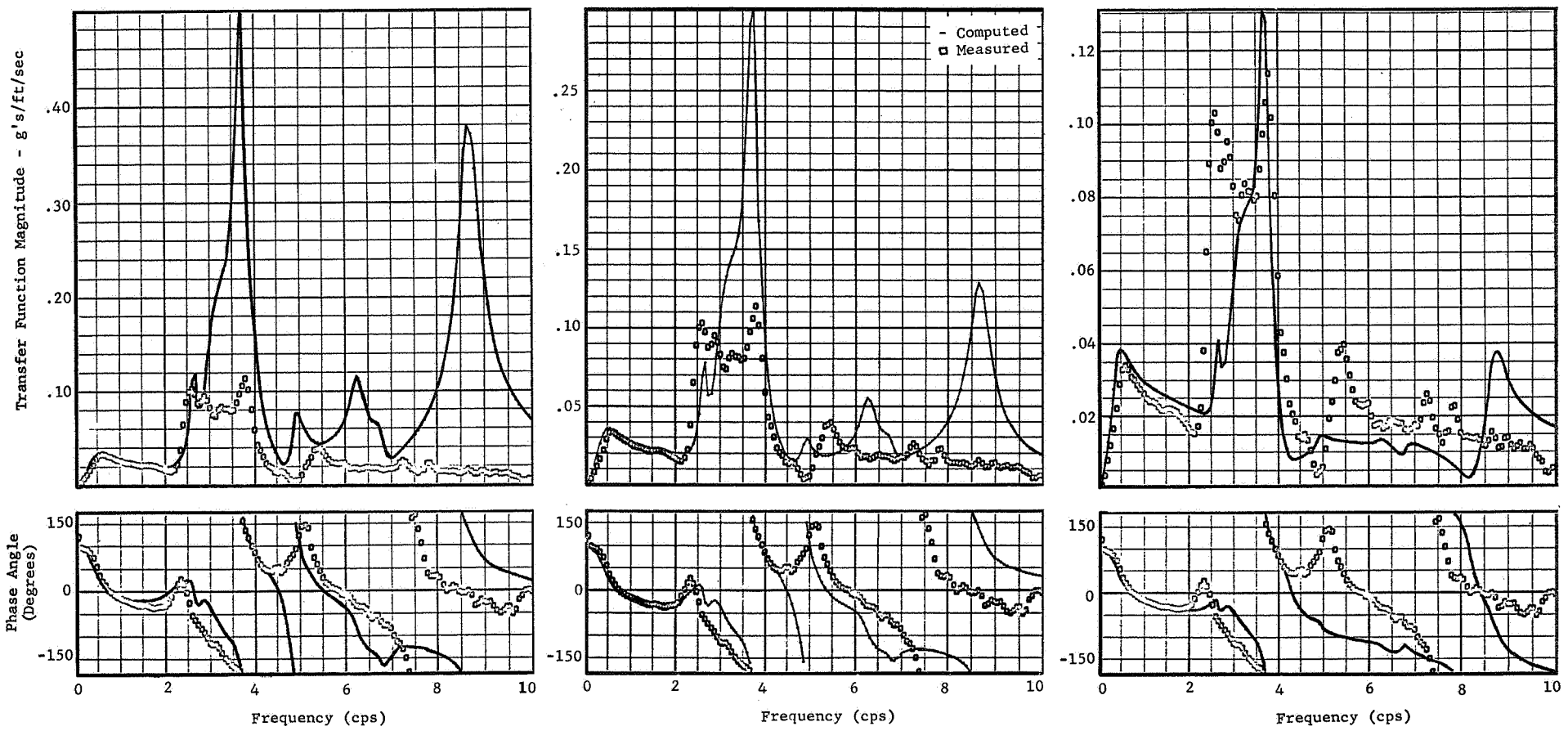

Analysis Parameters

ρ = .002241 slugs/ft^3, Mach = 0.80, V = 921 ft/sec, SAS ON, N = 10, C.G. = 26.8% MAC

Figure 35 Comparison of Computed Transfer Functions at Three Stations With Measured Transfer Function at Station 286.3, A428, Run 131-3

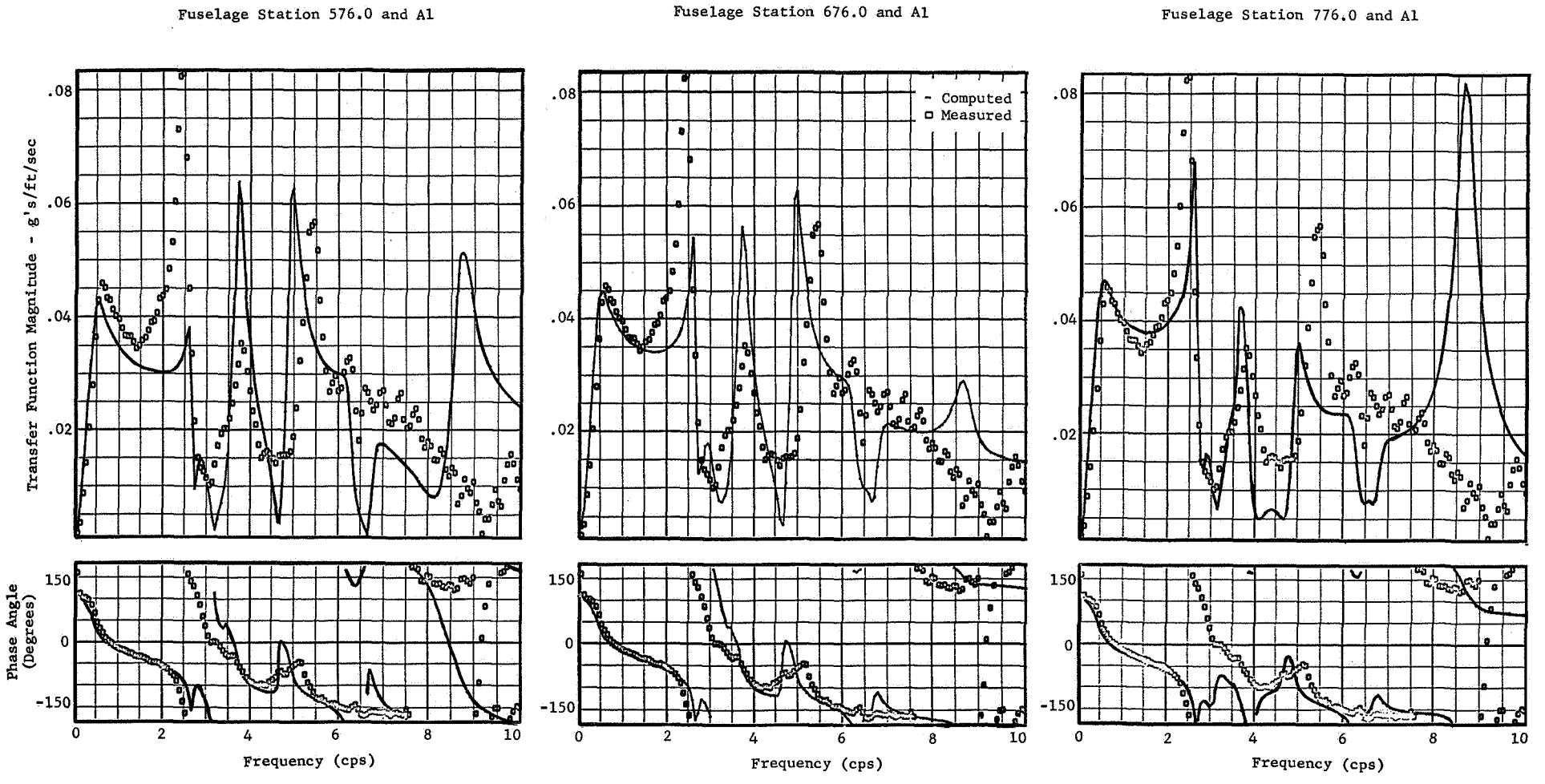

Analysis Parameters

ρ = .002241 slugs/ft^3, Mach = 0.80, V = 921 ft/sec, SAS ON, N = 10, C.G. = 26.8% MAC

Figure 36 Comparison of Computed Transfer Functions at Three Stations With Measured Transfer Functions at Station 676.0, A1, Run 131-3

for the station 100 inches aft of A1 compares better with measured data from zero to 5 cps but compares less favorable above 5 cps. Considering the entire frequency range it appears that the computed transfer function for the fuselage station which coincides with the accelerometer A1 location correlates best with the measured data.

Computed transfer functions (1) at station 1021.3 (100 inches forward of the accelerometer A11 location), (2), at station 1121.3 (coinciding with the accelerometer A11 location) and (3) at station 1161.6 (extreme aft fuselage station) are shown on figure 37. It can be seen that the transfer function computed for the station 100 inches forward of A11 compares more favorable with the measured data over the entire frequency range with the exception of the frequency range between 0.5 and 1.5 cps.

Variations in $\bar{A}$ and N_o With Fuselage Station

$\bar{A}$ and N_o data computed at twelve fuselage stations for run 131-3 using a 2000 feet altitude density are listed in table 17. Computed data for 1, 2 and 10 DOF are tabulated. These data are also plotted in figure 38 along with the measured data. $\bar{A}$ and N_o data computed for a density which actually existed during run 131-3 (4600 feet standard day) are also shown at the three accelerometer locations as flagged symbols. Restricting attention first to the computed data for 10 DOF on figure 38 it can be seen that the computed $\bar{A}$ and N_o at a station approximately 50 inches aft of A428 compare very well with the measured data at A428. The computed $\bar{A}$ and N_o data at the A1 location compare very well with the measured data at A1. However, it requires approximately 100 inch forward shift in the computed data to obtain reasonable correlation with the data measured by accelerometer A11. It is also of interest to compare the computed data from the 1 and 2 DOF solutions. The 1 DOF $\bar{A}$ and N_o data compare very well with the measured data at A1. It also agrees very well with the $\bar{A}$ data at A428 although the N_o value is only about one half of the measured value. It considerably underestimates the $\bar{A}$ and N_o measured data at A11. The $\bar{A}$ values for

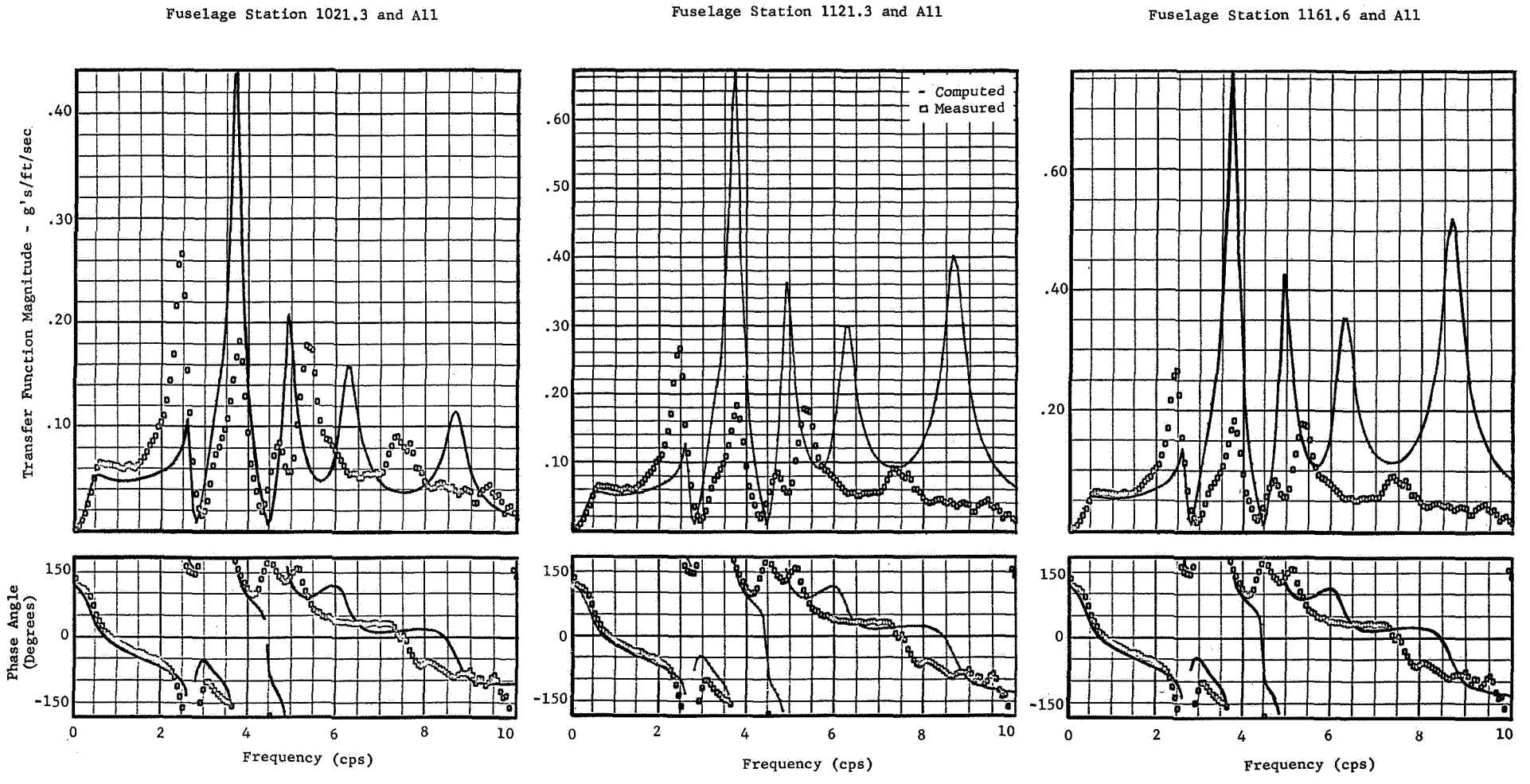

Analysis Parameters

ρ = .002241 slugs/ft^3, Mach = 0.80, V = 921 ft/sec, SAS ON, N = 10, C.G. = 26.8% MAC

Figure 37 Comparison of Computed Transfer Functions at Three Stations With Measured Transfer Functions at Station 1121.3, A11, Run 131-3

Table 17 $\bar{A}$ and N_o Versus Fuselage Station, Run 131-3

F.S. (in)	Accel.	Computed (2000 Ft. Alt.)						Measured	
		N = 1		N = 2		N = 10			
		$\bar{A}$	N_o	$\bar{A}$	N_o	$\bar{A}$	N_o	$\bar{A}$	N_o
61.5		.02679	1.4577	.01865	2.0962	.08365	4.8392		
130.0				.01965	1.8416	.06852	4.5611		
186.3				.02054	1.6707	.05658	4.2043		
286.3	A428			.02224	1.4566	.03855	3.1525	.02814	2.391
386.3				.02409	1.3516	.02844	1.9876		
576.0				.02787	1.3701	.02890	1.6918		
676.0	A1			.02998	1.4417	.03071	1.5443	.03019	1.638
687.				.03021	1.4509	.03088	1.5449		
776.				.03214	1.5292	.03260	1.6462		
1021.3				.03762	1.7516	.05523	3.1070		
1121.3	A11			.03991	1.8354	.07690	4.0427	.05888	2.454
1161.6		.02679	1.4577	.04084	1.8676	.08693	4.2932		

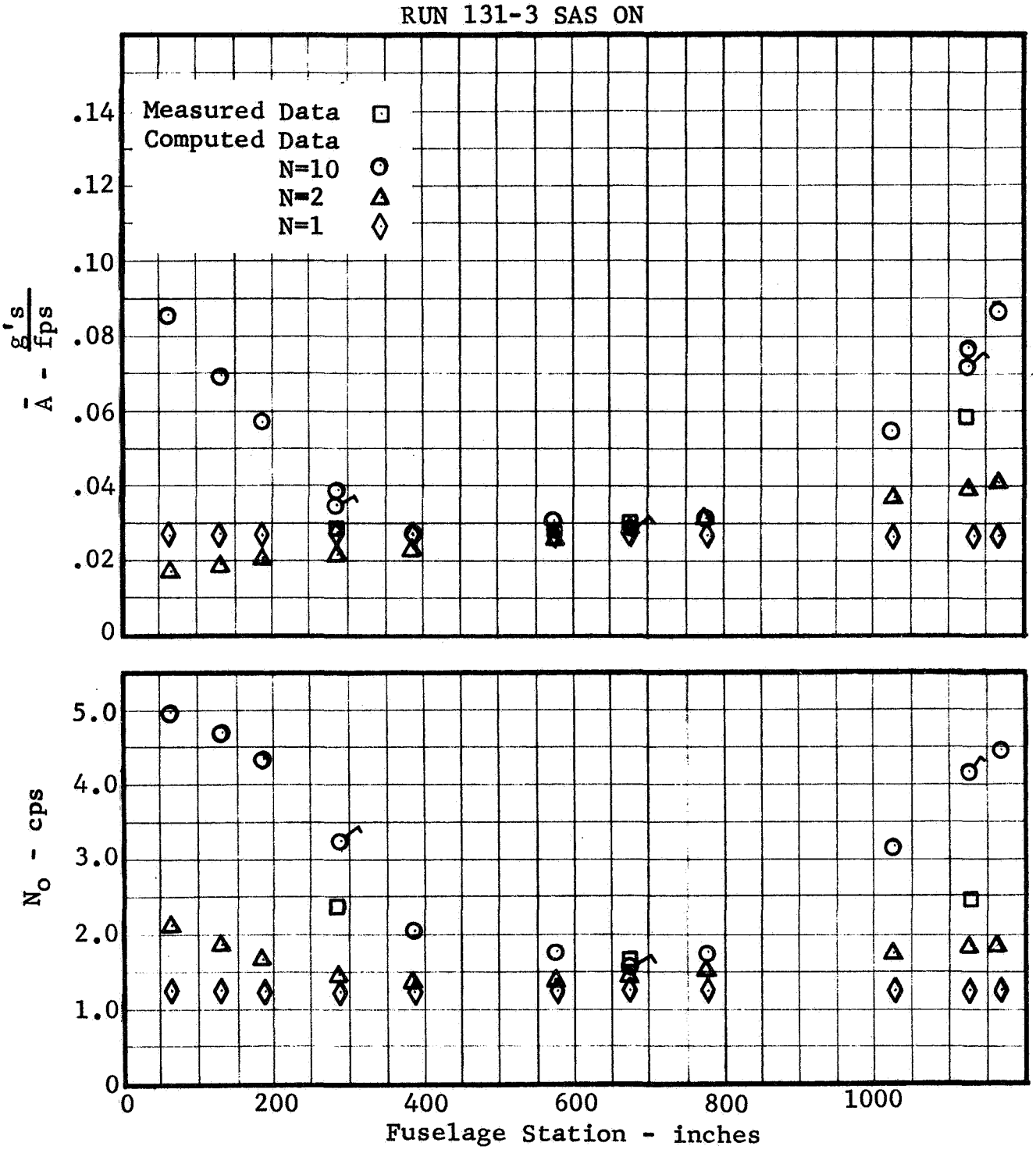

Figure 38 $\bar{A}$ and N_o Versus Fuselage Station Run 131-3

2 DOF agrees with the 1 DOF value near the c.g. but decreases forward of the point and increases aft of the point. Similarly the N_O value for 2 DOF is very close to the 1 DOF value at stations near the c.g. but increases for stations both fore and aft of the point. In general, the 2 DOF $\bar{A}$ and N_O values correlate better with the measured data than does the 1 DOF values. The 10 DOF $\bar{A}$ and N_O values are very close to the 2 DOF values near the c.g. but are considerable greater as the fore and aft distance from this point is increased.

$\bar{A}$ and N_O data computed at twelve fuselage stations for run 131-10 using a 2000 feet altitude density are listed in table 18. These data are also plotted on figure 39. Comparing the values obtained from the 10 DOF solution with the measured data it can be seen that the computed $\bar{A}$ and N_O at a station approximately 50 inches aft of the A428 location would compare very well with the A428 measured data. The correlation between computed data and measured data at A1 is very good. The correlation between computed and measured $\bar{A}$ values at A11 is also very good but could be improved by comparing with computed values at a station approximately 50 inches forward. However, to obtain a good comparison with N_O measured at A11 it is necessary to compare with the computed values approximately 200 inches forward of the A11 location. The $\bar{A}$ computed by the 1 DOF analysis again compares very well with the measured data at A1 although it underestimates the N_O considerably. The N_O computed by the 2 DOF analysis compares as well or better with the measured data than the N_O computed by the 10 DOF analysis at all three accelerometer locations. The 2 DOF $\bar{A}$ values match the measured $\bar{A}$ values at A428 and A1 very closely.

$\bar{A}$ and N_O data computed at 12 fuselage stations for run 134-7 using a 2000 feet altitude density are listed in table 19. These data are plotted on figure 40. The $\bar{A}$ data computed by the 10 DOF analysis compares very well with the measured data at all three accelerometers locations. However, the comparison can again be improved by comparing $\bar{A}$ measured at A428 with the computed data approximately 50 inches aft of A428 and the $\bar{A}$ measured at A11 with the computed value approximately 50 inches forward of A11. The N_O computed by the 10 DOF analyses also compares very well with the measured data at A428 and A1 but over estimates the measured N_O at A11 by almost a factor to two.

Table 18 $\bar{A}$ and N_o Versus Fuselage Station, Run 131-10

F.S. (in)	Accel.	Computed (2000 Ft. Alt.)						Measured	
		N = 1		N = 2		N = 10			
		$\bar{A}$	N_o	$\bar{A}$	N_o	$\bar{A}$	N_o	$\bar{A}$	N_o
61.5		.05195	1.7225	.02702	2.4855	.07403	4.2739		
130.0				.02852	2.1847	.06130	4.0383		
186.3				.03007	2.0000	.05181	3.7119		
286.3	A428			.03339	1.8222	.04684	3.1506	.03188	2.473
386.3				.03727	1.7999	.03738	1.9542		
576.0				.04564	1,9563	.04866	2.4226		
676.0	A1			.05041	2.0650	.05516	2.2682	.05440	1.957
687.				.05094	2.0768	.05585	2.2353		
776.				.05534	2.1693	.06198	1.9762		
1021.3				.06789	2.3842	.09901	3.3465		
1121.3	A11			.07314	2.4548	.13412	3.9744	.11590	2.436
1161.6		.05195	1.7225	.07527	2.4809	.14830	4.1571		

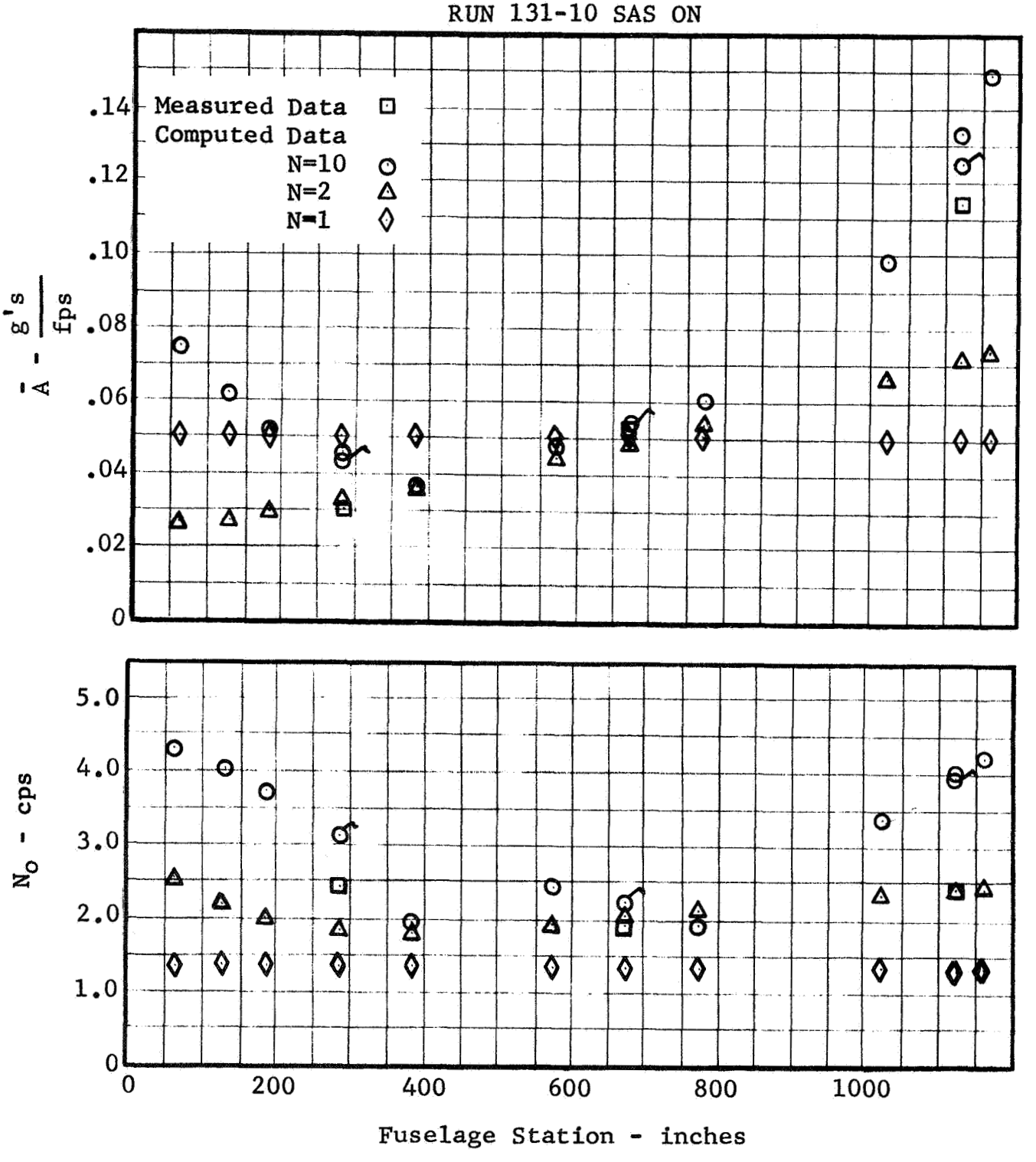

Figure 39 $\bar{A}$ and N_o Versus Fuselage Station Run 131-10

Table 19 $\bar{A}$ and N_o Versus Fuselage Station, Run 134-7

F.S. (in)	Accel.	Computed (2000 Ft. Alt.)						Measured	
		N = 1		N = 2		N = 10			
		$\bar{A}$	N_o	$\bar{A}$	N_o	$\bar{A}$	N_o	$\bar{A}$	N_o
61.5		.04515	1.6596	.02187	3.0282	.07281	4.0718		
130.0				.02254	2.5915	.05983	3.9026		
186.3				.02360	2.2694	.04984	3.6673		
286.3	A428			.02641	1.8811	.03589	2.8887	.03178	2.411
386.3				.03010	1.7545	.03106	2.0324		
576.0				.03860	1.9010	.04146	2.1778		
676.0	A1			.04356	2.0277	.04863	2.0569	.04334	1.711
687.0				.04412	2.0415	.04941	2.0356		
776.				.04872	2.1472	.05617	1.9008		
1021.3				.06189	2.3805	.09045	2.9924		
1121.3	A11			.06740	2.4533	.11586	3.6402	.1041	2.070
1161.6		.04515	1.6596	.06964	2.4797	.12687	3.8255		

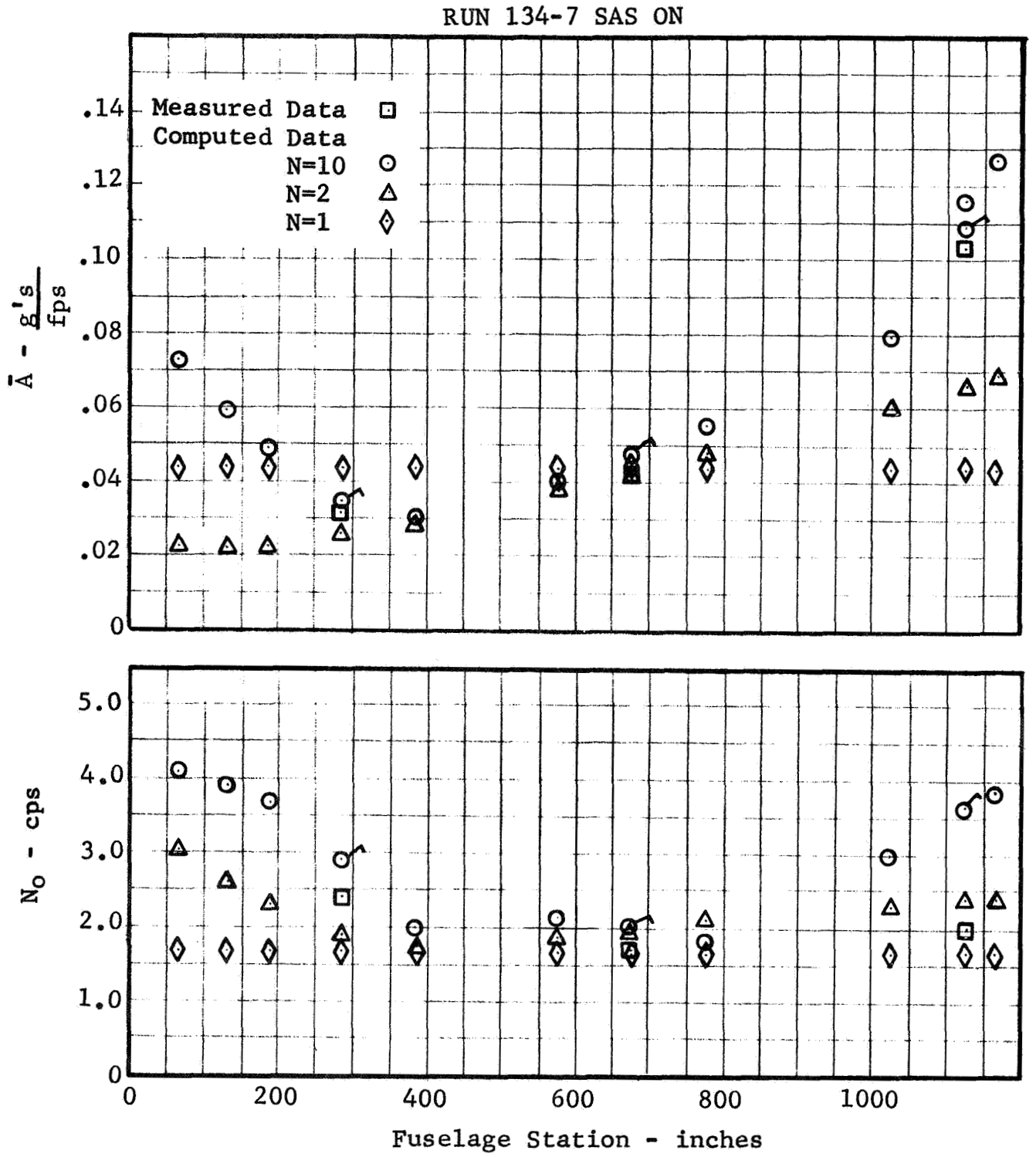

Figure 40 $\bar{A}$ and N_o Versus Fuselage Station Run 134-7

Summarizing, the computed data compares very well with the data measured by accelerometer A1. This accelerometer is near the c.g. and in this region the $\bar{A}$ and N_o values change very little with fuselage station. At the pilot station accelerometer A428 and the aft fuselage accelerometer A11 the $\bar{A}$ and N_o values change rapidly with fuselage station. At these stations the correlation between computed and measured data is not as good as at the c.g.

VARIATIONS IN MACH NUMBER

To evaluate the effect on the transfer functions which would be produced by small errors in the measured Mach number or true air speed, transfer functions were computed for small variations in Mach number. The transfer functions computed for run 131-3 using a 2000 feet altitude standard day density were used as a reference and recomputed changing the Mach number from 0.8 to 0.77 and 0.83. The true air speed was changed by the ratio of the Mach numbers. The Mach numbers and true air speeds which were used for this part of the investigation are listed in table 20.

Table 20 Mach Number and Velocity Variations for Run 131-3

M	V(Ft/Sec)	M/0.80
0.77	886.5	.9625
0.80	921.0	1.0
0.83	955.5	1.0375

Computed Transfer Functions, Run 131-3, For Mach No. 0.77

Computed transfer functions for run 131-3 assuming the Mach number to be reduced from 0.80 to 0.77 are plotted on figure 41. Computed transfer functions at fuselage station 286.3, 676.0 and 1121.3 are shown for comparison with measured data from accelerometers A428, A1, and A11 respectively. The

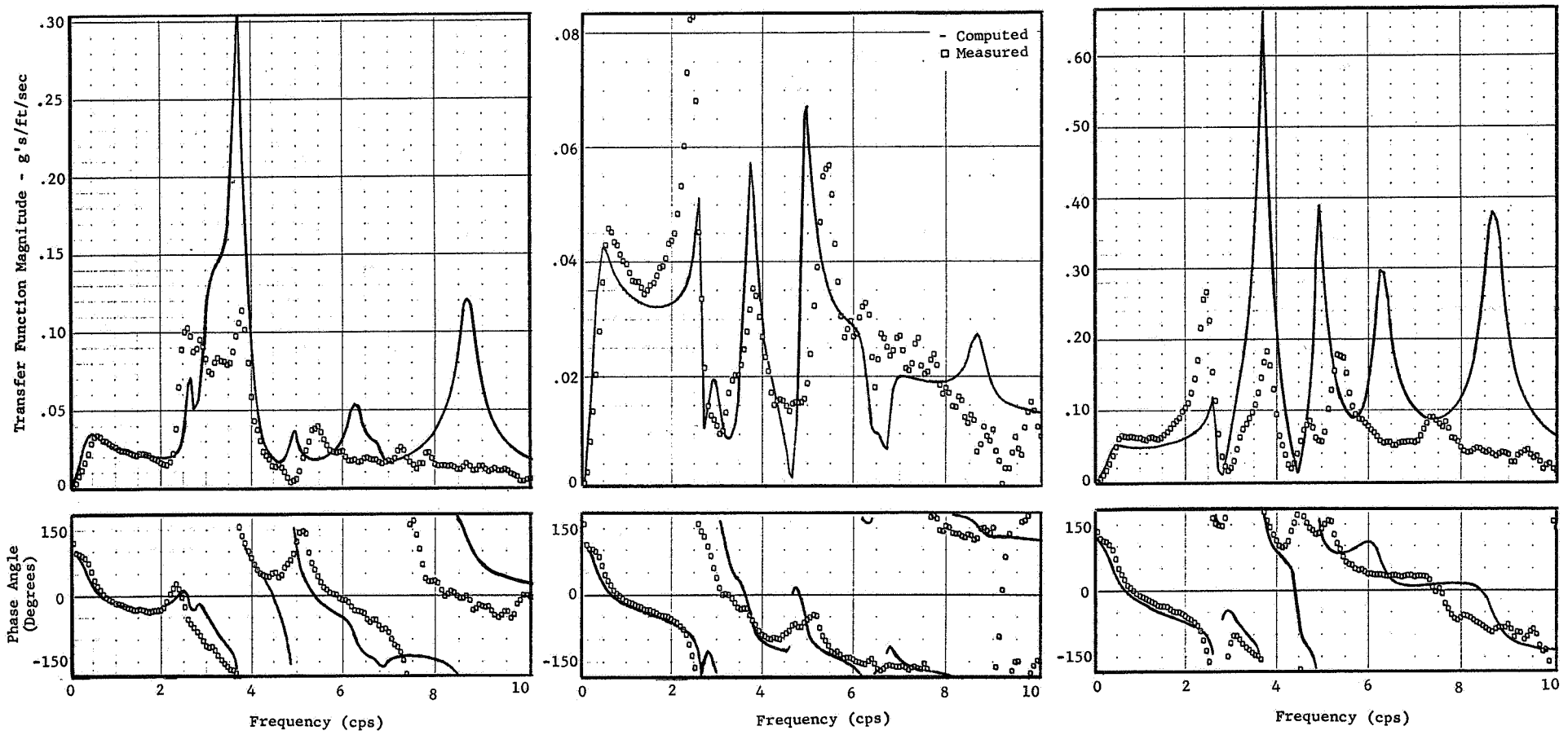

Analysis Parameters

ρ = .002241 slugs/ft^3, Mach = 0.77, V = 886.5 ft/sec, SAS ON, N = 10, C.G. = 26.8% MAC

Figure 41 Comparison of Computed and Measured Transfer Functions, Run 131-3, Mach 0.77

principal effect of the Mach number reduction is to reduce the frequency of the short period mode. The reduction of the velocity by the ratio .9625 produces about a 2 percent reduction in the frequency of the short period mode. This change slightly degrades the correlation between the computed and measured magnitude of the transfer functions in the vicinity of the short period natural frequency for all three stations. The amplitude of the peak near 2.6 cps is also reduced which further degrades the correlation with the measured peak at that frequency. The ratios of the computed transfer functions at 0.77 Mach number to the measured transfer functions for run 131-3 are shown in figure 42. Comparing these ratios with the ratios obtained using computed transfer functions for Mach No. 0.8, figure 26, the slight degradation in the ratios can be seen. To see the effect on the computed transfer functions produced by the Mach number change, the ratios of the computed transfer functions for Mach No. 0.80 are shown in figure 43. This figure shows that the transfer function ratio is not constant with Mach number. However, the variations appear to fluctuate about a ratio which is slightly less than unity. The lower velocity produces a small increase in phase angle lag.

Computed Transfer Functions, Run 131-3, For Mach No. 0.83

Computed transfer functions for run 131-3 assuming the Mach number to be increased from 0.80 to 0.83 are plotted in figure 44. Again the principal effect of the small Mach number increase is in the short period mode. The approximately 4 percent increase in velocity produces approximately a 2 percent increase in the frequency of the short period mode. This effect improves the correlation with the measured data at A1 and A11 while degrading the correlation at A428 slightly. The increased Mach number also increases the magnitude of the peak near 2.6 cps which improves the correlation. The ratios of the computed transfer functions at 0.83 Mach number to the measured transfer functions for run 131-3 are shown in figure 45. By comparing figures 42 and 45 the changes in the degree of correlation produced by the small Mach number changes can be observed. The ratios of the computed transfer functions at 0.83 to the computed transfer function at 0.80 are plotted in figure 46. These ratios again vary widely but the variations appear to fluctuate about an average value that is slightly greater than unity. The higher velocity decreases the phase angle lag.

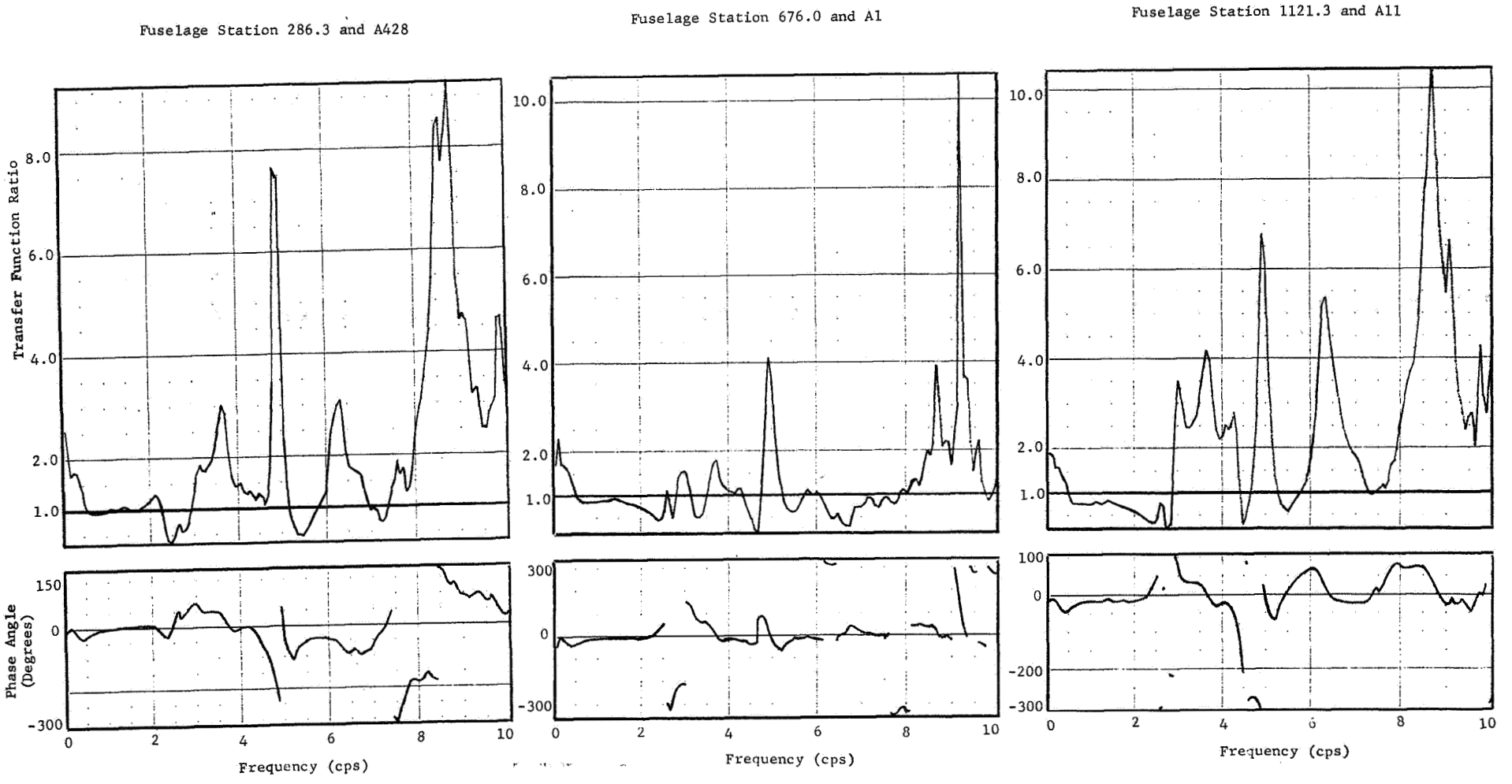

Analysis Parameters

ρ = .002241 slugs/ft^3, Mach = 0.77, V = 886.5 ft/sec, SAS ON, N = 10, C.G. = 26.8% MAC

Figure 42 Ratio of Computed to Measured Transfer Functions, Run 131-3, Mach 0.77

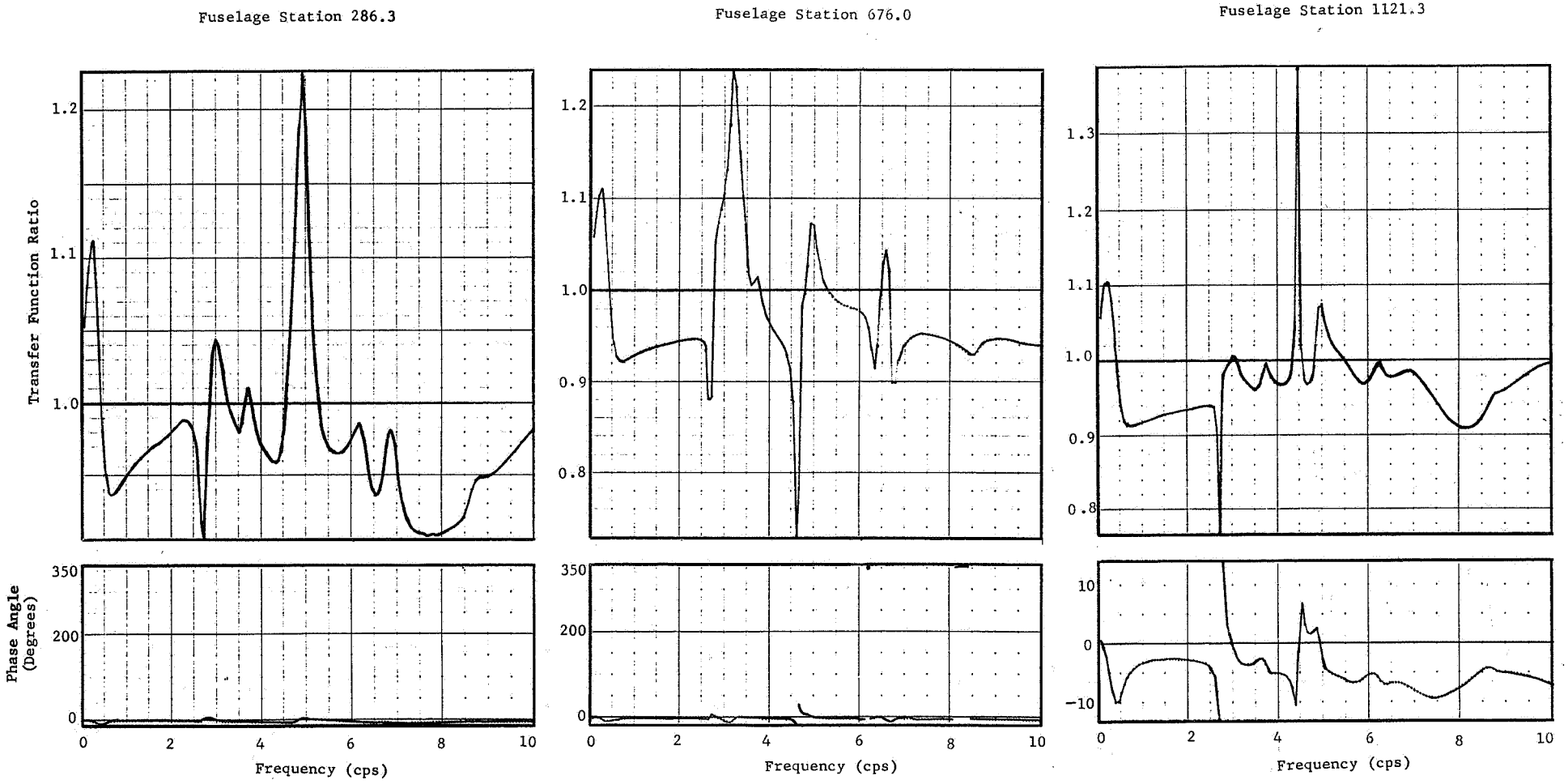

Analysis Parameters

ρ = .002241 slugs/ft^3, SAS ON, N = 10, C.G. = 26.8% MAC

Figure 43 Computed Transfer Function Ratio, Run 131-3, Mach 0.77 to Mach 0.80

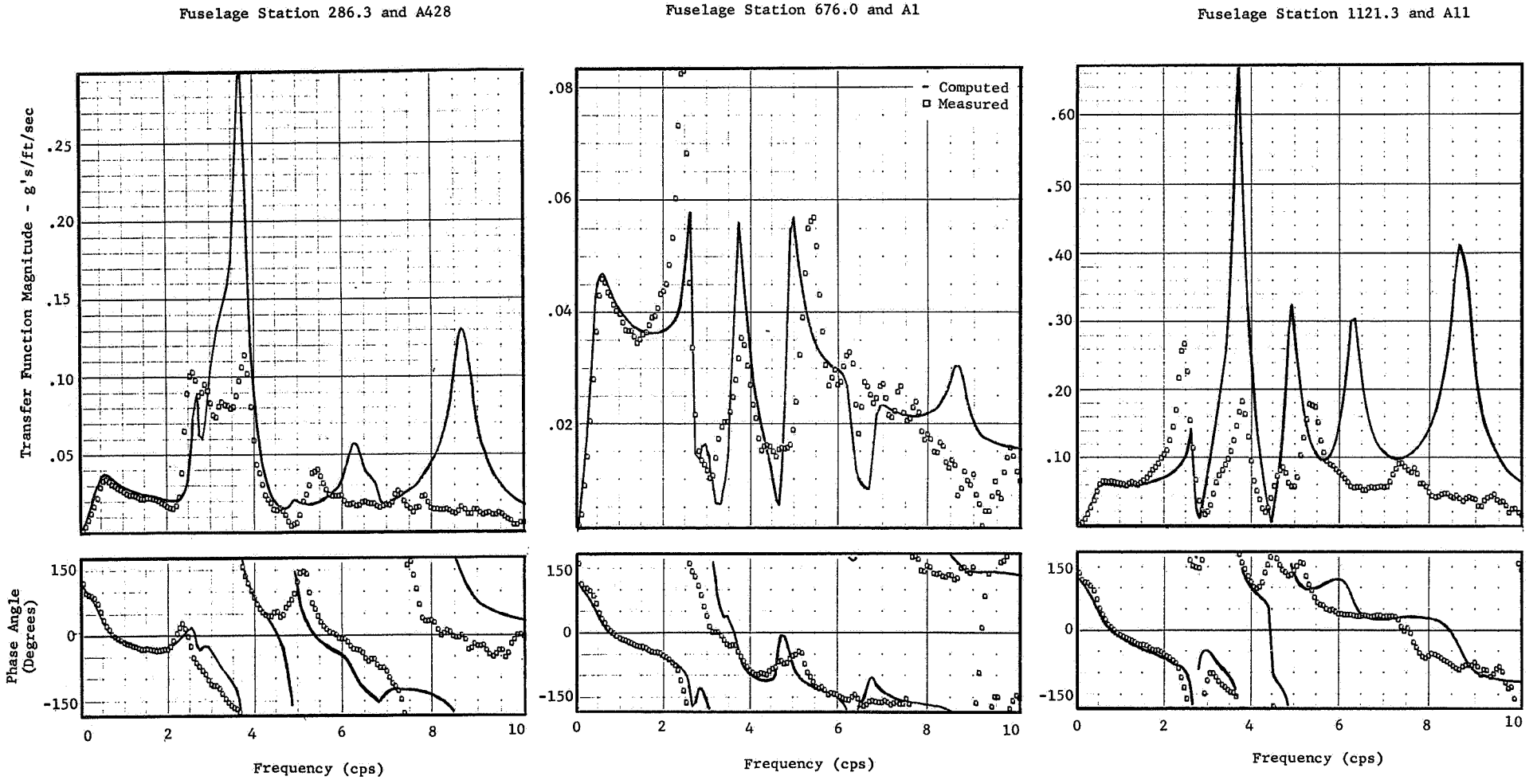

Analysis Parameters

ρ = .002241 slugs/ft^3, Mach = 0.83, V = 955.5 ft/sec, SAS ON, N = 10, C.G. = 26.8% MAC

Figure 44 Comparison of Computed and Measured Transfer Functions, Run 131-3, Mach 0.83

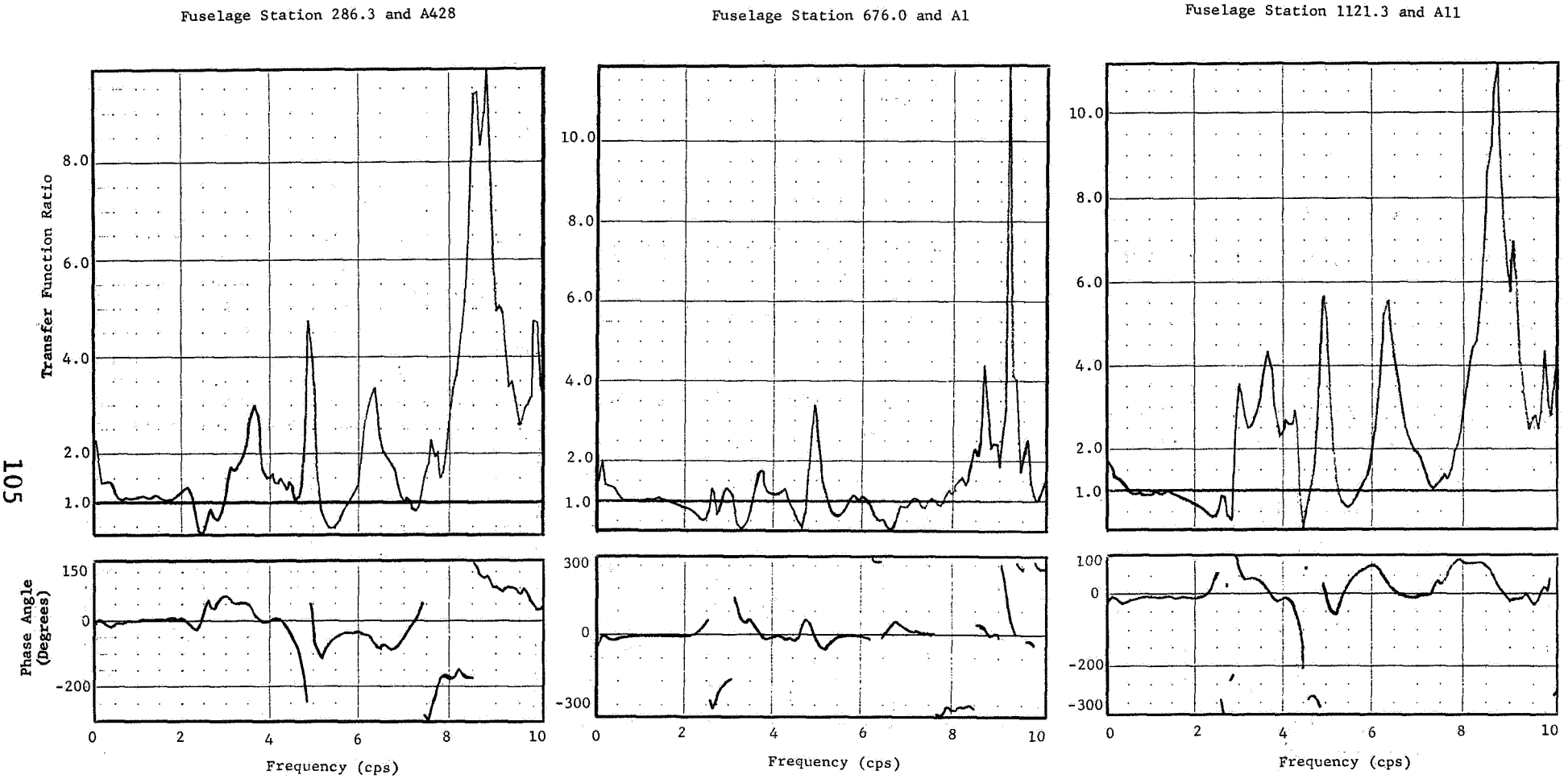

Analysis Parameters

ρ = .002241 slugs/ft^3, Mach = 0.83, V - 955.5 ft/sec, SAS ON, N = 10, C.G. = 26.8% MAC

Figure 45 Ratio of Computed to Measured Transfer Functions, Run, 131-3, Mach 0.83

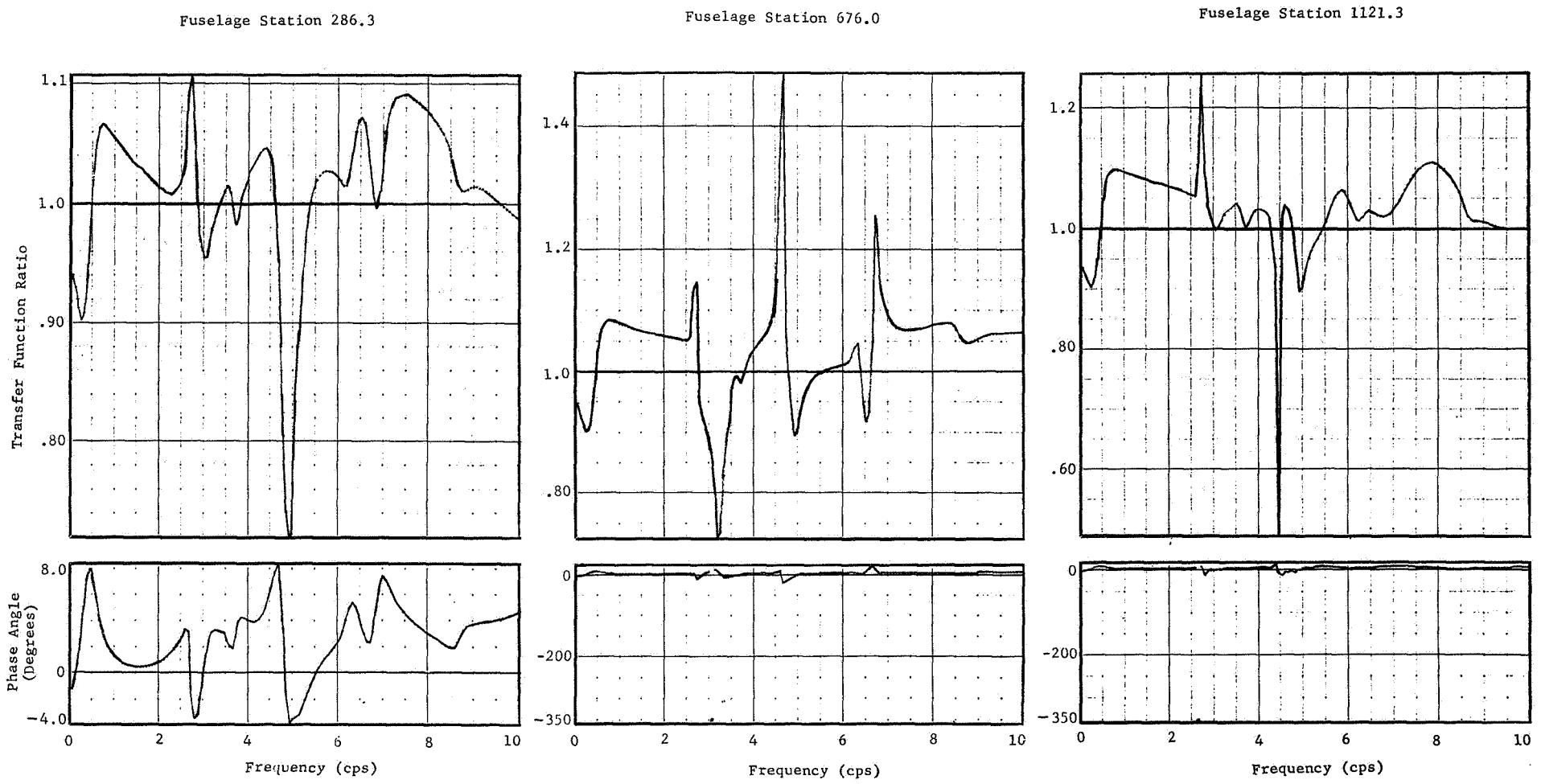

Analysis Parameters

ρ = .002241 slugs/ft^3, SAS ON, N = 10, C.G. = 26.8% MAC

Figure 46 Computed Transfer Function Ratio, Run 131-3, Mach 0.83 to Mach 0.80

$\bar{A}$ and N_o Variations With Mach Number

The transfer functions computed for run 131-3 for Mach numbers 0.77 and 0.83 were combined with the Dryden gust spectrum using a velocity compatable with Mach 0.80. Hence, the $\bar{A}$ and N_o obtained in this manner reflect only the change in transfer functions produced by Mach number and velocity changes, without changes in the gust spectrum with which they were combined. These $\bar{A}$ and N_o values are tabulated in table 21. Large reductions in Mach number and velocity would be required to obtain good correlation between computed and measured $\bar{A}$ and N_o data at accelerometers A428 and A11.

Table 21 $\bar{A}$ and N_o Versus Mach Number, Run 131-3

F.S. (in)	Accel.	Computed (2000 Ft. Alt.)					
		M = 0.77		M = 0.80		M = 0.83	
		$\bar{A}$	N_o	$\bar{A}$	N_o	$\bar{A}$	N_o
286.3	A428	.03829	3.1254	.03855	3.1525	.03862	3.1634
676.0	A1	.02985	1.5455	.03071	1.5443	.03152	1.5447
1121.3	A11	.07488	4.0487	.07690	4.0427	.07876	4.0197

VARIATIONS IN C.G. LOCATION

Transfer functions were computed for run 131-3 to evaluate the effect of small fore and aft variation in the c.g. No attempt was made to define the weight redistribution which would be compatable with the shift in c.g. location. The natural frequencies and mode shapes computed for run 131-3 were assumed to be uneffected by the small shift in c.g. Similarly, the weight distribution used to compute these modes was not changed so the generalized masses for each of the natural modes was not changed. The location of the pitch axis for the rigid body

pitch degree of freedom was not changed. The shift in c.g. was introduced into the analysis by changing only the mass coupling terms between rigid body pitch and rigid body translation which would result from the c.g. shift.

The c.g. during run 131-3 as measured by flight test data was located a distance 26.8 percent of the MAC aft of the MAC leading edge. Transfer functions were recomputed with the c.g. shifted forward 3 percent of the MAC and then aft 3 percent of the MAC. The fuselage station of each of these c.g. positions together with the changes in the short period mode frequency as predicted by equation (56) are shown in table 22.

Table 22 C.G. Variations for Run 131-3

C.G. Location		Frequency of Short Period Mode by Equation (56)
% MAC	F.S. (in)	
23.8	653.29	.5698
26.8	666.31	.4667
29.8	679.33	.3333

Computed Transfer Functions, Run 131-3, With C.G. Shifted Forward to 23.8% MAC

Computed transfer functions for run 131-3 using a 2000 feet altitude standard day density and with the c.g. shifted forward to the 23.8 percent MAC position (13 inches forward of the measured c.g. position for run 131-3) are plotted on figure 47 for comparison with the measured data. The forward c.g. shift increases the frequency of the short period mode slightly more than predicted by equation 56, table 22. The correlation between computed and measured data is improved in the frequency range between 0.2 and 1.5 cps. The ratio of the computed transfer function to the measured transfer function is shown in figure 48. The magnitude ratio is very close to unity and the phase angle difference is close to zero in the frequency range from approximately 0.2 to 1.5 cps. The degree of correlation is not significantly improved above 1.5 cps.

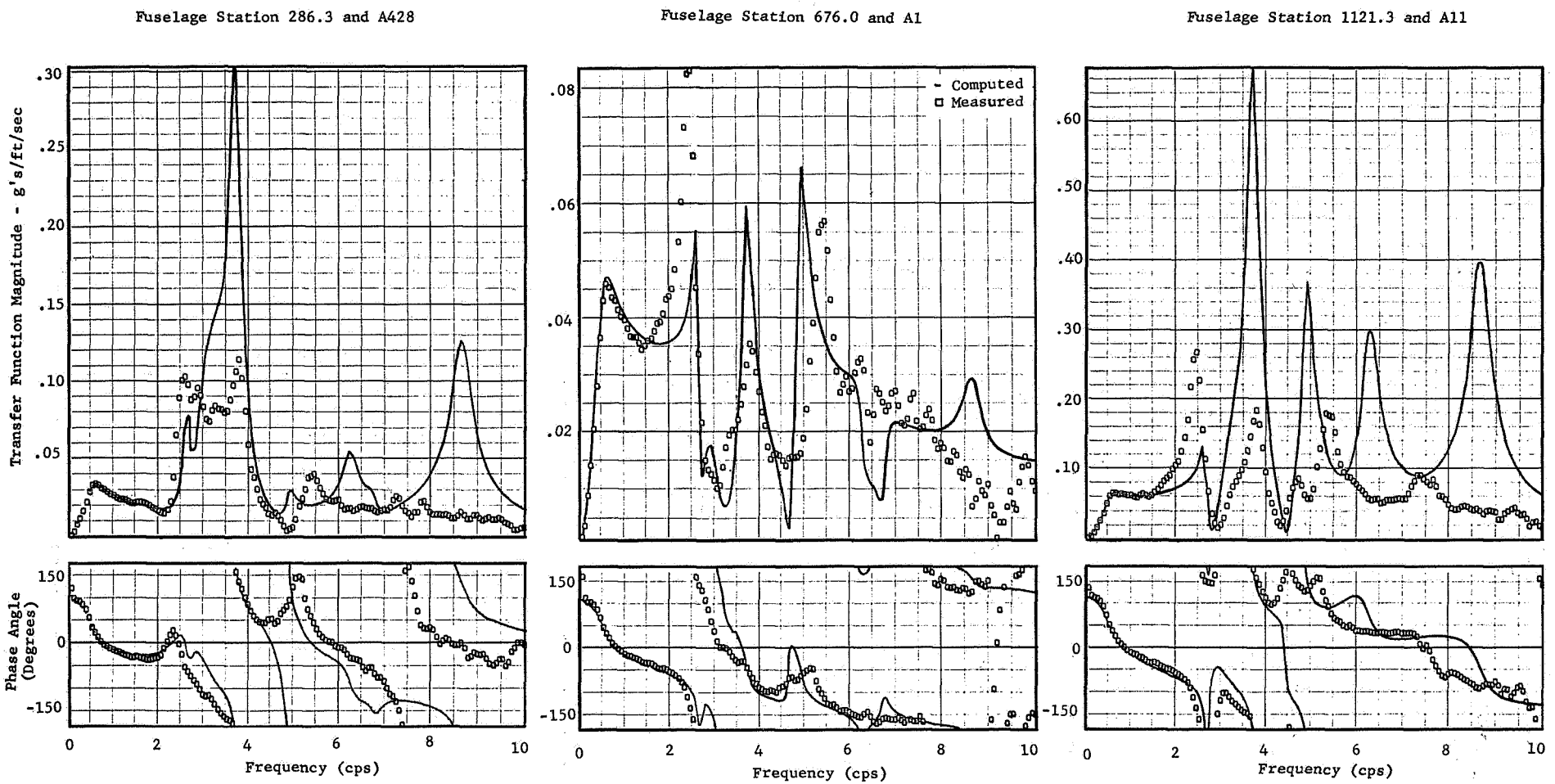

Analysis Parameters

ρ = .002241 slugs/ft^3, Mach = 0.80, V = 921, SAS ON, N = 10, C.G. = 23.8% MAC

Figure 47 Comparison of Computed and Measured Transfer Functions, Run 131-3, 23.8% MAC C.G. Location

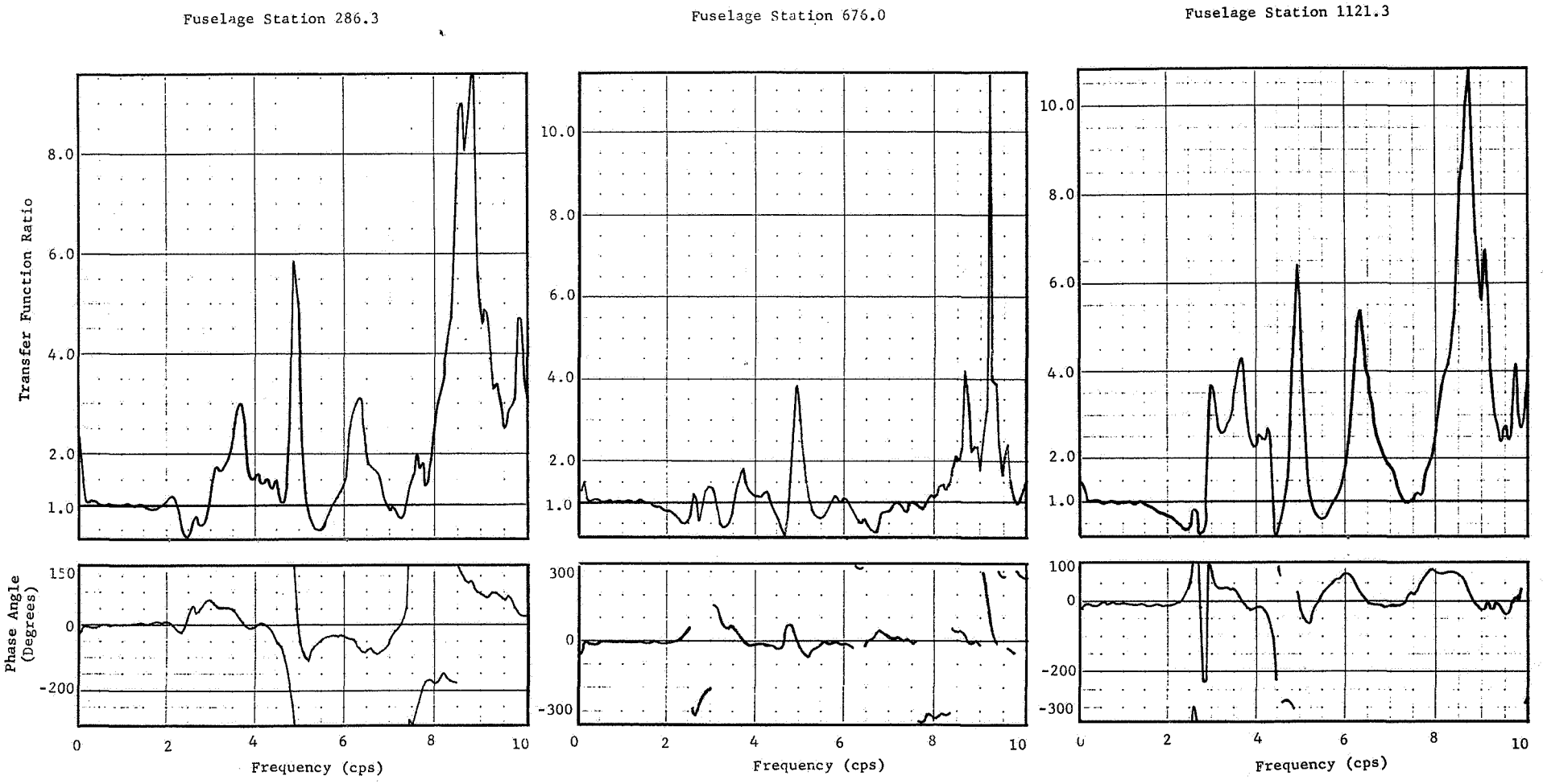

Analysis Parameters

ρ = .002241 slugs/ft^3, Mach = 0.80, V = 921, SAS ON, N = 10, C.G. = 23.8% MAC

Figure 48 Ratio of Computed to Measured Transfer Functions, Run 131-3, 23.8% MAC C.G. Location

The ratios of the computed transfer functions with c.g. at 23.8 percent MAC to the computed transfer functions with c.g. at 26.8 percent MAC are shown in figure 49. The ratio of the magnitudes varies through wide excursions in the frequency range below 1.5 cps. Above 1.5 cps the magnitude ratios are less than ± 10 percent. Very little change in the magnitude of the peaks above 1.5 cps is produced by the c.g. shift. Similarly large differences in the phase angles occur below 1.5 cps but the differences become small above 1.5 cps.

Computed Transfer Functions, Run 131-3, With C.G. Shifted Aft to 29.8% MAC

Computed transfer functions for run 131-3 using a 2000 feet altitude standard day density and with the c.g. shifted aft to the 29.8 percent MAC position (13 inches aft of the measured c.g. position for run 131-3) are plotted in figure 50 for comparison with the measured data. The aft c.g. shift lowers the frequency of the short period mode slightly more than predicted by equation (56), table 22. The degree of correlation between computed and measured magnitudes and phase angles is significantly degraded for frequencies below 1.5 cps. Above 1.5 cps the aft c.g. shift produces very little difference in the transfer functions. The ratios of the computed to the measured transfer functions are shown in figure 51. This figure clearly shows the degradation in the transfer function correlation below 1.5 cps which is produced by the aft c.g. shift.

The ratios of the computed transfer functions with c.g. at 29.8 percent MAC to the computed transfer functions with the c.g. at 26.8 percent MAC are shown in figure 52. The magnitude ratio is as high as 6.0 at 0.2 cps. Phase angle differences as high as 80 degrees also occur near 0.2 cps.

Variation In $\bar{A}$ and N_O With C.G. Location

$\bar{A}$ and N_O data were computed for run 131-3 with the c.g. shifted forward to the 23.8 percent MAC and aft to the 29.8 percent MAC. These data are listed in table 23 for comparison with the measured data. The predominant effect of shifting the c.g. can be observed by referring to the $\bar{A}$ and N_O data

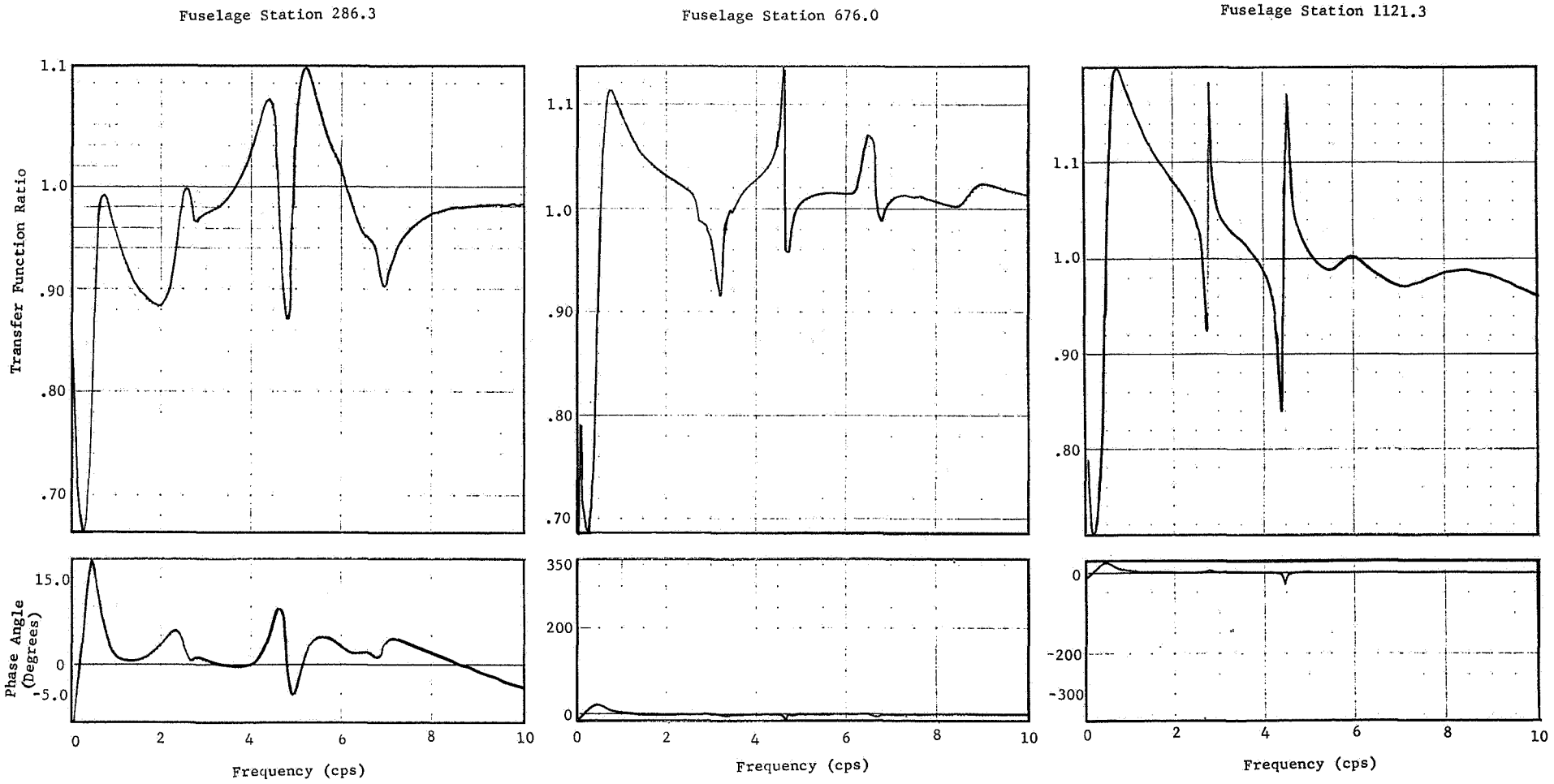

Analysis Parameters

ρ = .002241 slugs/ft^3, Mach = 0.80, V = 921, SAS ON, N = 10

Figure 49 Computed Transfer Function Ratio, Run 131-3, 23.8% to 26.8% MAC C.G. Location

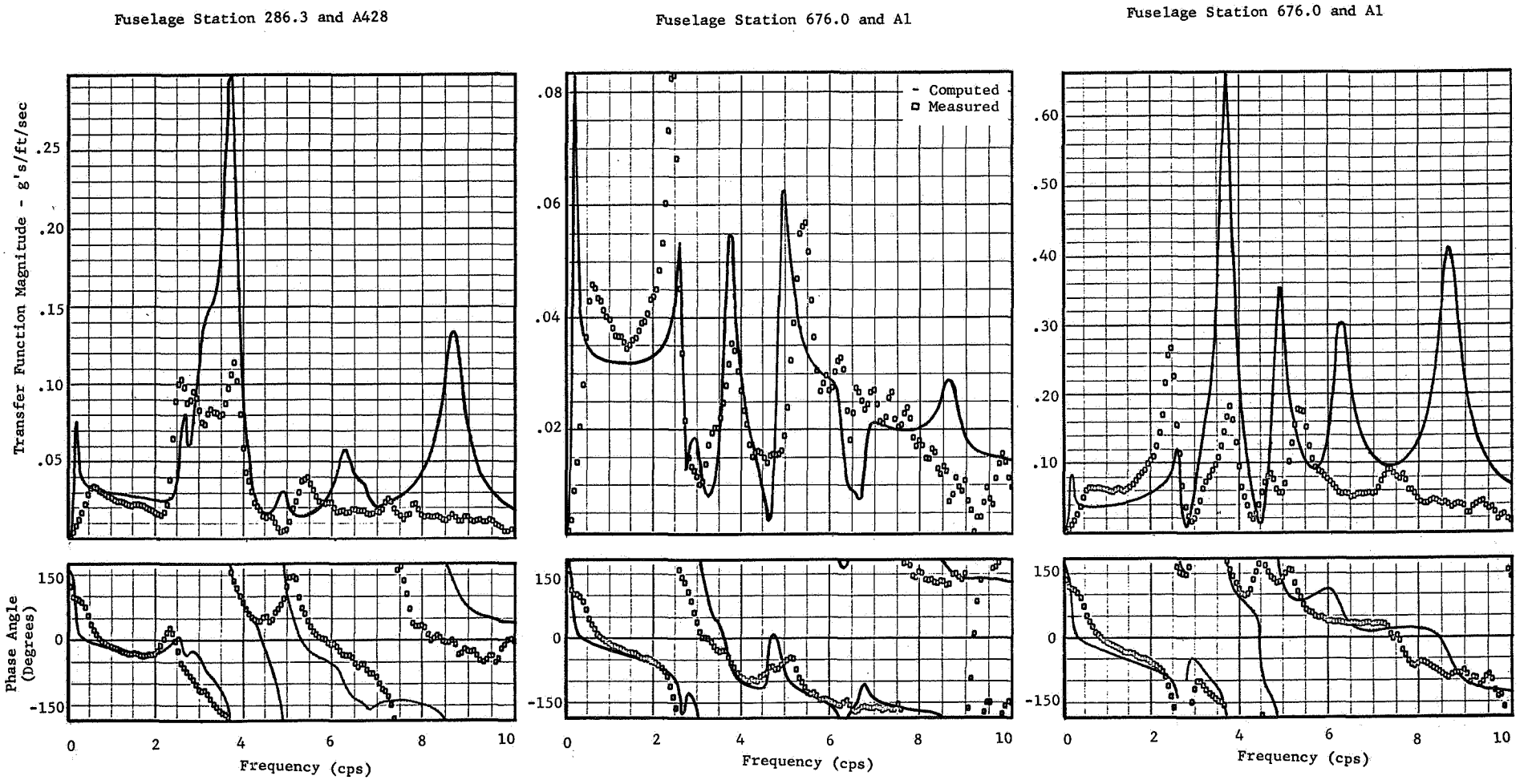

Analysis Parameters

ρ = .002241 slugs/ft^3, Mach = 0.80, V = 921, SAS ON, N = 10, C.G. = 29.8% MAC

Figure 50 Comparison of Computed and Measured Transfer Functions, Run 131-3, 29.8% MAC C.G. Location

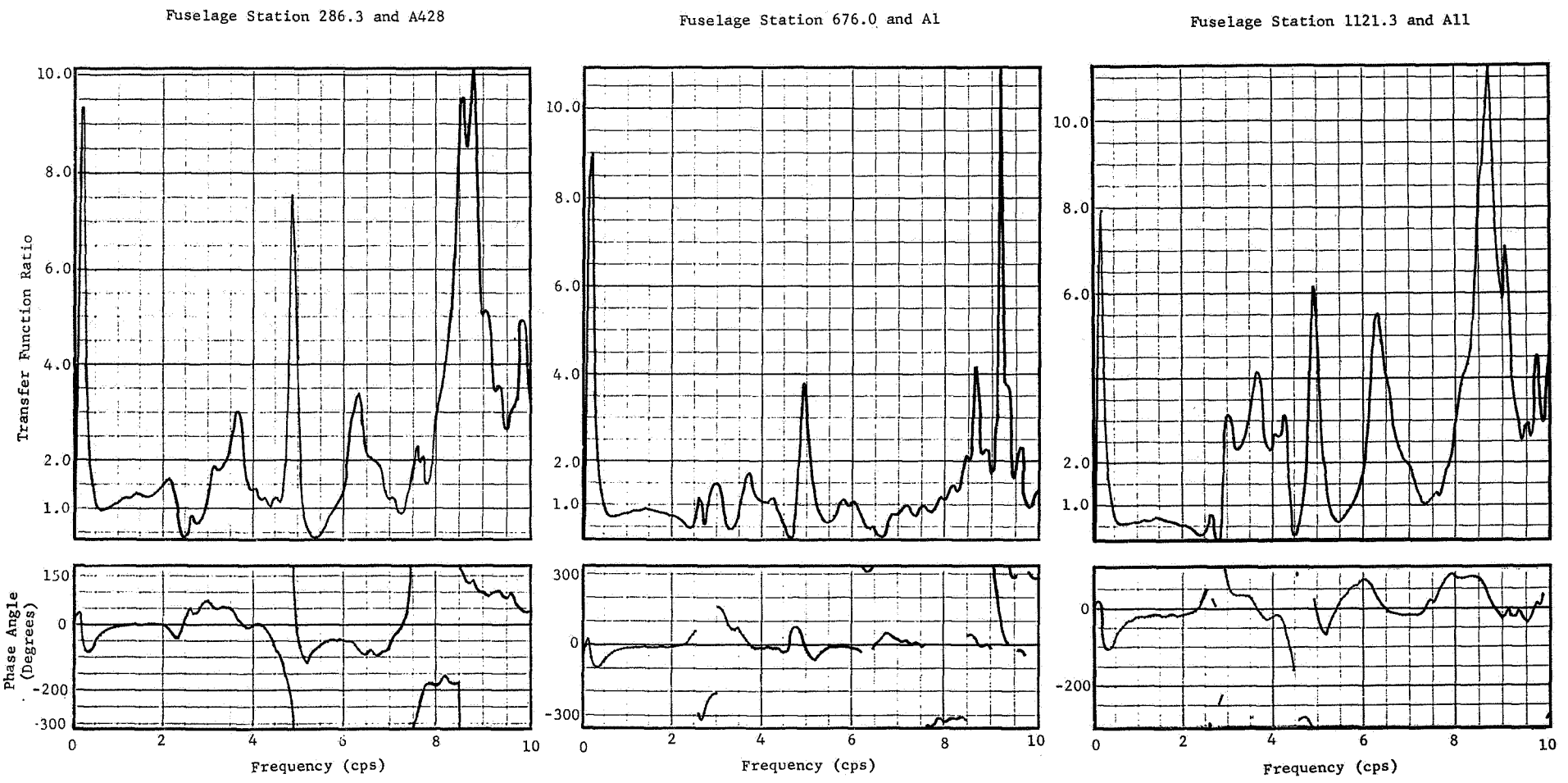

Analysis Parameters

ρ = .002241 slugs/ft^3, Mach = 0.80, V = 921, SAS ON, N = 10, C.G. = 29.8% MAC

Figure 51 Ratio of Computed to Measured Transfer Functions, Run 131-3, 29.8% MAC C.G. Location

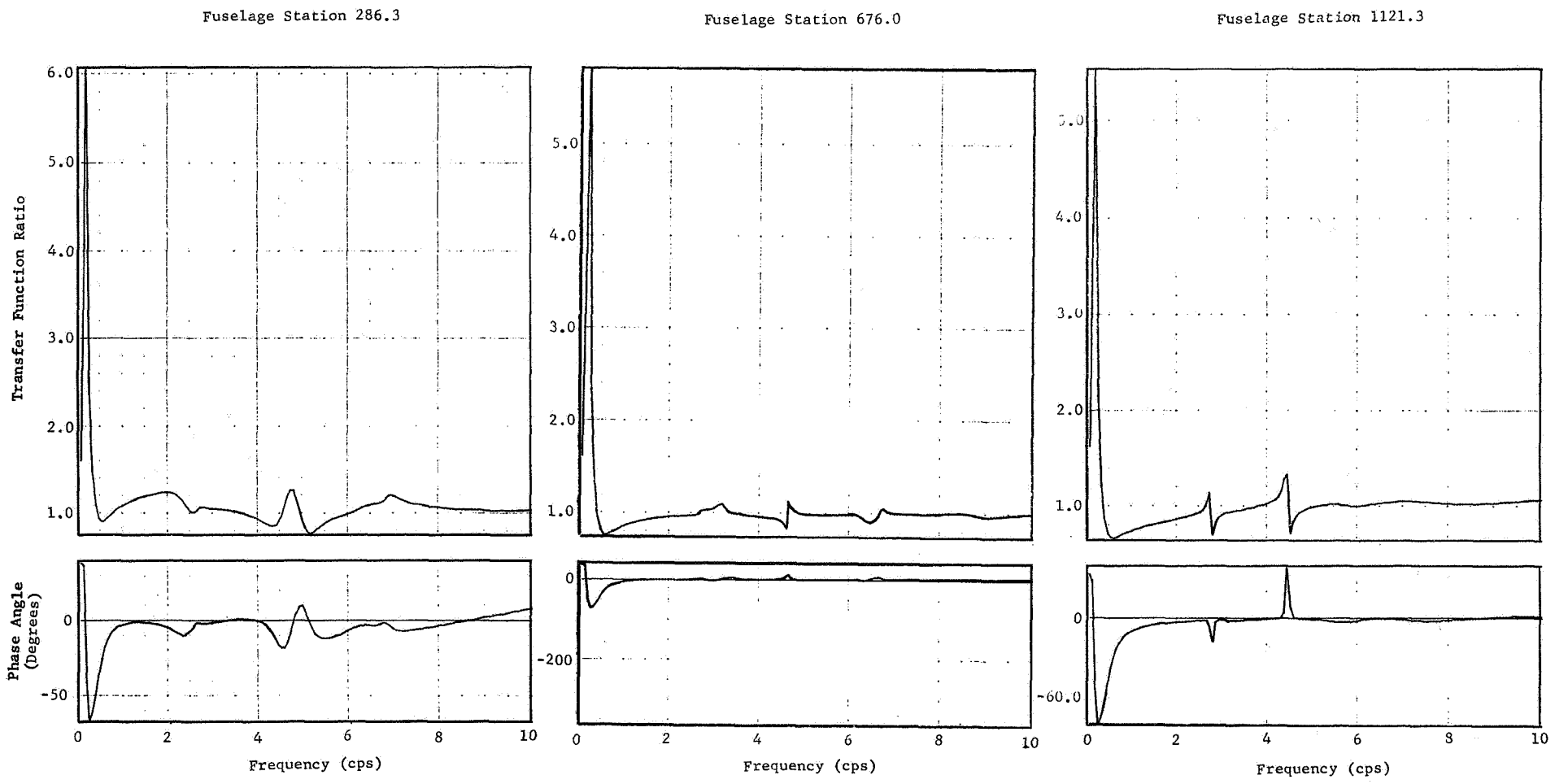

Analysis Parameters

ρ = .002241 slugs/ft^3, Mach = 0.80, V = 921, SAS ON, N = 10

Figure 52 Computed Transfer Function Ratio, Run 131-3, 29.8% to 26.8% MAC C.G. Location

Table 23 $\bar{A}$ and N_o Variation With C.G. Location, Run 131-3

F.S. (in)	Accel.	Computed (2000 Ft. Alt.)						Measured	
		C.G. = 23.8% MAC		C.G. = 26.8% MAC		C.G. = 29.8% MAC			
		$\bar{A}$	N_o	$\bar{A}$	N_o	$\bar{A}$	N_o	$\bar{A}$	N_o
N = 10									
286.3	A482	.03666	3.2891	.03855	3.1525	.04747	2.6072	.02814	2.391
676.0	A1	.03009	1.6099	.03071	1.5443	.03879	1.1844	.03019	1.638
1121.3	A11	.07860	3.9607	.07690	4.0427	.07757	4.0028	.05888	2.454
N = 2									
286.3	A428	.01924	1.5503	.02224	1.4566	.02994	1.2690	.02814	2.391
676.0	A1	.02941	1.5165	.02998	1.4417	.03294	1.2464	.03019	1.638
1121.3	A11	.04238	1.8844	.03991	1.8354	.03718	1.6623	.05888	2.454

tabulated for the 2 DOF analyses. The motion of the airplane at the short period frequency is a pitching motion about a pitch axis that is located upstream of the fuselage nose. A forward shift in the c.g. produces a large distance between the c.g. and a.c. causing a larger aerodynamic moment which in turn causes the short period mode pitch axis to move aft. This causes the $\bar{A}$ at the station 286.3 to decrease and the $\bar{A}$ at station 1121.3 to increase. Conversely, the aft shift in c.g. reduces the distance between a.c. and c.g., reducing the aerodynamic moment and causing the short period mode pitch axis to move forward. The result is to increase the $\bar{A}$ at station 286.3 and decrease the $\bar{A}$ at station 1121.3. The $\bar{A}$ at station 676.0 changes very little with c.g. shift. The forward shift in c.g. increases the frequency of the short period mode which in turn increases N_O. Conversely, the aft shift in c.g. reduces the frequency of the short period mode which in turn decreases N_O.

Turning attention to the $\bar{A}$ and N_O data obtained from the 10 DOF analysis it can be seen that the characteristics which are easily explained by the 2 DOF analysis remain in the 10 DOF results. A forward shift in c.g. decreases $\bar{A}$ at station 286.3 and increases $\bar{A}$ at station 1121.3. A forward shift in c.g. increases the value of N_O at all three stations.

It is concluded that shifting the c.g. forward to the 23.8 percent MAC position, improves the correlation between computed and measured transfer functions for run 131-3. The correlation between computed and measured $\bar{A}$ values is also improved for accelerometers A428 and A1 while only slightly degrading the correlation with accelerometer A11. The N_O correlation is slightly improved at A1 and slightly degraded at A428 and A11 by the forward c.g. shift.

VARIATIONS IN SAS GAINS

A block diagram of the stability augmentation system for longitudinal control was shown in figure 10. The elevon actuator receives three inputs which command elevator deflections. One input is from the pitch damper loop. The pitch rate is sensed by a pitch rate gyro located at fuselage station 687. The pitch damper gain is a function of altitude.

For example, its value is 0.05 at 2000 feet and 0.17 at 30,000 feet altitude. A second input is from the autotrim loop. The vertical acceleration is sensed by an accelerometer located at fuselage station 687. This loop has two variable gains, K_1 and K_2. The K_1 gain is a function of gross weight. Its value is 0.5 for gross weights less than 100,000 lbs. and 1.0 for gross weight above 135,000 lbs. Between 100,000 lbs. and 135,000 lbs. the gain varies continuously from 0.5 to 1.0. The K_2 gain is a function of Mach number, static margin, altitude, and gross weight. For the flight conditions compatible with run 131-3 the value of the K_2 gain was .062. If the altitude were increased to 30,000 feet holding all other flight conditions constant the K_2 gain would increase to a value of 0.135. The third input to the elevon actuator is from the stick position or pilot input. There are two gains, K_3 and K_4, associated with this input. Throughout all of the analyses it was assumed that no pilot input existed. Hence the K_3 and K_4 gains were zero for all of the computed transfer functions.

Transfer Functions for Run 131-3, With Variations in SAS Gains

To evaluate the effect of the SAS, transfer functions were computed for run 131-3, using a 2000 feet altitude standard day density, with the SAS disengaged. The transfer functions with SAS-OFF were found to be very close to the transfer functions with SAS-ON. The ratio of the SAS-OFF to the SAS-ON transfer functions are plotted in figure 53. When SAS is turned off, the magnitude of the transfer functions decrease as much as 20 percent at frequencies near 0.2 cps. Between 0.5 cps and 8 cps the difference in the transfer function magnitudes is less than $\pm$ 5 percent. At the peak frequency near 8.7 cps the magnitude of the transfer function with SAS-OFF is approximately 15 percent greater than with SAS-OFF. The slope of the fuselage deflection at the sensor location is large for the natural mode near this frequency. Hence the pitch damper loop of the SAS reduces this peak. The phase angle differences are very close to zero except for frequencies below 0.5 cps and above 8 cps.

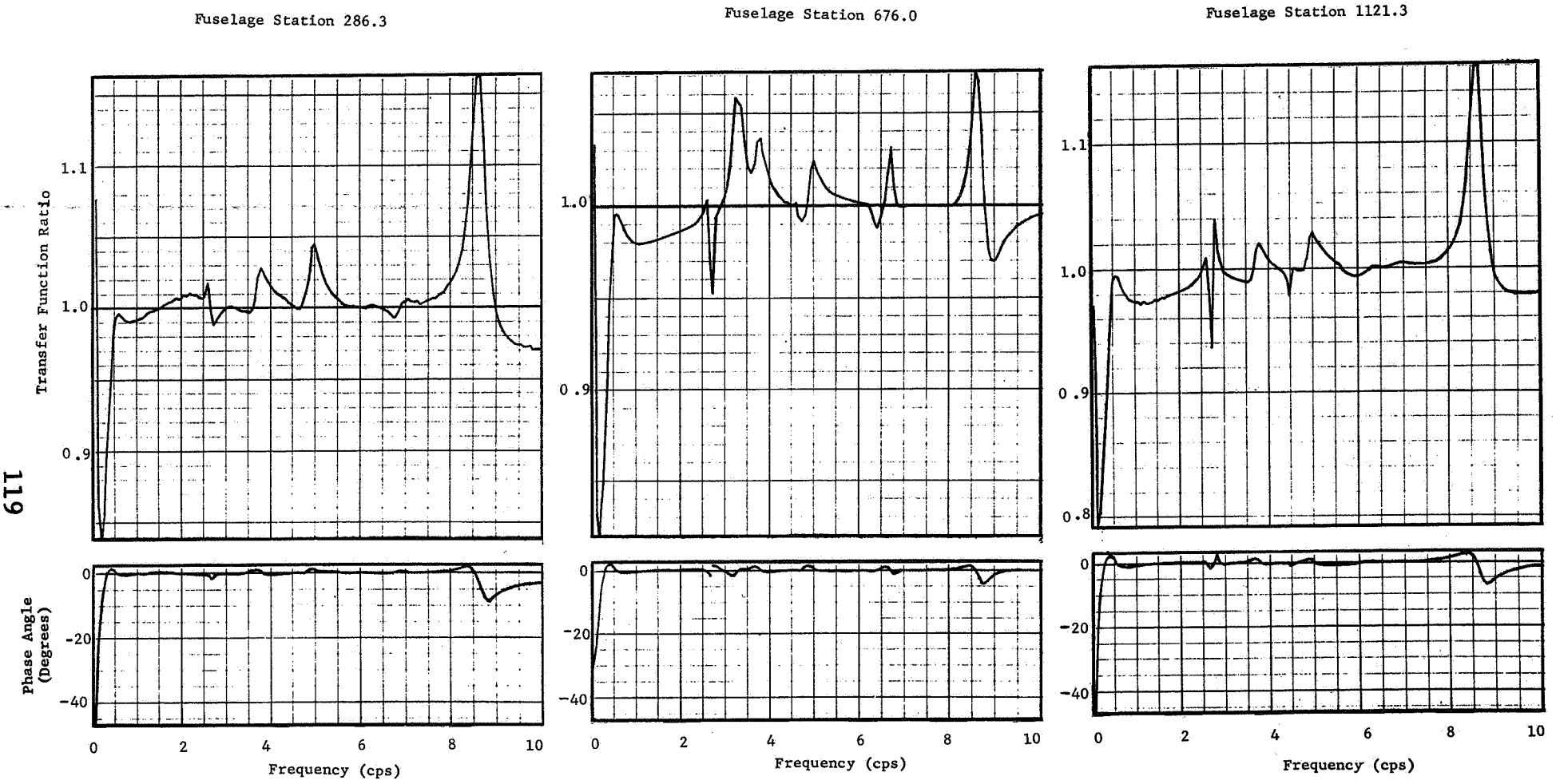

Analysis Parameters

ρ = .002241 slugs/ft^3, Mach = 0.80, V = 921 ft/sec, N = 10, C.G. = 26.8% MAC

Figure 53 Ratio of Computed Transfer Functions, Run 131-3, SAS-OFF to SAS-ON

Transfer functions were also computed for the same 2000 feet altitude but with the pitch damper gain and the K_2 gain increased to the value they would have if the altitude were increased to 30,000 feet. These gains were unrealistically high for a 2000 feet altitude but were chosen to illustrate the effect of an extreme increase in the gains. The realistic gains for 2000 feet and the gains at 30,000 feet are shown in table 24. The increased gains reduced the magnitude of the transfer functions in the vicinity of the short period mode, slightly degrading the correlation with the measured data.

Table 24 Variations in SAS Gains With Altitude

Altitude (Ft.)	Pitch Damper Gain	Autotrim Gain	
		K_1	K_2
2,000	.05	1.0	.062
30,000	.17	1.0	.135

It also reduced the magnitude of the peak near 8.7 cps approximately 25 percent at station 286.3 and 1121.3 and approximately 10 percent at station 676.0. The transfer functions between 2 cps and 8 cps were essentially unchanged by the increase in gains.

$\bar{A}$ and N_o Variations With SAS Gains

The $\bar{A}$ and N_o data were computed for the SAS-OFF transfer functions and the SAS-ON with 30,000 feet gain transfer functions. They are listed in table 25. The $\bar{A}$ and N_o data for the basic condition with the SAS gains compatible with a 2000 feet altitude are also listed for comparison. It is concluded that the SAS has very little effect on the computed $\bar{A}$ and N_o data.

Table 25 $\bar{A}$ and N_o Variations With SAS Gains

F.S. (in)	Accel.	Computed (2000 Ft. Alt.) N = 10					
		SAS OFF		2000 Ft. Gains		30,000 Ft. Gains	
		$\bar{A}$	N_o	$\bar{A}$	N_o	$\bar{A}$	N_o
61.5		.08538	4.9882	.08365	4.8392		
130.		.06965	4.7034	.06852	4.5611		
186.3		.05721	4.3351	.05658	4.2043		
286.3	A428	.03838	3.2362	.03855	3.1525	.03782	3.0843
386.3		.02780	2.0566	.02844	1.9876		
576.		.02807	1.7852	.02890	1.6918		
676.0	A1	.02980	1.5951	.03071	1.5443	.03023	1.5550
687.		.02995	1.5971	.02088	1.5449		
776.		.03163	1.7260	.03260	1.6462		
1021.3		.05462	3.1736	.05523	3.1070		
1121.3	A11	.07691	4.1474	.07690	4.0427	.07554	3.9386
1161.6		.08679	4.4053	.08693	4.2932		

EFFECT OF INCLUDING AN AEROELASTIC MODE

An initial step in applying Lagrange's equations of motion is to express the deformed shape of the structure as a summation of the products of predetermined deformed shapes and unknown generalized coordinates as expressed by equation (32). It is necessary to determine the stored elastic energy which results from deforming the structure into each of the predetermined deflection shapes. If an infinity of linearly independent generalized coordinates are employed, the structure is not constrained by expressing the deformation in this manner. If only N generalized coordinates are employed, the structure is constrained to deform in some linear combination of the N predetermined deformation shapes. Hence, Lagrange's equations of motion provide a practical means of obtaining good approximate solutions if N deformation shapes are chosen which provide a good approximation to the exact solution (obtained with an infinity of terms). The analyst is free to choose any set of deformation shapes (provided each cannot be expressed as a linear combination of the others) consistent with the boundary conditions imposed on the structure. Natural modes of vibration are often used as degrees of freedom in dynamic response analyses for two reasons:

1. Experience and intuition indicate that good approximate solutions can be obtained with fewer elastic degrees of freedom using normal modes than with any other type of deformation.

2. The stored elastic energy is known as soon as the mode shape, natural frequency, and mass distribution are known. The generalized spring constant can be expressed as the product of the natural frequency (rad/sec) squared times the generalized mass.

However, there are occasions when deformation shapes other than normal modes of vibration might improve the solution with fewer generalized coordinates. Consider the deformation shape of an aircraft responding to the excitation of a pure sine wave gust velocity tuned to the short period frequency of the airplane. If the short-period frequency is considerably below the first natural frequency of the structure, the deformation of the structure might be considerably different

from the first natural mode. Furthermore, it might take a rather large number of natural modes to provide sufficient freedom for the constrained structure to assume the shape of the short-period mode deformation. At higher frequencies, the normal mode coordinates might produce a very good approximation of the deformation of the structure. An aeroelastic mode was computed and incorporated in the equations of motion to observe its effect.

The aeroelastic mode was computed by the following steps:

Step One

The flexibility matrix which was used to compute the normal modes of vibration was computed with one point on the centerline of the fuselage fixed against rotation and displacement. Using the same flexibility matrix the fixed point was set at a unit angle of attack and a static aeroelastic analysis (for flight conditions corresponding to run 131-3) was conducted to determine the resulting elastic deformations $\{h_\alpha\}$ and compatible aerodynamic loads $\{L_\alpha\}$. These loads were reacted at the fixed point by a vertical load, R_α, and pitching moment, M_α.

Step Two

The operations of step one were repeated with the fixed point at zero angle of attack and the elevon set at a unit elevator angle of attack. A static aeroelastic analysis (for flight conditions corresponding to run 131-3) was conducted to determine the resulting elastic deformations $\{h_\delta\}$ and compatible load distribution $\{L_\delta\}$. These loads were reacted at the fixed point by a vertical load, R_δ, and a pitching moment, M_δ.

Step Three

A 1-g inertia load distribution $\{L_I\}$ was applied to the flexibility matrix and the resulting elastic deformations $\{h_I\}$ were computed for the weight distribution associated with run 131-3. These loads were reacted at the fixed point by the weight of the airplane, W, and the pitching moment of the weight about a pitch axis through the fixed point, M.

Step Four

To balance the airplane, the angle of attack and elevator angle need to remove the reactions at the fixed point were computed from the following pair of equations.

$$\begin{aligned} R_\alpha \alpha \quad + \quad R_\delta \delta \quad &= W \\ M_\alpha \alpha \quad + \quad M_\delta \delta \quad &= M \end{aligned} \tag{64}$$

As a matter of interest the angle of attack computed by this method was 2.81 degrees compared to the flight test measured trim angle of attack (measured from the angle of zero lift) of 3.0 degrees for run 131-3. The computed elevator angle was -2.58 degrees compared to the flight test value of -1.46 degrees. The combined balanced load distribution for the aeroelastic mode was obtained by the following relation

$$\left\{L_a\right\} = \left\{L_\alpha\right\}\alpha + \left\{L_\delta\right\}\delta - \left\{L_I\right\} \tag{65}$$

The corresponding combined elastic deformation of the aeroelastic mode was obtained as follows.

$$\left\{h_a\right\} = \left\{h_\alpha\right\}\alpha + \left\{h_\delta\right\}\delta - \left\{h_I\right\} \tag{66}$$

The aeroelastic mode deformation shape is plotted on figure 54.

The stored energy associated with the aeroelastic mode can be expressed as follows:

$$U_a = \tfrac{1}{2} \left\{ h_a \right\}^T q_a \left\{ L_a \right\} q_a \tag{67}$$

where the superscript T indicates transpose of the column matrix. The rate of change of the stored energy with respect to the aeroelastic generalized coordinate is

$$\frac{\partial U_a}{\partial q_a} = \left\{ h_a \right\}^T \left\{ L_a \right\} q_a \tag{68}$$

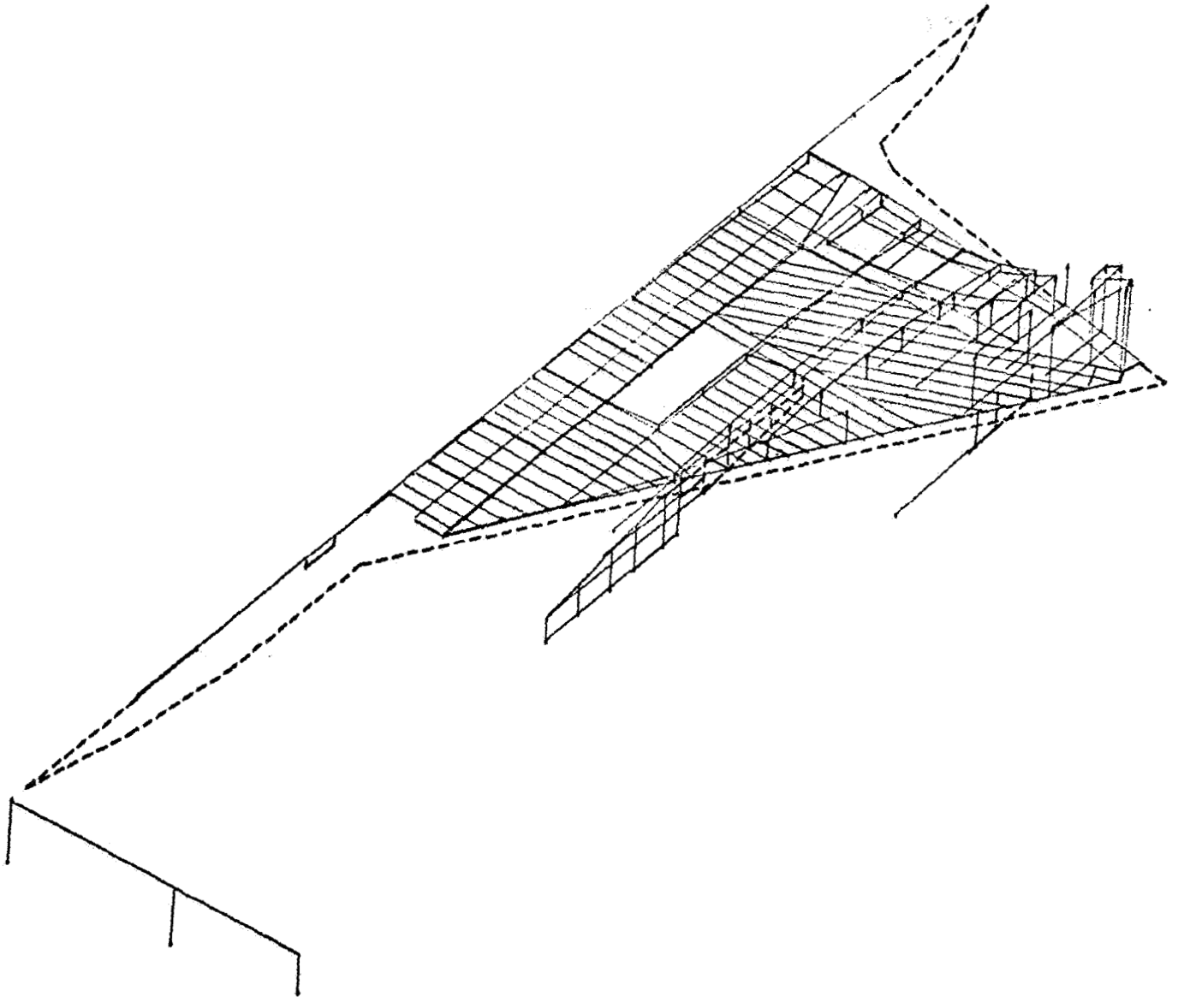

Figure 54 Aeroelastic Mode

To place the right hand side of equation (68) in the same form as used for each of the normal modes of vibration a fictious frequency was associated with the aeroelastic mode and computed by the following relation

$$\omega_a^2 M_{aa} = \left\{ h_a \right\}^T \left\{ L_a \right\} \tag{69}$$

where M_{aa} is the generalized mass of the aeroelastic mode

and ω_a is the fictious frequency associated with the aeroelastic mode.

The generalized mass for the aeroelastic mode was computed in the same manner as the generalized masses for each of the normal modes of vibration, namely,

$$M_{aa} = \left\{ h_a \right\}^T \left[m \right] \left\{ h_a \right\} \tag{70}$$

where m is a diagonal mass matrix of the lumped mass representation of the airplane mass.

Transfer Functions with Aeroelastic Mode

The aeroelastic mode was used to replace the last flexible mode of vibration (mode 8) used in the previous 10 DOF analysis. The generalized aerodynamic terms for the aeroelastic mode was computed in the same manner as the other modes. Mass coupling terms between the aeroelastic mode and all other degrees of freedom were computed. The transfer functions computed with the aeroelastic mode included for run 131-3 with a 2000 feet altitude standard day density are plotted in figure 55. (These transfer functions were computed with the SAS-OFF but as previously discussed the SAS makes very little difference in the transfer functions). The comparison between computed and measured transfer functions is very good in the frequency range near the short period mode. However, the addition of the aeroelastic mode degrades the comparison in the frequency range between 2 cps and 4 cps. The frequency of the peak associated with the

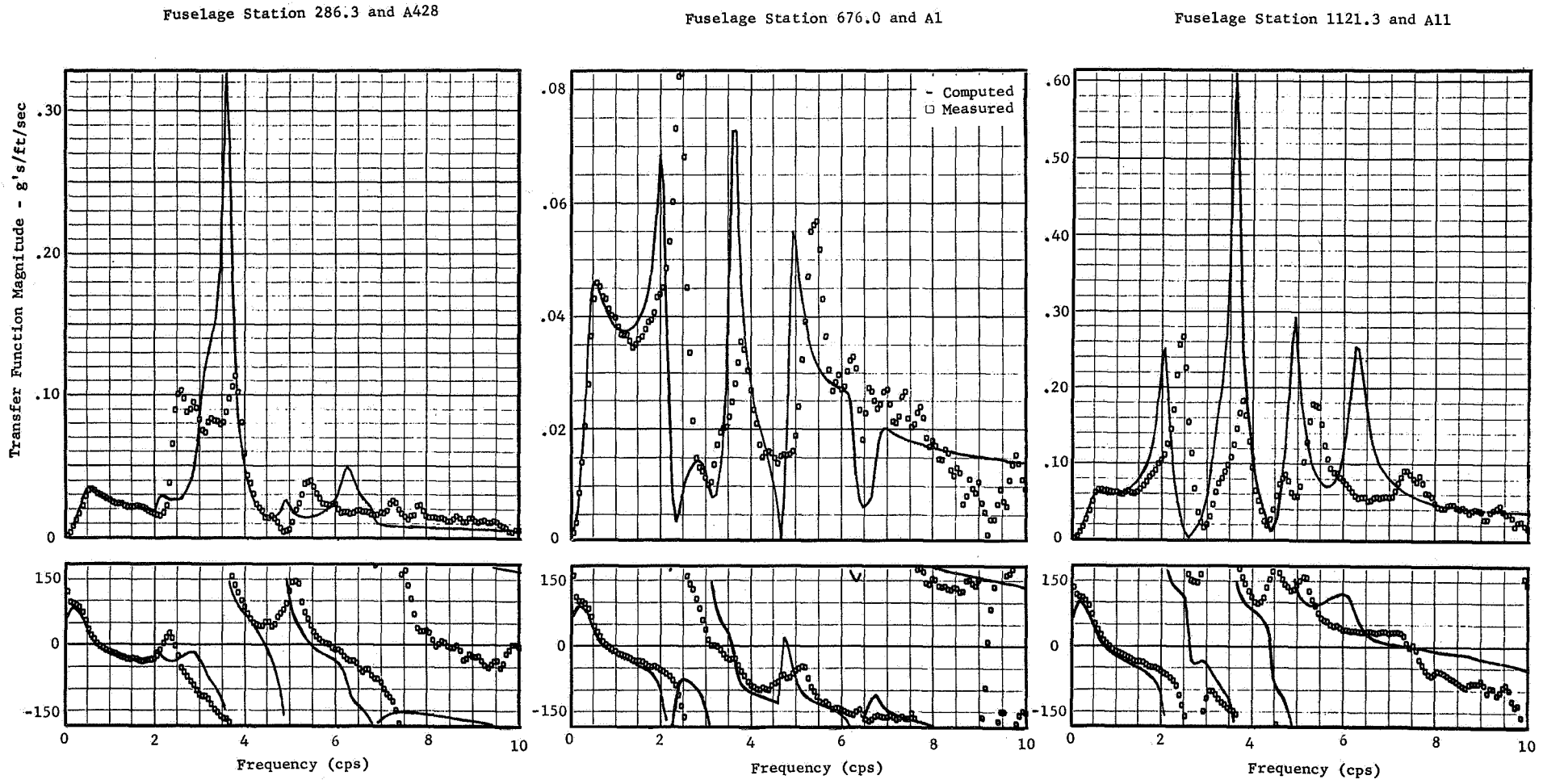

Analysis Parameters

ρ = .002241 slugs/ft^3, Mach = 0.80, V = 921 ft/sec, SAS OFF, N = 10, C.G. = 26.8% MAC

Figure 55 Comparison of Computed and Measured Transfer Functions, Run 131-3, With Aeroelastic Mode

first natural mode has been shifted down to approximately 2 cps compared to the measured peak at 2.5 cps. The comparison appears to be better above 7 cps but this is primarily due to the removal of the eighth natural mode of vibration as a degree of freedom. The ratio of the computed transfer functions with the aeroelastic mode to the measured transfer functions are plotted in figure 56. The ratio of the magnitudes appears to be closer to unity over most of the frequency range than has been obtained with previous variations. Again part of this is due to the removal of the eighth mode which caused high magnitude ratios near 8.7 cps on previous plots.

The ratios of the transfer functions with the aeroelastic mode to the basic transfer functions (SAS OFF) are plotted in figure 57. The addition of the aeroelastic mode produces large variations in the magnitude ratios but very small differences in phase angle.

Effect of Aeroelastic Mode on $\bar{A}$ and N_o Values

The $\bar{A}$ and N_o values obtained from the computed transfer functions obtained with the inclusion of the aeroelastic mode are listed in table 26. The computed $\bar{A}$ and N_o data without the aeroelastic mode as computed with SAS-OFF are also listed in table 26.

Table 26 Effect of Aeroelastic Mode On $\bar{A}$ and N_o
N = 10

F.S. (in)	Accel.	Computed (2000 Ft. Alt.) SAS OFF				Measured Data	
		Basic		With Aeroelastic Mode			
		$\bar{A}$	N_o	$\bar{A}$	N_o	$\bar{A}$	N_o
286.3	A428	.03838	3.2362	.03496	2.8274	.02814	2.391
676.0	A1	.02980	1.5951	.03080	1.5103	.03019	1.638
1121.3	A11	.07691	4.1474	.07413	3.0464	.05888	2.454

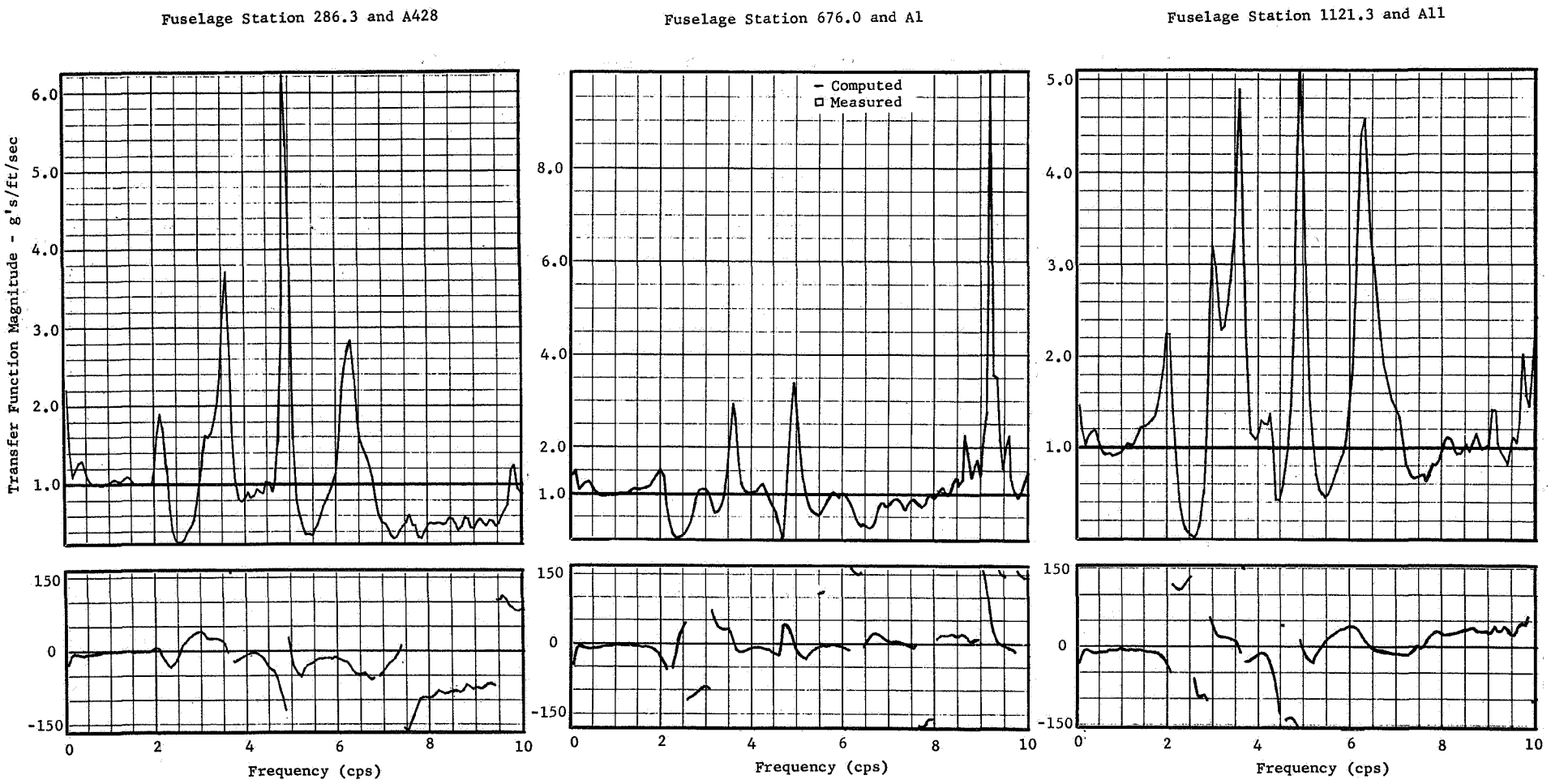

Analysis Parameters

ρ = .002241 slugs/ft^3, Mach = 0.80, V = 921 ft/sec, SAS OFF, N = 10, C.G. = 26.8% MAC

Figure 56 Ratio of Computed to Measured Transfer Functions, Run 131-3, With Aeroelastic Mode

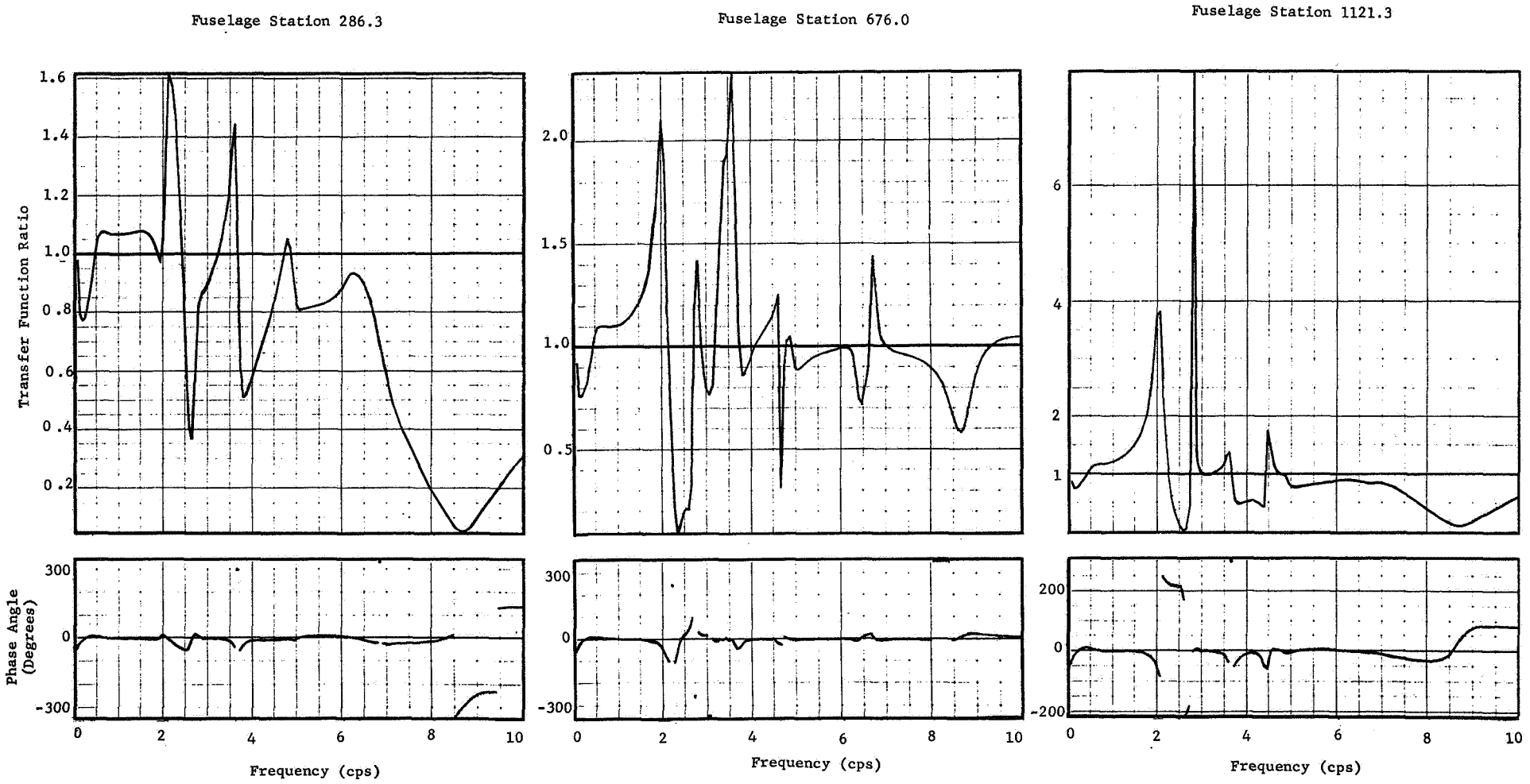

Analysis Parameters

ρ = .002241 slugs/ft^3, Mach = 0.80, V = 921 ft/sec, SAS OFF, N = 10, C.G. = 26.8% MAC

Figure 57 Ratio of Computed Transfer Functions, Run 131-3, Aeroelastic Mode Analysis to Basic Analysis

The aeroelastic mode improves the correlation between computed and measured $\bar{A}$ and N_o data. However, part of this improvement results from deleting the eighth natural mode of vibration.

COMPUTED TRANSFER FUNCTIONS USING QUASI-STEADY AERODYNAMICS

The oscillatory pressure as computed by the kernel function method is a complicated implicit function of the oscillation frequency. This complication makes it more attractive to use digital techniques to compute transfer functions at discrete frequencies than to use analog techniques. However, when non-linearities are important the transfer function approach is no longer applicable and it is necessary to turn to solutions in the time domain. Here the analog approach is more attractive if the aerodynamic terms can be expressed as an explicit function of frequency. The objective of this portion of the investigation was to evaluate quasi-steady aerodynamic methods in computing transfer functions. The term Quasi-Steady is used here to mean any method which reduces the aerodynamic elements from a complicated implicit function of frequency to a relatively simple explicit function of frequency. Two quasi-steady methods of computing the $[Q_{rs}]$ elements of equation (35) were investigated. No attempt was made to compute the gust aerodynamic terms $\{Q_{rg}\}$ by quasi-steady methods.

Quasi-Steady Method One

The downwash for unit amount of each generalized coordinate as expressed by equation (40) is composed of two parts. One part is a function of the streamwise slope distribution and the other part is a function of the vertical displacement distribution associated with each generalized coordinate. To evaluate the $[Q_{rs}]$ terms for the wing by the first quasi-steady method, the $[B]$ matrix of equation (39) was evaluated for zero frequency. The $V\alpha$ portion of the downwash was substituted into equation (39) and the resulting a_μ coefficients were substituted into equation (38) to obtain the steady pressure distribution. This pressure was then used to evaluate the integral on the right side of equation (35). The operation was repeated using the vertical deflection, h, in place of the downwash $V\alpha$. The quasi-steady $[Q_{rs}]$ terms for the wing were then obtained by the following equation

$$\left[Q_{rs}\right] = \left[Q_{rs}\right]_{v\alpha} + i\,\omega\left[Q_{rs}\right]_{h} \qquad (71)$$

where $\left[Q_{rs}\right]_{V\alpha}$ is the matrix of aerodynamic terms due to the $V\alpha$ portion of the downwash associated with generalized coordinate s, and

$\left[Q_{rs}\right]_{h}$ is the matrix of aerodynamic terms due to the h portion of the downwash associated with generalized coordinate s.

The $[Q_{rs}]$ terms for the nacelles and pylons were not altered since they were already computed by a quasi-steady method. The $[Q_{rs}]$ terms for the fuselage were not altered since they were computed by slender body theory and were already expressable as simple explicit functions of frequency. The additional aerodynamic terms due to the SAS were not changed and hence were based upon modified strip theory as previously described. The gust aerodynamic terms $\{Q_{rg}\}$ were also unaltered. The quasi-steady aerodynamic terms computed by method one agree exactly with the unsteady aerodynamic terms at zero frequency but deviate from the unsteady aerodynamic terms to an increasing extent with increasing frequency.

Transfer functions for run 131-3 with a 2000 feet altitude standard day density were computed using the quasi-steady method-one described above. The transfer functions are plotted on figure 58 for comparison with measured data. Comparing figure 58 with figure 25 it can be seen that the transfer functions computed using quasi-steady aerodynamic method-one have peaks with magnitudes that are generally higher than those obtained using unsteady aerodynamics. The comparison between computed and measured transfer function magnitudes is degraded. However, the phase angle comparison between computed and measured data is practically the same as obtained by unsteady aerodynamics. The ratios of the computed transfer functions, using quasi-steady method-one, to the measured transfer functions are shown in figure 59. This method apparently reduces the aerodynamic damping associated with each resonant frequency but otherwise the transfer functions are good approximations to the transfer functions obtained with unsteady aerodynamics.

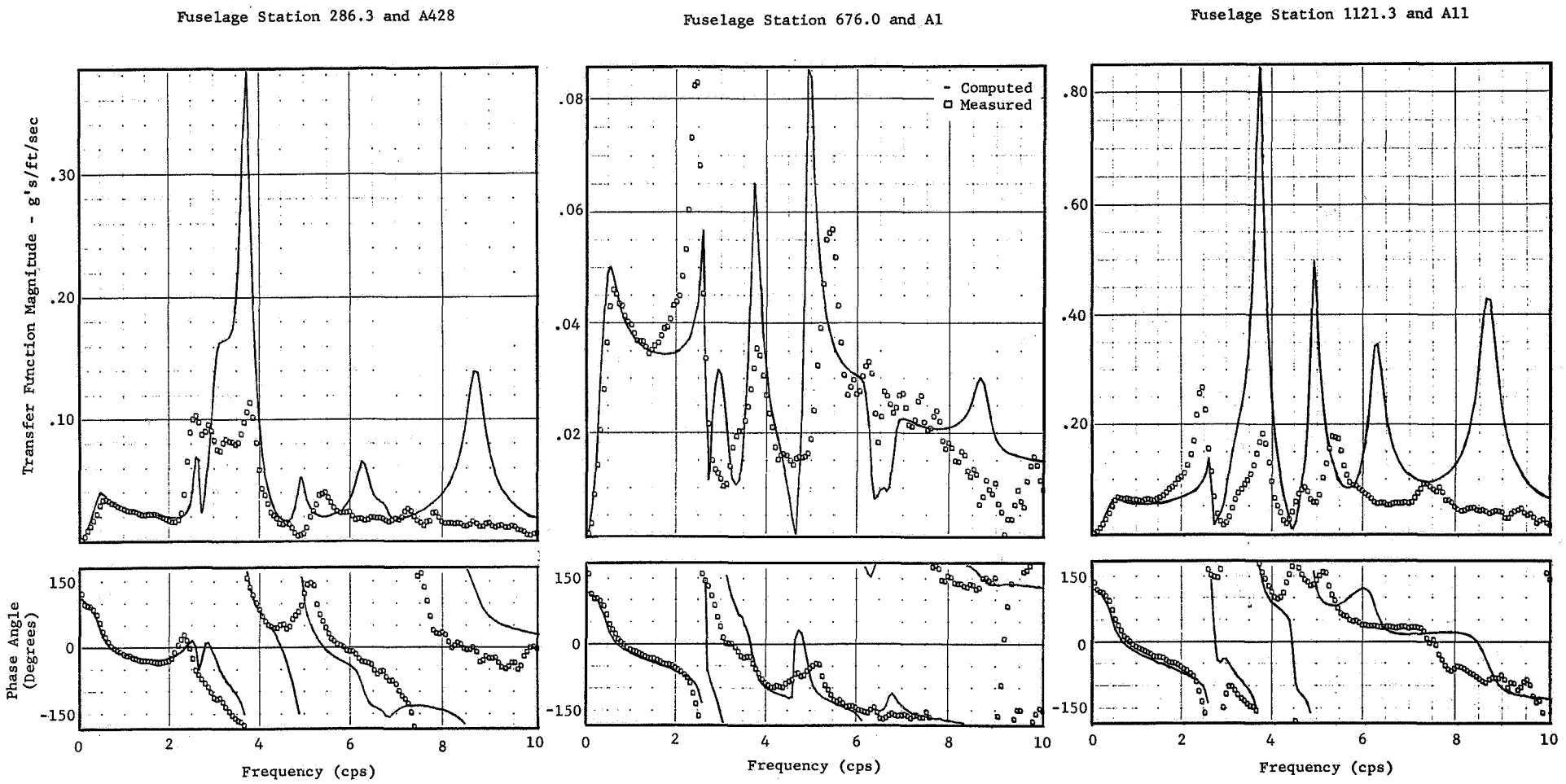

Analysis Parameters

ρ = .002241 slugs/ft^3, Mach = 0.80, V = 921 ft/sec, SAS ON, C.G. = 26.8% MAC

Figure 58 Comparison of Computed and Measured Transfer Functions, Run 131-3, Quasi-Steady Method-One

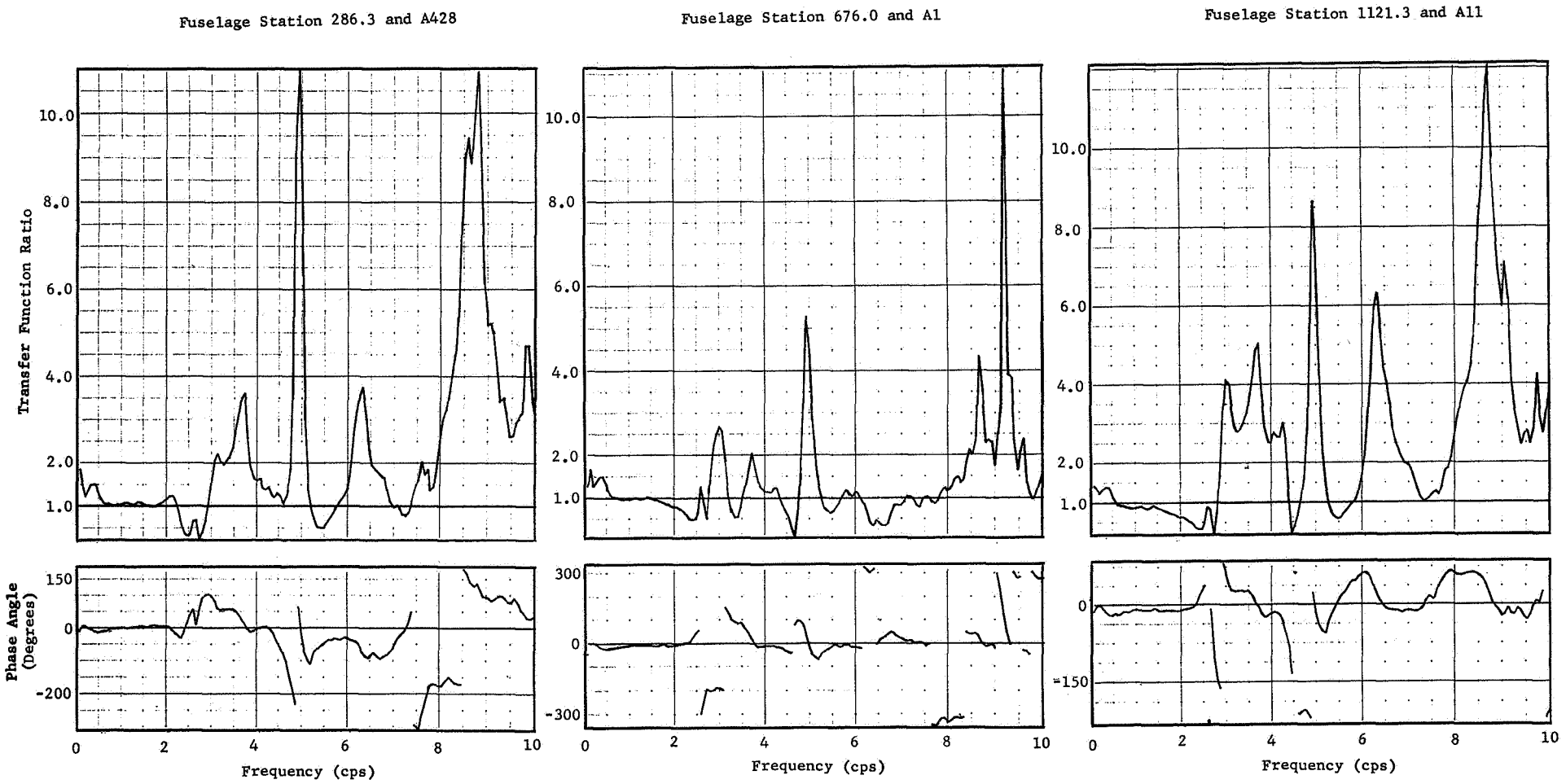

Analysis Parameters

ρ = .002241 slugs/ft^3, Mach = 0.80, V = 921 ft/sec, SAS ON, C.G. = 26.8% MAC

Figure 59 Ratio of Computed to Measured Transfer Functions, Run 131-3, Quasi-Steady Method-One

Quasi-Steady Method Two

The aerodynamic terms containing pressures due to rigid body degrees of freedom are the same for method two as previously described for method one. However, the remaining aerodynamic terms were altered. The aerodynamic terms which contain the pressures due to the first elastic mode as computed using unsteady aerodynamics at the frequency of the first elastic mode were used to approximate these terms for all other frequencies. This approximation was made by assuming the real part to be invariant with frequency and the imaginary part to vary linearly with frequency. The procedure is repeated in a like manner for each of the elastic degrees of freedom. The quasi-steady aerodynamic terms in the second method which contain pressures produced by the first flexible mode agree exactly with the corresponding unsteady aerodynamic terms at the natural frequency of the first flexible mode and are approximate at other frequencies. The quasi-steady aerodynamic terms which have pressures produced by flexible mode two, agree exactly with the corresponding aerodynamic terms at the natural frequency of mode two and are approximate elsewhere; etc.

Transfer functions for run 131-3 with a 2000 feet altitude standard day density were computed using the second quasi-steady method. The transfer functions are plotted on figure 60 for comparison with measured data. Comparing figure 60 with figure 25 it can be seen that the transfer functions computed using the second quasi-steady method agrees very closely with those obtained using unsteady aerodynamics. The degree of correlation with the measured data is almost the same as obtained with unsteady aerodynamics. The ratio of the computed transfer functions using quasi-steady method two to the measured data is shown in figure 61.

$\bar{A}$ and N_o Data Using Quasi-Steady Aerodynamics

The $\bar{A}$ and N_o data computed by both the quasi-steady aerodynamic methods are listed in table 27. The corresponding $\bar{A}$ and N_o data obtained using unsteady aerodynamics are also listed for comparison. The $\bar{A}$ and N_o data obtained by the first method are a good approximation to the unsteady data. However, the $\bar{A}$ and N_o obtained by the second method are almost identical to the unsteady data.

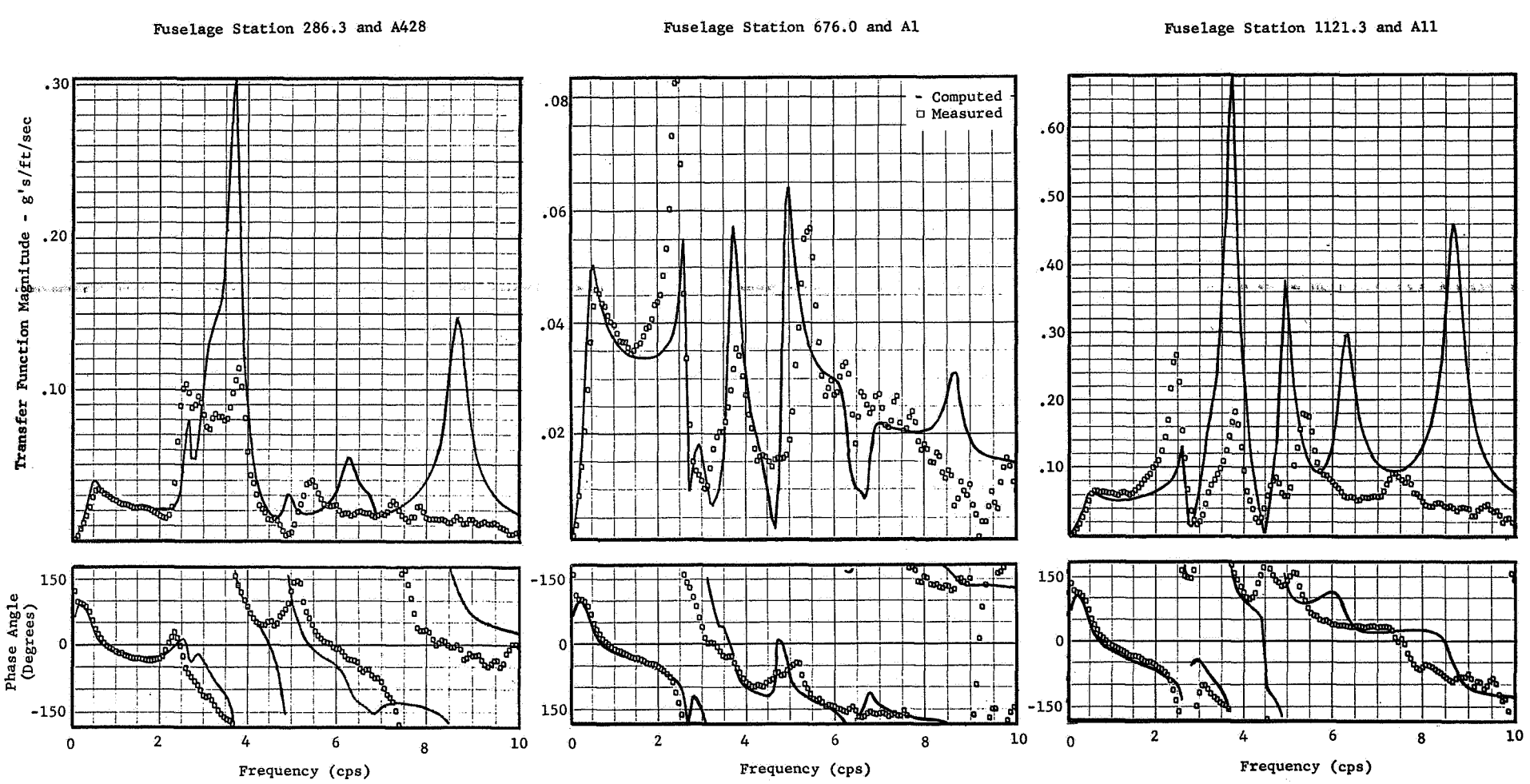

Analysis Parameters

ρ = .002241 slugs/ft^3, Mach = 0.80, V = 921 ft/sec, SAS ON, N = 10, C.G. = 26.8% MAC

Figure 60 Comparison of Computed and Measured Transfer Functions, Run 131-3, Quasi-Steady Method-Two

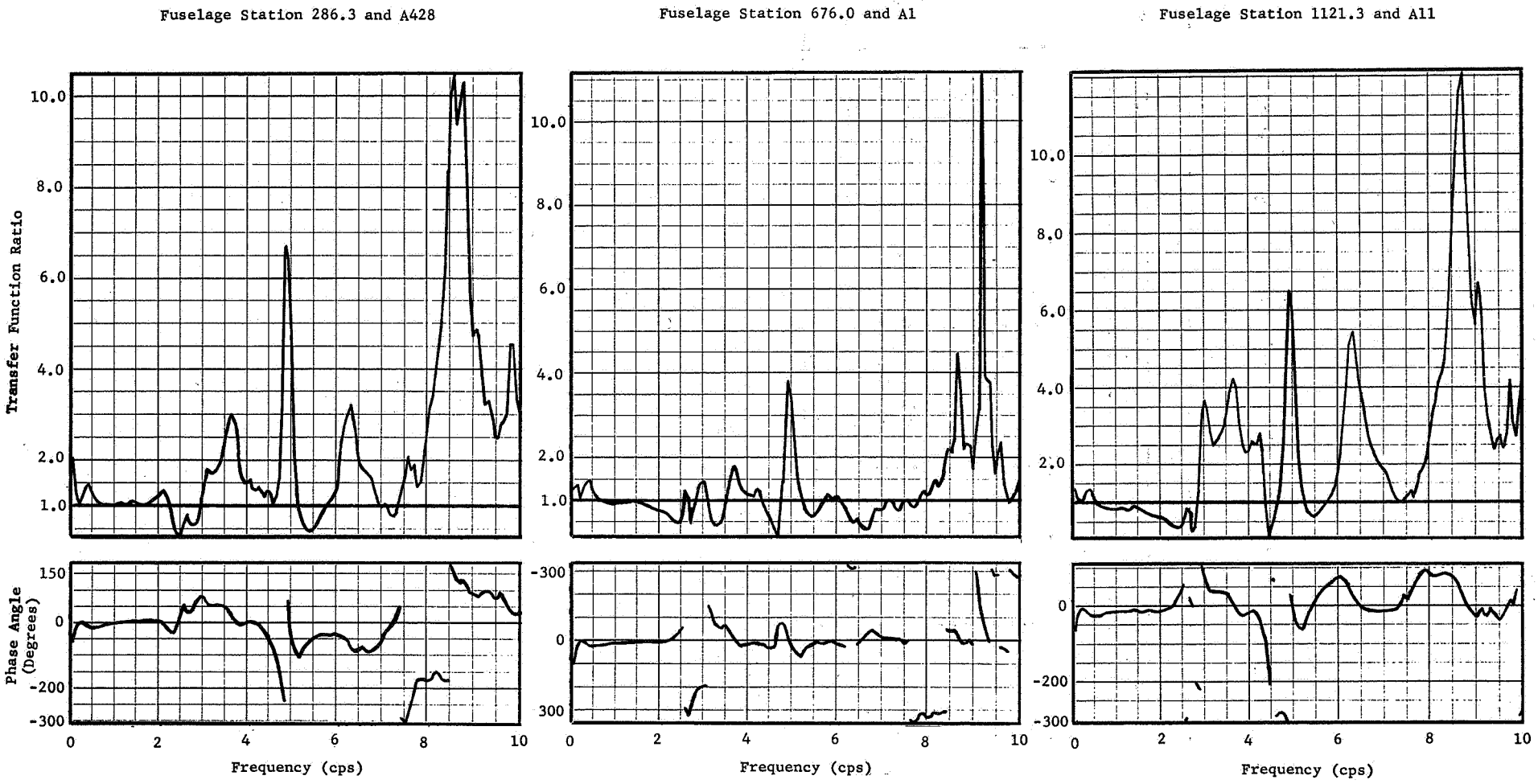

Analysis Parameters

ρ = .002241 slugs/ft^3, Mach = 0.80, V = 921 ft/sec, SAS ON, N = 10, C.G. = 26.8% MAC

Figure 61 Ratio of Computed to Measured Transfer Functions, Run 131-3, Quasi-Steady Method-Two

Table 27 $\bar{A}$ and N_o Data Using Quasi-Steady Aerodynamics

F.S. (in)	Accel.	Quasi-Steady				Unsteady	
		Method One		Method Two			
		$\bar{A}$	N_o	$\bar{A}$	N_o	$\bar{A}$	N_o
N = 10							
286.3	A428	.04240	3.2472	.03862	3.1881	.03855	3.1525
676.0	A1	.03236	1.5812	.03139	1.5263	.03071	1.5443
1121.3	A11	.08635	4.0090	.07833	4.0628	.07690	4.0427

TWO DIMENSIONAL TURBULENCE TRANSFER FUNCTIONS

The proceding sections have been concerned with computing the response to one dimensional turbulence which varies in the flight direction but does not vary in the spanwise direction (perpendicular to the flight direction). A method of computing the response to two dimensional turbulence was developed in reference 9 which considers the vertical component of the gust velocity to be random in both the flight direction and the span direction.

The concept of dividing the lifting surface into strips is employed in reference 9 as a means of describing the procedure. The method is readily extended to permit the utilization of the kernel function as a means of computing the oscillatory pressure distribution. For clarity, the method of analysis as applied herein is briefly developed.

As previously described a collocation method is used to obtain approximate solutions to the integral equation relating downwash, pressure, and kernel function, equation (37). As employed here the downwash is satisfied at 25 collocation points on each side of the fuselage centerline. Five chordwise points are located on each of the five streamwise lines on the wing on each side of the centerline. Hence, the traveling gust velocity wave is described along ten streamwise paths as shown in figure 62.

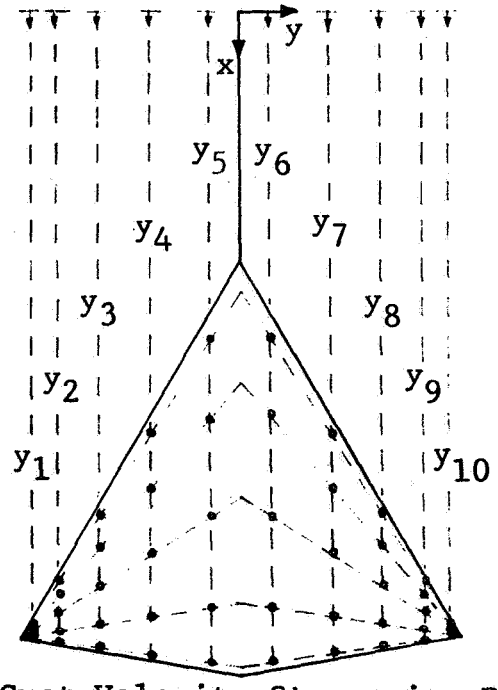

Figure 62 Gust Velocity Streamwise Paths for Downwash Collocation Points

The one dimensional traveling gust velocity wave is expressed as

$$w_g = \bar{w}_g e^{i\omega t} = e^{i\omega(t - \frac{x}{V})} \quad (72)$$

$$\bar{w}_g = e^{-i\omega x/v} \quad (73)$$

where x is measured from the location of the gust probe. For collocation purposes the gust wave is defined along the ten streamwise paths illustrated in figure 62. In matrix notation, the gust velocity is defined by a 50 x 1 column matrix which can also be expressed as the sum of ten column matrices

$$\left\{\bar{w}_g\right\} = \left\{\bar{w}_{g_1}\right\} + \left\{\bar{w}_{g_2}\right\} + \ldots + \left\{\bar{w}_{g_{10}}\right\} \quad (74)$$

where $\left\{\bar{w}_{g_n}\right\}$ is a 50 x 1 column matrix in which all the elements are zero except the five elements corresponding to the five downwash points along the nth streamwise path

Each column on the right hand side of equation (74) represents the gust velocity along one path with the gust velocity along all other paths set equal to zero. The sum of the oscillatory pressures produced by each of the ten sets of gust velocities is equal to the pressure produced by a continuous one dimensional gust wave.

$$\Delta p_g(\omega) = \Delta p_{g_1}(\omega) + \Delta p_{g_2}(\omega) + \ldots + \Delta p_{g_{10}}(\omega) \quad (75)$$

where $\left\{\Delta p_{g_n}\right\}$ is the pressure produced by satisfying the gust velocity on the collocation points along the nth streamwise path

The generalized aerodynamic terms produced by the one dimensional gust wave can be expressed by

$$\left\{Q_{rg}\right\} = \left\{Q_{rg_1}\right\} + \left\{Q_{rg_2}\right\} + \ldots + \left\{Q_{rg_{10}}\right\} \quad (76)$$

The sinusoidal response to the one dimensional sinusoidal gust wave (transfer function) can then be expressed as the sum of the responses to each of the ten forcing functions on the right side of equation (76)

$$H(\omega) = H_1(\omega) + H_2(\omega) + \ldots + H_{10}(\omega) \tag{77}$$

where $H_n(\omega)$ is the response to the forcing function produced by satisfying the gust velocity downwash at the collocation points along the nth streamwise path.

The Fourier transform of equation (77) yields the following relation.

$$h(t) = h_1(t) + h_2(t) + \ldots + h_{10}(t) \tag{78}$$

where $h(t)$ is the response of some point on the airplane due to flight through a unit impulse downwash located along the $x = 0$ axis and

$h_n(t)$ is the contribution to $h(t)$ produced by satisfying the downwash at the collocation points along the nth streamwise path due to flight through the line of unit impulses located along the $x = 0$ axis.

Therefore, the response of some item due to flight through random turbulence which can have a different profile along each of the ten flight paths, can be expressed as

$$a(t) = \int_{-\infty}^{\infty} w_{g_1}(\tau)\, h_1(t-\tau)\, d\tau + \int_{-\infty}^{\infty} w_{g_2}(\tau)\, h_2(t-\tau)\, d\tau + \ldots + \int_{-\infty}^{\infty} w_{g_{10}}(\tau)\, h_{10}(t-\tau)\, d\tau \tag{79}$$

The Fourier transform of equation (79) yields

$$H_a(\omega) = W_{g_1}(\omega)\, H_1(\omega) + W_{g_2}(\omega)\, H_2(\omega) + \ldots + W_{g_{10}}(\omega)\, H_{10}(\omega) \tag{80}$$

where $W_{g_n}(\omega)$ and $H_n(\omega)$ are the Fourier transforms of $w_{g_n}(t)$ and $h_n(t)$ respectively.

The PSD of the response can be expressed as

$$\phi_a(\omega) = \lim_{T\to\infty} \frac{1}{2\pi T} H_a(\omega)\, H_a(-\omega)$$

$$= \phi_{g_1g_1} H_1(\omega)\, H_1(-\omega) + \phi_{g_2g_2} H_2(\omega)\, H_2(-\omega) + \ldots$$

$$+\phi_{g_1g_2} H_1(\omega)\, H_2(-\omega) + \phi_{g_2g_1} H_1(-\omega)\, H_2(\omega) + \ldots$$

$$+ \phi_{g_1g_3} H_1(\omega)\, H_3(-\omega) + \ldots \qquad (81)$$

Reference 9 shows that equation (80) can be reduced to the following form

$$\phi_a(\omega) = \phi_g\left(|H_1(\omega)|^2 + |H_2(\omega)|^2 + \ldots + |H_{10}(\omega)|^2 \right)$$

$$+ \phi_{12}\ 2\,\mathrm{Re}\left[H_1(\omega)\, H_2(-\omega) + H_2(\omega)\, H_3(-\omega) + \ldots \right.$$

$$\left. + H_9(\omega)\, H_{10}(-\omega) \right] + \phi_{13}\ 2\mathrm{Re}\left[H_1(\omega)\, H_3(-\omega) \right.$$

$$\left. + H_2(\omega)\, H_4(-\omega) + \ldots + H_8(\omega)\, H_{10}(-\omega) \right] + \ldots.$$

$$+ \phi_{1,10}\ 2\,\mathrm{Re}\left[H_1(\omega)\, H_{10}(-\omega) \right] \qquad (82)$$

where ϕ_a is the response PSD

ϕ_g is gust velocity PSD

ϕ_{1n} is the gust cross spectrum between the gust velocity along streamwise path one and streamwise path n

R_e means real part

Equation (81) can be recast with the gust spectrum factored out to yield the following

$$\phi_a(\omega) = \left|H_e(\omega)\right|^2 \phi_g \tag{83}$$

where H_e is the equivalent transfer function and should be much closer to being equivalent to the transfer function measured during flight tests than are the one dimensional transfer functions.

The procedure reduces to computing the response PSD from equation (82) and then solving for the effective transfer function by equation (83). In order to compute the response PSD it is necessary to compute each of the ten transfer functions in equation (82). In order to obtain the response to the gust velocity acting on the collocation points along a single streamwise path, it is necessary to compute (1) the symmetric response to gust velocities acting on pairs of streamwise paths equally distant from the fuselage centerline, and (2) the antisymmetric response to equal but opposite gust velocities acting along the same streamwise paths. The transfer functions for the gust acting along a single streamwise path is obtained by adding and substracting the symmetric and antisymmetric response and dividing by two. The concept is illustrated in figure 63.

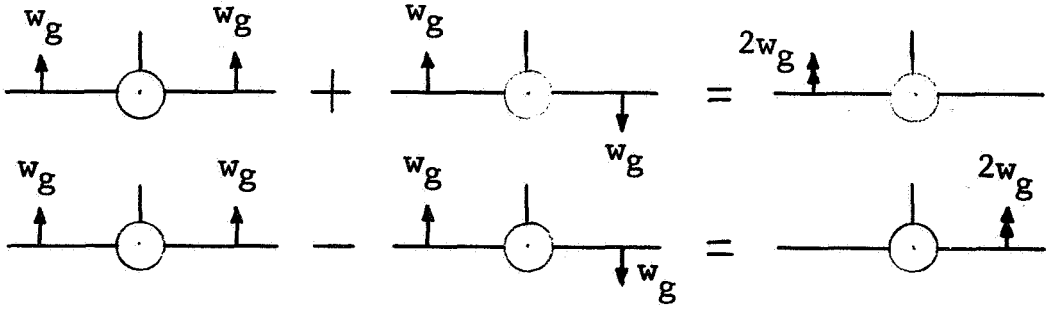

Figure 63 Combining Symmetric and Antisymmetric Response to Obtain Asymmetric Response

In general, it is necessary to compute the response to antisymmetric excitation using antisymmetric rigid body modes and antisymmetric natural modes of vibration as well as the response to symmetric excitation. However, when attention is limited to vertical acceleration response along the fuselage centerline there is no response due to antisymmetric excitation. Hence, the computational task is only one half of the task associated with the general case.

The description of the two dimensional turbulence analysis to this point has considered only the gust excitation forces produced on the wing as computed by the kernel function. To complete the description of the analysis, the $\{Q_{rg}\}$ terms for each nacelle and pylon were added to the $\{Q_{rg}\}$ terms for the wing, equation (76), computed for the streamwise path closest to the nacelle centerline. Similarly, the fuselage $\{Q_{rg}\}$ terms were dividing by two and one half was added to the wing $\{Q_{rg}\}$ terms computed for the streamwise paths on each side and adjacent to the fuselage centerline (streamwise paths 5 and 6).

The gust cross spectra relations are also developed in reference 9 for the Dryden gust spectrum. It should be noted that the equivalent transfer function is not unique but is dependent on the gust spectra and cross spectra. The Dryden gust spectrum with a 500 feet scale of turbulence was used throughout the two dimensional analysis.

Equivalent Transfer Functions For Two-Dimensional Turbulence

Transfer functions were computed for run 131-3 using a 2000 feet altitude standard day density and considering the turbulence to be two-dimensional. The computed transfer functions are plotted on figure 64 for comparison with the measured data. The equivalent transfer function magnitudes correlate with the measured data somewhat better than the computed one-dimensional transfer functions. The magnitude of the peak near 2.7 cps is slightly higher at all three stations whereas the magnitudes of the peaks at higher frequencies are reduced. No phase angle information is obtained for this method of computing the response to two-dimensional turbulence. The ratios of the equivalent transfer function for two-dimensional turbulence to the measured data are plotted in figure 65.

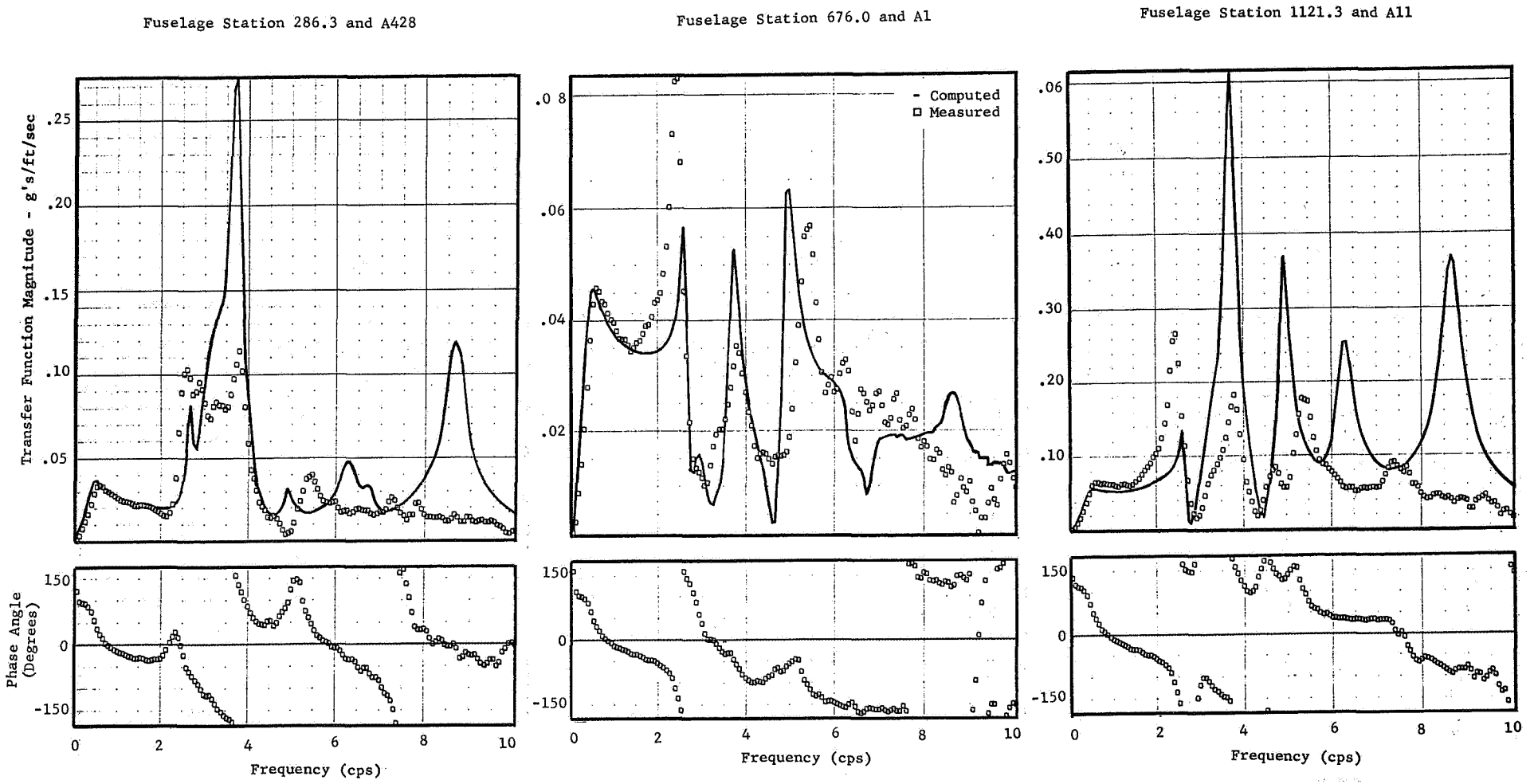

Analysis Parameters

ρ = .002241 slugs/ft^3, Mach = 0.80, V = 921 ft/sec, SAS ON, N = 10, C.G. = 26.8% MAC

Figure 64 Comparison of Computed and Measured Transfer Functions, Run 131-3, Two Dimensional Turbulence

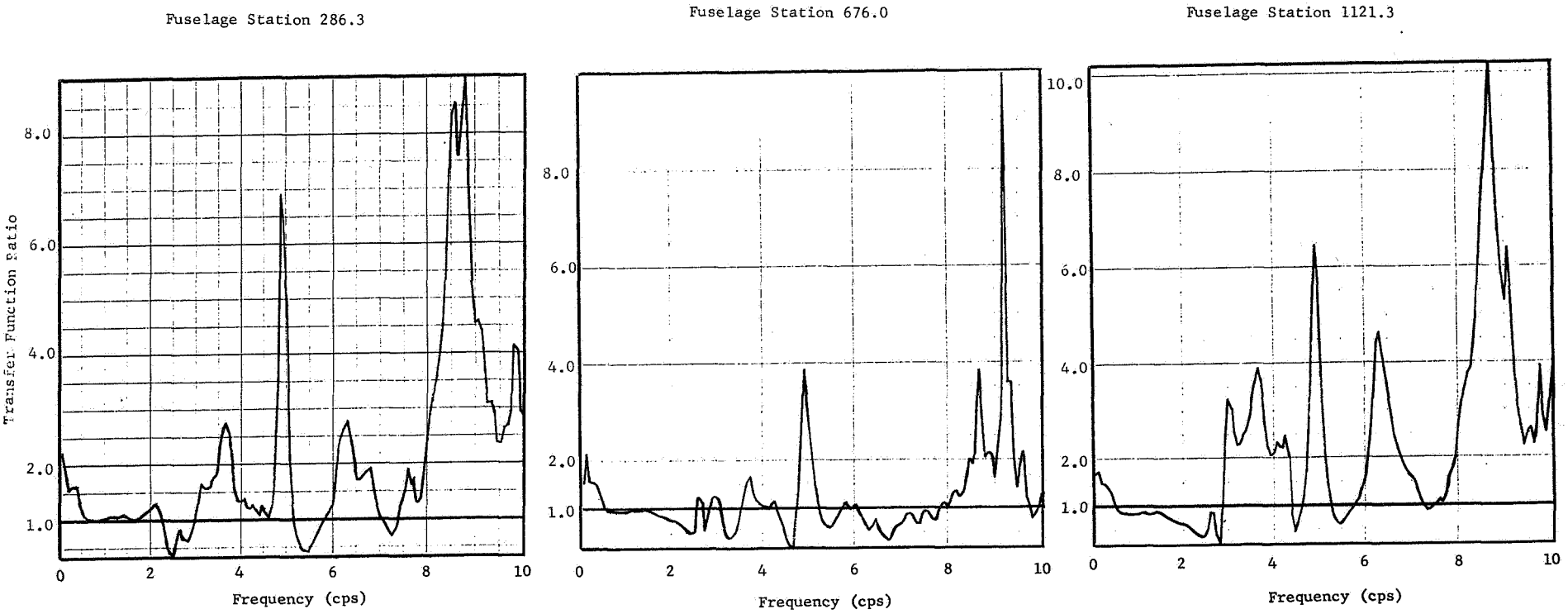

Analysis Parameters

ρ = .002241 Slugs/Ft^3, Mach = 0.80, V = 921 Ft/Sec, SAS On, N = 10, C.G. = 26.8% MAC

Figure 65 Ratio of Computed to Measured Transfer Functions, Run 131-3, Two Dimensional Turbulence

The effect of two-dimensional turbulence on the transfer functions can be seen more clearly in figure 66 where the ratios of the computed two-dimensional transfer functions to the computed one dimensional transfer functions are plotted. This ratio would be expected to approach unity as the frequency approaches zero. This trend appears to be taking place except for the behavior of the ratios at the lowest frequency. The ratios at 1/15 cps are from 0.92 to 0.95 at the three stations. However, the ratios from 2/15 cps to approximately 1.5 cps are all slightly greater than unity. The ratios are predominantly less than unity for frequencies above 1.5 cps. Exceptions are noted at the transfer function peak near 2.7 cps which is increased approximately 5 percent at each station. The ratios which are larger than unity at higher frequencies are all associated with valleys in the transfer functions. The large peaks near 3.7 cps are reduced by 7 to 8 percent at the three stations. The large peaks near 8.7 cps are also reduced by 7 to 8 percent. Since the airspeed for this run is 921 feet per second the gust wave length at 10 cps is 92.1 feet. The ratio of this wave length to the B-58 wing span is 1.621.

$\bar{A}$ and N_o Data For Two-Dimensional Turbulence

The $\bar{A}$ and N_o data computed for the two-dimensional turbulence analyses are listed in table 28 along with the corresponding data computed for one-dimensional turbulence for comparison. The two-dimensional effects reduce the computed A at stations 286.3 and 1121.3 by approximately 4 percent while the $\bar{A}$ at station 676.0 increases approximately 1 percent. The two-dimensional effects reduce the value of N_o by approximately 3 percent at all stations. These trends are in the right direction for improving correlation with the $\bar{A}$ and N_o data but are not of sufficient magnitude to significantly improve the correlation.

Table 28 $\bar{A}$ and N_o Data For Two-Dimensional Turbulence

F.S. (in)	Accel.	Computed (2000 Ft. Alt.)				Measured	
		One - Dim.		Two - Dim.			
		$\bar{A}$	N_o	$\bar{A}$	N_o	$\bar{A}$	N_o
286.3	A428	.03855	3.1525	.03687	3.0484	.02814	2.391
676.0	A1	.03071	1.5443	.03110	1.5052	.03019	1.638
1121.3	A11	.07690	4.0427	.07342	3.9307	.05888	2.454

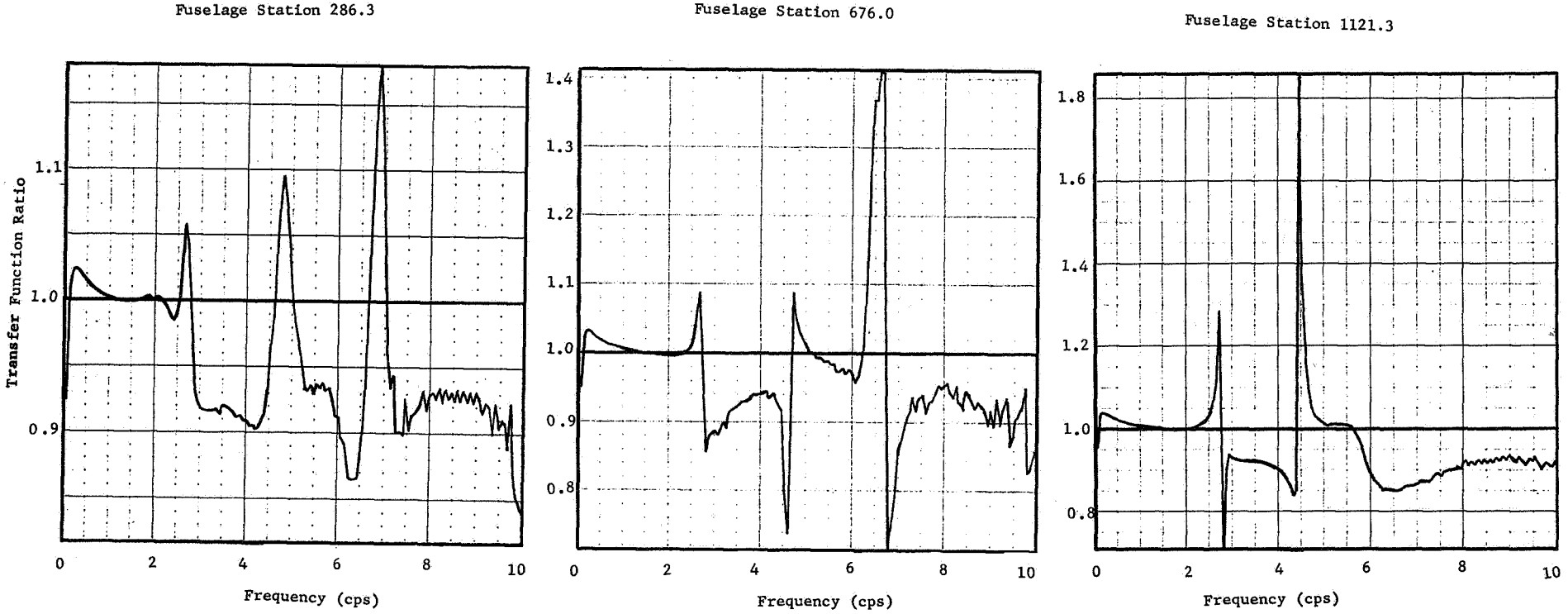

Analysis Parameters

ρ = .002241 slugs/ft^3, Mach = 0.80, V = 921 ft/sec, SAS ON, N = 10, C.G. = 26.8% MAC

Figure 66 Ratio of Computed Transfer Functions, Run 131-3, Two Dimensional Turbulence

EFFECT OF SPECTRAL AVERAGING

There are many sources of potential error in the measured PSD data. Among the potential sources of errors is the sensors, the recording system, the playback system and the analog-to-digital converter which samples the gust velocity and response time histories at equal time increments. In addition, errors or distortions are introduced by the calculations which are performed on the digitized time series to obtain measured spectral estimates. This distortion is produced by using measurements, at discrete time intervals rather than continuous measurements, by truncating the autocorrelation function and by using numerical integration techniques. It is this source of error or distortion that is the subject of this portion of the investigation and is referred to as spectral averaging herein. The distortion produced by spectral averaging cannot be removed from the measured data but it can be introduced into the computed data and its effect observed. To be more specific, suppose the time series of gust velocity and response represented by equation (7) have been taken from a continuous time history of gust velocity and response for which the exact PSD of both are known. Performing the operations defined by equations (8) through (18) yields estimates of the PSD. The question to be investigated is; how do the spectral estimates of equation (18) compare with the true PSD and if differences do exist how do they effect the transfer functions obtained by equation (19) and equation (20) ?

Effect of Spectral Averaging on the Response PSD

Since only the response PSD, and the cross spectrum obtained by combining the computed transfer functions with the Dryden Gust Spectrum were available, operations must be made on these functions rather than the autocorrelation and cross-correlation functions.

In reference 10 it is shown that the process of computing the autocorrelation function at equal time intervals as indicated by equation (10) and the raw estimates of the PSD by equation (11) can be viewed as being equivalent to any of the following three relationships

View One

$$L_h = \int_{-\infty}^{\infty} \left[Q_o \left(\frac{h}{2M\,\Delta t} - f' \; ; \Delta t \right) \right] P(f')\, df' \qquad (84)$$

where P(f) is the true PSD defined over both positive and negative frequencies, that is

$$|P(f)| = \tfrac{1}{2}\,\phi(f) \qquad (85)$$

and

$$Q_o\left(\frac{h}{2M\,\Delta t} - f' \; ; \Delta t\right) = \frac{\Delta t \sin\left[2\pi M \Delta t \left(\frac{h}{2M\,\Delta t} - f'\right)\right]}{\tan\left[\pi \Delta t \left(\frac{h}{2M\,\Delta t} - f'\right)\right]} \qquad (86)$$

View TWO

$$L_h = \int_{-\infty}^{\infty} Q_o \left(\frac{h}{2M\,\Delta t} - f'\right) P_a(f')\, df' \qquad (87)$$

where $P_a(f)$ is the aliased PSD defined over both positive and negative frequencies, and

$$Q_o\left(\frac{h}{2M\Delta t} - f'\right) = \frac{\sin\left[2\pi M \Delta t \left(\frac{h}{2M\Delta t} - f'\right)\right]}{\pi\left(\frac{h}{2M\Delta t} - f'\right)} \qquad (88)$$

View Three

$$L_h = \int_{-\frac{1}{2\Delta t}}^{\frac{1}{2\Delta t}} \left[Q_o \left(\frac{h}{2M\Delta t} - f' \; ; \Delta t \right) \right] P_a(f')\, df' \qquad (89)$$

All three views can be interpretted as viewing the true spectrum or the aliased spectrum through a filter window. All three views are equivalent but the integration requirements differ. View one requires the integration from minus infinity to plus infinity but the true computed response PSD was available only over the frequency range from -10 cps to + 10 cps. Although the frequency range could have been extended, it obviously could not have been extended to cover an infinite frequency range.

View two requires the integration from minus infinity to plus infinity. Although the aliased spectrum is periodic in frequency with period equal to twice the Nyquist frequency, the filter window defined by equation (88) is not periodic. Hence, view two has a double infinity integration range requirement that is as unattractive as the requirements for view one.

View three requires the integration from the negative Nyquist frequency to the positive Nyquist frequency convoluting the filter window defined by equation (86) with the aliased spectrum. Although the aliased response spectrum was not available, it is only necessary to assume the true response spectrum to be zero for frequencies greater than the positive Nyquist frequency and less than the negative Nyquist frequency, to conclude that the true PSD and the aliased PSD are one and the same. The measured data were filtered by a low pass filter designed to remove all frequencies components above the Nyquist frequency in an attempt to minimize foldback and hence make the aliased PSD as close as possible to the true PSD. Although, perfect low pass filters do not exist, the assumption that the aliased computed response PSD is the same as the true computed response PSD is equivalent to applying a perfect low pass filter to the true computed response PSD removing all frequencies outside the $-\frac{1}{2\,\Delta t}$ to $+\frac{1}{2\,\Delta t}$ frequency range while the PSD inside this range remained unchanged. The filter window defined by equation (86) is also periodic in frequency with the period equal to twice the Nyquist frequency. The filter window as applicable to run 131-3 is plotted in figure 67. The filter window is symmetric in frequency about the center frequency so only one half the filter window from the center frequency to the Nyquist frequency is plotted in figure 67. Note that the magnitude of the filter window is zero at each 1/15 cps frequency increment. Since the computed response PSD was determined only at the same 1/15 cps frequency increments it is necessary to make an assumption with respect to the variation of the response PSD between each of the computed points. It was assumed that the response PSD varied linearly between adjacent computed points. The response PSD and the filter window were evaluated at 40 equal frequency subincrements across each 1/15 cps frequency increment to perform the integration expressed by equation (89). The integration was performed numerically by the trapezoidal integration method.

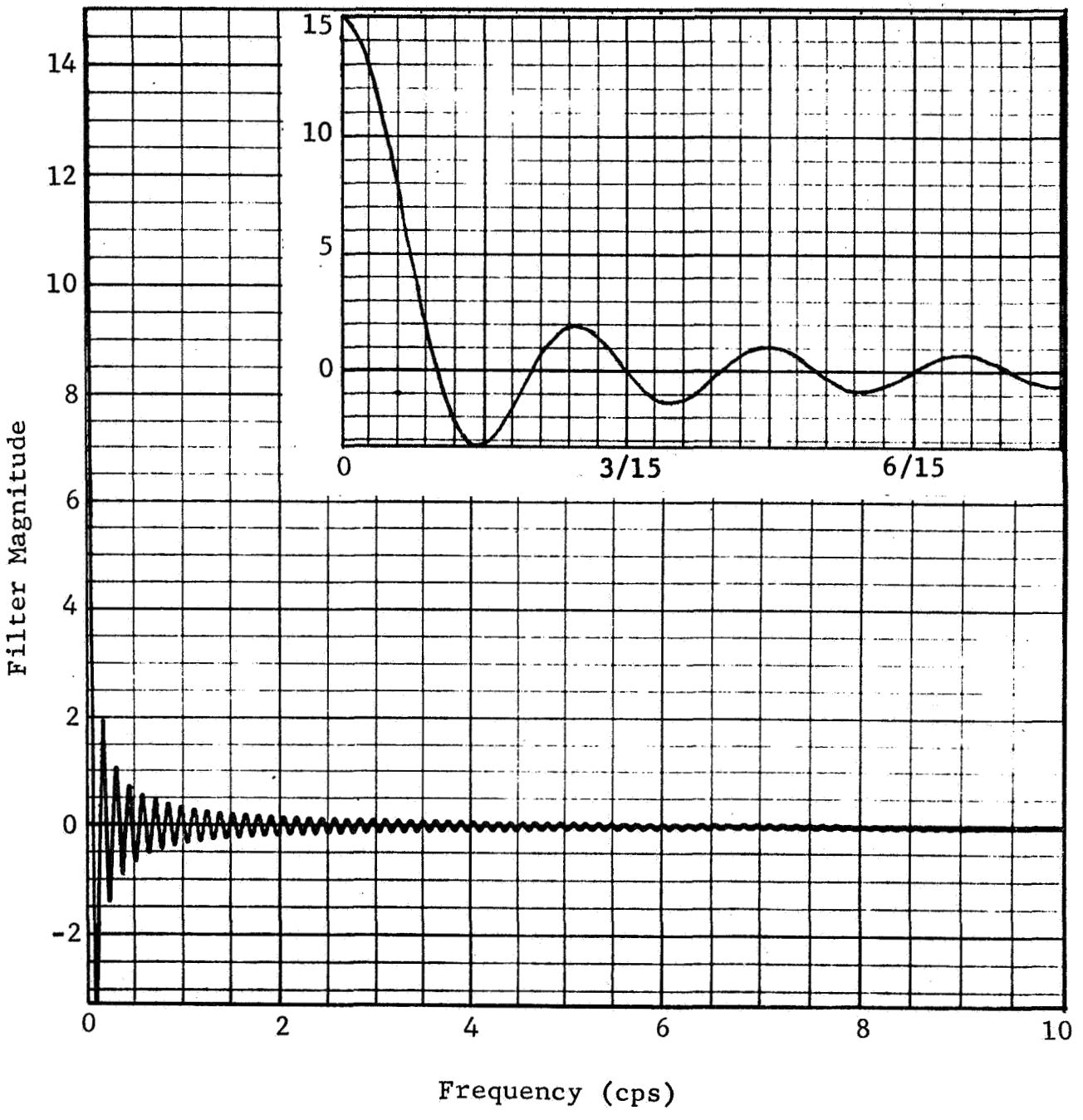

Figure 67 Filter Function for Run 131-3, Eq. (88)

The steps involved in evaluating the effect of spectral averaging are summarized as follows:

Step One

Compute the response PSD for run 131-3 by combining the computed transfer functions plotted in figure 25 with the Dryden gust spectrum with a 500 feet scale of turbulence. These response PSD are defined from zero to 10 cps.

Step Two

Multiply each response PSD computed in step one by the square of the magnitude of the prewhitening transfer function defined by equation (9). These response PSD are from zero to 10 cps.

Step Three

Divide the prewhitened PSD by two and fold about the zero frequency axis to obtain the two sided PSD defined over both negative and positive frequencies P(f).

Step Four

Convolute the filter window and the two sided response PSD of step three by performing the integration indicated in equation (89). Due to symmetry the integration need only be performed with the center frequency of the filter window located at each 1/15 cps frequency increment from zero to 10 cps.

Step Five

Double the spectral estimates obtained by step four to return to the one sided response spectrum defined from zero to 10 cps. These spectral estimates correspond to the "raw" prewhitened estimates of the PSD indicated by equation (11).

Step Six

Smooth the "raw" estimates of the PSD by applying the operations indicated by equation (12).

Step Seven

Post darken the smoothed PSD estimates by applying the operation indicated by equation (18).

The response PSD as obtained at the end of step seven are plotted in figure 68. To see the effect of spectral averaging, the ratios of the averaged spectrum as obtained by step seven to the original spectrum obtained by step one are plotted in figure 69. The spectral estimate for the first frequency increment is most effected by this operation. Since the true PSD at 1/15 cps is very low and the slope of the PSD is very large small amounts of "power" which "leak" through the lobes of the filter window produce large percent changes in the averaged spectrum. Furthermore the prewhitening operation which was designed to prewhiten the gust spectrum is not effective in prewhitening the response spectrum. In the very low frequency range the prewhitening operation increases the slope of the response PSD rather than reducing it to the desired zero slope. The ratio of the averaged PSD to the true PSD at 1/15 cps ranges from 11 to 12.6 for the three fuselage stations. This ratio rapidly reduces to unity at a frequency near 0.5 cps which corresponds to the frequency at which the first peak in the PSD occurs. Above 0.5 cps the ratios are very close to unity over most of the frequency range. By comparing figures 68 and 69 it can be seen that the ratios of figure 69 have the largest deviations from unity near the frequencies at which peaks and valleys occur on the PSD. In general the ratios are greater than unity near valleys in the PSD and less than unity near peaks in the PSD. Hence, spectral averaging tends to increase the valleys of the true PSD and decrease the peaks of the true PSD.

The effect of spectral averaging on the cross spectra of gust velocity and response was investigated in a similar manner. The cross spectrum is obtained from Equation (90) by combining the computed transfer functions plotted in figure 25 with the Dryden gust spectrum with a 500 feet scale of turbulence.

$$P_{xy}(f) = \tfrac{1}{2} H(f) \Phi_D(f) \qquad (90)$$

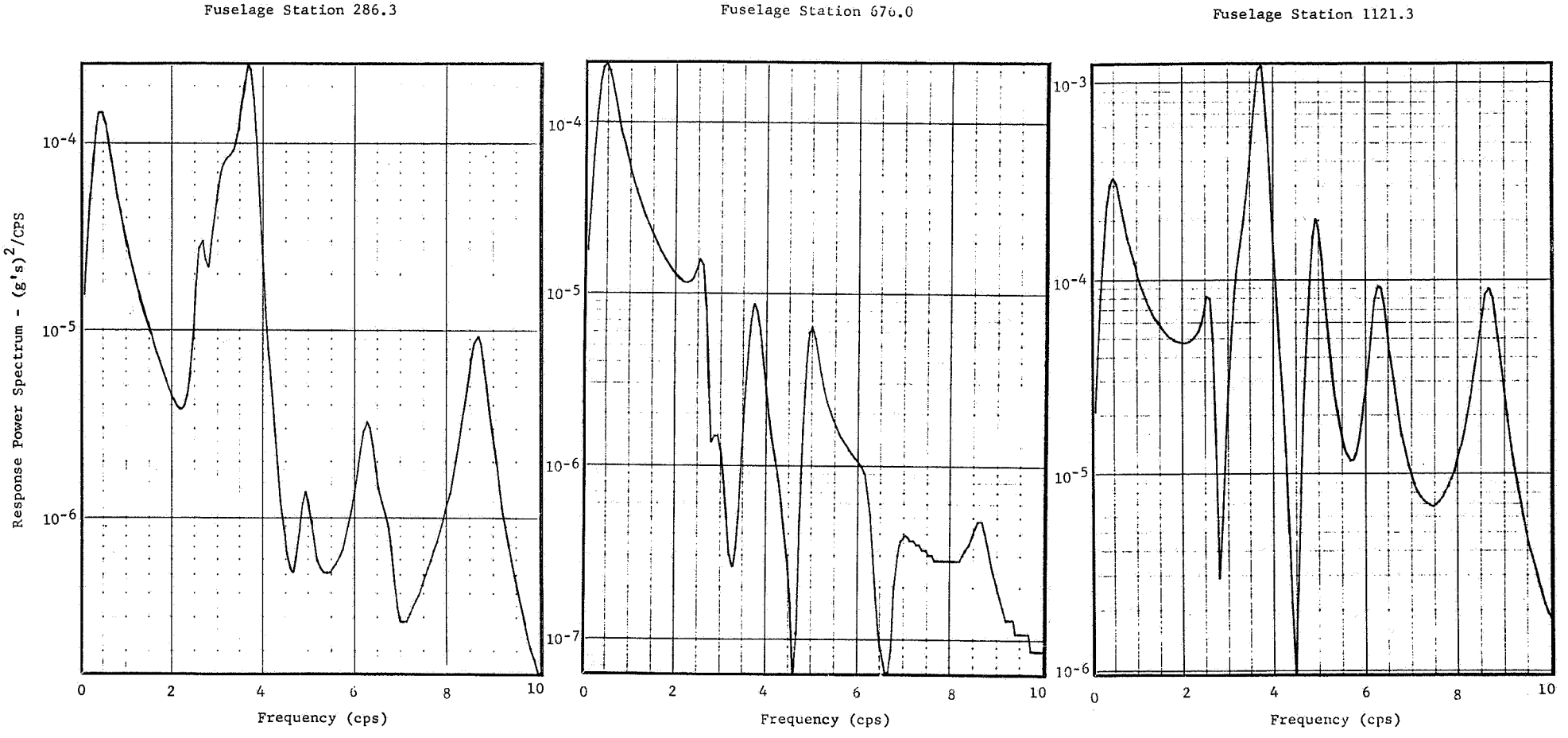

Analysis Parameters

ρ = .002241 slugs/ft^3, Mach = 0.80, V = 921 ft/sec, SAS ON, N = 10, C.G. = 26.8% MAC

Figure 68 Computed Response PSD, Run 131-3, After Spectral Averaging

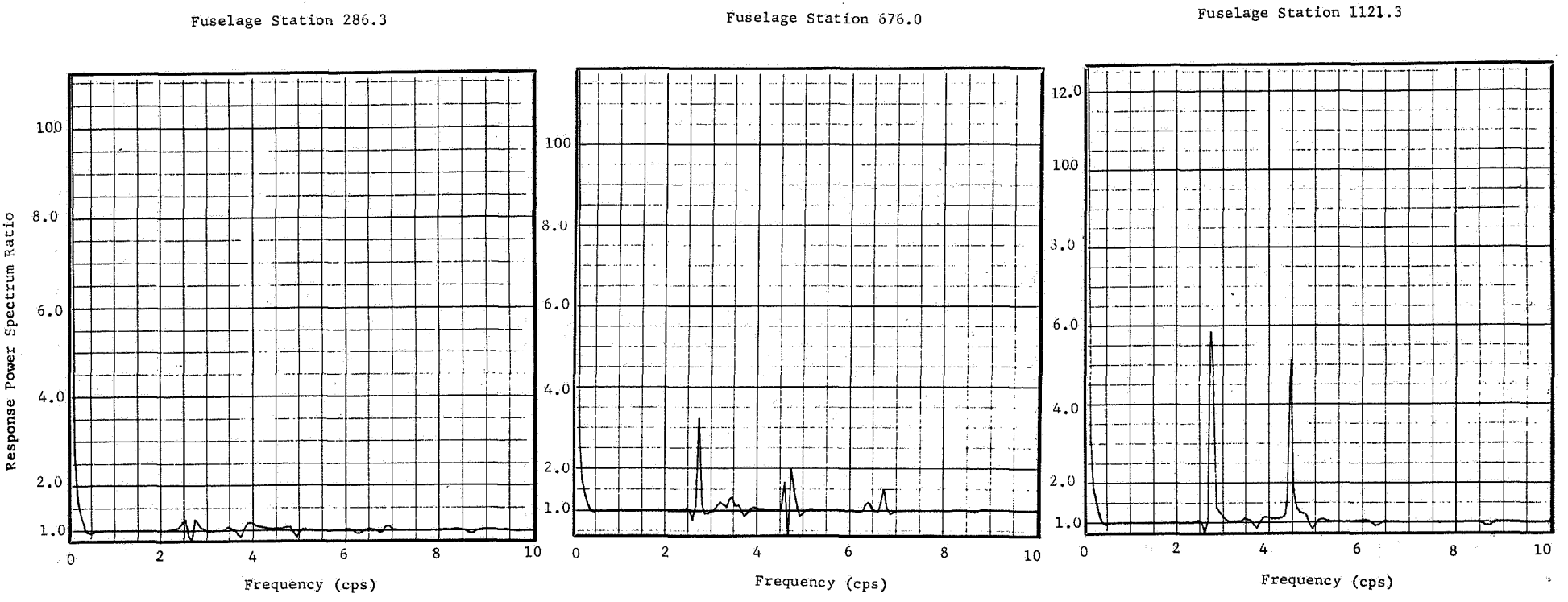

Analysis Parameters

ρ = .002241 slugs/ft^3, Mach = 0.80, V = 921 ft/sec, SAS ON, N = 10, C.G. = 26.8% MAC

Figure 69 Ratio of Computed Response PSD After Spectral Averaging to PSD Before Spectral Averaging, Run 131-3

The cospectrum and quadspectrum can be computed as follows

$$c_{xy}(f) = \tfrac{1}{2} H_R(f) \quad \phi_D(f) \quad , \quad f > o \tag{92}$$

$$q_{xy}(f) = \tfrac{1}{2} H_I(f) \quad \phi_D(f) \quad , \quad f > o \tag{93}$$

where $H_R(f)$ and $H_I(f)$ are the real and imaginary parts of the computed transfer function for gust run 131-3.

Since the cospectrum is symmetric in frequency and the quadspectrum is antisymmetric in frequency both are known over negative as well as positive frequencies. The aliased two-sided cospectrum and quadspectrum was assumed to be equal to the non-aliased cospectrum and quadspectrum. Replacing the response PSD, first by the cospectrum and then by the quadspectrum and performing the operations of steps two through step seven above yields the averaged cospectrum and quadspectrum. It should be noted that the raw estimates of the quadspectrum are zero at h=0 and h=M. The cospectrum and quadspectrum are then combined to yield the cross spectrum magnitude and phase angle distorted by spectral averaging.

Effect of Spectral Averaging on the Dryden Gust PSD

The Dryden gust spectrum and its Fourier transform or autocorrelation function provide a means of evaluating the effect of spectral averaging on the gust PSD by operating on either the autocorrelation function or the PSD. The Dryden autocorrelation function for unit rms gust velocity can be expressed as

$$R_D(t) = \left(1 - \frac{Vt}{2L} \right) e^{-Vt/L} \tag{94}$$

Hence, the Dryden autocorrelation function can be evaluated at 1/20 second time intervals.

$$R_D(m) = R_D(m \, \Delta t) \tag{95}$$

The Dryden autocorrelation function evaluated at 150 time intervals of 1/20 second each for the velocity compatible with run 131-3 is plotted in figure 70. The autocorrelation function after the prewhitening operation on the time series, equation (8), can be computed from the autocorrelation function of the time series before prewhitening, by the following operations

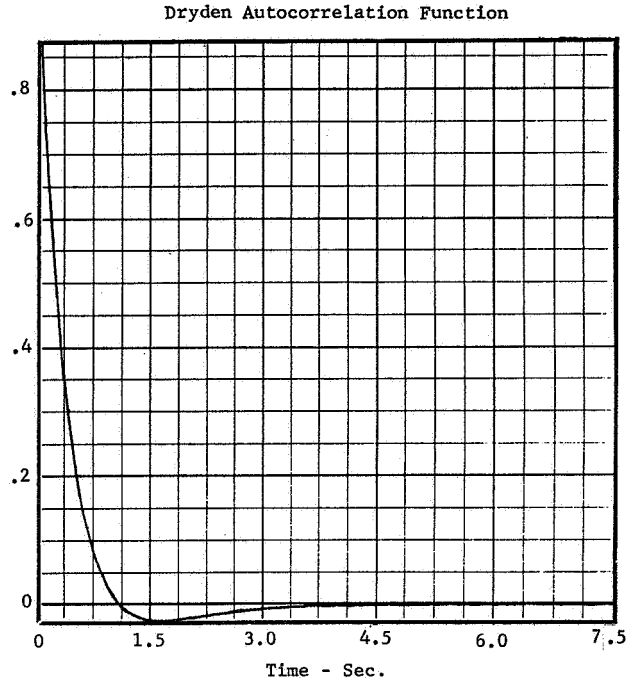

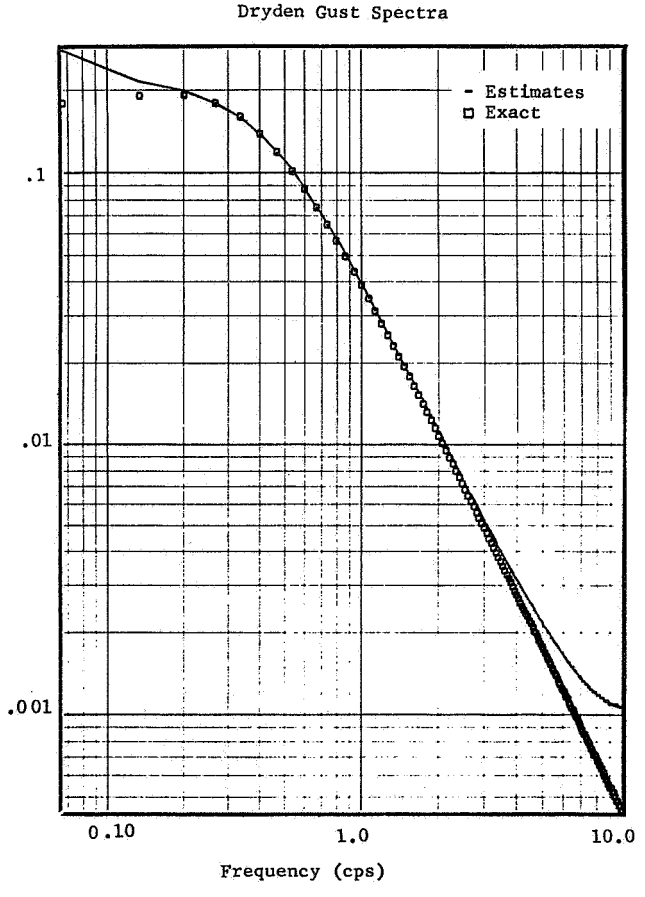

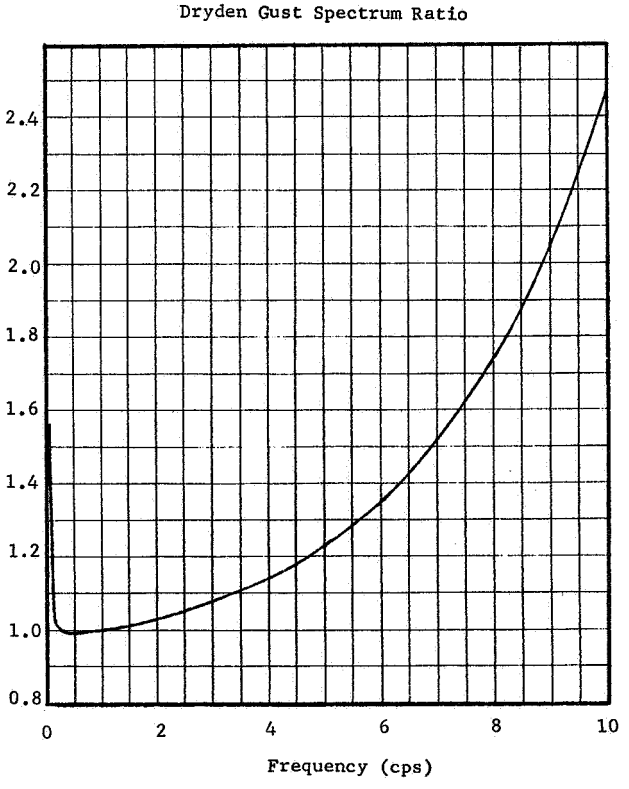

Figure 70 Dryden Autocorrelation Function, True PSD, Distorted PSD and Ratio of Distorted PSD to True PSD

$$\hat{R}_D(m) = -R_D(m-1) + 2R_D(m) - R_D(m+1) \quad (96)$$

where $\hat{R}_D(m)$ is the Dryden autocorrelation function after prewhitening the gust velocity time series.

Replacing equation (10) with equation (96), and performing the operations indicated by equations (11), (12), and (18) yields 150 estimates of the Dryden gust spectrum. These estimates are plotted on figure 70 for comparison with the exact Dryden gust spectrum. The ratio of the estimates to the exact spectra is also plotted on figure 70. It can be seen that the numerical operations produce estimates that are higher than the exact values at both the low and high ends of the frequency range. The estimates are very close to being exact in the middle of the frequency range. The increase at the low frequency end is caused primarily by the prewhitening operation. The increase at the high frequency end is caused by fold-back or aliasing because the Fourier transform of the Dryden autocorrelation function has components above the Nyquist frequency.

It is also possible to determine the effect of spectral averaging on the non-aliased Dryden gust spectrum. Assume the aliased gust spectrum and the Dryden gust spectrum between zero and 10 cps to be identical. The steps involved in evaluating the effect of spectral averaging upon the non-aliased gust spectrum are summarized as follows:

Step One

Multiply the gust spectrum by the square of the magnitude of the prewhitening transfer function defined by equation (9).

Step Two

Divide the prewhitened gust spectrum by two and fold about the zero frequency axis to obtain the two sided gust spectrum defined over both negative and positive frequencies.

Step Three

Convolute the filter window and the two sided gust spectrum of step two by performing the integration indicated in equation (89). Due to symmetry the integration need only be performed with the center frequency of the filter window located at each 1/15 cps frequency increment from zero to 10 cps.

Step Four

Double the spectral estimates obtained by step three to return to the one sided gust spectrum defined from zero to 10 cps.

Step Five

Smooth the "raw" estimates of the gust spectrum by applying the operations indicated by equation (12).

Step Six

Post darken the smoothed PSD estimates by applying the operation indicated by equation (18).

The ratio of the spectral estimates obtained in this manner to the true gust spectrum is plotted on the left side of figure 71. It can be seen that spectral averaging produces practically no distortion of the non-aliased spectrum except in the very low frequency region which again can be attributed to the prewhitening operation. The ratio of the spectral estimates with aliasing (as shown in figure 70) to the spectral estimates without aliasing is plotted on the right hand side of figure 71.

Effect of Spectral Averaging on Transfer Functions

The transfer functions obtained from the ratio of the spectral averaged PSD (without aliasing), figure 68, to the spectral averaged Dryden gust PSD (with aliasing) are plotted in figure 72 for comparison with the measured data. These computed transfer functions are analogous to the measured H_s transfer functions computed by equation (19). The correlation between computed and measured data is degraded in the frequency range below 0.5 cps. Above 0.5 cps the correlation is somewhat improved due to the reduction in the amplitude of the peaks and the overall reduction in transfer function magnitudes across the entire frequency range.

The ratio of the cross spectra after spectral averaging (without aliasing) to the Dryden gust spectrum after spectral averaging (with aliasing) are plotted in figure 73 for comparison with the measured data. These computed transfer functions are analogous to the measured H_c transfer functions computed by equation (20). This process produces significant improvements in the comparison between the computed and measured data by

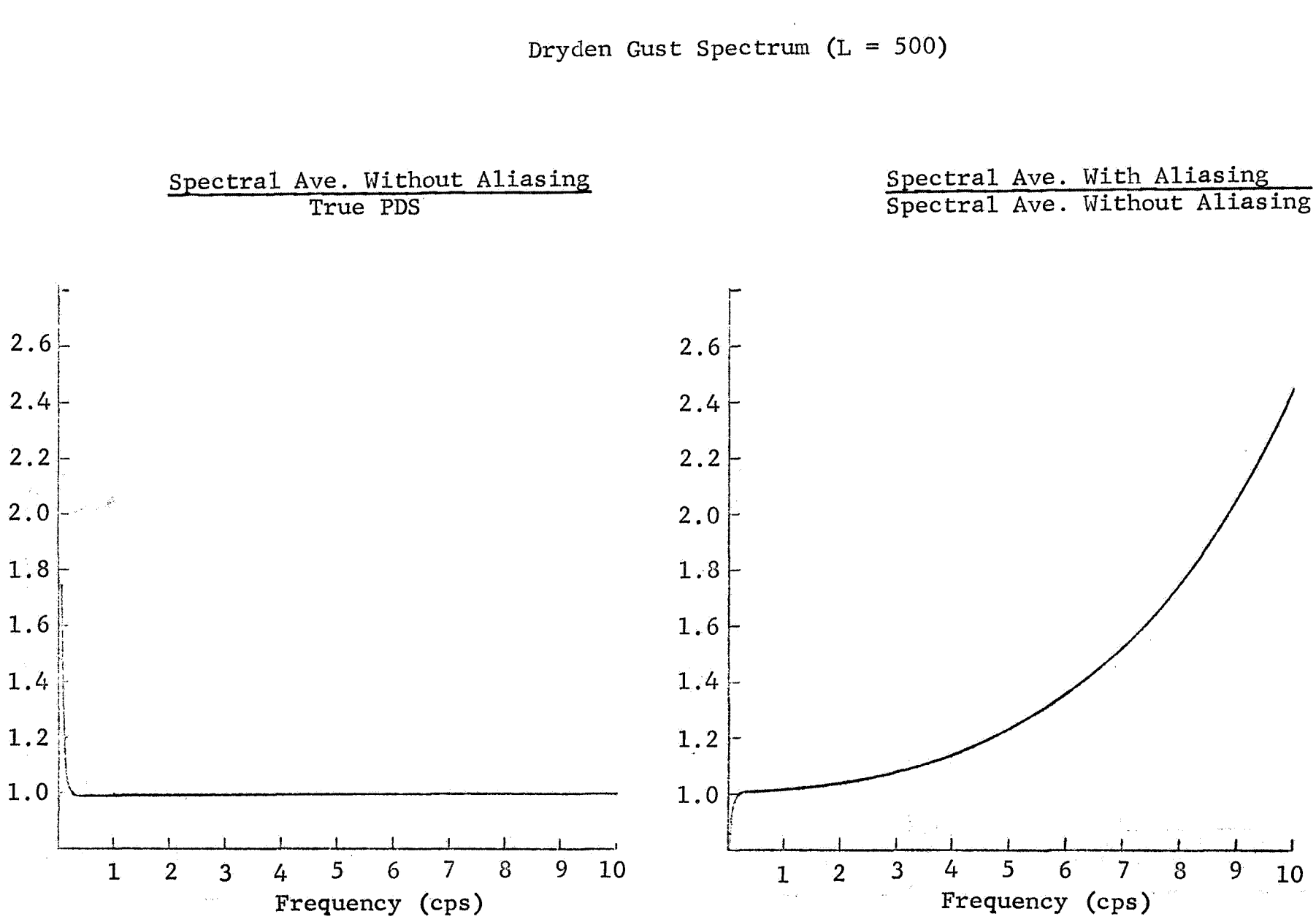

Figure 71 The Effect of Spectral Averaging on Non-Aliased Dryden Spectrum

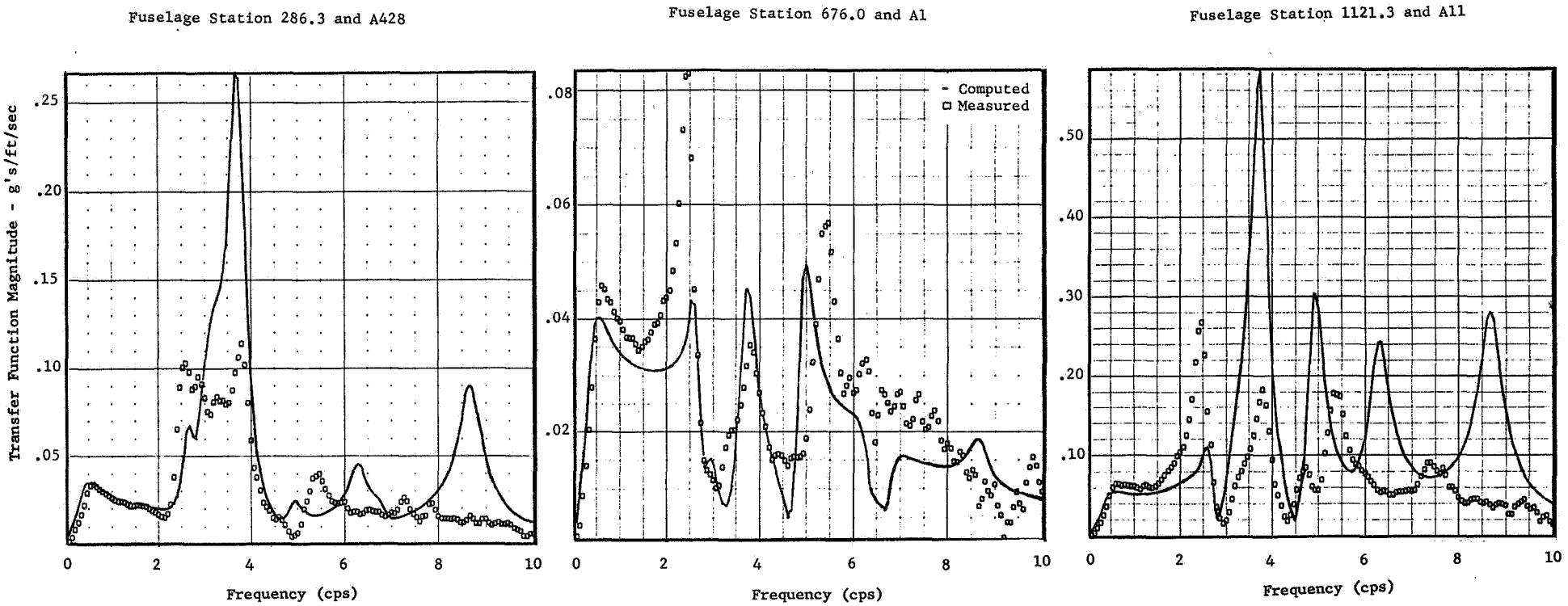

Analysis Parameters

ρ = .002241 slugs/ft^3, Mach = 0.80, V = 921 ft/sec, SAS ON, N = 10, C.G. = 26.8% MAC

Figure 72 Comparison of Computed H_s and Measured Transfer Functions, Run 131-3, Spectral Averaging

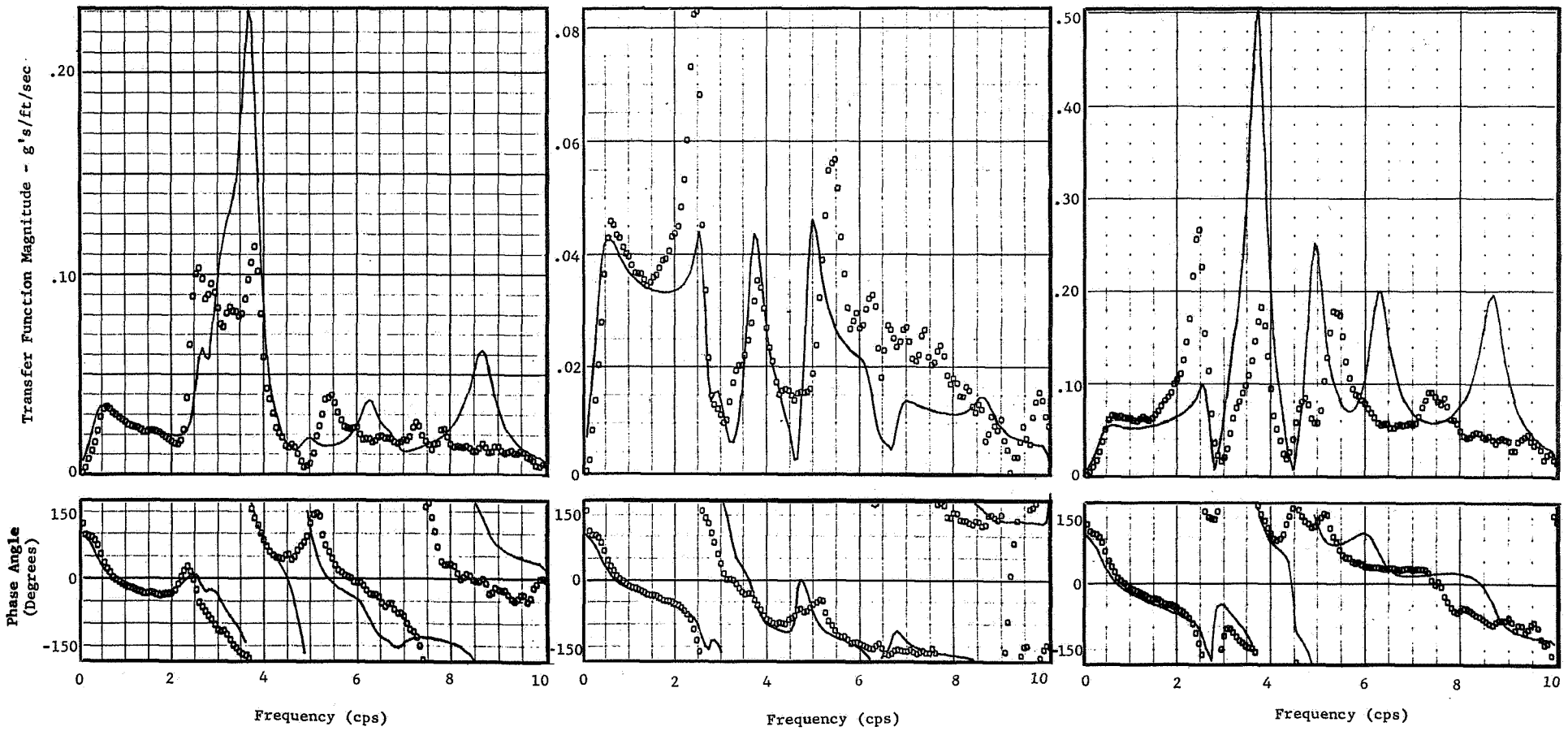

Figure 73 Comparison of Computed H_c and Measured Transfer Functions, Run 131-3, Spectral Averaging

rounding-off the peaks and filling-in the valleys of the computed transfer function magnitudes, and by an overall reduction of the magnitudes with increasing frequency. However, there is no justification for assuming that the measured gust spectrum was fully aliased and the measured response spectra and cross spectra were completely non-aliased. As mentioned earlier the measured gust velocity and response records were filtered by the same low pass filter in an attempt to minimize fold-back. Therefore the transfer function comparisons presented in figures 72 and 73 represents an extreme effect producted by spectral averaging.

The transfer functions obtained from the ratio of the spectral averaged response PSD (without aliasing), figure 68, to the spectral averaged Dryden gust PSD (without aliasing) are plotted in figure 74 for comparison with the measured data. The correlation between computed and measured data is degraded in the frequency range below 0.5 cps. Above 0.5 cps the correlation is somewhat improved due to the reduction in the amplitude of the peaks. The overall reduction in the magnitude seen in figure 72 does not appear in figure 74 because the gust spectrum without aliasing is lower in the high frequency range than the aliased gust spectrum (figure 71).

The ratio of the cross spectra after spectral averaging (without aliasing) to the Dryden gust spectrum after spectral averaging (without aliasing) are plotted in figure 75. For comparison with the measured data. This process produces some improvements in the comparison between the computed and measured data by rounding-off the peaks and filling-in the valleys of the computed transfer function magnitudes.

Effect of Spectral Averaging on the Coherency Function

The effect of spectral averaging on the coherency function can be observed by dividing the computed H_c transfer function magnitude by the computed H_s transfer function magnitude and squaring the ratio. First consider the case in which the response PSD and cross spectrum are considered to be non-aliased and the gust spectrum is considered to be completely aliased. The H_s and H_c transfer functions for this case are plotted in figures 72 and 73. The coherency functions computed with these transfer functions are plotted in figure 76 for comparison with the measured coherency function. It should be noted at this point that the

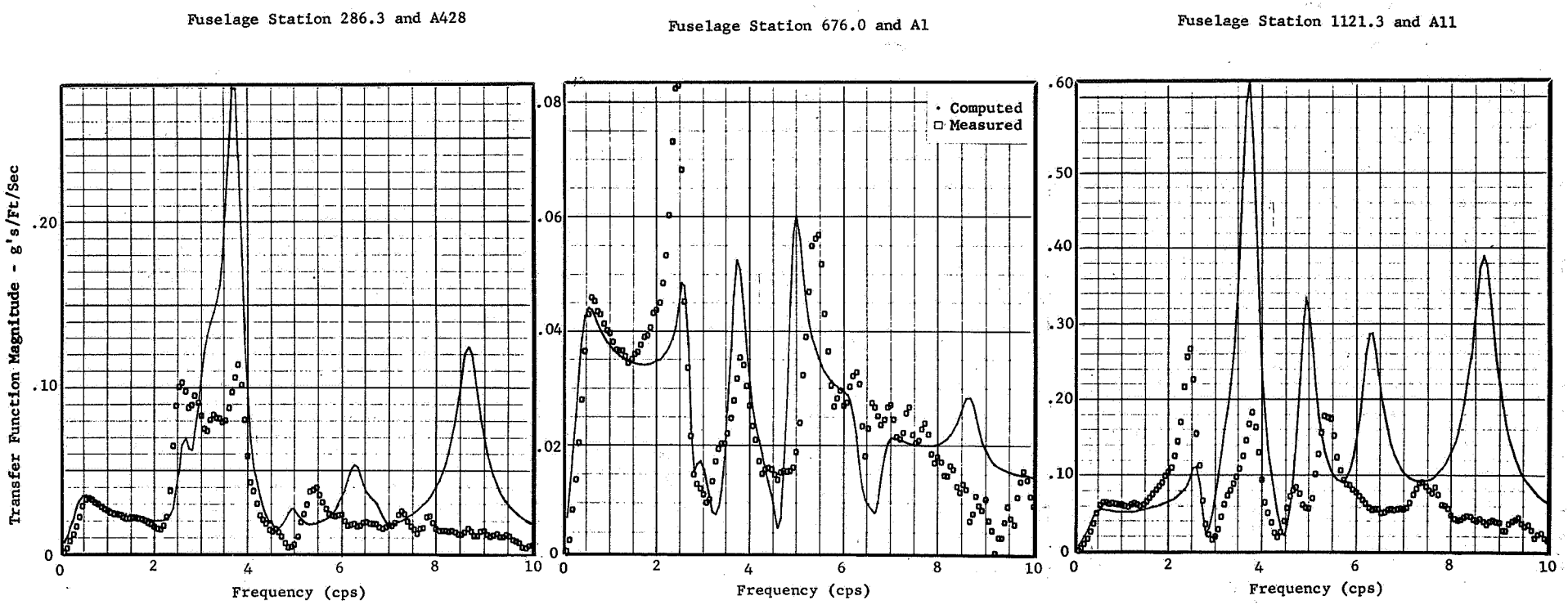

Analysis Parameters

ρ = .002241 slugs/ft^3, Mach = 0.80, V = 921 ft/sec, SAS ON, N = 10, C.G. = 26.8% MAC

Figure 74 Comparison of Computed H_s and Measured Transfer Functions, Run 131-3, Spectral Averaging Without Aliasing

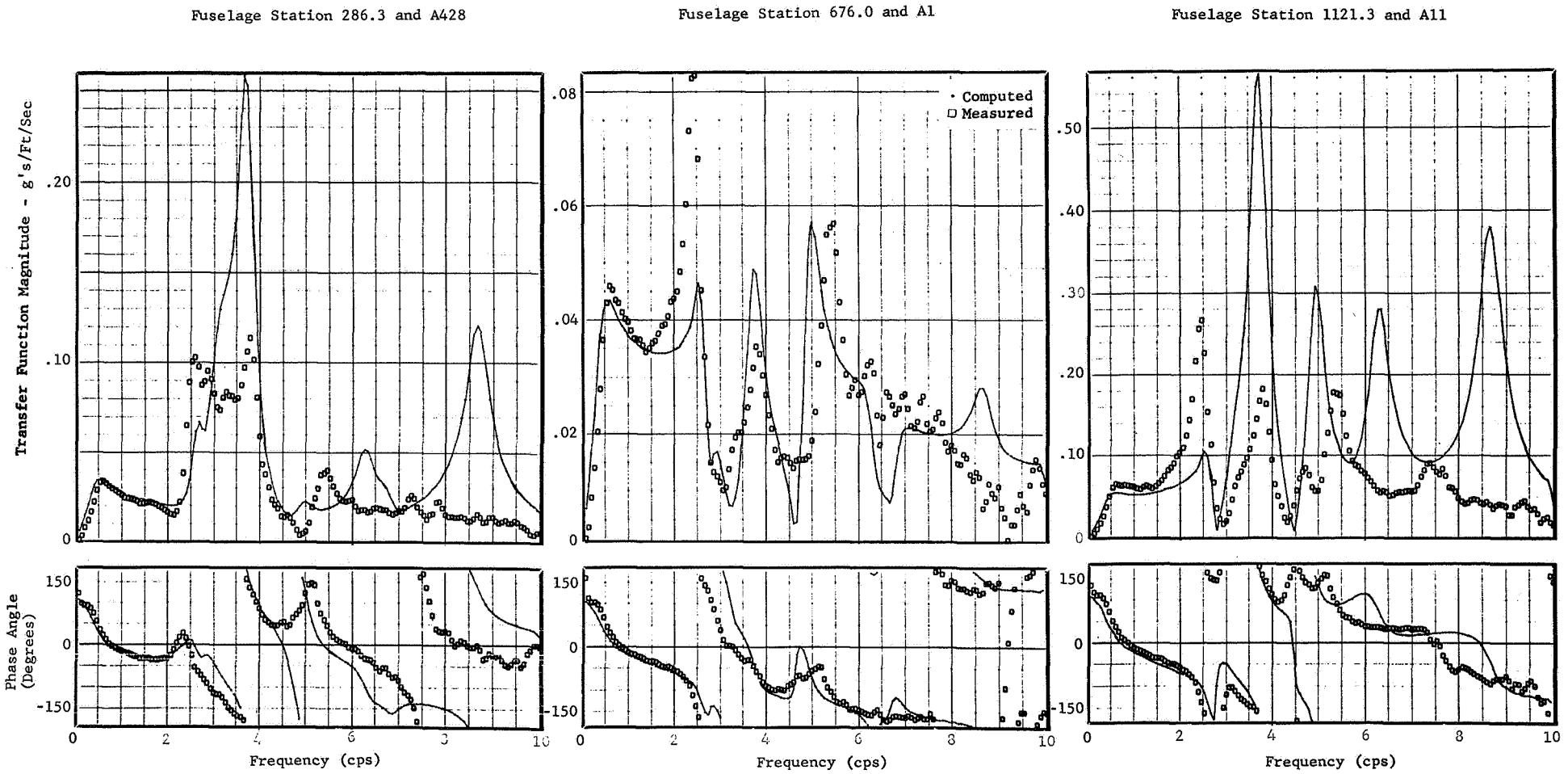

Analysis Parameters

ρ = .002241 slugs/ft^3, Mach = 0.80, V = 921 ft/sec, SAS ON, N = 10, C.G. = 26.8% MAC

Figure 75 Comparison of Computed H_c and Measured Transfer Functions, Run 131-3, Spectral Averaging Without Aliasing

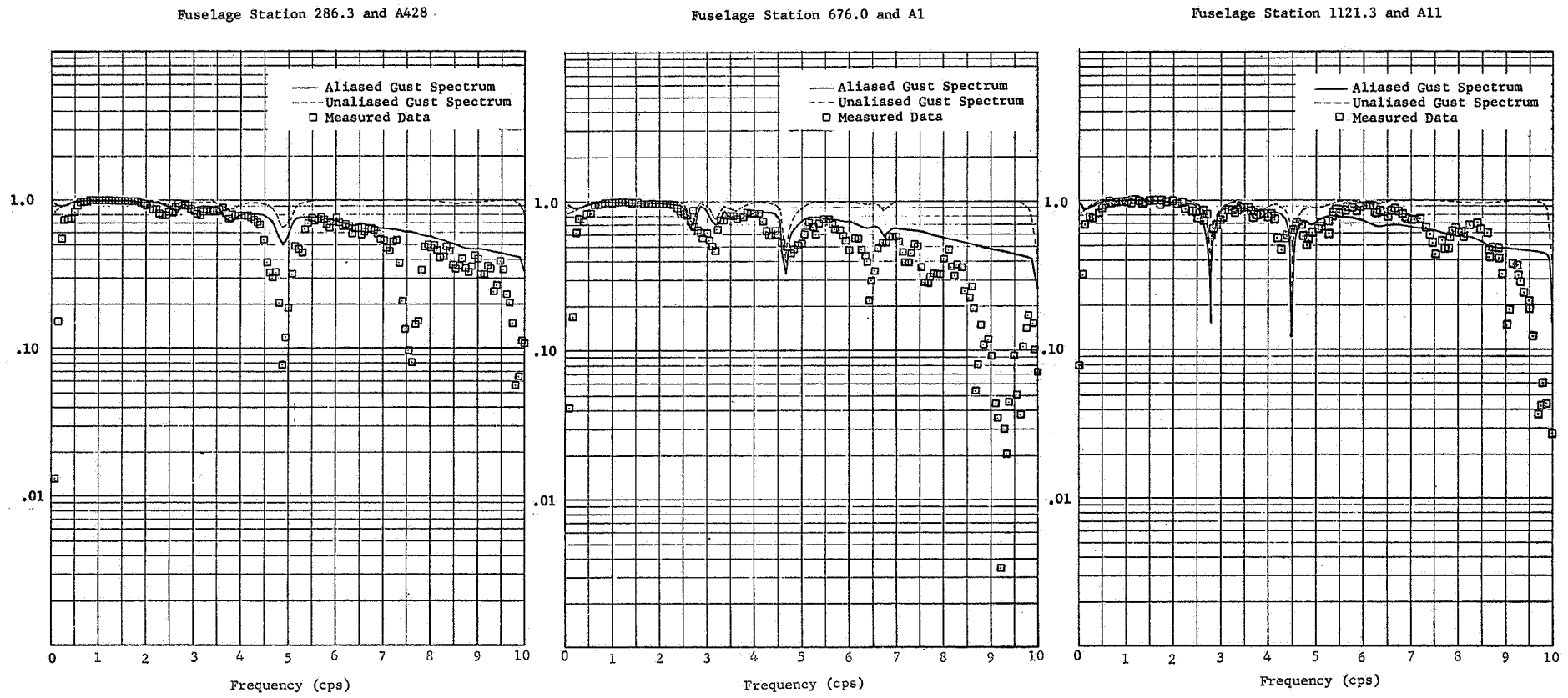

Analysis Parameters

ρ = .002241 Slugs/Ft^3, Mach = 0.80, V = 921 Ft/Sec, SAS On, N = 10, C.G. = 26.8% MAC

Figure 76 Comparison of Computed and Measured Coherency Functions, Run 131-3

computed and measured coherency functions should agree exactly only if,

(1) the measured gust PSD is closely approximated by the Dryden PSD with L = 500,

(2) the computed transfer function is the true transfer function,

(3) there are no other sources of error other than spectral averaging,

(4) the measured gust spectrum was fully aliased (no frequency components above the Nyquist frequency were removed before passing the measured data through the analog to digital converter), and

(5) the measured response spectrum and cross spectrum contained no aliasing or foldback.

Although none of these conditions are realized the similarities between the computed and measured coherency functions are interesting to observe. The coherency function computed in this manner can be interpretted as an extreme effect or a limiting case on the extent to which the coherency function can be reduced by spectral averaging (minimum foldback in the response spectrum and cross spectrum and maximum foldback in the gust spectrum).

Next, consider the case in which the gust spectrum as well as the response spectrum and the cross spectrum is considered to be completely non-aliased. The H_s and H_c transfer functions for this case are plotted in figures 74 and 75. The coherency functions computed with these transfer functions are plotted in figure 76 for comparison with the measured coherency function. The computed coherency function obtained in this manner should agree with the measured coherency function only if condition (1), (2), (3) and (5) of the previous paragraph are met and condition (4) is replaced by the statement that the measured gust spectrum contained no aliasing or foldback. The coherency function computed in this manner represents another limiting case (minimum foldback in the response spectrum, cross spectrum and gust spectrum). This operation shows that without aliasing, spectral averaging does not reduce the coherency function significantly below the unity

level except over the frequencies in the vicinity of valleys in the transfer function magnitude. The realistic effect of spectral averaging on the coherency function is somewhere between the two extremes which have been examined.

Spectral Averaging Effects on $\bar{A}$ and N_O

The computed transfer functions distorted by spectral averaging were combined with the true Dryden gust velocity PSD to obtain $\bar{A}$ and N_O data. These data are listed in table 29 for comparison with similar data using the original (no spectral averaging) transfer functions and for comparison with the measured data.

The upper part of the table shows the results which are obtained when the response spectrum and cross spectrum are assumed to be non-aliased and the gust spectrum is assumed to be completely aliased. Using the H_S transfer function the $\bar{A}$ data are reduced from 3 to 8 percent by spectral averaging and the N_O values were reduced from 6 to 9 percent. Using the H_C transfer function, the $\bar{A}$ values at the pilot station and aft fuselage station were reduced by 10 and 15 percent while the $\bar{A}$ at the c.g. was reduced only 2 percent. The N_O values were reduced by approximately 15 percent.

The lower part of the table shows the results which are obtained when the gust spectrum as well as the response spectrum and the cross spectrum is assumed to be non-aliased. In general, the $\bar{A}$ and N_O data obtained with either the H_S or H_C transfer functions are changed by less than 2 percent due to spectral averaging. It is concluded that the filter window effect in the spectral averaging produced insignificant effects on the measured $\bar{A}$ and N_O. However, the effect of foldback in the spectral averaging could have produced significant effects.

Table 29 $\bar{A}$ and N_o Data by Spectral Averaging

F.S. (in)	Accel	Computed (2000 Ft. Alt.)						Measured	
		No Spectral Ave.		Non-Aliased Response and Aliased Gust Spectrum					
				Spectral Ave. H_s		Spectral Ave. H_c			
		$\bar{A}$	N_o	$\bar{A}$	N_o	$\bar{A}$	N_o	$\bar{A}$	N_o
286.3	A428	.03855	3.1525	.03735	2.9457	.03480	2.7761	.02814	2.391
676.0	A1	.03071	1.5443	.02833	1.3954	.03011	1.3000	.03019	1.638
1121.3	A11	.07690	4.0427	.07242	3.7086	.06563	3.4508	.05888	2.454

F.S. (in)	Accel	Computed (2000 Ft. Alt.)						Measured	
		No Spectral Ave.		Non-Aliased Response and Non-Aliased Gust Spectrum					
				Spectral Ave. H_s		Spectral Ave. H_c			
		$\bar{A}$	N_o	$\bar{A}$	N_o	$\bar{A}$	N_o	$\bar{A}$	N_o
286.3	A428	.03855	3.1525	.03885	3.1260	.03745	3.1005	.02814	2.391
676.0	A1	.03071	1.5443	.03125	1.5141	.03064	1.5089	.03019	1.638
1121.3	A11	.07690	4.0427	.07720	4.0201	.07390	4.0287	.05888	2.454

VARIATIONS IN STRUCTURAL DAMPING AND NATURAL FREQUENCY

Previous variations in parameters had relatively small effect on raising the magnitude of the computed peak near 2.6 cps and lowering the peak near 3.7 cps for run 131-3. The lack of correlation between the computed and measured peaks at these frequencies is a major factor in the failure to get good agreement between computed and measured $\bar{A}$ and N_o data at stations 286.3 and 1121.3. During the variation in the number of DOF, it was noted that the addition of the fourth natural mode introduces the peak near 3.7 cps and simultaneously reduces the magnitude of the peak near 2.6 cps. Therefore, in order to obtain better correlation between computed and measured transfer functions the damping associated with the fourth natural mode was increased. For all previous analyses the structural damping was assumed to be .03 for each natural mode. To reduce the magnitude of the peak near 3.7 cps, the structural damping of the fourth natural mode was increased to .08. To increase the magnitude of the peak near 2.6 cps the structural damping of the first natural mode was decreased to .02. Simultaneously, the natural frequencies of modes 1, 4 and 5 were changed by small precentages to make the peak frequencies in the computed transfer functions more nearly match the measured peak frequencies. The ratio of the adjusted natural frequencies to the computed natural frequencies and the changes in structural damping are listed in table 30.

Table 30 Variations In Structural Damping and Natural Frequency, Run 131-3

Natural Mode	Structural Damping Coefficient	$\frac{\text{Adjusted Freq.}}{\text{Computed Freq.}}$
1	.02	.96
2	.03	1.00
3	.03	1.00
4	.08	1.02
5	.03	1.06
6	.03	1.00
7	.03	1.00
8	.03	1.00

In addition to the changes indicated in table 30, the c.g. was shifted forward to a position 23.8% of the MAC aft of the MAC leading edge. An air density for a 4600 feet altitude standard day which matches the density measured during run 131-3 was also employed. The computed transfer functions obtained with these changes to the basic condition are plotted in figure 77 for comparison with the measured transfer functions. The magnitude of the transfer function peaks compare much more favorable with the measured peaks below approximately 4 cps. The phase angle comparisons are not significantly changed. The ratio of the computed to the measured transfer functions are shown in figure 78. The correlation between computed and measured transfer functions at the c.g. accelerometer A1, is very good and is much improved at the pilot station, A428, and tail cone, A11. Large discrepancies exist in the high frequency range.

In an attempt to further improve the transfer function correlation, flexible modes 6, 7, and 8 were deleted and a 7 DOF analysis was conducted with the same frequency and damping changes described in the above paragraph. These transfer functions are plotted in figure 79 for comparison with the measured data. It can be seen that the peak magnitude near 5.5 cps compares much more favorably with the measured data as a result of deleting the last three natural modes. The ratios of the computed to measured transfer functions are plotted in figure 80. Considering all three stations and the entire frequency range, the ratios shown in figure 80 represent the best correlation that was obtained between computed and measured transfer functions for run 131-3.

$\bar{A}$ and N_o Data With Variations in Structural Damping and Natural Frequencies, Run 131-3

The transfer functions computed with variations in structural damping and natural frequencies as described in the preceding paragraphs were combined with the Dryden gust spectrum to obtain $\bar{A}$ and N_o data. These data are listed in table 31 for comparison with the measured data. The $\bar{A}$ obtained from the 10 DOF analysis compare very well with the measured data. The computed $\bar{A}$ at the pilot station exceeds the measured value by only 4 percent.

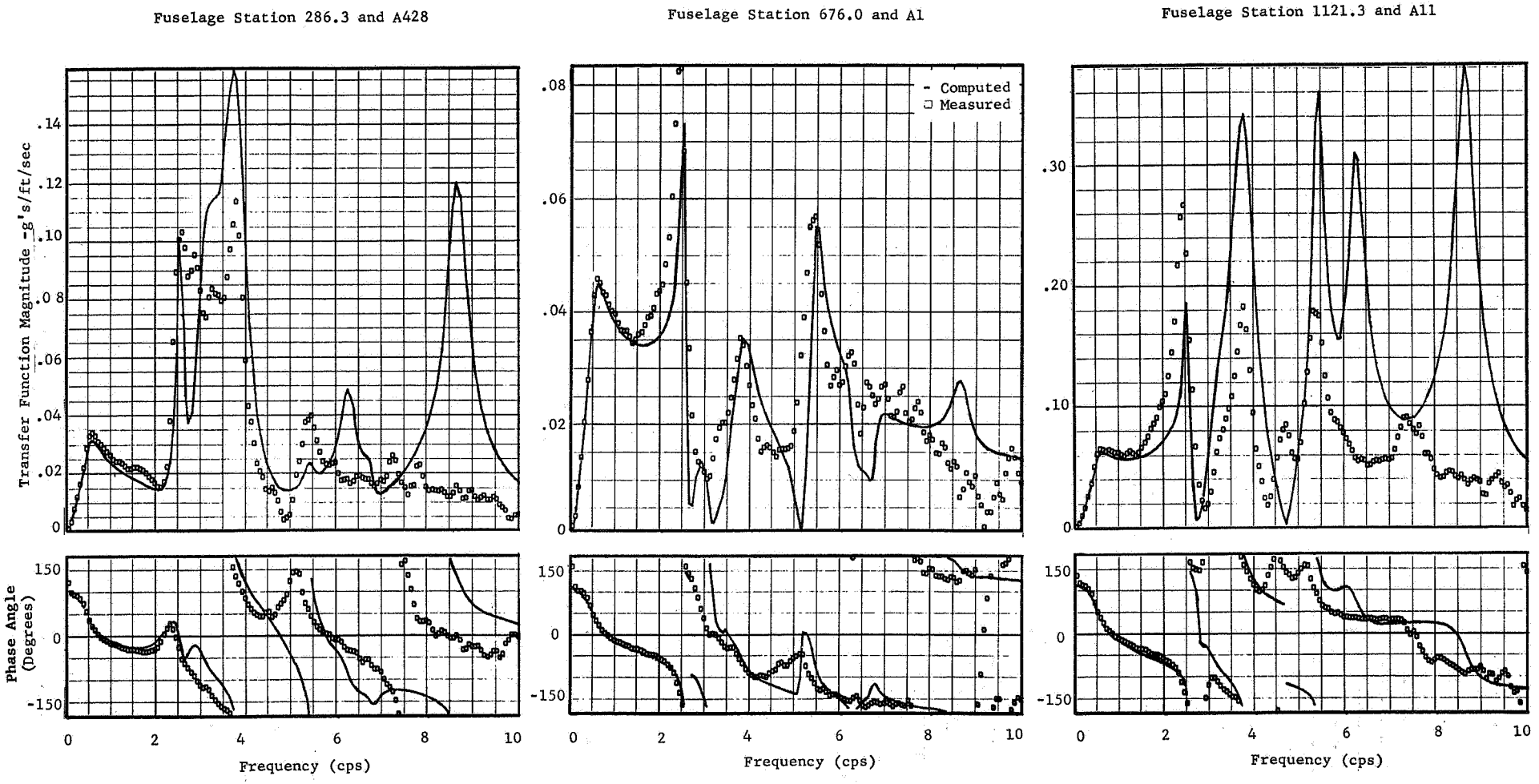

Analysis Parameters

ρ = .002073 slugs/ft^3, Mach = 0.80, V = 921 ft/sec, SAS ON, N = 10, C.G. = 23.8% MAC

Figure 77 Comparison of Computed and Measured Transfer Functions, Run 131-3, With Variations In Structural Damping and Natural Frequencies, N = 10

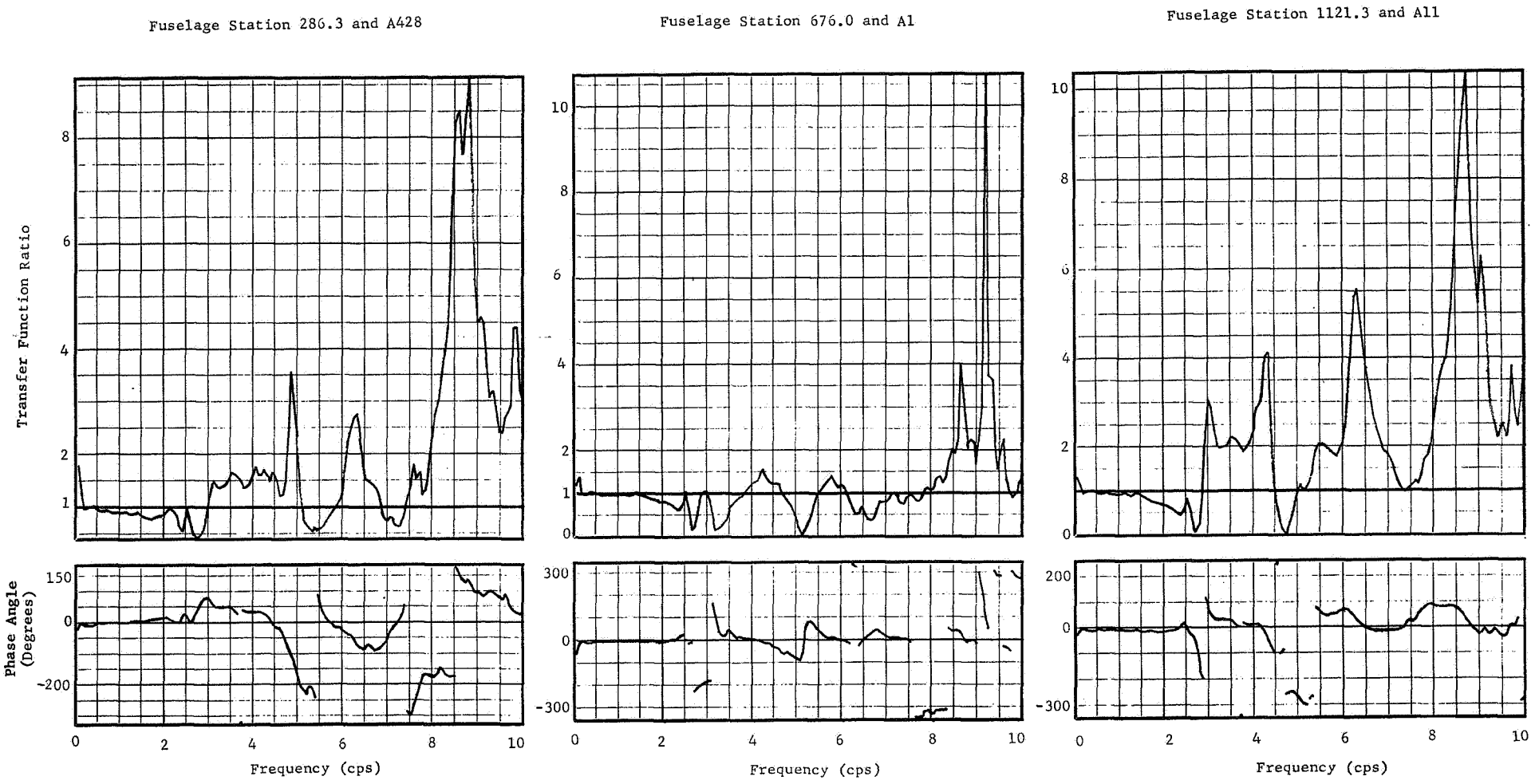

Analysis Parameters

ρ = .002073 slugs/ft^3, Mach = 0.80, V = 921 ft/sec, SAS ON, N = 10, C.G. = 23.8% MAC

Figure 78 Ratio of Computed to Measured Transfer Functions, Run 131-3, With Variations in Structural Damping and Natural Frequencies, N = 10

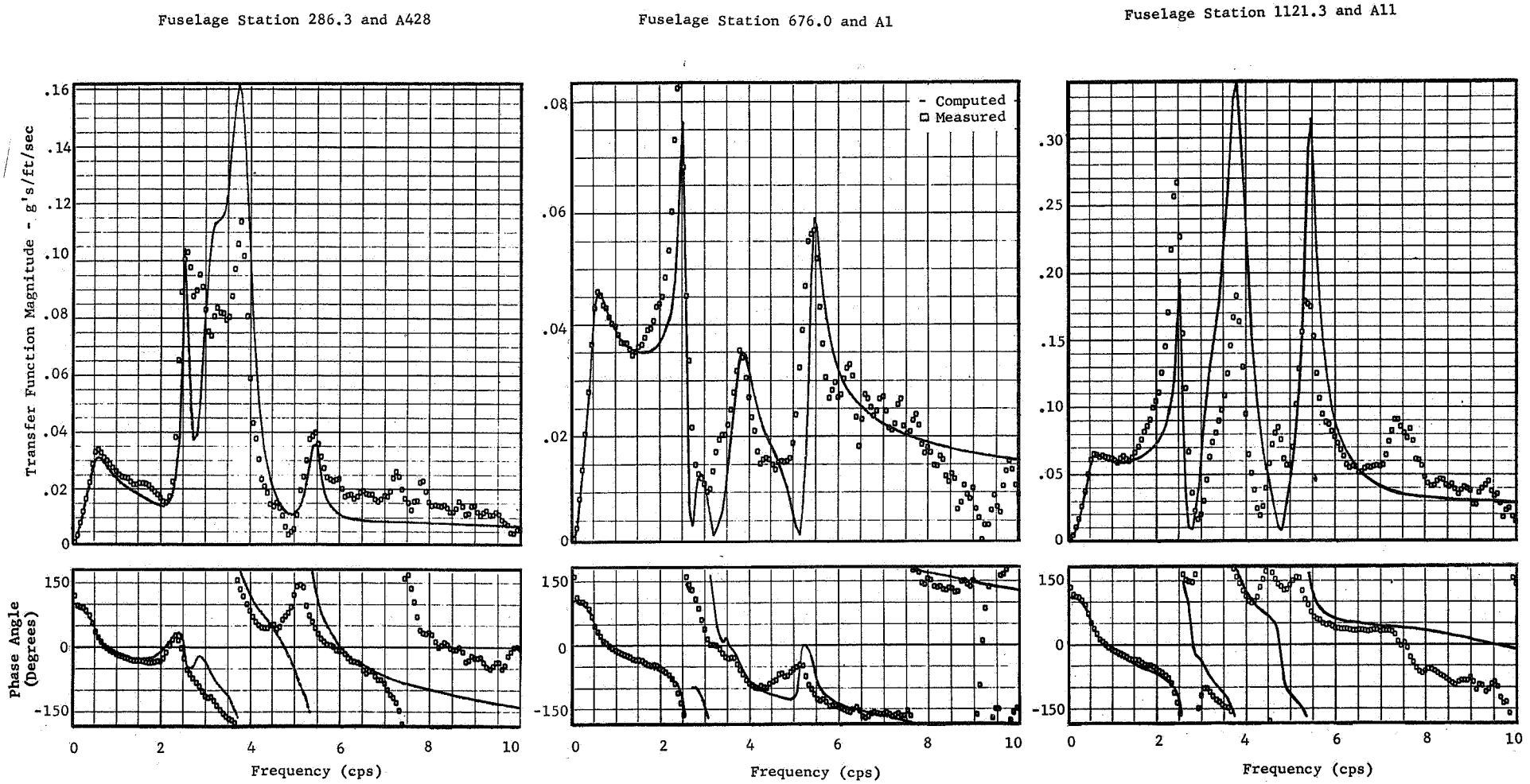

Analysis Parameters

ρ = .002073 slugs/ft^3, Mach = 0.80, V = 921 ft/sec, SAS ON, N = 7, C.G. = 23.8% MAC

Figure 79 Comparison of Computed and Measured Transfer Functions, Run 131-3, With Variations in Structural Damping and Natural Frequencies, N=7

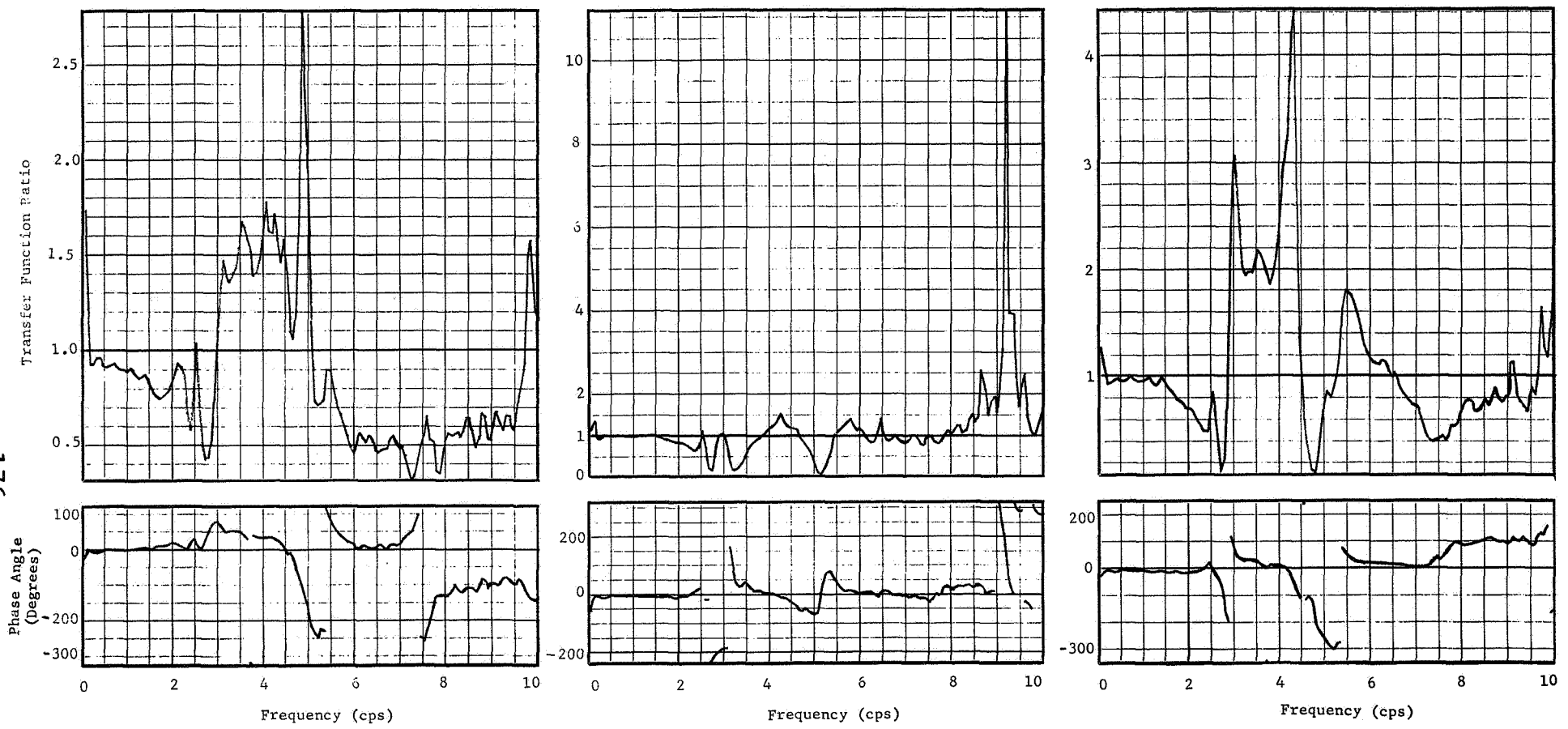

Analysis Parameters

ρ = .002073 slugs/ft^3, Mach = 0.80, V = 921 ft/sec, SAS ON, N = 7, C.G. = 23.8% MAC

Figure 80 Ratio of Computed to Measured Transfer Functions, Run 131-3, With Variations in Structural Damping and Natural Frequencies, N = 7

Table 31 $\bar{A}$ and N_o Data With Variations In Structural Damping and Natural Frequencies

F.S. (in)	Accel.	Computed		Measured	
		$\bar{A}$	N_o	$\bar{A}$	N_o
N = 10					
286.3	A428	.02939	3.1571	.02814	2.391
676.0	A1	.02869	1.5546	.03019	1.638
1121.3	A11	.06536	4.1086	.05888	2.454
N = 7					
286.3	A428	.02871	2.7233	.02814	2.391
676.0	A1	.02903	1.5856	.03019	1.638
1121.3	A11	.06008	3.0051	.05888	2.454

The computed $\bar{A}$ at the nominal c.g. is 5 percent less than measured and the $\bar{A}$ at fuselage tail cone is about 12 percent greater than measured. The computed values of N_o still exceed the measured values at the pilot station and fuselage tail cone by large percentages.

The $\bar{A}$ values for the 7 DOF analyses compare even better with the measured data. However, the big improvement obtained by deleting the highest three natural modes occurs in the N_o comparison. The computed values of N_o exceed the measured values at the pilot station and fuselage tail cone by only 15 and 23 percent, respectively.

CONCLUDING REMARKS

Computed transfer functions compare much better with measured transfer functions at the c.g. than they do at the pilot station and the tail cone. The peaks in the magnitude of the computed transfer function, which are associated with the flexible modes in general, far exceed the measured peaks at the pilot station and tail cone. The computed $\bar{A}$ and N_o values compare very well with measured data at the c.g. but exceed the measured data at the pilot station and tail cone.

Small variations in air density, Mach number (with compatible velocity), c.g. location, and SAS gains do not produce significantly improvement in the transfer functions for frequencies above the short period mode frequency. Only small improvements in $\bar{A}$ and N_o at the pilot station and tail cone are obtainable. The $\bar{A}$ and N_o values at the c.g. are least effected by any of the parameter variations.

The addition of the higher frequency modes into the analysis produce large differences between computed and measured transfer function magnitudes in the higher portion of the frequency range. The degree of correlation between computed and measured natural frequencies and mode shapes decreases with the order of the modes and undoubtly increases the difficulty of predicting the transfer functions at higher frequencies. The higher frequencies make much larger contributions to N_o than to $\bar{A}$.

Transfer functions computed for fuselage stations near the c.g. are relatively insensitive to small variations in fuselage station. However, small variations in fuselage station make large differences in transfer functions at the pilot station and tail cone. Plots of fuselage deflection in each normal mode show small variations near the c.g. and large variations as the fuselage extremeties are approached.

The inclusion of an aeroelastic mode as a degree of freedom in the equations of motion improves the transfer function comparison in the low frequency range but degrades the comparison near the frequency of the first natural mode.

Transfer functions computed using quasi-steady aerodynamics compare favorable with those computed using unsteady aerodynamics. The second quasi-steady method is the better of the two employed herein.

The application of two-dimensional turbulence reduces the magnitude of the transfer functions as compared with transfer functions computed for one-dimensional turbulence. The effect is more pronounced at the high end of the frequency range and improves the comparison with the measured transfer functions. However, the improvement in the correlation between computed and measured transfer functions, $\bar{A}$ and N_o is very small for the B-58. The effect would be more pronounced on aircraft with smaller ratios of airspeed to wing span.

Spectral averaging consists of two interrelated effects, namely, the effect of the filter window and the effect of fold-back. The filter window reduces the magnitude of the peaks and increases the magnitude of the valleys in the computed transfer functions. If the response spectrum and the cross spectrum are assumed to be completely non-aliased and the gust spectrum is considered to be completely aliased, spectral averaging decreases the overall magnitude of the transfer function from an insignificant amount near zero frequency to a significant amount near the Nyquist frequency. When the gust spectrum as well as the response spectrum and cross spectrum is assumed to be non-aliased, there is no reduction in the transfer function magnitude other than that produced by the filter window. The low values of the coherency function which typically occur below the frequency of the

short period mode for all of the B-58 gust runs is partially attributable to spectral averaging. The low values of the coherency function over frequencies in the vicinity of valleys in the transfer function magnitude are also partially attributable to spectral averaging. When the response spectrum and cross spectrum are considered to be non-aliased and the gust spectrum is considered to be completely aliased, spectral averaging produces significant reductions in the $\bar{A}$ and N_o values. However, when the gust spectrum as well as the response spectrum and cross spectrum are assumed to be non-aliased, spectral averaging produces no significant change in the $\bar{A}$ and N_o values.

Good comparisons between computed and measured transfer functions for run 131-3 was obtained only after increasing the structural damping of the fourth mode from .03 to .08 and decreasing the structural damping of the first mode from .03 to .02. The correlation was further improved by deleting the highest three natural modes from the analysis. The measured structural damping varies from mode to mode and somewhat from airplane to airplane. The range in structural damping on the B-58 varies from approximately .02 to .05. Hence, the increase in structural damping of mode four to .08 is somewhat above a credible level. Therefore, the need for such a large increase in structural damping is probably due to the failure of the analysis to predict sufficient aerodynamic damping.

APPENDIX A

COMPARISON OF GROUND VIBRATION TEST MODES AND COMPUTED MODES

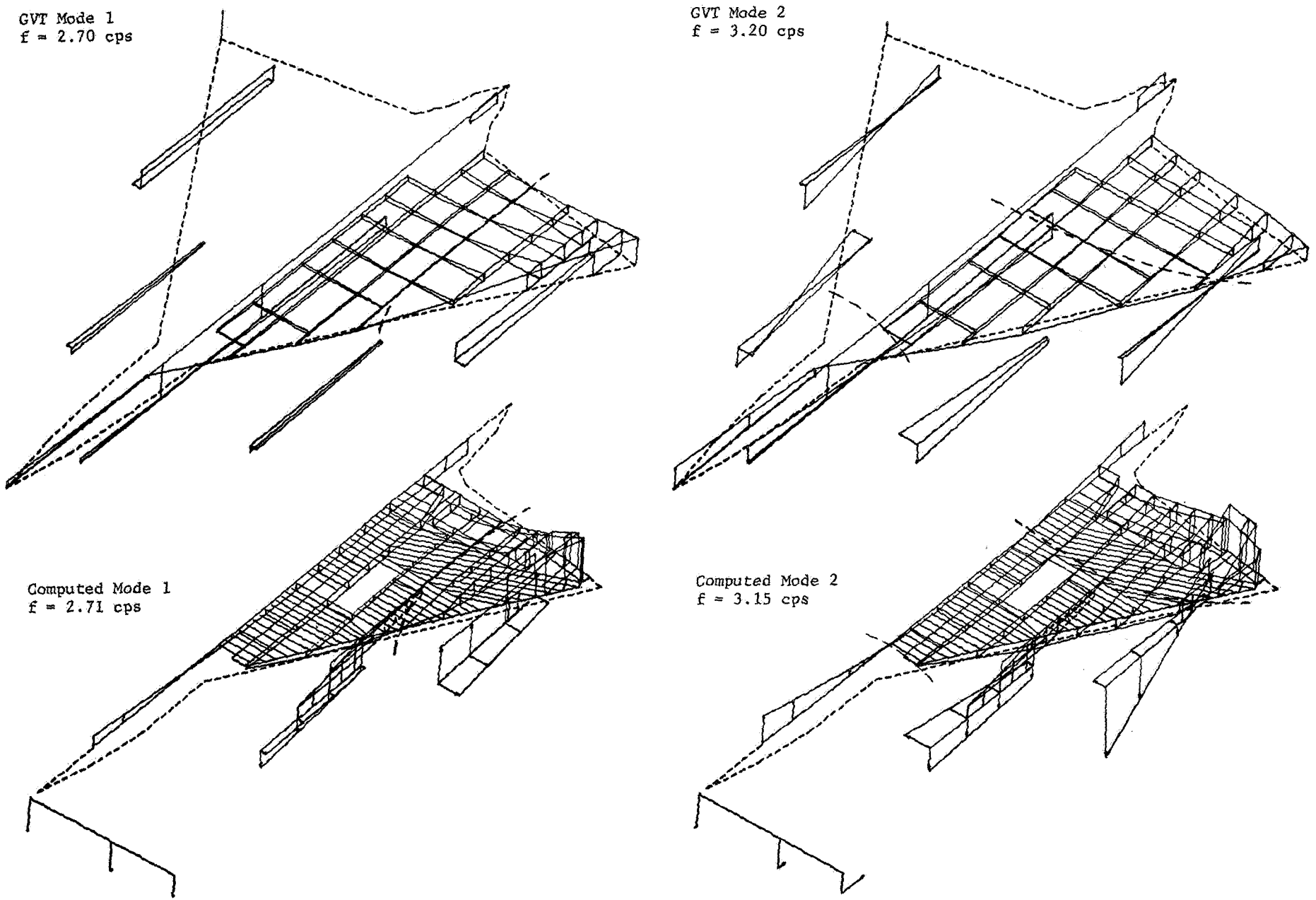

Figure A1 Comparison of Ground Vibration Test Modes and Computed Modes

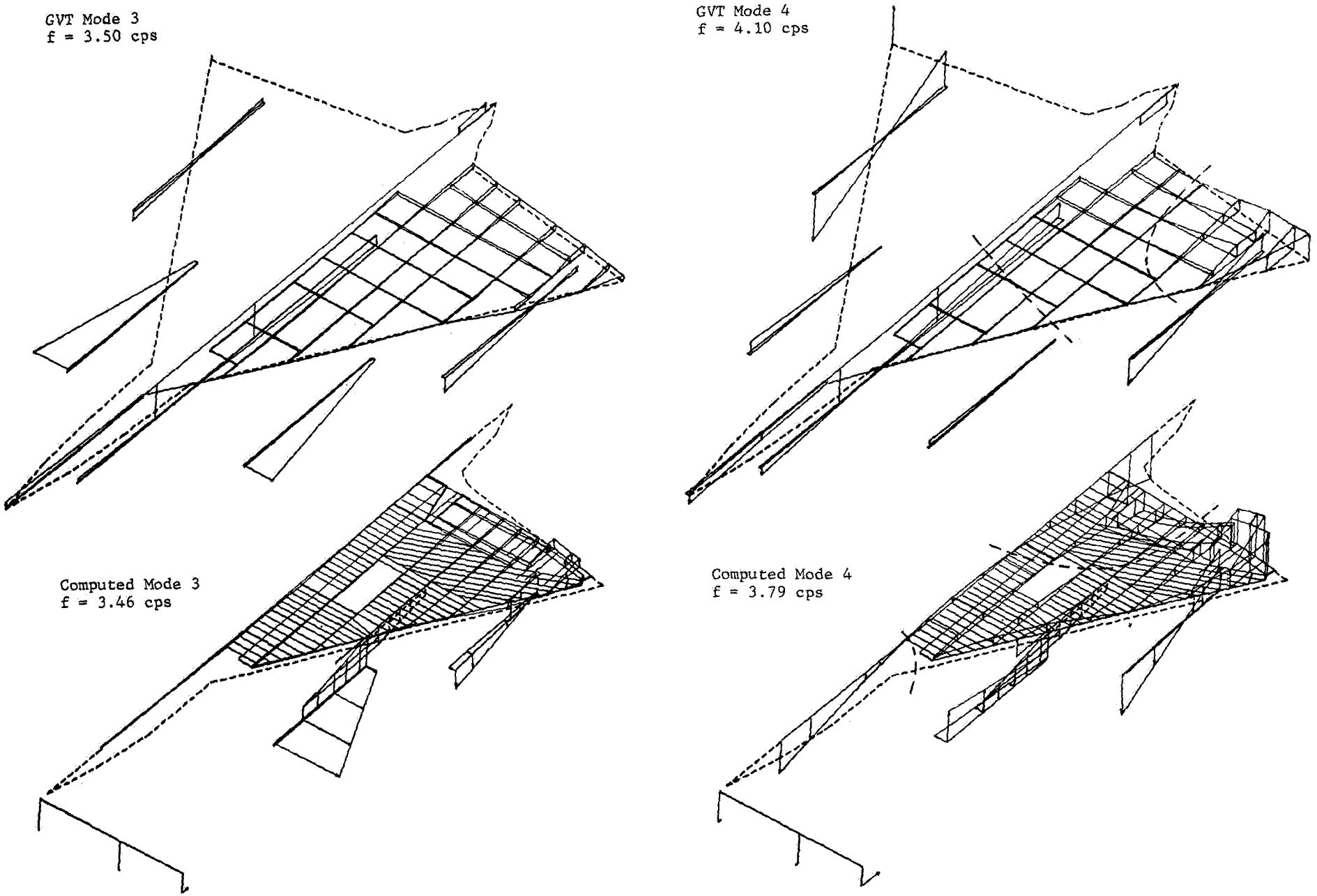

Figure A1 Continued Comparison of Ground Vibration Test Modes and Computed Modes

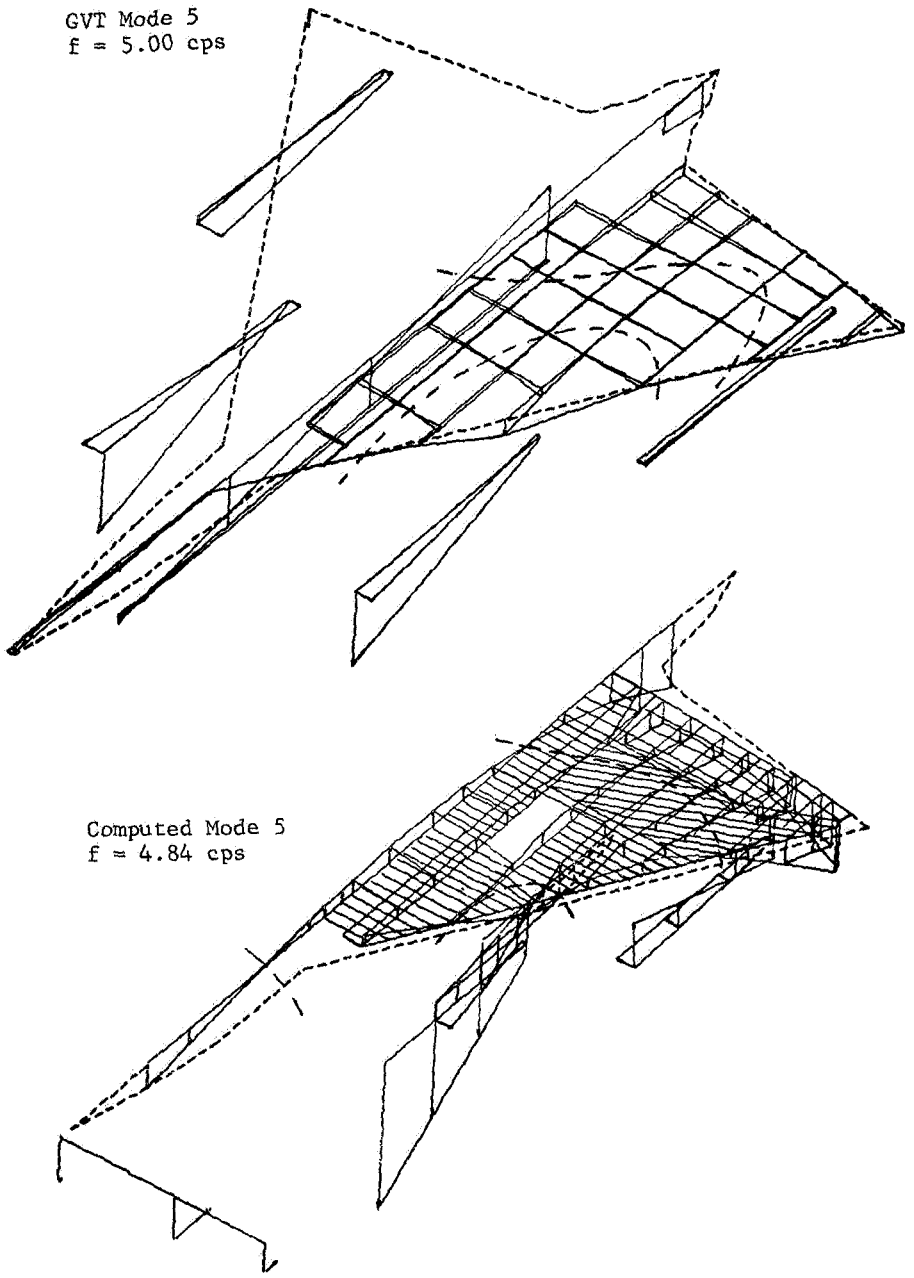

Figure A1 Continued Comparison of Ground Vibration Test Modes and Computed Modes

APPENDIX B

COMPUTED MODES FOR MATCHED FLIGHT CONDITIONS

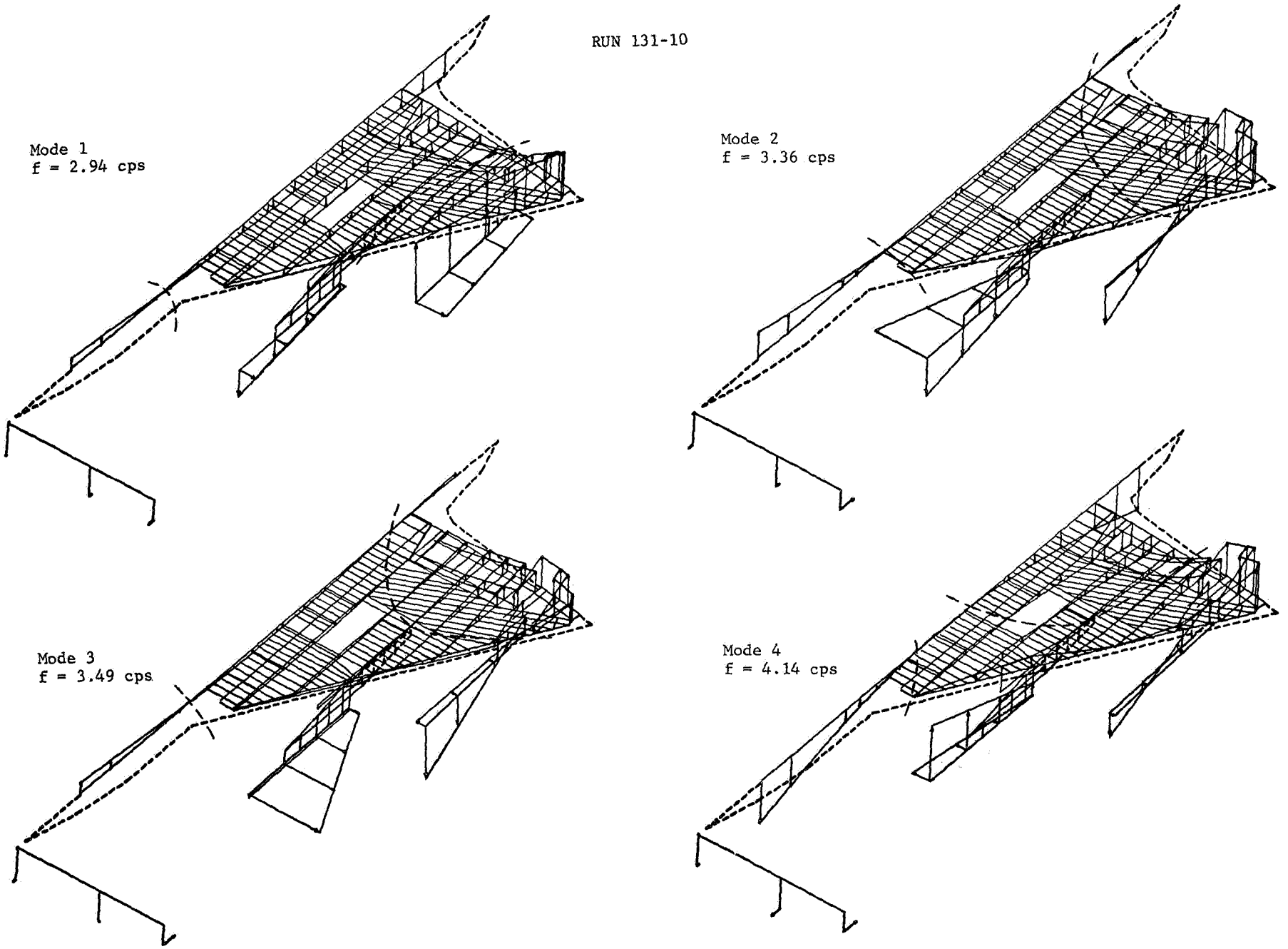

Figure B1 Computed Modes, Run 131-10

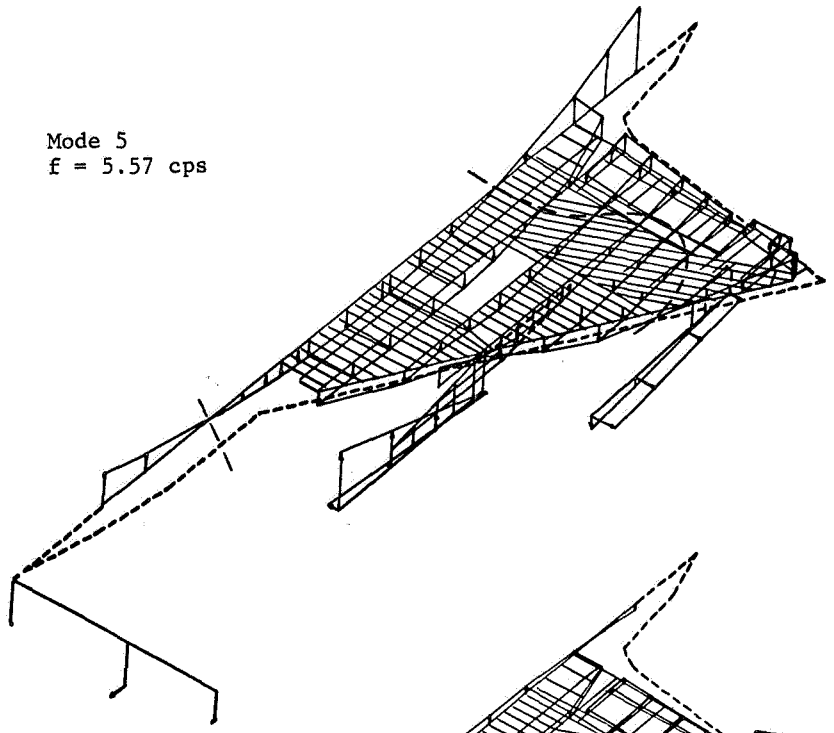

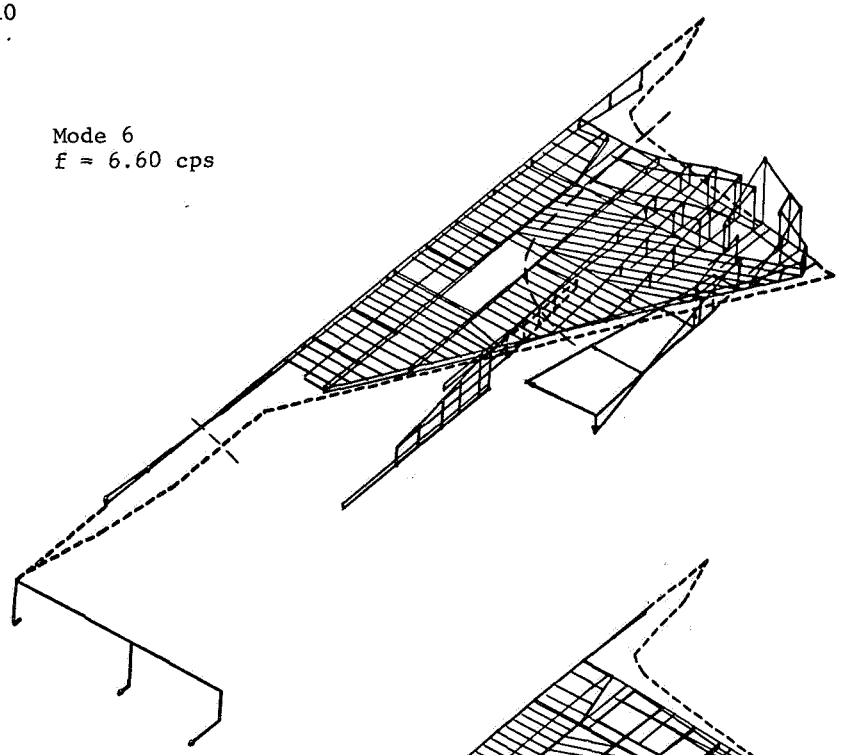

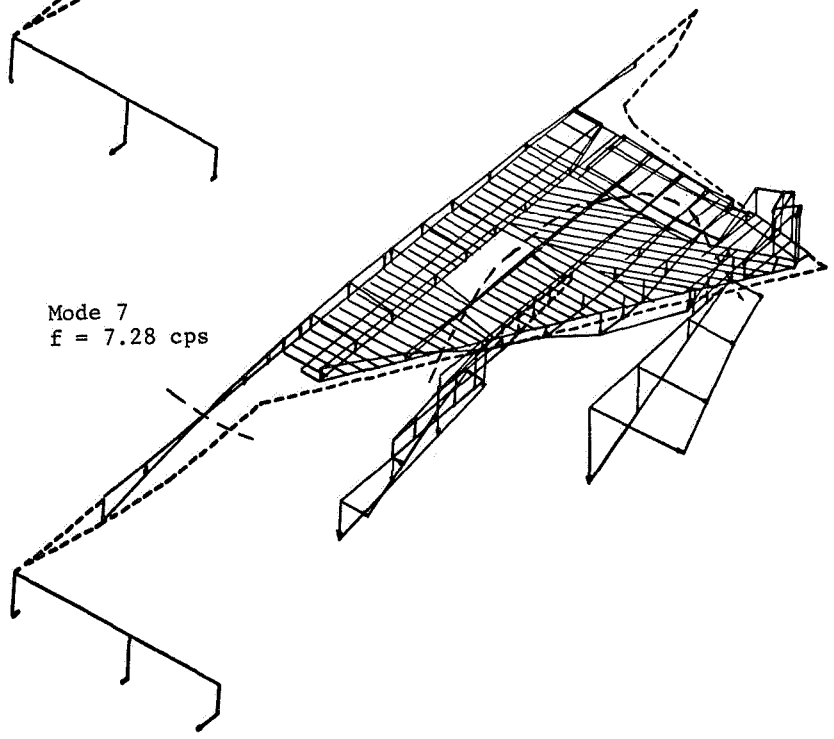

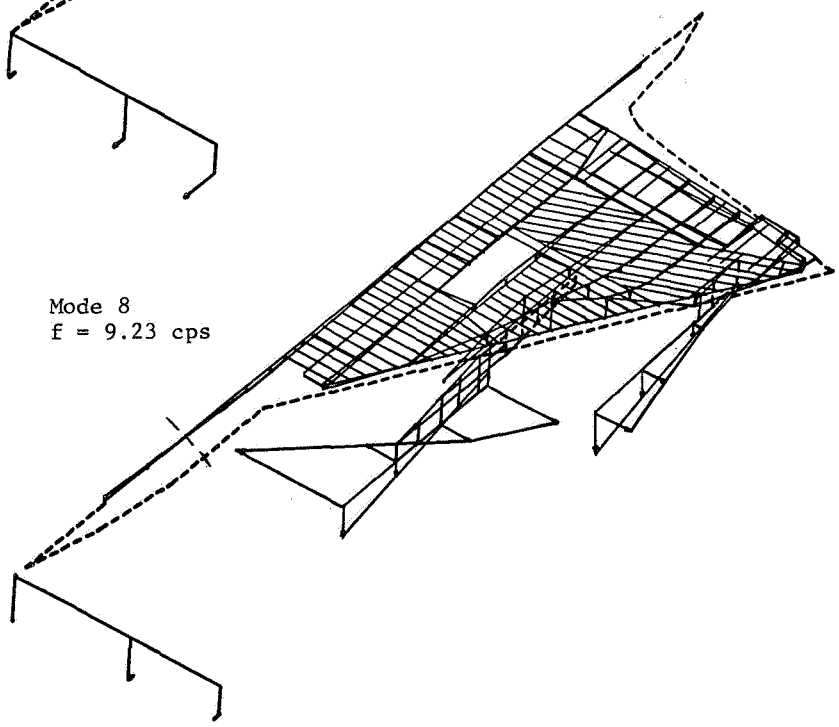

Figure B1 Continued Computed Modes, Run 131-10

RUN 134-7

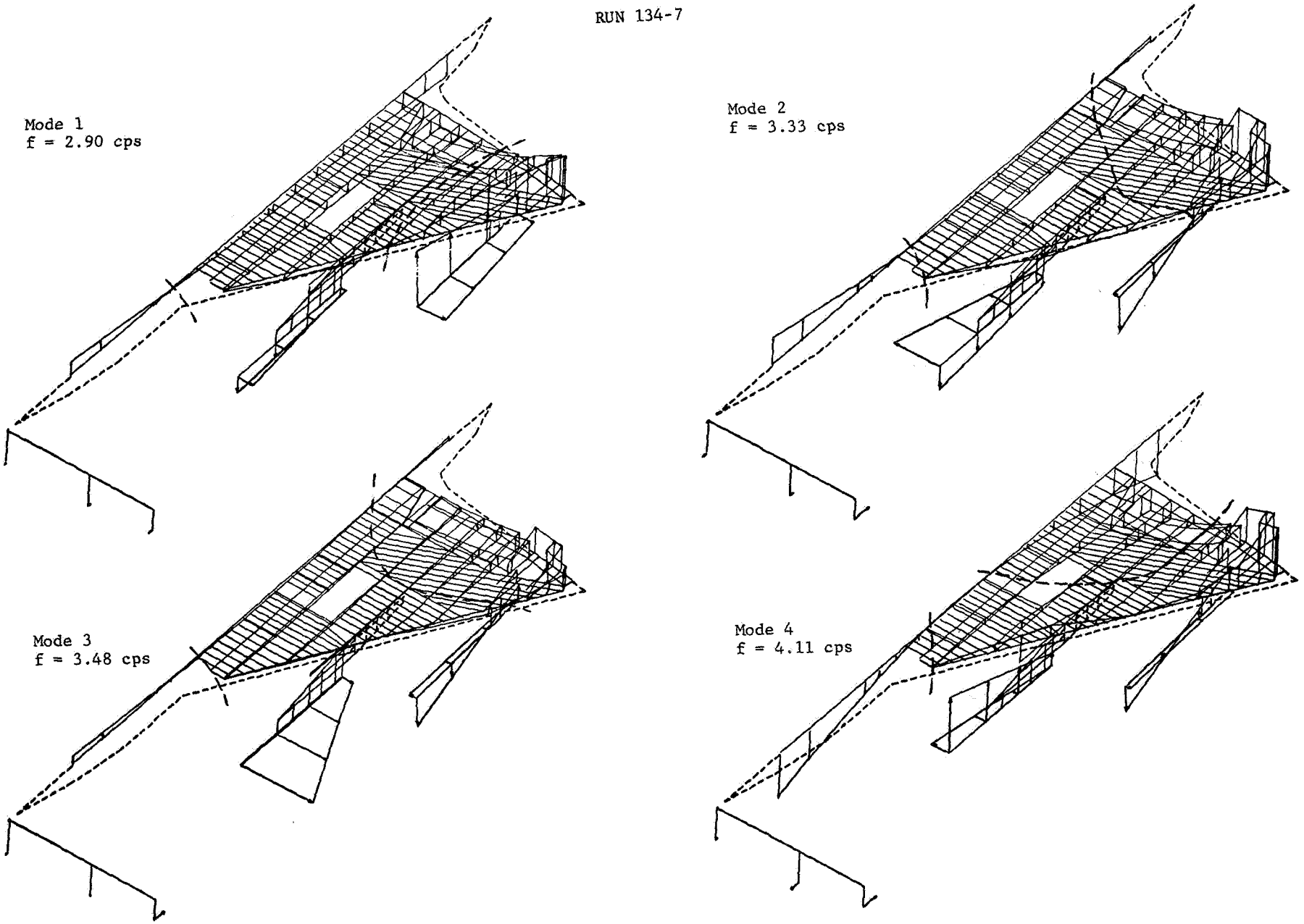

Figure B2 Computed Modes, Run 134-7

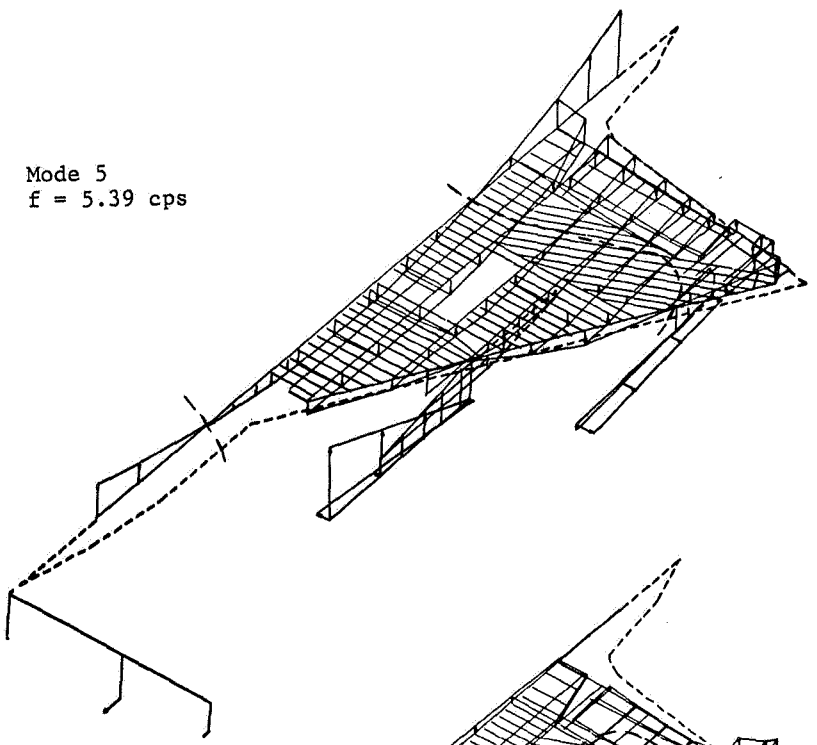

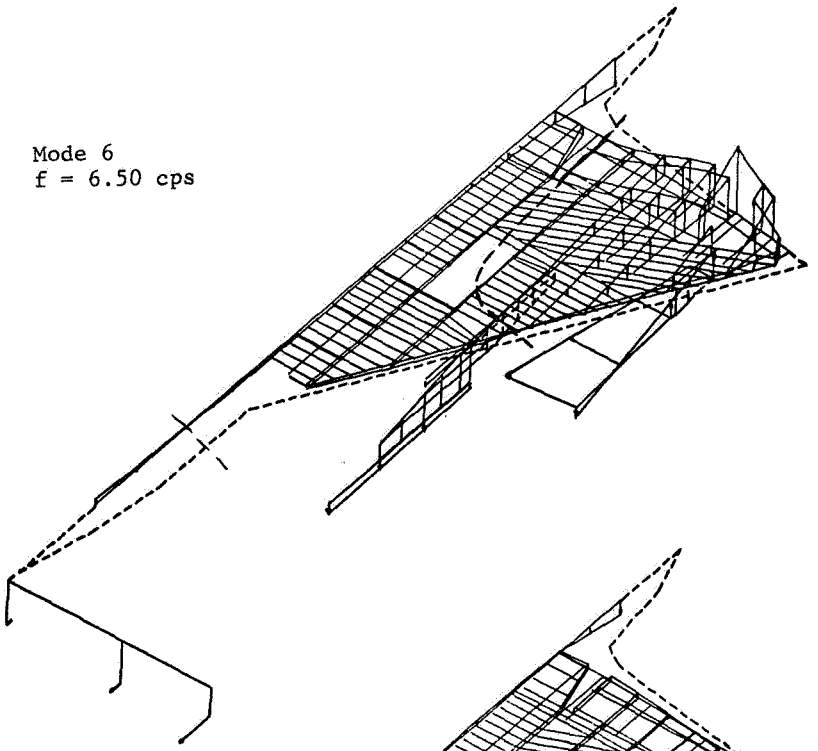

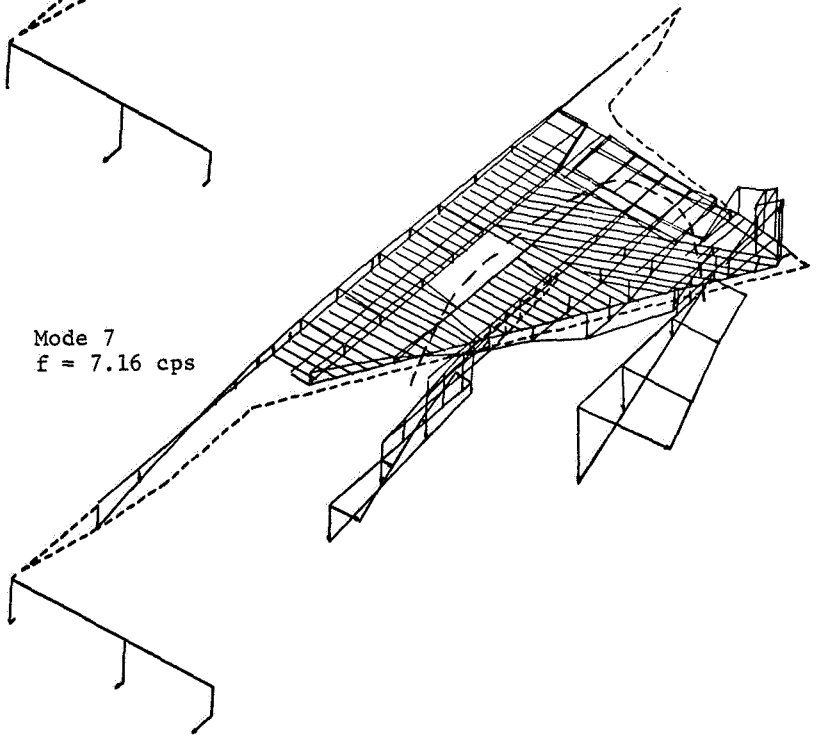

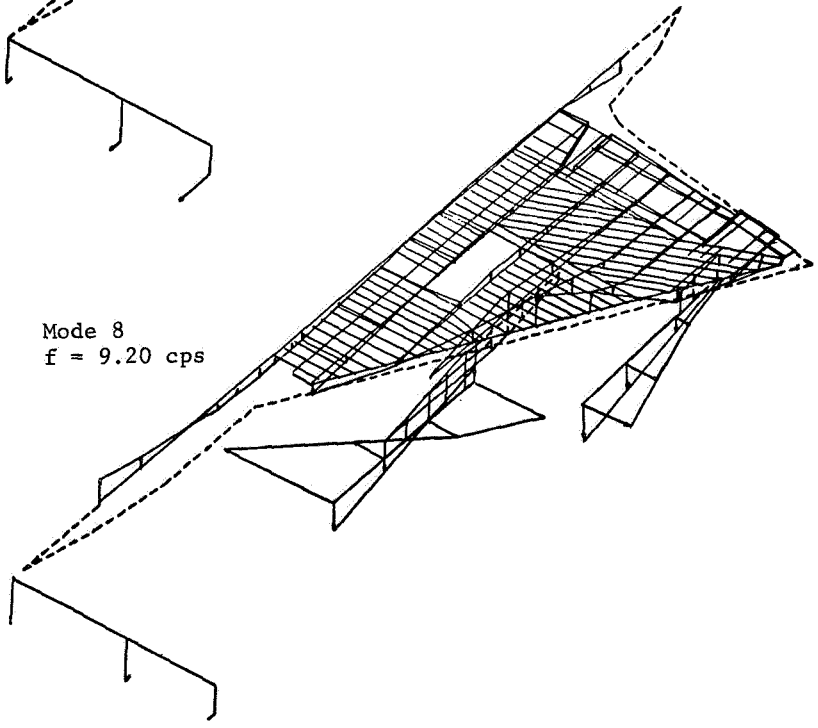

Figure B2 Continued Computed Modes, Run 134-7

RUN 131-3

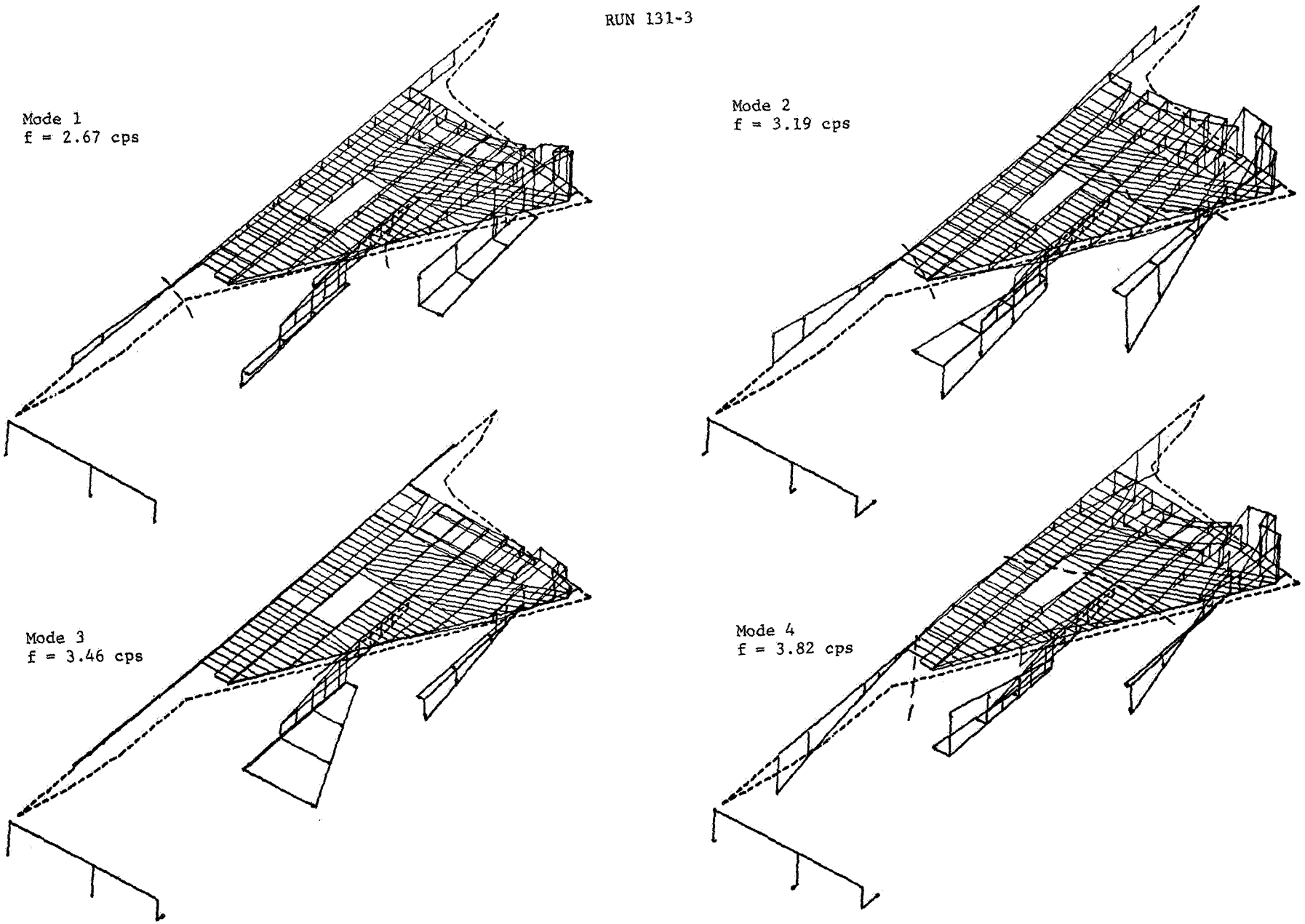

Figure B3 Computed Modes, Run 131-3

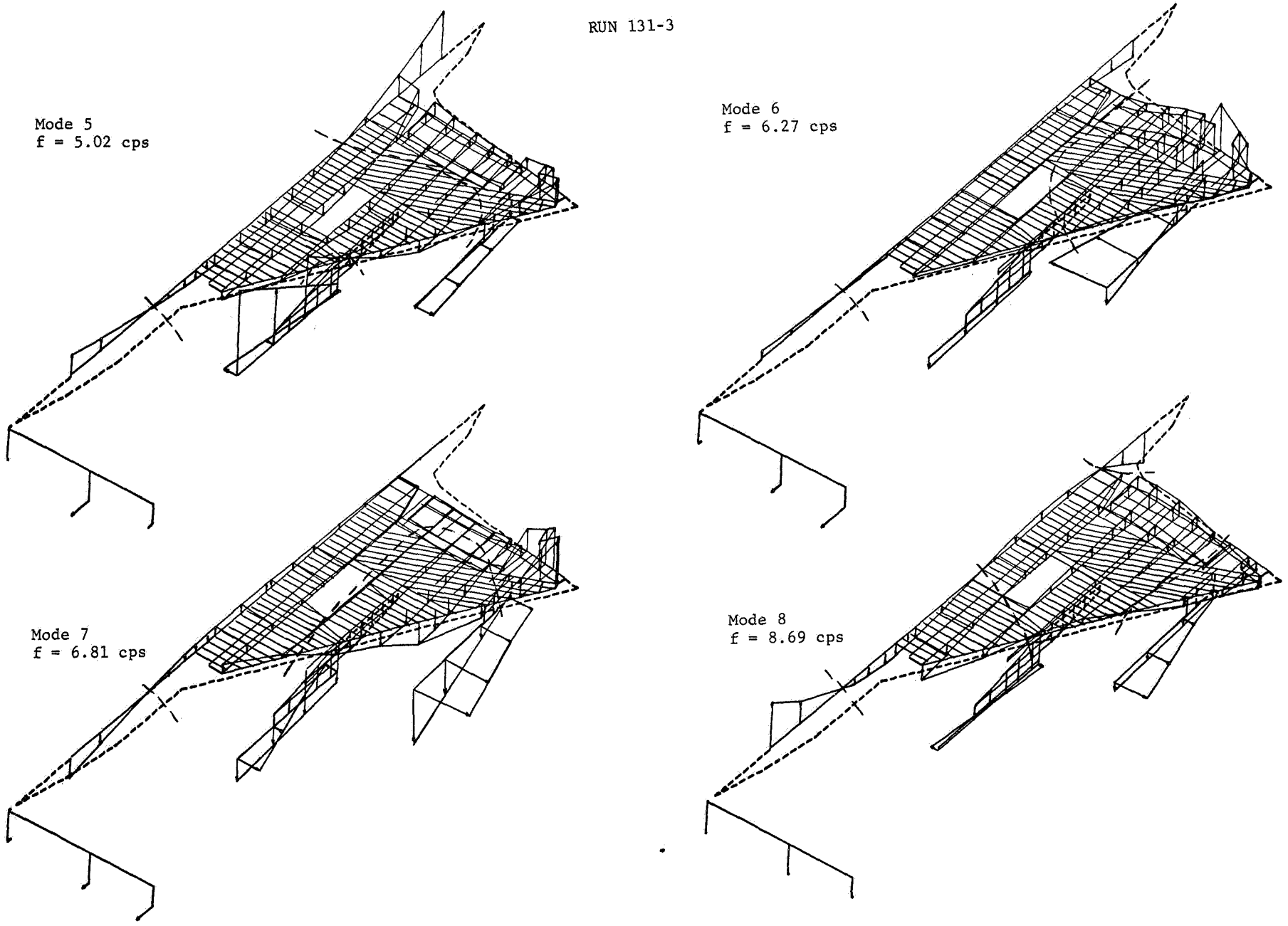

Figure B3 Continued Computed Modes, Run 131-3

APPENDIX C

SYMBOLS

APPENDIX C - SYMBOLS

The primary symbols used in this report are listed as follows:

$\bar{A}$ rms response to unit rms gust velocity

a acceleration

a_μ coefficient in pressure series

a.c. aerodynamic center location

C_{L_α} slope of lift versus angle of attack curve

C_{M_α} slope of moment versus angle of attack curve

$\hat{c}_{xy}$ raw estimate of prewhitened cospectrum

f frequency, cps

g_r structural damping of rth mode

H transfer function

H_c transfer function obtained from the ratio of the cross spectrum to the gust PSD

H_e equivalent transfer function by ratio PSD response to two-dimensional turbulence to gust PSD

H_L lower 90 percent confidence level on H_c transfer function

H_S transfer function obtained from the square root of response PSD to the gust PSD

H_U upper 90 percent confidence level on H_c transfer function

h(x,y,z) deflection of structure perpendicular to surface at point x,y,z

h	index indicating $h\Delta f$ frequency
h(t)	response to unit impulse
k	reduced frequency $b\omega/V$
L_a	loads compatible with deformed shape of aeroelastic mode
L_h	raw estimates of power spectrum
L	scale of turbulence
ℓ	distance from gust sensor to aerodynamic center
MAC	mean aerodynamic chord
M	maximum number of lags in autocorrelation function
M	Mach number
M_{rs}	generalized mass coupling between generalized coordinates r and s
m	mass
N	number of degrees of freedom
N	maximum number of data points in time series
N_o	characteristic frequency, cps
P	two sided power spectrum over negative and positive frequency range
P_a	aliased P power spectrum
Δp	difference in aerodynamic pressure between upper and lower surface
Q_r	generalized force acting on rth generalized coordinate
Q_{rs}	generalized force acting on rth generalized coordinate produced by unit deflection of sth generalized coordinate

Q_o	filter function or spectral window
$\hat{q}_{xy}$	raw estimate of prewhitened quadrature spectrum x and y time series
q_r	rth generalized coordinate
R	autocorrelation function
$\hat{R}$	autocorrelation function of prewhitened data
$\hat{R}_{xy}$	autocorrelation function of prewhitened x and y time series
R_D	autocorrelation function of Dryden gust spectrum
t	time
V	true airspeed
w	downwash
w_g	vertical component of gust velocity
x,y,z	Cartesian coordinate system
x,y	input and output time series, respectively
α	angle of attack
α'	slope of elastic deflection of gust boom
γ^2	coherency function
Δ	incremental value
δ	elevator deflection
θ	pitch angle
θ	phase angle
θ	pitch rate

ρ	air density
τ	time
ϕ	one sided power spectrum over positive frequencies
ϕ_D	Dryden gust spectrum
ω	frequency, radians per second
$\{\ \}$	column matrix
$[\ ]$	row matrix
$[\ ]$	square matrix
$[\ ]^T$	transpose of $[\ ]$ matrix

REFERENCES

1. Mitchell, D. B., Starkey, L. R., and Dills, T. A.: Instrumentation and Data Reduction Systems and Techniques for the B-58A Airplane Dynamic Response Flight Test Program, Fort Worth Division of General Dynamics Report FZS-4-249, January 1963.

2. Allen, R. V. and Archambault, R. G., Flight Test Calibration of The Douglas 5-Probe Differentail Head For Measuring Angles of Attach and Sideslip, Douglas Aircraft Company Inc., Santa Monica, California, Report No. DEV-1865, May 1955.

3. Peloubet, R. P. and Haller, R. L., Application of a Power Spectral Gust Design Procedure to Bomber Aircraft, AFFDL-TR-66-35, June 1966.

4. Goodman, N. R., On the Joint Estimation of the Spectra, Cospectrum and Quadrature Spectrum of A Two-Dimensional Stationary Gaussian Process, Scientific Paper No. 10, Engineering Statistics Laboratory, New York University, 1957.

5. Houbolt, J. C., Steiner, R., and Pratt, K. G., Dynamic Response of Airplanes to Atmospheric Turbulence Including Flight Data on Input and Response, NASA TR R-199, June 1964.

6. Watkins, C. E., Runyan, H. L., and Woolston, D. S., On the Kernel Function of the Integral Equation Relating The Lift and Downwash Distribution of Oscillating Finite Wings in Subsonic Flow, NACA Rep. 1234, 1955.

7. Hsu, Pao-Tan, Flutter of Low-Aspect-Ratio Wings, Part I, MIT - TR - 64-1, October 1957.

8. Murphy, A. C. and Wilson, L. E., B-58 Multiple Weapon Configuration Ground Vibration Test, Fort Worth Division Of General Dynamics Report FZS-4-224, February 1962.

9. Houbolt, J. C., On the Response of Structures Having Multiple Random Inputs, Jahr. 1957 der WGL, Friedr, Vieweg & Sohn (Braunschweig).

10. Blackman, R. B. and Tukey, J. W., The Measurement of Power Spectra, Dover Publications Inc., 1959.